

# **Fundamental Investigations into Screen Printing**

by

**Elisabeth Diane Dolden**

**Submitted in accordance with the requirements  
for the degree of Doctor of Philosophy.**

**The University of Leeds  
School of Mechanical Engineering**

**August 2005**

**The candidate confirms that the work submitted is her own  
and that appropriate credit has been given where  
reference has been made to the work of others.**

**This copy has been supplied on the understanding that it is copyright material  
and that no quotation from the thesis may be published without proper  
acknowledgement.**



## IMAGING SERVICES NORTH

Boston Spa, Wetherby

West Yorkshire, LS23 7BQ

[www.bl.uk](http://www.bl.uk)

**BEST COPY AVAILABLE.**

**VARIABLE PRINT QUALITY**

# Acknowledgements

I would like to thank firstly my supervisors, Prof. Phil Gaskell and Dr. Nik Kapur, who have provided me with great support and guidance throughout my studies, in particular for their knowledge and expertise. I'm also sincerely grateful to my sponsor, Prof. Steven Abbott for all his assistance and continual enthusiasm of my work.

I'd also like to thank Dr. Jon Summers for always assisting and fixing with any computer related problems I encountered. And also Dr. Mark Wilson for his help with FLOW3D. And of course thanks to my fellow PhD friends.

I would also like to thank Devon Darby for his superb technical advice. And a huge thanks also to Paul Banks for manufacturing and assembling the cell filling rig to my design; and also for his frequent help in the lab, and for the numerous occasions on which my lab equipment needed to be transported back and forth throughout the mechanical engineering building.

I must also give special thanks to my family for supporting me with their continual encouragement offered throughout all of my studies over the numerous years that I've been at university. To my great network of friends, for often distracting me away from my studies and in doing so giving me both motivation and inspiration, and again providing me with great support through a really challenging experience. In particular, Steph and Mike, Alex, Steve, Damian, Armando – to name just a few.

Without receiving funding, I would not have been able to complete this work, and so I owe a massive thanks to the School of Mechanical Engineering, the EPSRC, and to my sponsors, Autotype.

# Abstract

The focus of this thesis is a fundamental investigation of the process of mechanisms involved in the process of screen printing. Accordingly, the process is sub-divided into three distinct stages: the flooding of excess ink onto the mesh; the metering of the ink; the printing of the image. This differs from the normal one of viewing it as a two-stage process where metering and printing are not distinguished from each other.

Experiments are conducted using a purpose built contact screen printing apparatus that allows a detailed study of the effect of each of the press variables on the final print thickness. The results show that the process is relatively insensitive to many of these factors, with the geometry of the mesh (dictated by thread count and diameter) and, to a lesser extent, the fluid properties, being the overriding parameters that affect the print thickness. The work also highlights, for the first time, that the mesh is only approximately half filled with ink prior to printing, and the semi-empirical models used by industry to predict print thickness have been refined and improved accordingly.

Computational fluid dynamics (CFD) simulations of the problem have also been performed to highlight the mechanism of ink transfer at the printing stage of the process. The results reveal a free-surface dominated process, one that shows little dependence on many operating parameters, and in accordance with the above complementary experimental investigations.

Finally, the process by which fluid fills the screen under the action of a moving blade is studied. An idealised novel geometry is adopted, that of a single cell cut into a smooth plate. A precision test rig and optical viewing system were designed and built for this purpose, with high speed photography used to reveal a rich dynamic process where a number of final states are possible. These include cells that are completely full, partially full or empty of fluid, and the dependence of filling type on the properties of the system has been determined.

This thesis is dedicated to my mum, dad, and little sister Michele.

# Contents

<b>1</b>	<b>Screen printing</b>	<b>1</b>
1.1	General introduction to screen printing.....	1
1.2	The importance of controlling the screen printing process.....	4
1.3	Experimental work into screen printing.....	6
1.3.1	Characterising the fluid.....	6
1.3.2	Characterising print quality.....	8
1.4	Modelling the print process.....	11
1.5	Fundamental studies of screen printing.....	16
1.6	Related flows.....	18
1.7	Outline of the work presented.....	19
<b>2</b>	<b>Experimental apparatus and equipment</b>	<b>21</b>
2.1	Introduction.....	21
2.2	Manual screen printing rig.....	22
2.2.1	The main support frame.....	23
2.2.2	The vacuum system.....	23
2.2.3	The main motor and control unit for the vacuum platform raising mechanism.....	25
2.2.4	The meshes and frames.....	29
2.2.5	The squeegee blade.....	31
2.3	Cell filling rig.....	32
2.3.1	Main unit.....	33
2.3.2	Test cell pieces.....	33
2.3.3	Blade.....	35
2.3.4	Blade drive mechanism.....	35
2.3.5	Optical Viewing system.....	38
2.4	Image capturing.....	39
2.4.1	High speed camera and illumination.....	39
2.4.2	Microscope, camera and illumination.....	41
2.5	Measuring mass.....	44

2.6	Measuring dimensions and surface profiles of screen meshes and substrates.....	45
2.6.1	Single dimension measurement – Co-ordinate measuring machine KEMCO 400.....	45
2.6.2	2-dimensional measurement – Nikon Profile Projector Model V-16D.....	47
2.6.3	Surface profiling.....	48
2.6.3.1	Interferometry.....	49
2.6.3.2	Stylus profilometry.....	51
2.7	Fluid properties.....	55
2.7.1	Viscosity.....	55
2.7.2	Density.....	59
<b>3</b>	<b>Printed film thickness</b> .....	<b>61</b>
3.1	Introduction.....	61
3.2	Experimental method.....	62
3.3	Theoretical Ink Transfer Model (ITM) method.....	67
3.4	Experimental results and discussion.....	71
3.4.1	Effect of the mesh-substrate separation rate on the film thickness.....	71
3.4.2	Effect of mesh geometry on the film thickness.....	73
3.4.3	Effect of the fluid type on the film thickness.....	75
3.4.4	Effect of the substrate type on the film thickness.....	78
3.5	Theoretical model results and discussion.....	80
3.6	Comparison of experimental and theoretical results.....	81
3.7	Summary.....	83
<b>4</b>	<b>Initial ink volume in the mesh and the percentage ink transfer to the substrate</b> .....	<b>84</b>
4.1	Introduction.....	84
4.2	Experimental method.....	85
4.3	Experimental results and discussion.....	90
4.3.1	Mesh images of the printing process.....	90

4.3.2	Experimental printed thicknesses and ink transfers.....	105
4.3.3	Effect of varying fluid viscosity.....	109
4.3.4	Effect of varying fluid density.....	112
4.4	Development of theoretical models of the mesh.....	113
4.4.1	Model 1 – Circular cross-sectional thread.....	115
4.4.2	Model 2 – Adapted circular cross-sectional thread.....	117
4.4.3	Model 3 – Elliptical cross-sectional thread.....	118
4.4.4	Model 4 – Incomplete mesh filling.....	120
4.4.5	Model 5 – Refined estimation of the thread geometry.....	126
4.4.6	Ink Transfer Model (ITM).....	137
4.5	Results and discussion of the geometric mesh models.....	138
4.6	Comparison of experimental and theoretical results.....	154
4.7	Summary.....	162
<b>5</b>	<b>CFD study into the ink transfer process</b>	<b>164</b>
5.1	Introduction.....	164
5.2	Computer simulation method.....	167
5.2.1	FLOW3D software.....	167
5.2.2	2D problem setup.....	171
5.2.3	3D problem setup.....	177
5.3	FLOW3D results and discussion.....	181
5.3.1	2D problem transfer and average thickness results.....	182
5.3.2	2D simulation results graphically displayed with FLOW3D.....	193
5.3.3	3D problem results.....	197
5.4	Comparison of simulated and experimental results.....	200
5.5	Summary.....	204
<b>6</b>	<b>Individual cell filling</b>	<b>206</b>
6.1	Introduction.....	206
6.2	Design of the cell filling rig.....	208
6.2.1	Design of the main unit.....	209
6.2.2	Design of the test piece and cells.....	211
6.2.3	Design of blade unit.....	212



6.2.4	Design of optical viewing system.....	214
6.3	Experimental method.....	217
6.4	Experimental cell filling results and discussion.....	221
6.4.1	Captured images.....	222
6.4.2	Complete filling.....	223
6.4.3	Partial filling.....	228
6.4.4	Incomplete filling.....	238
6.4.5	No fill.....	243
6.4.6	Incomplete filling changing to partial filling.....	245
6.4.7	Effect of a manufactured flaw on the surface ahead of the cell.....	249
6.4.8	A comparison of fluid velocities within the cell.....	251
6.4.9	Effect of varying fluid.....	253
6.4.10	Effect of blade variables.....	256
6.4.11	Effect of cell geometry.....	260
6.5	Summary.....	263
<b>7</b>	<b>Conclusions and future work</b>	<b>264</b>
7.1	Conclusions.....	264
7.2	Suggested future work.....	267
7.2.1	Mesh filling process.....	267
7.2.2	Mesh emptying process.....	268
7.2.3	Simulations and geometric thread models.....	269
7.2.4	Related work.....	270
<b>Appendix 1</b>	<b>Experimental measurement theory of viscosity</b>	<b>271</b>
<b>Appendix 2</b>	<b>Printed film thickness</b>	<b>273</b>
<b>Appendix 3</b>	<b>Cell filling rig design drawings</b>	<b>276</b>
<b>References</b>		<b>288</b>

# List of figures

1.1	Diagram showing how the squeegee blade tip causes the brief contact between mesh and substrate.....	3
1.2	Illustrations of the forces involved in the transfer of ink of the mesh to the substrate: (a) adhesion zone; (b) extension zone; (c) flowing zone; (d) separation zone (Messerschmitt, E. (1982)).....	12
1.3	Illustration of a single mesh unit (represented 2-dimensionally), highlighting the open mesh area.....	14
2.1	Schematic drawing of the manually operated screen printing rig.....	22
2.2	Photograph of the vacuum pump and tubing connected to the vacuum platform.....	24
2.3	Photograph of the top view of the vacuum platform showing the channel system.....	24
2.4	Photograph of the mechanism for adjusting the height of the vacuum platform: the main motor and output shaft connected to cam that has the follower for the vacuum platform resting on it.....	25
2.5	Non-linear peel-off scale relationship for the 10 selected motor settings....	27
2.6	Results of the experiments to observe if slight relative height variations between the mesh and vacuum platform influenced the printed ink deposit on the substrate.....	28
2.7	Sketch showing the formation of plain weave (PW).....	29
2.8	Photograph of the squeegee side of a 90-40 mesh with no ink. The left-hand side of the photograph shows the capillary stencil. The reflective light strips at the thread knuckles are used to highlight the direction of the upper knuckle since the orientation is the same (see section 4.3.1 for further detail).....	29
2.9	Photograph of the cell filling rig.....	32
2.10	Photograph of the test piece mounted on the rig.....	34
2.11	Photograph of the steel blade tips.....	35
2.12	Photograph of the blade drive mechanism of the rig.....	36

2.13	Graph for converting motor voltage to equivalent linear blade speed.....	37
2.14	Photograph of the optical system – an adjustable angled mirror, a beam splitter and a right angled mirror.....	38
2.15	Photograph of the high speed camera connected to two recordable output devices: PC and video.....	39
2.16	Screen shot image of Pixelink Capture software control parameters.....	42
2.17	Photograph of the Nikon microscope, mounted to the support stand arm, viewing a mesh on the manually operated screen printing rig. Also connected to the microscope is the light supply and Pixelink camera.....	43
2.18	Photograph of the top loading mass measuring balance used to measure masses to a limit of 410g.....	44
2.19	Photograph of the co-ordinate measuring machine KEMCO 400. ....	45
2.20	Sketches highlighting how probe size can affect measured mesh thickness: (a) thickness correctly measured when positioned directly on the peak of the knuckle; (b) under-measurement of thickness occurs if probe is placed anywhere else on the surface of the mesh.....	46
2.21	Diagram of the mesh sandwiched by metal, removing the need for precise probe positioning on peaks of thread knuckles, whilst ensuring measured thickness is not comprised.....	47
2.22	Photograph of the Nikon Profile Projector Model V-16D.....	47
2.23	Photograph of the WYKO NT3300 machine in use.....	49
2.24	Surface profile and Ra roughness parameter.....	50
2.25	The Form Talysurf 120L machine used to measure surface roughness parameters.....	52
2.26	Sketch highlighting two limit situations of the stylus for surface measurements: (a) acute angles; (b) undercuts. The red dashed lines depict the path followed by the stylus.....	53
2.27	2D surface profiles of MA10 and matt substrates.....	54
2.28	A Bohlin rheometer.....	55
2.29	Effect of shear rate on viscosity, measured using cone (4° Ø40mm) and plate geometry, for a non-Newtonian ink (Sericol seri disc cyan) and a Newtonian fluid (Glycerine).....	57

2.30	Sketches demonstrating the correctly filled gap between the rheometer plates.....	58
2.31	Photograph of the cup used for density measurement of inks.....	59
2.32	Photograph of water filled density cup highlighting potential calculated volume error due to the meniscus shape.....	60
3.1	Graph showing the measured viscosity of the 10 test fluids in the shear rate range of $1-100\text{s}^{-1}$ at $20.0^\circ\text{C}$ ; viscosities extrapolated to shear rates of $1000\text{s}^{-1}$ .....	64
3.2	Schematic of the initial state of the mesh filled with fluid.....	67
3.3	Schematic development of the liquid bridge as the separation between substrate and threads is increased (Abbott, Gaskell and Kapur (2001, private communication)).....	67
3.4	Diagram of adjacent threads in cross-section.....	68
3.5	System used to solve the problem (Abbott, Gaskell and Kapur (2001, private communication)).....	69
3.6	The printed film thickness of the tested inks and grease for peel-off rates in the range $1.7-14.1\text{mms}^{-1}$ using the 150-31 mesh. Each point on the graph is the average of 5 prints with the same set-up conditions.....	72
3.7	Graph showing the printed film thicknesses for the 3 meshes using the 10 tested fluids. The fraction of mesh open area is established from the dimensional measurements of the meshes, rather than using manufacturer's values.....	73
3.8	Graph showing the non-dimensional printed film thickness for the 3 meshes using the 10 tested fluids. The confidence limits for the meshes' two extreme fluid printing thicknesses are also displayed. The best fit lines relate to: R3 grease (positive correlation), Sericol black ink (negative correlation) and Sericol white ink (no correlation).....	74
3.9	Comparison of the non-dimensional printed film thickness range with the density of the 10 test fluids. The confidence limits shown apply for the 3 meshes used.....	76
3.10	The effect of substrate roughness on the printed film thickness of NAZDAR black ink.....	78

3.11	Diagram illustrating how the surface roughness may affect the actual film thickness even if the same volume of ink is deposited.....	79
3.12	The ITM non-dimensional film thickness results compared to the 2 extremes of experimentally observed film thicknesses of the inks and grease, for the 3 screen meshes.....	81
4.1	Graph of the measured viscosity of the NAZDAR black <sub>[2]</sub> dilutions in the shear rate range of 1-100s <sup>-1</sup> . Shear rate versus viscosity measured using a cone (4° Ø40mm) and plate geometry at 20.0°C.....	86
4.2	Image of the clean 120-34 mesh (outer region) overlaid with the image of the mesh just after printing with NAZDAR black <sub>[2]</sub> ink (inner region)....	90
4.3	The initial 90-40 mesh state filled with Sericol black ink. N.B. the main features of the image are labelled to assist with identifying features in the following images (i.e. up to Figure 4.5): white regions are light reflectance from surfaces perpendicular to the microscope.....	92
4.4	150-31 mesh filled with Sericol black ink. N.B. The twin line feature, highlighting the orientation of the lower thread, is yellow for the 150-31 mesh. The white circular regions at cell centres are caused due to reflectance from the ink (as described in Figure 4.3).....	92
4.5	The initial 90-40 mesh state filled with Sericol white ink.....	93
4.6	Interferometry surface results taken using WYKO machine of the 120-34 light framed mesh filled with Sericol white ink just after the metering squeegee stroke.....	94
4.7	Two slice profiles of the squeegee side surface of the Sericol ink filled 120-34 light framed mesh, measured with the WYKO apparatus.....	95
4.8	Photograph showing the square-like shape with rounded corners of the Sericol magenta ink menisci remaining in the 150-31 mesh after printing. .....	97
4.9	Photograph showing circular menisci of NAZDAR black <sub>[2]</sub> ink remaining in the 120-34 mesh after printing. ....	97
4.10(a)	Photograph just after printing occurred using 90-40 mesh and Sericol white ink.....	99

4.10(b) Photograph taken 5 seconds after image in Figure 4.10(a), highlighting the reduction of meniscus radius in the central cell causing progression of a “closed” cell.....	100
4.10(c) Photograph taken 5 seconds after image in Figure 4.10(b), showing a fully developed “closed” cell.....	100
4.11(a) Photograph of 90-40 mesh after printing R3 grease, showing a “closed” cell.....	101
4.11(b) Photograph of 120-34 mesh after printing R3 grease, showing “closed” cells.....	102
4.11(c) Photograph of 150-31 mesh after printing R3 grease, showing a higher proportion of “closed” cells than with the other meshes.....	102
4.12 Presence of “closed” cells also observed with the NAZDAR black <sub>[2]</sub> ink, but only with the 150-31 mesh.....	103
4.13 Sketches of various stages of the mesh during the printing process.....	104
4.14 Diagrams of capillary sections used to illustrate Laplace’s Law.....	105
4.15 A comparison of the open area of 3 light framed meshes with the non-dimensional film thickness for the fluids printed. The dividing line on the graph highlights that the region above generated square-like menisci with the ink remaining in the mesh, and the region below exhibited circular menisci.....	106
4.16 Effect of shear rate (in the range of 1-100s <sup>-1</sup> ) on viscosity measured using a cone (4° Ø40mm) and plate geometry at 20.0°C. Graph is extended for shear rates up to 1000s <sup>-1</sup> , using power law assumptions to estimate the corresponding viscosities.....	110
4.17 Comparison of the viscosity of 3 NAZDAR black <sub>[2]</sub> ink dilutions with the non-dimensional film thickness.....	111
4.18 Graph showing the effect of viscosity on the percentage fluid transfer to the substrate, for the 3 NAZDAR black <sub>[2]</sub> dilutions.....	112
4.19 3-dimensional illustration of the woven thread structure of the unit cell ( $M \times M \times 2D$ ).....	115
4.20 The geometric variables of the mesh unit cell.....	116
4.21 Unit cell mesh parameters for the adapted circular cross-sectional thread model.....	117

4.22	The unit cell parameters involved for considering elliptical cross-sectional threads. N.B. The warp and weft labelling is in the “direction of” and is not specific to the thread type. $D_{warp}$ (and $D_{weft}$ ) refer only to the major diameter of the thread width, and not the minor diameter in the thickness direction.....	119
4.23	Illustration of ink levels introduced for incomplete mesh filling.....	120
4.24	The main thread dimensions for each model 4 version, highlighting the cross-sectional area shape. Model 4.3 incorporates the geometrically measured difference between weft and warp threads, indicated by *.....	121
4.25	Diagram of the ellipse and an example segment cross-sectional area generated from horizontal thread slicing. The points labelled $-c$ and $c$ are the ellipse foci, occurring on the centre-line of the minor axis.....	122
4.26	Diagram highlighting the equal ellipse segment area for successive horizontal slices.....	123
4.27	Illustration modelling the thread using torus and cylinder geometry.....	126
4.28	Diagram focusing on the centre-line of a thread of diameter $D$ and thread spacing $M$ , to establish the value of $\theta$ .....	127
4.29	Diagram showing how rotation of a circle forms a torus.....	129
4.30	Diagram showing a horizontal slice through the torus highlighting the parameters involved to calculate the slice area.....	130
4.31	Diagram showing a horizontal slice through the additional torus section highlighting the limits $x_{min}$ and $x_{max}$ involved for calculating slice area...	132
4.32	Diagram showing the ellipse segment of a horizontal slice through the central cylindrical section of the thread highlighting the parameters used to calculate slice area. The points labelled $-c$ and $c$ are the ellipse foci...	133
4.33	Diagram showing the “progression back” of the ellipse segment limits through the range of $h_c$ when $q$ is constant and equal to $q_{max}$ ; the limit points of Figure 4.32 are labelled.....	135
4.34	A graphical representation of the calculated maximum film thicknesses using model 1 – the key depicts 10 $\mu$ m ranges of these film thickness values ( $\mu$ m).....	142
4.35	A graphical representation of the effect of thread compression on the calculated maximum film thickness ( $\mu$ m) using model 2.....	143

4.36	Graphical representations of model 3 variables on the calculated maximum film thickness. The key depicts the calculated maximum film thickness values ( $\mu\text{m}$ ).....	144
4.37	Graphical representations of model 3 variables on the calculated maximum film thickness. The key representing ranges of the calculated maximum film thickness values ( $\mu\text{m}$ ).....	145
4.38	Relation between the level the ink fills to in the mesh cells and the calculated theoretical dimensionless maximum film thickness for model 4.3. (L indicates light framed mesh.).....	147
4.39	Comparison of the calculated theoretical maximum film thicknesses for the 90-40 mesh geometry, when the cells are partially filled. (L – light framed mesh; H – heavy framed mesh.).....	148
4.40	Graph showing the relation between the level the ink fills to in the meshes and the calculated theoretical dimensionless maximum film thickness. ....	150
4.41	Theoretical non-dimensional maximum film thicknesses for incomplete mesh filling, observing the influence of the mesh count.....	151
4.42	Theoretical maximum film thickness for incomplete mesh filling for the mesh geometries.....	152
4.43	Comparison of the non-dimensional initial ink thicknesses in the meshes for the experimental data and the theoretical models using equivalent meshes.....	155
4.44	Comparison of the amount of ink initially in the experimental mesh, represented as a thickness (equivalent to the maximum film thicknesses obtained assuming 100% ink transfer from the mesh to the substrate), with the mathematical models developed to incorporate partially filled cells.....	157
4.45	Theoretical maximum film thickness results for incomplete mesh filling calculated from the adapted models 4 and 5 that limit the maximum mesh thickness to the measured experimental mesh thickness.....	158
4.46	Illustration of the effect of lowering the initial ink level: (a) 100% ink filled mesh; (b) initial ink level lowered comparable to experimental.....	161



5.1	(a) Image of the printed surface obtained printing Sericol UV speed blue ink through a 120-20 mesh. The darker regions in the print indicate a higher concentration of ink due to a local increase of film thickness i.e. peaks (Abbott, S. (2005, private communication)). (b) Image (a) overlaid with the corresponding mesh image, aligned using the edges of the stencil (Abbott, S. (2005, private communication)).....	165
5.2	Arrangement of the geometries defined in the 2D problem using both a full mesh unit and a half mesh unit.....	171
5.3	Diagram showing the boundary conditions and type.....	172
5.4	Initial ink height levels: (a) fills to the maximum thread height with the gap; (b) fluid volume is set filling to the thread peak with no gap, then the gap is introduced causing the ink height to be lower than the maximum height of the initial placement of the thread.....	175
5.5	Diagram of the simplified joins used in the 3D problem to replace true woven structure of screen printing meshes.....	177
5.6	Initial setup of the thread and substrate geometry in a quarter mesh unit (QMU).....	178
5.7	The effect viscosity has on the simulated average film thickness deposit. Setup modelled 90-40 screen mesh, using Sericol cyan values of density, surface tension and contact angles, with a peel-off rate equivalent to motor setting 7.0. Initial filling level has been compensated for the gap. 184	
5.8	The effect viscosity has on the simulated percentage transfer to the substrate. The setup modelled is the same as that in Figure 5.6.....	185
5.9	The effect surface tension has on the simulated average deposited film thickness. Setup modelled 90-40 screen mesh, using Sericol cyan values of density, viscosity and contact angles, with a peel-off rate equivalent to motor setting 7.0. Initial filling level was adapted for the gap.....	186
5.10	The effect surface tension has on the simulated percentage transfer to the substrate. The setup modelled is the same as that in Figure 5.8.....	186
5.11	The effect of the contact angle on the average film thickness for both gap adapted and maximum initial filling types. Setup modelled 90-40 screen mesh, using Sericol cyan values of density, viscosity, surface tension and contact angle (substrate contact angle maintained at 45° while thread	

	contact angle is varied – labelled as THREAD in the key, and thread contact angle remaining constant at 15° for variation of substrate contact angle – labelled as SUBSTRATE in the key), with a peel-off rate equivalent to motor setting 7.0. ....	187
5.12	The effect of the contact angle on the percentage transfer for both gap adapted and maximum initial filling types. The setup modelled is the same as that in Figure 5.10. ....	188
5.13	The effect fluid density has on the calculated average deposited film thickness for both gap adapted and maximum initial filling types. Setup modelled 90-40 screen mesh, using Sericol cyan values of viscosity, surface tension and contact angle, with a peel-off rate equivalent to motor setting 7.0. ....	189
5.14	The effect density has on the percentage transfer for both gap adapted and maximum initial filling types. The setup modelled is the same as that in Figure 5.12. ....	190
5.15	Comparison of the peel-off rate and the calculated average film thickness for both gap adapted and maximum initial filling types. Setup modelled 90-40 screen mesh, using Sericol cyan fluid property values. Confidence limits depict the peel-off rate increase equivalent to experimental chapter 3 observations for time range 0-0.15s. ....	191
5.16	Graph showing the effect the peel-off rate has on the percentage transfer for both gap adapted and maximum initial filling types. The setup modelled is the same as that in Figure 5.14. Peel-off rate confidence limits are omitted for clarity. ....	192
5.17	Image representing the fluid fractions between 0 and 1 in the calculation zone – indicated on the key. The contours for the lower section are labelled with the corresponding fractions. ....	193
5.18	FLOW3D simulations graphically displaying a series of images of the 2D HMU problem, mirrored forming a full mesh unit. The colour coding represents z-velocity ( $\text{ms}^{-1}$ ) of each calculation cell, each simulation time having an individual key as shown. Problem setup: 90-40 screen mesh, using Sericol cyan fluid property values, with peel-off rate equivalent to motor setting 7.0. Initial filling level was adapted for the gap. ....	195

5.19	Graphical display of the initial and end results for the same setup as Figure 5.17, but with MAX initial filling.....	196
5.20	FLOW3D simulations graphically displayed of the 3D problem for an idealised 90-40 mesh. Colour coding is the same as used in Figure 5.17. .....	197
5.21	QMU simulated view from above the threads ( $200 < z < 250 \mu\text{m}$ ) at 0.107s.	199
5.22	Average film thickness comparison of FLOW3D simulated results with equivalent experimental and ITM results of chapter 4.....	200
5.23	Percentage transfer comparison of FLOW3D simulated results with equivalent experimental and ITM results of chapter 4.....	201
5.24	Illustration of the effect of lowering the initial simulated ink level on the residual ink: (a) adapted gap initial level; (b) further reduction of initial ink to be comparable with experimental initial mesh filled state.....	202
5.25	Average film thickness comparison of FLOW3D calculated results with equivalent experimental results (90-40) of chapter 3.....	203
6.1	3D image of the cell filling rig designed with IDEAS software.....	209
6.2	Simple arrangement of prisms/mirrors used to direct two different simultaneous views of the cell to the camera.....	214
6.3	Arrangement of prisms/mirrors so that the two image beams have the same focal length.....	215
6.4	Arrangement of mirrors with a beam splitter for directing the two images of the cell region to the camera.....	216
6.5	Graph of the measured viscosity of HVI 60, HVI 160, EP80 and EP90 oils in the shear rate range of $1-100\text{s}^{-1}$ at $18.0^\circ\text{C}$ and $20.0^\circ\text{C}$ .....	217
6.6	Diagram of the test piece upper surface illustrating initial positions of blade and fluid addition.....	218
6.7	High speed camera aligned to capture cell filling events.....	219
6.8	(a) Photograph of two cell views captured simultaneously before the blade tip passes the cell. (Setup: HVI 160, $10^\circ$ blade, 0.10mm gap, 15.00V motor setting, and cell geometry $3 \times \text{Ø}3$ ) (b) Key features of image (a) are highlighted: a white dashed line is positioned at the division of the two views, the green line indicates fluid menisci, the blue	

	line locates blade edge, the blue arrow shows the blade direction, and the red line aligns with surface boundaries of the test piece or cell walls.....	222
6.9	Diagram of simplified completely filled screen and gravure printing cells.....	223
6.10	Sequence of images (continued on the next page) showing the removal of air and consequent complete filling of the cell with oil. (Exp 25, ID# 10 setup: HVI 160, 10° blade, 0.10mm gap, 7.00V motor setting, and cell geometry 3×Ø3).....	224
6.11	Simplified diagram of partially filled cells. Ink transfer from the cells is potentially more successful with screen printing cells than gravure cells.	228
6.12	Sequence of images (continued on the next page) showing bubble formation and subsequent removal as the blade tip passes. (Exp 24, ID# 9 setup: HVI 160, 10° blade, 0.10mm gap, 12.00V motor setting, and cell geometry 3×Ø3).....	229
6.13	Sequence of images showing bubble formation and subsequent removal as the blade tip passes. (Exp 46, ID# 32 setup: HVI 60, 10° blade, 0.10mm gap, 20.0V motor setting, and cell geometry 3×Ø3).....	232
6.14	Sequence of images showing formation of an air bubble that is removed after blade tip pass occurs. (Exp 41, ID# 27 setup: HVI 160, 20° blade, 0.10mm gap, 20.0V motor setting, and cell geometry 3×Ø3).....	234
6.15	Sequence of images showing formation of an air bubble that is removed after blade tip pass occurs. (Exp 31, ID# 16 setup: HVI 160, 30° blade, 0.10mm gap, 12.00V motor setting, and cell geometry 3×Ø3).....	236
6.16	Diagram of incomplete filling, highlighting that ink transfer is potentially more successful with gravure cells than screen printing cells.....	238
6.17	Sequence of images showing entrapment of air resulting in incomplete filling. (Exp 22, ID# 7 setup: HVI 160, 10° blade, 0.10mm gap, 15.00V motor setting, and cell geometry 3×Ø3).....	239
6.18	Sequence of images showing the fluid meniscus entrapping air resulting in incomplete filling. The surface of entrapped air deforms as the blade passes. (Exp 21, ID# 6 setup: HVI 160, 10° blade, 0.10mm gap, 80.0V motor setting, and cell geometry 3×Ø3).....	241

6.19	Diagram of simplified screen and gravure printing cells containing no fluid.....	243
6.20	Sequence of images showing the blade passing the cell with no fluid entering. (Exp 44, ID# 30 setup: HVI 160, 10° blade, 0.50mm gap, 100.0V motor setting, and cell geometry 3×Ø3).....	243
6.21	Sequence of images (continued on the next page) showing the meniscus passing along the base of the cell forming an enclosed bubble which is subsequently removed. (Exp 35, ID# 21 setup: HVI 160, 30° blade, 0.10mm gap, 40.0V motor setting, and cell geometry 3×Ø3).....	245
6.22	Sequence of images (continued on the next page) showing a thin layer of fluid added to the cell which breaks converting incomplete filling to partial filling. (Exp 23, ID# 8 setup: HVI 160, 10° blade, 0.10mm gap, 13.50V motor setting, and cell geometry 3×Ø3).....	247
6.23	Sequence of images showing the effect a manufactured surface flaw has on the filling behaviour. (Setup: EP80, 30° blade, 0.10mm gap, 10.00V motor setting, and cell geometry 3×Ø3).....	249
6.24	Simplified diagram of the view underneath the cell showing two key events used to define a non-dimensional time expression for filling behaviour comparison: (a) meniscus front reaches the cell edge and initially pins ( $T=0$ ); (b) cell closure occurs as the fluid coats the opposite cell edge ( $T=1$ ); (c) average velocities of the meniscus within the cell.....	251
6.25	Graph of expected shear rates for the cell filling rig.....	253
6.26	Photographs captured from the underside view of the cell, showing the fluid meniscus position as fluid commences entry to the cell (i.e. end of delay period) for a range blade speeds.....	257
6.27	Effect of blade angle on filling.....	258
A1.1	Diagram determining the required gap used between cone and plate surfaces.....	272
A2.1	Average film thickness using 90-40 mesh for a range of mesh-substrate separation rates.....	274
A2.2	Average film thickness printed on 120-34 mesh for a range of mesh-substrate separation rates.....	275

A3.1	Location sites of the support stands on the breadboard.....	284
A3.2	Image of some of the rig components mounted on the breadboard.....	285
A3.3	Image of the rig partially completed incorporating all optical components and some components of the blade drive section.....	286
A3.4	Image of the rig without: the motor, flexible coupling and end bearing....	287

# List of tables

2.1	The available meshes – data relates to the manufacturers’ provided data (Saati (2002b), Sefar (1999a)).	30
2.2	Available cell geometry of the test pieces.	34
2.3	Measured roughness data of the available substrates performed on the Taylor Hobson Talysurf machine.	54
2.4	Densities of the test fluids.	60
3.1	Results of the ITM theoretical printed thickness for the meshes used experimentally.	80
4.1	The meniscus shape of the fluids remaining in the mesh after printing. “Closed” cells are highlighted.	98
4.2	Table showing the percentage fluid transfer and the initial ink thickness for the 3 light framed meshes.	107
4.3	Calculated shear rates ( $s^{-1}$ ) of the NAZDAR black <sub>[2]</sub> dilutions for the three meshes at peel-off operating at motor rate 7.0.	110
4.4	The measured mesh dimensions of the light-framed meshes.	114
4.5	Table of equations used to calculate the main model 4 geometrical thread parameters.	125
4.6	Table of the calculated $\theta$ values for the mesh geometries.	128
4.7	The co-ordinates of the 6 limit points of Figure 4.32.	134
4.8	Mathematical results for models 1-3.	138
4.9	Theoretical maximum printed film thickness ( $\mu m$ ) results for 100% filled cells calculated using model 4.	146
4.10	Theoretical maximum printed film thickness ( $\mu m$ ) results for 100% filled cells calculated using model 5.	149
4.11	The ITM calculated results established by solving the percentage fluid remaining in the mesh after printing.	153
4.12	Comparison of the experimental percentage fluid transfer with the calculated ITM value for equivalent meshes.	160

5.1	Table of the number of cells in each $x$ , $y$ , $z$ direction for the simulations run.....	173
5.2	Thread diameter and spacing used in the calculations.....	174
5.3	The ranges of solved fluid properties.....	175
5.4	Initial ink levels for MAX and gap adapted filling.....	176
5.5	Table of the number of cells in each $x$ , $y$ , $z$ direction for the quarter mesh unit simulation run.....	179
5.6	Summary of FMU and HMU results, with coarse and fine meshing. The setup models 90-40 screen mesh, Sericol cyan ink fluid properties filled initially to the gap adapted level, with the substrate lowered at speed equivalent to motor setting 7.0 of the experimental rig used in chapter 3.	182
5.7	Table of results for the simplified screen mesh geometries solved using the HMU simulation.....	183
6.1	Comparative results between fluids.....	255
6.2	Comparative results of the blade variables: angle, speed and gap.....	256
6.3	Comparative results of the cell geometry.....	260
A1.1	Gap setting and test fluid volume for available cone and plate geometry.	272



# Nomenclature

The following definitions of these symbols are applied throughout this thesis. Any local variations of these symbols are clearly defined within the relevant text, with the use of diagrams where appropriate.

$A$	Area	$m^2$
$a$	Half of the major diameter of an ellipse	
$ao$	Percentage open area of the mesh	
$b$	Half of the minor diameter of an ellipse	
$c$	Half of the distance between the 2 ellipse foci	
$Ca$	Capillary number	
$circ$	Angled distance through thread to slice level (model 5 – chapter 4)	
$D$	Thread diameter, width	$\mu m$
$h$	Distance of height, ink level	m
$H$	Non-dimensional ink thickness	
$H(X)$	Distance from thread centre	
$h_{av}$	Average film thickness	m
$H_{max}$	Theoretical maximum ink thickness	m
$H_o$	Half the distance between consecutive threads, gap between blade tip and test piece surface	m
$L$	Length	m
$m$	Mass	kg
$M$	Mesh spacing	$\mu m$
$P$	Pressure	$Nm^{-2}$
$q$	Sagatti length	
$R$	Radius of thread	m
$r$	Roughness	$\mu m$
$R_a$	Arithmetic mean roughness parameter	$\mu m$
$S$	Surface distance of slices used in (model 5 – chapter 4)	
$T$	Mesh thickness	m

$T$	Non-dimensional time	
$t$	Time	s
$U$	Linear blade speed	$\text{ms}^{-1}$
$u$	Peel-off rate	$\text{ms}^{-1}$
$V$	Volume	$\text{m}^3$
$V_{1,2,3,4}$	Velocity of fluid meniscus	$\text{ms}^{-1}$
$V_{th}$	Theoretical ink volume	$\text{cm}^3\text{m}^{-2}$
$X$	Dimension in Cartesian co-ordinates	m
$x, y, z$	Cartesian co-ordinates	
$Y$	Dimension in Cartesian co-ordinates	m
$\mu$	Fluid viscosity	Pa.s
$\varnothing$	Cell diameter	m
$\theta, \beta$	Arbitrary angle	degrees
$\rho$	Fluid density	$\text{kgm}^{-3}$
$\sigma$	Surface tension	$\text{Nm}^{-1}$
$\omega$	Angular rotational speed	$\text{rads}^{-1}$

# Chapter 1

## Screen printing

---

### 1.1 General introduction to screen printing

Screen printing is one of the oldest printing processes with its origins dating back thousands of years to ancient Chinese printing (Riemer, D. E. (1988), Parikh, M., et al. (1991)). It was originally called silk screen printing (Hohl, D. (1997b), Parikh, M., et al. (1991)) and traditionally used primarily in the graphic art industries (Riemer, D. E. (1988)). The basic process has undergone only minor modifications from its original process and yet has been widely adopted by many industries due to the attractiveness of its simple nature, relative cheapness, and great versatility of being able to print on a wide range of substrates and with a myriad of inks (Barker, M. J. (c1999)). These advantages make printing with this process not purely favourable but also superior compared to other more recently developed printing techniques that tend to be both more complex and expensive. Some of the industries that use screen printing for their products include: graphics, textiles, glass and ceramic decoration, music, electronics and medical.

Screen printing is used to manufacture an extensive range of products. One of the most commonly recognised products are t-shirt logo designs. Other products that are screen printed include: lottery scratch cards, credit cards, posters, road signs, CD

labelling, container labelling, membrane switches, printed circuit boards (PCB), sensors, encapsulated perfume scratch cards etc. (Barker, M. J. (c1999), Stephens, J. (1996)). Transfers are another commonly screen printed product, which may range greatly in not only size, but also in the final product application (i.e. from the label on a plastic bottle to the huge decoration logos applied to lorry side panels) (Barker, M. J. (c1999)). Ghiurcan, G. A., et al. (2003) have shown the viability of screen printing a thick film alkaline-battery. Other electronic applications include solar cells (Swiatek, Z., et al. (2003), Aernouts, T., et al. (2004)).

### **The process**

Screen printing is a relatively simple technique to apply, with ink being transferred through a stencilled pattern, held in position with a mesh constructed of woven threads, to reproduce the corresponding image on the print surface. There are primarily three printing stages involved in this transfer of ink: filling, metering and emptying of the mesh.

The filling and metering stages are controlled by strokes of a blade sweep. The first stroke applies an excess of ink to the screen filling it. The second stroke is performed in the opposite direction, removing the excess ink and thereby metering the volume of ink held in the mesh, ready to transfer the ink to the print.

Parikh, M., et al. (1991) states that “in an ideal screen printing process, the objective is to fill the pattern on the screen completely with the ink during the squeegee pass and leave all the ink on the substrate in the exact pattern as on the screen after the squeegee passes”. This is the theoretical optimal performance of both mesh and ink, with the complete transfer of ink to the substrate. However, it is accepted in industry that the process of transferring ink from the mesh to the substrate is an inefficient one; otherwise the procedure of screen cleaning to remove residual ink, ghost images and haze images (formed due to ink particles that become trapped in the mesh) would not be necessary (McCue, G. (2003)).

There are two main types of screen printing processes – contact and off-contact (Parikh, M., et al. (1991)). The main difference between these types is the control of when separation between mesh and substrate occurs. This separation mechanism enables the ink held in the mesh to transfer to the substrate and generate a print that corresponds with the patterned stencil. For off-contact printing, the mesh is positioned with a gap above the substrate, called the off-contact distance. The mesh makes contact with the substrate only during the metering stroke (as illustrated in Figure 1.1), with mesh release occurring shortly afterwards to transfer the ink onto the substrate surface (Hohl, D. (1997a)). Contact printing differs in respect that the screen is held in contact with the substrate throughout the filling and metering stages. The mesh release (also called peel-off) is initiated as a separate mechanism independent of the blade. The timing and rate of when mesh release occurs is therefore more controllable than with off-contact printing.

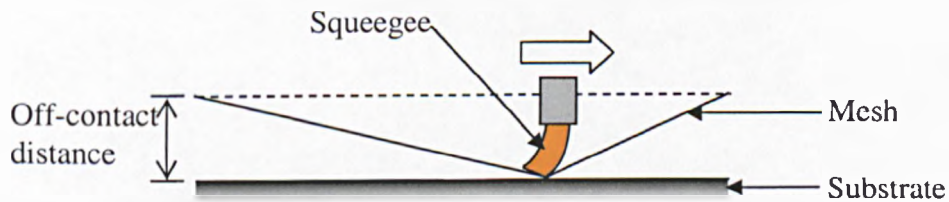


*Figure 1.1: Diagram showing how the squeegee blade tip causes the brief contact between mesh and substrate.*

### **The key components**

A screen mesh consists of threads (typically of polyester or steel) which are aligned in two perpendicular directions (warp and weft) and woven together as either a plain or twill type. For a plain weave construction, weft threads pass over one warp thread and then under the next warp thread (whilst the same weave pattern occurs in the warp direction passing over and under one weft thread) – this sequence is repeated throughout the mesh fabric (Sefar (1999b)), and so generates a structure comparable with the strings of a squash racket. For a twill weave, the threads pass over more than one thread of the perpendicular direction, which is then repeated so as to obtain a

constant pattern throughout the mesh fabric (Sefar (1999b)). The woven mesh fabric is tensioned, to be held within a frame. There is a vast range of mesh geometries available with differences in the thread diameter and spacing.

On the underside of the mesh, a stencil is applied to block regions that require no ink transfer to occur; therefore this creates a pattern held in place by the mesh threads. For graphic applications, the type of ink used greatly varies depending on the printed film requirements of the product. All coloured inks consist of particles called pigments – these give the ink colour (Sericol (2002)).

A blade motion is required to flood the ink on top of the mesh. Typically the off-contact process uses a metal flood bar for this sweep. A second blade is used for the printing sweep – this is typically a deformable squeegee blade, although other variations exist including metal blades. There are a vast array of blade speeds, angles, pressures, and materials used in its operation (Sefar (1999b)).

There are a large number of variations of the press arrangement from manual hand presses to those with automated controls. A vacuum bed is typically positioned beneath the screen to hold the substrate in place during the printing stage, when the contact between the ink filled mesh and substrate is made.

## **1.2 The importance of controlling the screen printing process**

Film thickness is a focal parameter when using screen printing. It dictates the necessary print setup (choice of mesh, stencil etc.) to obtain the required thicknesses specified by the design or function of the product. The range of film thicknesses that can be produced with screen printing typically lies in the range of 8-30 $\mu\text{m}$  – Barker, M. J. (c1999).

Control of film thickness is crucial for the industries working in this area. The thin film industry is reacting to a continual push for miniaturization, particularly for electrical components.

Film thickness becomes important when printing electrical circuits since it is inversely proportional to the resistance (Hunt, D. and Hohl, D. (1996c)), and for magnetic media the strength of the field is affected. Without control of the printed film thickness it is unlikely that the required resistance or magnetic strength will be attained, rendering the component potentially useless; or if used in combination with other components the impact may be disastrous to the working of the final product. If a non-uniform film thickness is printed, this will also lead to variation of the product functionality with potentially detrimental results. Both the printed film thickness and control of this parameter are crucial, if sacrificing quality and performance is not a feasible option.

Another, rapidly developing market is for organic light emitting diode (OLED) and polymer light emitting diode (PLED) devices, which require multiple thin layers of dry thickness coat of approximately 100nm (Pardo, D. A., et al. (2000)) – here control to the highest level is essential, without which results in significant loss in quality. Ultra-thin screen printed layers, less than 15nm, can be achieved (Jabbour, G., et al. (2001)). These fine layers were generated using a novel technique, by using a 0.2 $\mu$ m filter positioned above the screen mesh, to significantly reduce the initial volume of solution within the mesh, and subsequently reduce the deposit printed to the substrate. Polishing a printed surface also reduces thickness; in this way (polishing with SiC paper refined with mechanical and electrolytic polishing) Kühberger, M., et al. (2005) obtain film thicknesses of 2 $\mu$ m.

Achieving control of the film thickness is also crucial for opening up other new markets. For example, in the application of screen printing to sensors – typically prints of thickness of 5 $\mu$ m (Llobet, E., et al. (2003)) are required. There is a vast range of screen printed sensors available, including sensors for detecting compounds in beer (Cummings, E. A., et al. (2001)) to gases (for pollution monitoring devices – Traversa, E., et al. (2000)), with biosensors detecting substances such as glucose (Turkusic, E., et al. (2005)), or identifying e-coli bacteria (Ertl, P., et al. (2003)), whilst other sensors detect temperature change (Barker, M. J. (c1999)) or the presence of gamma radiation (Arshak, K., et al. (2004)).

When printing images for viewing (as opposed to those for electronic functionality) prints are generated by printing four colour halftones (cyan, yellow, magenta and black – CYMK). Halftones are an arrangement of dots that vary in concentration to imitate a full colour and tonal range. In regions where strong colours are required a high concentration of dots is necessary. If more than one ink is also required to be located in high concentrated halftone regions, then it is essential that the inks have a degree of transparency so that previous printed ink colours can be still viewed in the image. Thicker films reduce the ink transparency and therefore can affect the overall image (Claypole, T. C. (2002)). This requires consideration, particularly for posters or other visual media, to ensure quality is comparable to that of original photographic images or is at least of suitable quality when viewed from the intended distance.

An example of when reducing ink transparency is beneficial is observed with the metallic thick film layer printed on lottery scratch cards, applied to hide an underlying image, until the layer is intentionally removed (scratched) to reveal the image. Conversely, fluorescent inks require thick films to enhance the optical nature of the ink; screen printing produces a superior quality to other printing techniques (Barker, M. J. (c1999)).

### **1.3 Experimental work into screen printing**

#### **1.3.1 Characterising the fluid**

A key measurement in screen printing is that of the printed film thickness and there are numerous methods which can be used to measure film thickness. Firstly it should be acknowledged that there is a thickness difference between the printed wet and dried film states; incurred during the drying or curing process which causes some shrinkage of the ink. Although ultimately it is the dried film state which enables practical use of the final product, the wet state of the film (literally just after print and prior to any other treatment) provides better experimental data relating to the fluid mechanics of the printing process. The state of the film affects which film thickness measuring method can be implemented. Wet films ideally require non-intrusive techniques if the



print surface is not to be damaged. The measurement of dry films can use either non-intrusive or contact techniques without surface damage occurring, such as using a deltascopes or micrometers (Hunt, D. and Hohl, D. (1996c)). Depending upon the dry film thickness, less sensitive measuring equipment may also be suitable: i.e. for (dry) thick films a co-ordinate measuring machine (described in section 2.6.1) may be used ( $\pm 2\mu\text{m}$ ) – however any local variation in film thickness is likely to be undetected.

Many measurements rely on optical approaches to determine the film thickness. This includes the use of microscopes to measure the film thickness by applying a “depth focus” method or a light-section method (Hunt, D. and Hohl, D. (1996c)). The method requires part of the substrate to be visible with no ink, to provide a base level for ink measurements. Other optical approaches, such as interferometry (more commonly used for surface profiling) may be applied. This technique relies on light reflectance from both substrate and ink surface to measure the film thickness. A significantly smaller (and therefore more practical) instrument, more commonly used by printers, is a densitometer. The instrument is used primarily to monitor the colour quality of images (Thompson, B. (2004)). It measures ink reflectance, or transmittance of light wavelengths, calculating ink optical density. This data can be used to determine film thickness (Ruff, M. (2001), Thompson, B. (2004)).

A second class of non-intrusive measuring techniques is to determine the mass of the printed ink. The film thickness is established by combining the ink mass and density with the area of print (Riemer, D. E. (1973, 1974)). This method essentially calculates the average film thickness, without regard for identifying any local variations that may exist.

A novel intrusive technique, for use only with wet films, is a “blade wet deposit tester” (Hunt, D. and Hohl, D. (1996b)). The deposit tester is essentially a calibrated inclined rule, with fine saw-like teeth which is pressed into the wet film, to establish contact with the substrate surface below. Removing the piece without lateral motion, enables the wet film thickness to be directly read from the teeth marks without the need of a microscope: ink coating to the highest tooth mark indicates the thickness of the wet

film. This technique incurs unavoidable damage to the ink film surface, but offers a useful check of print setup.

Film thickness measurements have been used to determine the relationship between the choice of operating parameters (e.g. mesh, ink, and press setup), with a view to offering ways for printers to estimate the quantity of ink they require for a given job.

Martin, R. E., et al. (1974) used experiments that volumetrically measured the deposited ink and mesh residual ink. The deposited ink was dried before weighing and the residual ink was flushed from the mesh using solvent that was subsequently evaporated leaving the ink behind; it was found that approximately 30% of the ink remained in the mesh and 70% transferred to the substrate.

Hunt, D. (1999) reports the effects of the squeegee pressure and the length of the blade on the deposited film thickness. He concludes that increasing the pressure has the effect of an initial decrease of the film thickness which is then reversed with further increase of pressure; shorter length squeegee blades print more consistent film thicknesses, independent of the pressure applied.

Hohl, D. (1995) identifies that the mesh geometry is one of the primary factors affecting the thickness of the deposited film, which may also be used to characterise predicted thicknesses. This is discussed further in section 1.4.

### **1.3.2 Characterising print quality**

As well as the film thickness, which is a gross measure of the ink transfer, there are also a number of variables that affect the quality of the print. Many of these will be specific to the particular industry that screen printing is being used in. For example, the visual appearance of the print is paramount in the graphics industry, but is of secondary importance when tracks are printed for microelectronic circuitry (here resistance is crucial).

Extensive experimental work has identified printing factors that affect or deteriorate the quality of the print – so that ultimately unwanted features in the image may be avoided. For visual appearance it is important that the reproduced printed image is a faithful representation of the original positive image used to generate the negative stencil on the mesh. There are various identified features which may cause image distortion.

Claypole, T. C., et al. (1996) conducted experiments to investigate the effect of many printing parameters, including mesh tension, squeegee operation, and ink type, on the dimensional distortion of a printed image from that of the original film positive. The work concludes that the relationship is so complex that it fails to identify an isolated parameter that has a dominant effect on this type of image distortion. The effect of the off-contact distance was not investigated in this work, but it is highlighted that minimising this parameter reduces the distortion of the screen that is necessary to bring it into contact with the substrate during the printing stroke (Claypole, T. C., et al. (1996)); however simply reducing this parameter alone is likely to result in less effective separation between substrate and mesh, and consequently other press variables, such as screen tension, need adjustment to ensure good print quality is attained (Hohl, D. (1997a)).

Dot gain is a feature that must be considered particularly when printing using halftones (the tonal range generated by printing an arrangement of dots, as described in section 1.2). Dot gain can be sub-divided into two types: optical and mechanical dot gain (Lee, C.-H., et al. (1999)). Optical dot gain is a result of how the human eye processes the visual image, misinterpreting it from the true image – for example, due to light scatter from the dots or the poor frequency resolution inherent of the human eye. Mechanical dot gain is a result of the spreading of the printed dot on the print surface. Visually this affects the brightness, tone of colour, and resolution (Lee, C.-H., et al. (1999)).

Claypole, T. C., et al. (1997) investigated how both types of dot gain were affected by the thread spacing, the percentage of halftone (fraction of open area required for the halftone dot arrangement to produce the appropriate tone) and the shape of dot. Dot

loss was a common feature for halftones less than 50%, whereas in general, dot gain occurs above this halftone value (i.e. where the open fraction is greater than 50% and consequently the applied dot size is also greater). Claypole has also investigated the effect of the sequence of printing colour (varying the order of CMY) has on the perceived tone for a range of halftones – for the higher halftone percentages there is a tendency for the printed dots to overlap (Hamblyn, S. M., et al. (2002)). The work concludes that the order of print has significant effect on the final tone.

The definition of a printed edge may reduce in quality with the spreading of the printed ink. Liang, T.-X., et al. (1996) have experimentally investigated the effect of surface energies on edge definition, and conclude that reducing the wettability of the substrate minimises the spreading of the printed ink on the substrate and therefore improves the resolution of the printed edge.

Other unwanted features that affect the quality of the print include: streaking – due to an ink trail on the rear of the squeegee edge; pin-holes – due to the ink path to the substrate being blocked, i.e. by dust; stencil sawtooth – due to poor stencil selection; mottled appearance – due to insufficient mixing of the ink (Avery Dennison (2001)).

Hunt, D. (1999) notes that there have been more than 500 variables that affect the printing process. These can be grouped into five categories (Parikh, M., et al. (1991)):

- Ink rheology
- Screen printer setup
- Stencilled pattern
- Screen
- Substrate

Understanding the interaction of even these five variables is clearly a highly complex task.

## 1.4 Modelling the print process

An alternate approach, to purely measuring film thicknesses from actual prints, is the use of predictive models enabling a printer to approximate the expected film thickness for a given printing setup. The use of a predictive theoretical model is essential for designing the appropriate printing setup to generate film thicknesses defined by product design. This reduces the need of experimental trial and error, and therefore saves setup and printing time, and other resources (such as ink, substrates etc.). There is also another economical reason to predict the film thickness since this can be used to calculate the amount of ink used in a print run and therefore estimate the cost incurred (Hohl, D. (1998)).

An improved knowledge of the fundamentals of the process also allows the printing technique to be developed into areas it is not currently being predominantly used in, and to therefore push its capabilities. For example, OLED and PLED formulation have been available for some time, yet there is still considerable development work required to produce large displays economically; screen printing may be suitable for one (or more) processing steps if the process can be adapted for printing, for example, low viscosity solutions.

As early as 1982, Messerschmitt, E. (1982), in response to an article describing screen printing as an almost mystical process (“Spielvögel Schlep”), identified the screen printing process as one where cohesive and adhesive forces could be used to explain the ink transfer from the mesh to the substrate.

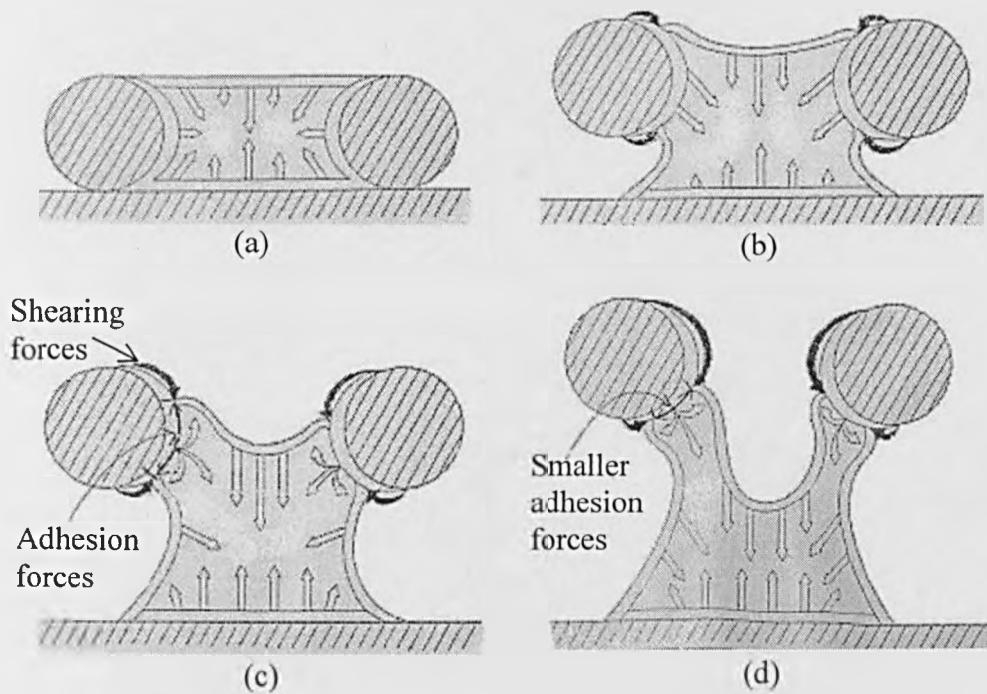


*Figure 1.2: Illustrations of the forces involved in the transfer of ink of the mesh to the substrate: (a) adhesion zone; (b) extension zone; (c) flowing zone; (d) separation zone (Messerschmitt, E. (1982)).*

The images Messerschmitt drew (Figure 1.2) clearly show a process where the free surface of the ink plays a key role in the transfer. Subsequent researchers chose not to treat the problem in such a way, but generally treated the mesh as either a smooth or a porous media plate, and tried to relate the pressure generated under the blade to the film thickness. A key deficiency of these models is that they do not offer predictive capabilities.

Riemer developed (1988) an analytical model to explain the effects of screen printing focusing on hydrodynamics of the squeegee rolled ink, with one recirculation zone, entering the mesh and depositing on the substrate after the squeegee passes and mesh separation occurs; there is no inclusion of surface effects in the model. He concluded that “any screening parameter which causes an increase of hydrostatic ink pressure will produce an increase in the thickness of the deposit on the substrate”. Variables that affect the ink pressure include the squeegee angle and speed, and ink viscosity: increased hydrostatic pressure is attained with increased squeegee speed and viscosity.

Earlier work done by Riemer, D. E. (1987) investigated the transfer of ink as “creeping flow”. Again there was no inclusion of surface effects, but he considered the effect the solid particles within the ink have on the transfer behaviour. He concludes that the solid particles displace to concentrate in the central regions of the mesh cells and that the ink near the threads is vehicle-rich and so acts as a lubricant during the ink transfer through the mesh. Solid particle size can greatly affect the ink transfer through the mesh; particles greater than a third of the open mesh size cause a blockage tendency and reduction of ink transfer to the substrate (Sefar (1999b)).

Huner, B. (1989) uses Lubrication Theory to analyze the interaction between blade and ink on a smooth plate, concluding also that increased squeegee speed and ink viscosity deposit thicker films. This work neglects the screen mesh and it is questionable if a smooth plate can represent the screen.

Owczarek, J. A. and Howland, F. L. (1990) developed a similar model of the ink roll at the squeegee tip to Riemer, D. E. (1988), which is more complex involving three recirculation zones: “pressurised region” (at the squeegee tip), “downward screen cross-flow region”, and “paste accumulation region”.

More recently, Fox, I., et al. (2003) have numerically (incorporating adaptations of Darcy’s Law) and experimentally studied the effect of hydrodynamic forces with a roller squeegee; their results can also be applied to screen printing with a blade squeegee. The results oppose Riemer’s earlier conclusions, finding that not all parameters that increase hydrostatic forces increase the deposit: increased blade speed (increasing the hydrodynamic force) was reported as actually reducing film thickness.

In a return to modelling the process as one where free surfaces dominate, Abbott, S., et al. (2001, private communication) proposed an ink transfer model that describes how ink interacts with the mesh and substrate. This is described in greater detail in chapter 3, but it essentially considers the separation of the mesh from the substrate and how this causes some fraction of the ink to remain on the threads with the remainder on the substrate. This model offers predictive capabilities and will be assessed as part of this work.

Given the lack of predictive capabilities from the majority of these models, a number of authors have concentrated on developing semi-empirical models to describe the process.

These models estimate a theoretical maximum thickness based solely upon the mesh geometry: mesh open area and mesh thickness (Hohl, D. (1995)). Developed from such a basic approach, adaptations to this model incorporate improvements to mesh geometry and acknowledgement of the existence of residual ink (remaining within the mesh after a print) by incorporating an arbitrary ink transfer fraction (Hohl, D. (1997b)). As noted previously, there is a degree of film thickness shrinkage experienced during the drying/curing process. Therefore, further amendments to include a shrinkage factor (determined for a typical dried ink) can be applied to predict the dry film thickness (Hunt, D. and Hohl, D. (1996a)). The starting point for many of these models is a simple expression of the volume of the mesh itself; as shown in Figure 1.3.

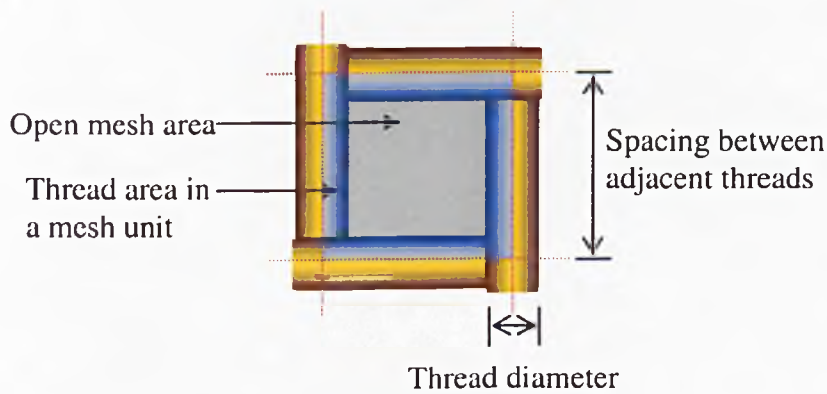


*Figure 1.3: Illustration of a single mesh unit (represented 2-dimensionally), highlighting the open mesh area.*

$$\text{Theoretical ink volume, } V_{th} = \frac{ao \times T}{100} \text{ [units: cm}^3\text{/m}^2\text{]}, \quad (1.1)$$

where  $ao$  is the percentage open area of the mesh,  
and  $T$  is the mesh thickness.



Hohl has published numerous papers aimed at developing and improving the accuracy of equation (1.1) (Hunt, D. and Hohl, D. (1990), Hohl, D. (1997b)). The developed Screen Printing Technical Foundation (SPTF) mathematical model divides the mesh into individual identical cells, and geometrically models these as cuboids with limits defined to be equal to simplified measured dimensions of the mesh and threads. Ink is assumed to occupy all space in the cuboids; the thread geometry is also simplified. From this Hohl advances a mathematical expression for calculating the maximum initial ink volume in meshes. The SPTF model is viewed by industry to be relatively accurate since it includes more accurate dimensions of the mesh cell whilst older models concentrated on purely the open area of the cell, disregarding the threads (equation (1.1)).

A greatly simplified version of the expression (removing most mesh parameters), is found in the bulletin (Hohl, D. (1995)) – shown below in equations (1.2) and (1.3). Hohl uses this simplified expression (in combination with print area and number of prints) to calculate an estimate of ink consumption for print runs (excluding ink required for print setup) that compare well to the actual measured ink consumption (Hohl, D. (1995)). This ink model is adapted for the printer to estimate total ink consumption for a print job and so includes: stencil thickness factors, image coverage, ink setup allowance, and number of printed sheets (Hohl, D. (1998)).

$$\text{Ink height} = 0.285 \times \text{mesh thickness}, \quad (1.2)$$

for thread counts 40-139 threads per cm.

$$\text{Ink height} = 0.35 \times \text{mesh thickness}, \quad (1.3)$$

for thread counts exceeding 140 threads per cm.

Sefar (1999b) used equation (1.1) as a basis for a model to create a more accurate approximation of ink consumption incorporating factors to account for substrate porosity and ink thinning. However equation (1.1) remains the established expression used by screen manufacturers (such as Sefar (1999b), Saati (2002a) and Koenen (2003)) to describe the mesh technical specification, based upon non-tensioned thread fabric dimensions.

Lomas, M. and Short, I. (1999) developed an equation for predicting ink consumption focusing on fabric absorbency of mesh material, and included a constant factor for print set up. The predicted results were accurate to within  $\pm 20\%$  of experimental consumption, and so indicate a potential for improvement if they are to be used to obtain more comparable results for practical predictive purposes.

## 1.5 Fundamental studies of screen printing

There have been relatively few fundamental studies into screen printing where the basic mechanisms of the process have been explored. This overlook of the area could be for a number of reasons. Before relatively new printing techniques were developed (such as ink jet printing) there would have been little competition for the screen printing industry, and so there was no apparent driving reason to improve the process. And so as this competition increases, the screen printing industry must now react and drive for improvement of the process through a greater understanding, which previously had not been deemed necessary to investigate. Other reasons for the lack of fundamental studies relate directly to the mechanisms of the process: the dimension and geometry of the mesh are such that direct visual access is difficult, and the process is very quick. There is some work into the way a (solder) paste flows into the apertures of a stencil, in stencil printing.

The process of stencil printing is very similar to contact screen printing; both use the motion of a blade to fill apertures in a stencil with fluid, whilst in contact with the printed surface, and the subsequent print is achieved with the separation of the stencil and printed surface (TKB-4U (2001)). The medium used to hold the stencil differs for these two printing techniques. As discussed previously, screen printing uses a woven mesh to hold the stencil in position. The stencil used in stencil printing is (most commonly) made from a steel sheet consisting of apertures cut by a laser (Stencils Unlimited (2004)) and the typical stencil thickness is 100-200 $\mu\text{m}$  (TKB-4U (2001)) – thicker than the screens typically used in screen printing.

Mannan, S. H., et al. (1994) observed that the squeegee not only forces solder paste into the apertures of the stencil, but also causes paste to be scooped out resulting in deformation of the upper paste surface. Soft polyurethane squeegee blades (similar material to those used in screen printing) scooped greater amounts of paste out of the aperture in the pre-print state than the rigid metal ones where no scooping occurred. This agrees with the theoretical work done by Owczarek, J. A. and Howland, F. L. (1990) based on off-contact screen printing, but they were unable to experimentally measure the squeegee penetration into the mesh. Instead, through the use of an abrupt squeegee stoppage to interrupt the print, the thickness of the deposited paste was measured, in the region of the stopped blade tip. The harder the blade, the thicker the measured deposit was and so implies that less paste was removed by the action of squeegee penetration.

Although there are differences between the typical aperture and cell dimensions of stencil and screen printing, Mannan observed experimentally that the pre-print state can be filled less than 100%. This will have implications on the initial amount of ink held within the mesh, which could also affect the final film thickness. The aperture widths investigated were 150-640 $\mu\text{m}$ , which is significantly greater than the open mesh cell widths used in screen printing (35-71 $\mu\text{m}$  is the open cell width of the experimental meshes used in this thesis). The stencil thickness (152 $\mu\text{m}$ ) is also much thicker than screen printing mesh thicknesses.

No published work has investigated the pre-print ink filled screen printing mesh state. There has been considerable work into the state of the mesh after mounting and tensioning, but it is specifically the dimension of the threads that has been studied (Hohl, D. and Hunt, D. (1992), Anderson, J. (2003a, b)), rather than their ability to hold ink.

Hohl, D. and Hunt, D. (1992) note that the geometry of the cell openings is not square for most meshes. Tensioning appeared to have little effect on the width of the threads, but instead causes the mesh thickness to decrease. The spacing between successive threads increases as the mesh is tensioned; this affects not only the thread count, but also the open area of the cells which can considerably increase from the untensioned

mesh state – reporting increases in excess of 35% for tensioning from the untensioned to the recommended state for a typical plain weave mesh.

Anderson, J. (2003a, b) reports that a tensioned mesh has least deformation of thread in the central region of the mesh, and most occurring along the middle of the outer mesh edges.

## **1.6 Related flows**

Despite the direct lack of previous research done studying the mechanisms involved in the filling behaviour of ink into screen printing cells or the filling of apertures with a blade action, there are other areas of work that can be used to assist. In particular, flows involving the motion of fluid, or even entrapped air, through capillaries or porous material may provide a greater insight into the filling behaviour experienced in screen printing. Gravure and stencil printing (briefly described in section 1.5) exhibit similar key features with screen printing, and so the filling process transferring ink into and through these cells may also provide transferable knowledge to screen printing.

The process of gravure printing involves a cylinder, which is etched with cells of varying depth (so as to create a tonal range). The cells fill with ink by the rotation of the cylinder into a trough of ink. This action also coats the surface of the cylinder, and so a metal doctor blade is used to clean the surface and meter the ink of the cells (which therefore displays similar characteristics with the metering stage of screen printing). The ink is transferred from the cells onto a substrate which is fed as a web between the rotating cylinder and a second cylinder, introduced to apply the necessary pressure for the process (Birkenshaw, J. W. (c1999)).

## 1.7 Outline of the work presented

There is a real need for a series of fundamental investigations in screen printing. As the literature review has highlighted, there is a lack of work in this area, and it is imperative from industry that the process is developed further. Firstly, experiments are needed to assess the thickness of the transferred printed film and to relate this to the many parameters of the setup. A second area that also needs investigation is the extent that the mesh initially fills with ink and also the mechanism by which this may occur. Computational fluid dynamics (CFD) play a role in this investigation as it allows insight into a process difficult to visualise experimentally. This work is subdivided as follows.

The experimental rigs and equipment that are used in this thesis are introduced and described in chapter 2. Two rigs are used to gain an understanding of the dynamics of ink transfer motion in the screen printing procedure – these are a manually operated screen printing rig and a cell filling rig.

In chapter 3, the screen printing rig is used to investigate the effect the operating parameters have on the printed thickness of the film transferred onto a substrate. An average film thickness is calculated by weighing the substrate before and after the printing stage. Primarily, the effect of the mesh geometry and the separation rate of the substrate from the screen were investigated. The work also provides an insight into the effect that different inks and substrates have on the printed film thickness. The use of the Ink Transfer Model (ITM) – developed by Abbott, S., Gaskell, P. and Kapur, N. (2001, private communication) – was investigated to compare with these experimental results.

The work of chapter 3 leads naturally into a study of the percentage ink transfer to the substrate for a range of mesh geometries and inks (studying the effect of viscosity) in chapter 4. In addition to measuring the film thicknesses (as in chapter 3), photographic images are captured of the mesh and substrate before and after the printing process takes place. The work highlights potential refinements to improve the accuracy of both the ITM model and the geometric based models (commonly used by

the industry) to calculate estimated film thicknesses and percentage transfers. Development of these models is considered, by improving the accuracy of the geometry used to represent the threads. A further development is of the level that the ink fills to in a pre-print mesh state since it is shown to be significantly different from the commonly accepted full level, and so the models are amended correspondingly.

In chapter 5, computation fluid dynamic (CFD) simulations are used to investigate the problem of the substrate separating from the ink filled mesh. The commercial package FLOW3D is used to investigate the effect of the variables, such as fluid properties and mesh geometry on the printed film thickness. The calculations of the meniscus shape provide an insight into the interaction of the mesh threads with the transfer of ink to the print.

Chapter 6 includes the description of the design of the rig specifically devised to study the filling behaviour of an idealised aperture – based upon a single screen printing cell – through the displacement of air with fluid via the action of a sweeping blade; and also the performed experiments and results are detailed. The variables of the study are based on those of screen printing: blade angle, speed, and gap between blade tip and surface, fluid type, and cell geometry. These are systematically varied to determine the fundamental mechanisms involved filling the cell with the fluid and how this influences the fraction of ink held with the mesh.

Finally in chapter 7, the conclusions and future suggested work based on the thesis are included.

## **Chapter 2**

# **Experimental apparatus and equipment**

---

### **2.1 Introduction**

This chapter describes the apparatus and equipment used to obtain the experimental data presented in this thesis. Two experimental rigs were used: a manually operated screen printing rig (described in section 2.2) and a cell filling rig (outlined in section 2.3 and described in more detailed within chapter 6) for the work of chapters 3 and 4, and chapter 6 respectively. Section 2.4 describes cameras, microscopes and other equipment used to capture images from the two rigs.

Various measuring apparatus were used throughout the thesis: measurement of mass used the scales described in section 2.5; dimensional measurement of solids and surface profiling used the equipment described in section 2.6; and the properties (viscosity and density) of the experimental test fluids were determined using equipment described in section 2.7.

## 2.2 Manual screen printing rig

A manually operated on-contact screen printing rig was used to print ink through meshes onto a substrate. The rig consisted of an attachment location for the screen, which was angled to assist the peel-off stage; a vacuum platform to fix the position of a substrate during the print stages; and a motor to control the rate of peel-off.

Figure 2.1 below shows a schematic drawing of the rig. A squeegee blade was required to fill the mesh, and then to remove any excess ink from above the screen.

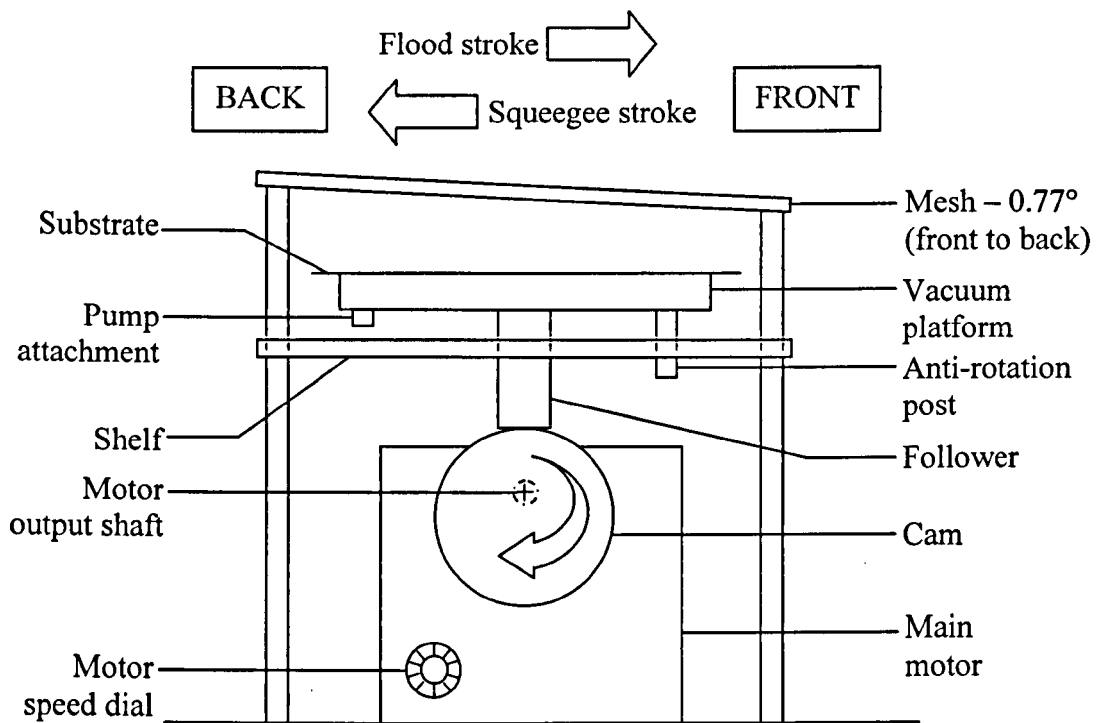


Figure 2.1: Schematic drawing of the manually operated screen printing rig.

The rig was located within a fume cupboard to prevent operator exposure to the volatile ink and the fumes from cleaning solvents that were present. The inks are described in section 2.7 and the cleaning solvents in section 2.2.4. The sides of the fume cupboard were darkened to minimise premature curing of the inks due to UV rays present in the atmosphere.



### **2.2.1 The main support frame**

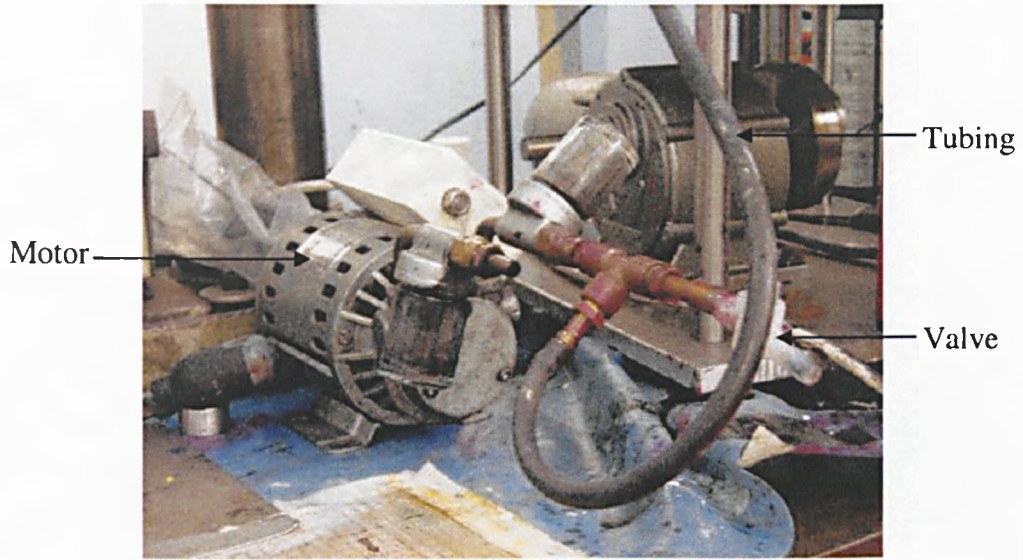
The components of the rig were mounted to the main steel support frame. The top of the frame has two unthreaded thru-holes that correspond with the equivalent fixing hole size of the screen frames. Four further clamps are used to mount the screen frames securely in position. The top of the frame was angled at  $0.77^\circ \pm 0.02^\circ$  from the back to the front (relative to the level vacuum platform) to give smooth separation of the screen from the substrate.

The anti-rotation post (shown in Figure 2.1) minimised lateral rotation of the vacuum platform. An electronic thermometer ( $\pm 0.1^\circ\text{C}$ ) was positioned at this level so that both the temperature of the rig and the ink under investigation could be monitored. The motor was bolted to the base of the main support frame.

### **2.2.2 The vacuum system**

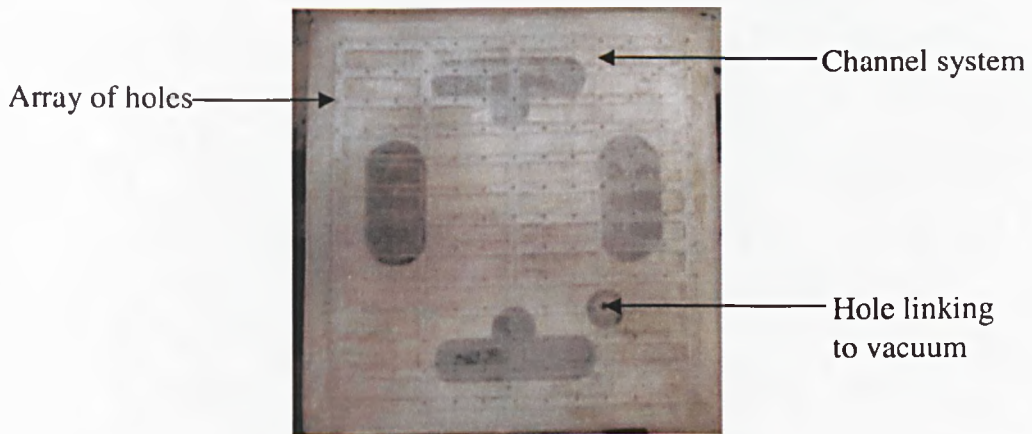
The vacuum system consisted of a level Perspex platform linked with rubber tubing to a pump driven by an AC motor (2850 rpm manufactured by GEC Machines), which when activated created sufficient suction to hold a substrate in place on the platform.

Figure 2.2 shows the vacuum pump. De-activating the pump enabled the substrate to be removed.



*Figure 2.2: Photograph of the vacuum pump and tubing connected to the vacuum platform.*

The platform consisted of a 13×13 array of inlet holes on the upper surface, all of which lead to channels, inside the platform, that are connected to the pump via the outlet tube. The channel arrangement and upper surface holes of the platform are shown in Figure 2.3 below.



*Figure 2.3: Photograph of the top view of the vacuum platform showing the channel system.*

The platform, located directly below the mesh, is raised and lowered during the printing operation so that the substrate is in contact with the screen for the initial stages of printing and so that it could also be easily separated from the screen for the latter stages of printing. This cyclic action was created by using a motor driving a cam that drove the follower of the vacuum platform.

### 2.2.3 The main motor and control unit for the vacuum platform raising mechanism

The motor was controlled by an RS analogue control unit; allowing the speed of the vacuum platform to be varied.

The Perspex platform was fixed to an aluminium platform (of thickness 12.5mm), the purpose of which is to increase the mass of the overall unit. This ensured contact was maintained between the vacuum platform follower (the centrally located shaft) and cam driven by the output of the main motor.

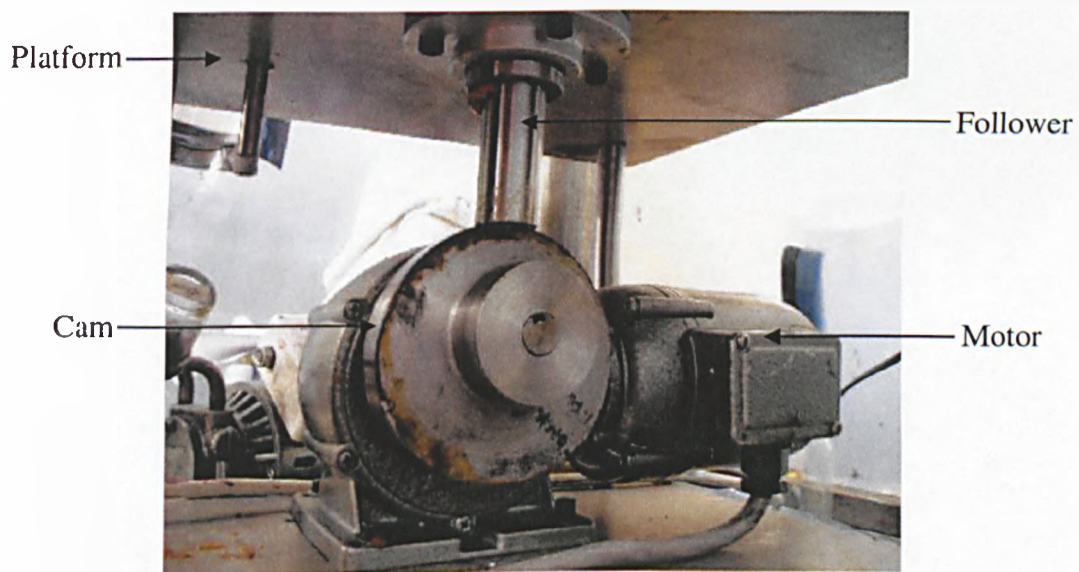


*Figure 2.4: Photograph of the mechanism for adjusting the height of the vacuum platform: the main motor and output shaft connected to cam that has the follower for the vacuum platform resting on it.*

Figure 2.4 shows the lower mechanism section responsible for raising and lowering the vacuum platform. A second shaft (attached to the vacuum platform) passes through the shelf of the main frame to prevent platform rotation occurring. This minimises smudging and improves the quality of the prints.

### **The drop-off rate**

The control unit had display settings of 0.0-10.0. These values were converted into actual drop rates ( $\text{mms}^{-1}$ ) of the vacuum platform. To do this, the angular speed,  $\omega$ , of the motor output shaft was measured by applying a method of timing a series of multiple rotations to calculate the average for a single rotation for a range of control unit settings. An angular protractor was fitted to the cam, which had markings to highlight where peel-off commenced at the back of the screen and when it was completed at the front during operation. The motor connection was temporarily disconnected: the cylinder could then move freely enabling rotation to specific desired angles through the peel-off range. The height variation of the vacuum platform for the peel-off range was measured using a displacement gauge whilst manually rotating the cam by  $0.5^\circ$  increments.

Combining the displacements at  $0.5^\circ$  rotations with the angular speeds (measured at equivalent motor settings) establishes the peel-off rates, calculated using the following equation.

$$\text{Peel-off rate, } \frac{dh}{dt} = \frac{dh}{d\theta} \times \frac{d\theta}{dt} = \omega \frac{dh}{d\theta} \quad (2.1)$$

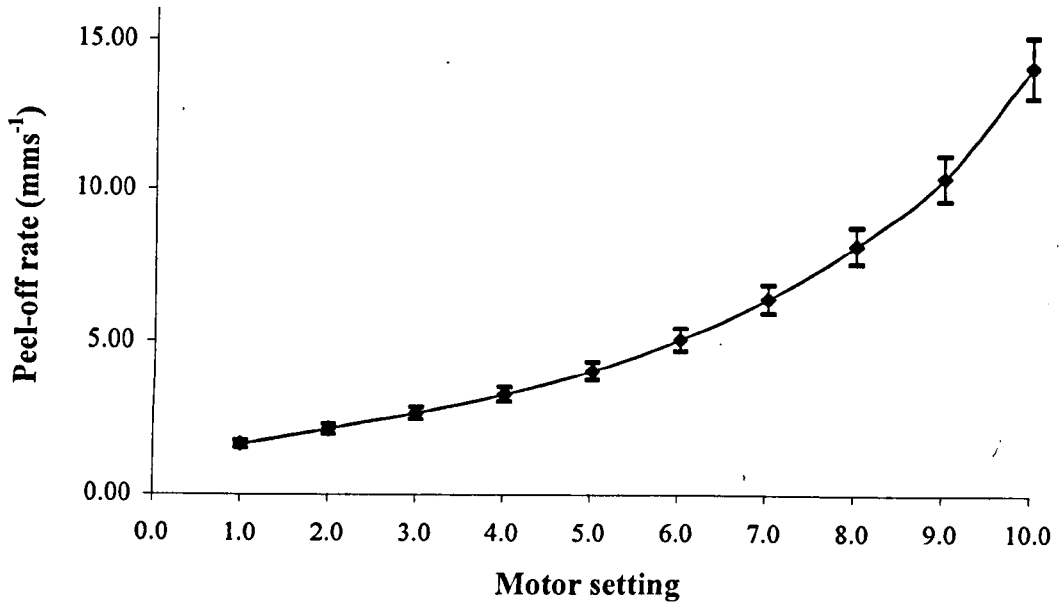


Figure 2.5: *Non-linear peel-off scale relationship for the 10 selected motor settings.*

Figure 2.5 shows the non-linear relationship between the peel-off rate and the motor control unit setting. The confidence limits for each control unit setting represent the range of peel-off rates due to the acceleration that is experienced from the back to the front of the vacuum platform (in consequence to the angle difference between vacuum platform and mesh, combined with the motion of the off-centred rotating cam). The lower confidence limit represents the behaviour that occurs at the back of the vacuum platform, and the upper confidence limit represents that occurring at the front. The fastest peel-off rate possible with this arrangement was  $14.1 \pm 1.0 \text{ mms}^{-1}$ .

### **Sensitivity of the vacuum platform maximum height**

The mesh tension, due to the loading of the platform against it, is controlled by the maximum height of the platform relative to the screen. Introducing a range of spacers (1.0, 1.5, 3.0, 4.0mm) to raise the height of the screen frame mounts on the main frame of the rig, and also between the centrally located steel pole and cam of the vacuum platform raising system, created a difference in the relative height of the vacuum platform and the screen frame. The vacuum platform was required to maintain contact

with the screen mesh when at maximum height for printing to occur. Varying the relative height of the vacuum platform and the screen frame therefore only varied the tension that the platform exerted on the mesh.

Figure 2.6 highlights that there is negligible effect on the amount of ink transferred to a substrate for the range of relative heights tested. Each graph point is the average of 5 quality prints all obtained with the same ink (NAZDAR black<sub>[1]</sub>), substrate (PPC1 transparency), mesh (Saati 120-34 OU-PW heavy frame) and peel-off rate (motor setting  $4.0 \equiv 3.3 \pm 0.2 \text{ mms}^{-1}$ ). The range of relative heights was significantly greater than that encountered in normal printing operations, when mounting different screen frames to the rig. Therefore after establishing a suitable maximum height that the vacuum platform should rise to, only a small change to the height position of the mesh occurs through mounting the different available meshes. The ink transfer was not sensitive to the relative height variations experienced giving confidence, that with tension maintaining contact of mesh and substrate, the thickness of ink printed was independent of the variable and so further investigation is not required for this study.

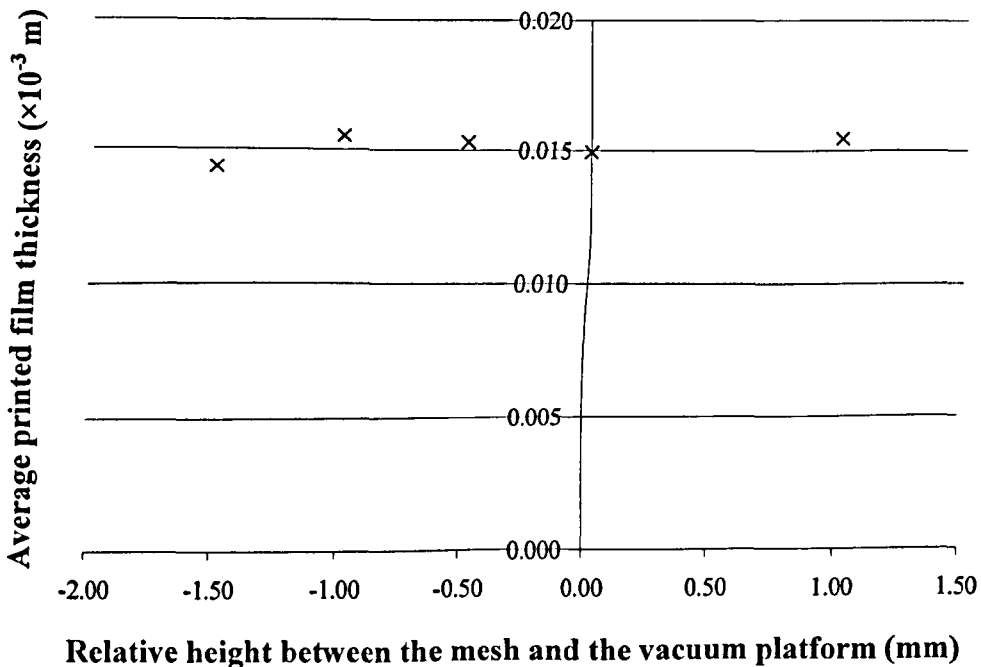


*Figure 2.6: Results of the experiments to observe if slight relative height variations between the mesh and vacuum platform influenced the printed ink deposit on the substrate.*

### 2.2.4 The meshes and frames

The threads of the meshes used for the tests were polyester, all of which have a plain weave (PW) construction. Figure 2.7 shows a sketch of a plain weave formation. Figure 2.8 shows a photograph of an actual plain weave mesh. Three meshes of different geometry were available. These are listed in Table 2.1.

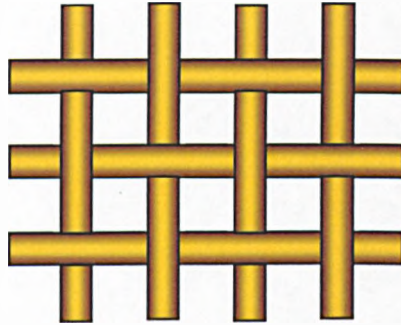


Figure 2.7: Sketch showing the formation of plain weave (PW).

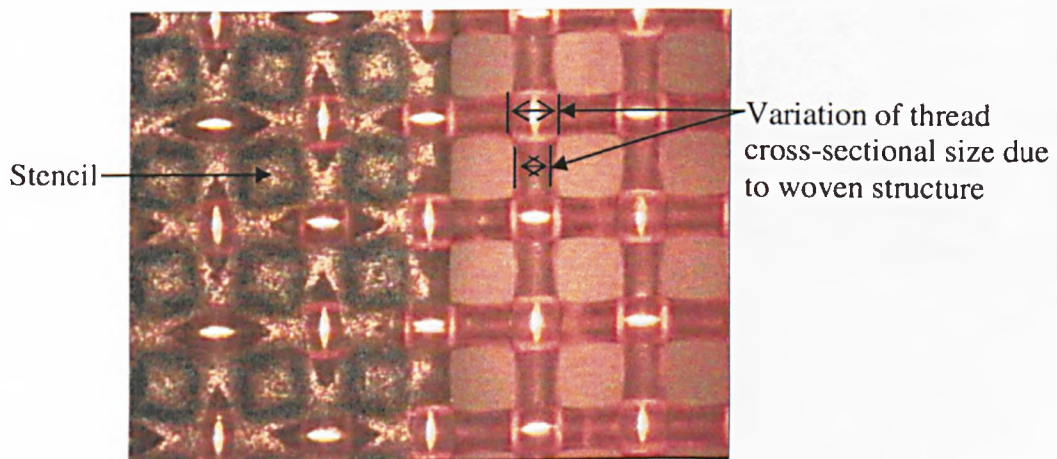


Figure 2.8: Photograph of the squeegee side of a 90-40 mesh with no ink. The left-hand side of the photograph shows the capillary stencil. The reflective light strips at the thread knuckles are used to highlight the direction of the upper knuckle since the orientation is the same (see section 4.3.1 for further detail).

Manufacturer	Description	Thread colour	Threads/cm	Thread thickness ( $\mu\text{m}$ )
Saati	90-40 PW	Orange (OU)	90	40
Saati	120-34 PW	Orange (OU)	120	34
Sefar	150-31 PW	Yellow (Y)	150	31

*Table 2.1: The available meshes – data relates to the manufacturers' provided data (Saati (2002b), Sefar (1999a)).*

Other mesh parameters include the fabric thickness, open area, and theoretical maximum printed ink thickness: all relate to the thread geometry and spacing. The manufacturers provided data for these parameters. However when the meshes were mounted on the frame under tension the data provided is no longer valid due to the fabric stretching. The fabric thickness and open area parameters can be measured using a Co-ordinate measuring machine KEMCO 400 (described in section 2.6.1) and a Nikon Profile Projector Model V-16D (section 2.6.2) respectively.

Two types of frames were also available for each mesh geometry. The first frame type was a standard steel frame (termed “heavy frame”). The second, a trimmed down steel frame version with a significantly lower mass (termed “light frame”) that did not exceed the maximum mass limit of the sensitive electronic scales used in the experiments (described section 2.5). The mesh threads were permanently fixed to the frames, after being suitably tensioned.

The purpose of the mesh threads is to hold any applied stencil in place so that the stencil can block ink transfer to the substrate at required positions of the print. The heavy frame meshes each had a capillary film stencil applied to the edges leaving a 170×170mm square open region. At the centre of the screen was a square 10×10mm stencil. This was used to check for ink bleeding. The light frame meshes had minimal stencil applied to them at the edges of the screen. Masking tape was used instead as a stencil material. The advantage of this method for use with the lighter meshes was that all excess ink, spread outside the open mesh printing area during printing, could



be removed with the tape leaving only the residual ink within the printable area in contact with the mesh.

Ink was applied to the upper surface of the mesh with a forward (flood) stroke of a squeegee blade. The same edge of the squeegee blade was used in the reverse direction to remove excess ink. The capillary stencil was fixed to the underside of the mesh to reduce damage by the squeegee strokes.

The meshes were cleaned using Seriwash Universal Screen Wash, which is a strong solvent that effectively removes all ink and does not damage either the stencil or the mesh threads. (Water was not used on the meshes since it degrades the stencil.) Lotoxane was used to initially clean the mesh when grease had been in contact with it. Lotoxane leaves a deposit so the Seriwash Universal Screen Wash was used for a second cleaning stage to ensure unwanted particles were removed from the mesh. The screen wash solvents were applied indirectly to the meshes using Tork Screen Wiper (strong) cleaning sheets. These cleaning sheets are lint-free to prevent small particles or fibres from the cloth getting trapped in the mesh, which would lead to unwanted printing defects. Protective gloves, clothing and goggles were worn whilst using the solvents.

### **2.2.5 The squeegee blade**

The flexible soft blade of the squeegee was manufactured by Sericol (SEF69M), and has the colour code orange-white-orange (triple ply – two soft layers sandwich the harder white layer that improves bending resistance). The blade was fixed to two metal plates and held in a wooden unit, which prevented bending over its length during the printing operation. The length of squeegee blade should be greater than the printable width of the mesh; the dimensions of the blade were 7×35×200mm.

The squeegee blade unit was cleaned with Tork Screen Wiper (strong) cleaning sheets to which Seriwash Universal Screen Wash was applied.

## 2.3 Cell filling rig

The purpose designed and built cell filling rig was used to observe the behaviour of air displacement by a liquid in a cell by the operation of a rigid blade – a brief description of the cell is defined in section 2.3.2. This section outlines the apparatus, whilst specific design criterion is highlighted in more detail within chapter 6. Chapter 6 includes information about the rig from the requirement function aspect – detailing the purpose of the sections described here. Development of integrated aligned components, possible optical arrangements, and design of the test piece, blade system and main unit are discussed within chapter 6.

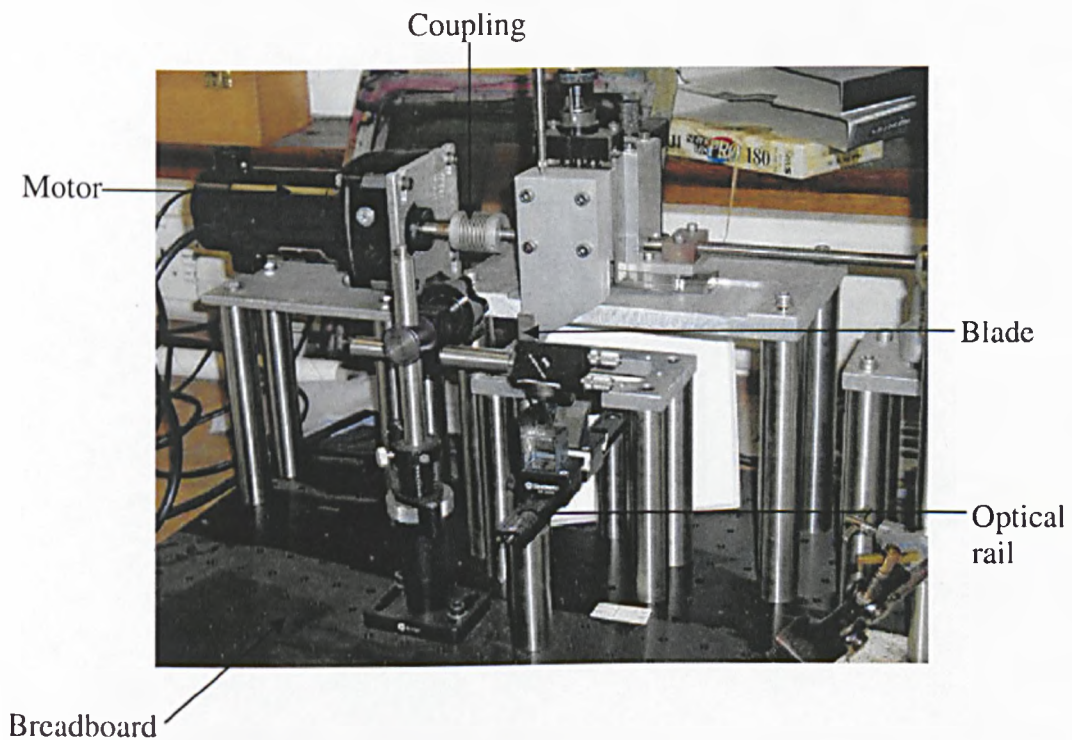


*Figure 2.9: Photograph of the cell filling rig.*

The situation represents a simplification of screen printing, where a large number of interacting small cells are filled with ink during the filling stage of the process. The rig consisted of several platforms to align the components. The test pieces contained a single cell and were mounted to one of the platforms. Other components of the rig included: the rigid blade, which was attached to a drive mechanism that controlled the movement over the cell; and an optical system that captured 2 different views

simultaneously of the filling behaviour. Figure 2.9 shows the general layout of the cell filling rig, without a test piece attached.

### **2.3.1 Main unit**

The main unit of the rig consists of a 600×600mm aluminium plate breadboard, which has an array of M6 threaded thru-holes (on 25mm centres) to which the platforms were fixed via support posts of various heights that ensured correct component alignment. It was ensured that the platforms were all level. The optical viewing system, described in section 2.3.5, was also easily mounted to the breadboard.

### **2.3.2 Test cell pieces**

The test piece is a flat ( $\pm 1\mu\text{m}$ ) Perspex block with a single hole called a “cell” located in it. The geometry of the cell is described in Table 2.2. The test piece was mounted to a rig platform with plastic screws so that the stresses experienced were minimised. Figure 2.10 shows the test piece mounted on the rig. A fluid drop was introduced onto the test piece between the groove and the cell. The fluid drop was moved to the cell by the action of the blade.

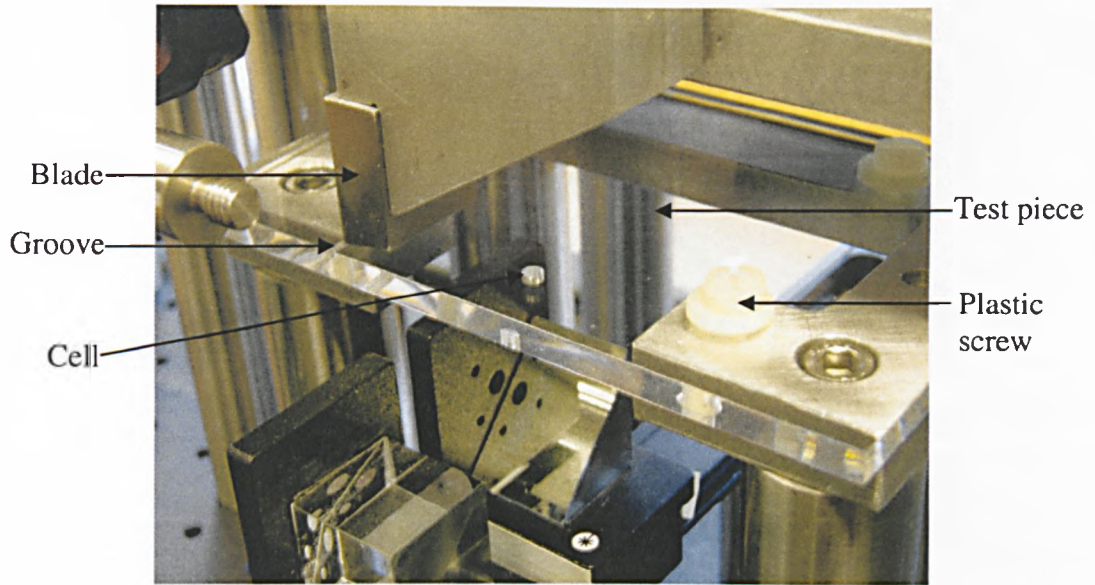


Figure 2.10: Photograph of the test piece mounted on the rig.

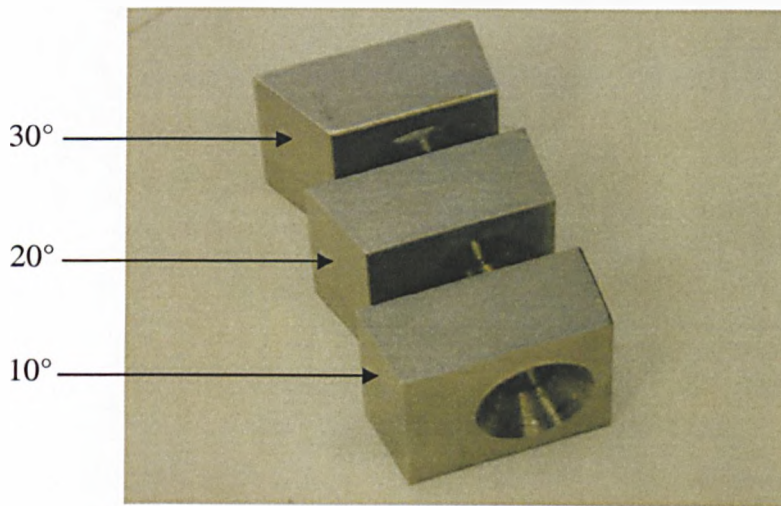
Cell cross-section	Depth (mm)	Diameter (mm)
Circular	1	2
Circular	2	1
Circular	2	2
Circular	2	3
Circular	3	2
Circular	3	3

Table 2.2: Available cell geometry of the test pieces.

The test pieces were cleaned using a mild detergent solution. Alcohol cleaning treatment was avoided to prevent optical damage.

### 2.3.3 Blade

3 rigid steel blades were available for the filling of the cell. The blade angles were  $10^\circ$ ,  $20^\circ$  and  $30^\circ$  (shown in Figure 2.11). These were bolted to the blade block that was part of the blade drive mechanism.



*Figure 2.11: Photograph of the steel blade tips.*

To prevent damage to test pieces, blade tips were removed from the rig for cleaning using propan-1-ol with lint-free Tork Screen Wiper (strong) cleaning sheets.

### 2.3.4 Blade drive mechanism

The blade drive mechanism was mounted to 3 of the platforms of the main unit. The mechanism drives the blade and the test fluid over the cell. The blade speed was controlled by a variable voltage controller (Kikusui Electronics Corp. Model PAB) connected to the motor (Bodine Electric Company motor, type 24D4BEPM-D3, rpm 136, ratio 18). A multimeter (Gunson Digital Engine Analyser) was connected to the variable voltage controller to improve repeatability during setting of the voltage. The range of the voltage controller unit was 0.6-110V. The controller caused the motor output shaft to rotate at the selected speed for the required blade speed; less than 7.0V produced undesired jolted rotational motion. The lead screw converts the rotational

motion of the motor output shaft to the desired linear motion of the blade. The flexible shaft coupling allows misalignment between the connection of the lead screw with the motor output shaft, whilst also isolating the blade drive mechanism motion from the motor vibration. The other end of the lead screw was held in place by an end bearing. The output shaft of the motor could rotate in either direction, so the blade moved either forwards or backwards.

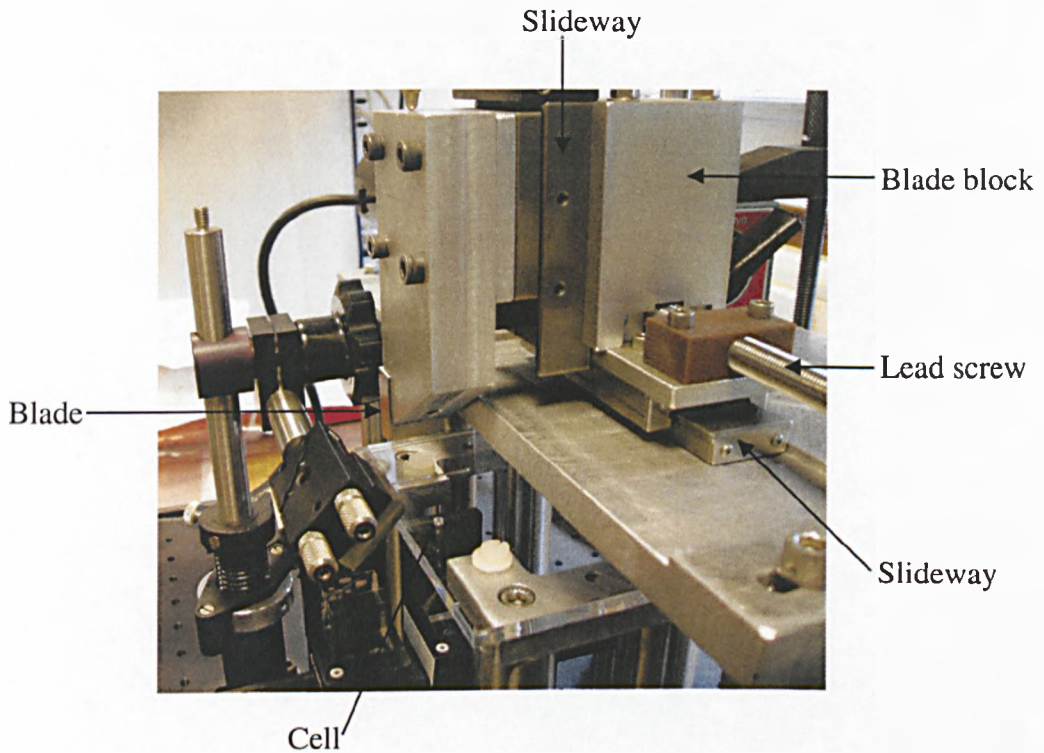


*Figure 2.12: Photograph of the blade drive mechanism of the rig.*

Two slideways were also part of the mechanism, as shown in the Figure 2.12. The first slideway operated horizontally and connected the blade block to the lead screw, ensuring smooth motion of the blade in the desired direction. The maximum stroke was 46mm. The location of the cell was the midpoint of the 45mm blade path. The total path length of the blade was 45mm. Motion limit stoppers were installed to this slideway preventing further travel which would result in damage to the mechanism. The second slideway operated vertically controlling the blade height and the pressure distribution of the test fluid under the blade. The gap between the tip of the blade and the test piece surface was measured using a displacement gauge ( $\pm 10\mu\text{m}$ ) that rested

on the top of the blade block. The gauge was zeroed by positioning the blade tip in contact with the surface of the test piece.

### Converting motor voltage to linear blade speed

The linear blade speed was determined by measuring rotational speed of the motor output shaft, when connected to the blade drive components as described above. The measured lead (distance travelled per 360° rotation) of the lead screw is 4.0mm. Therefore the linear speed, established using equation (2.2), is shown in Figure 2.13.

$$\text{Linear blade speed, } U = \text{lead} \times \omega \quad (2.2)$$

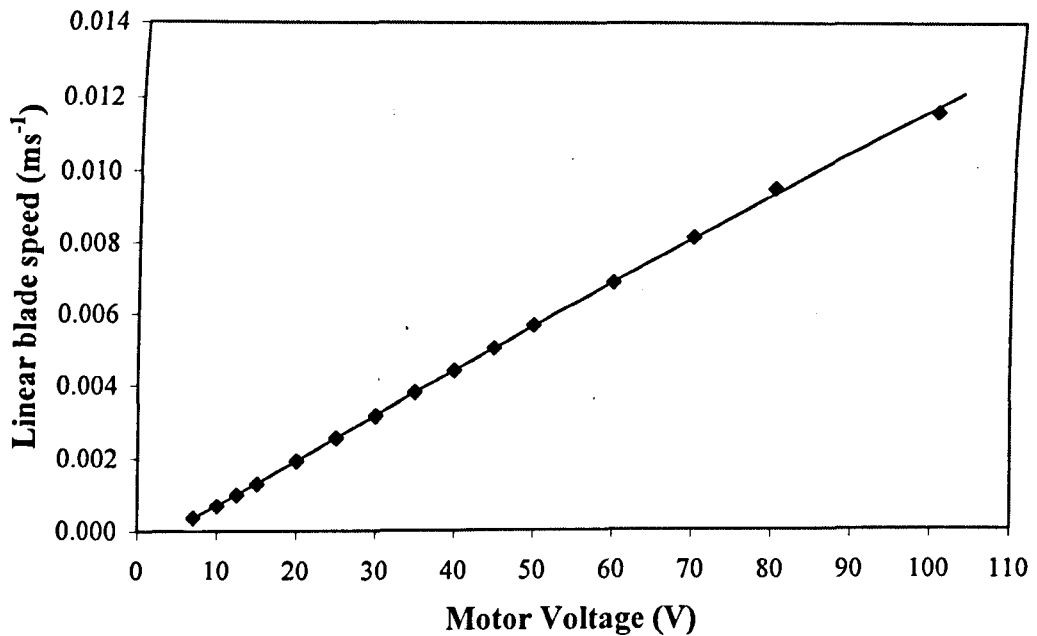
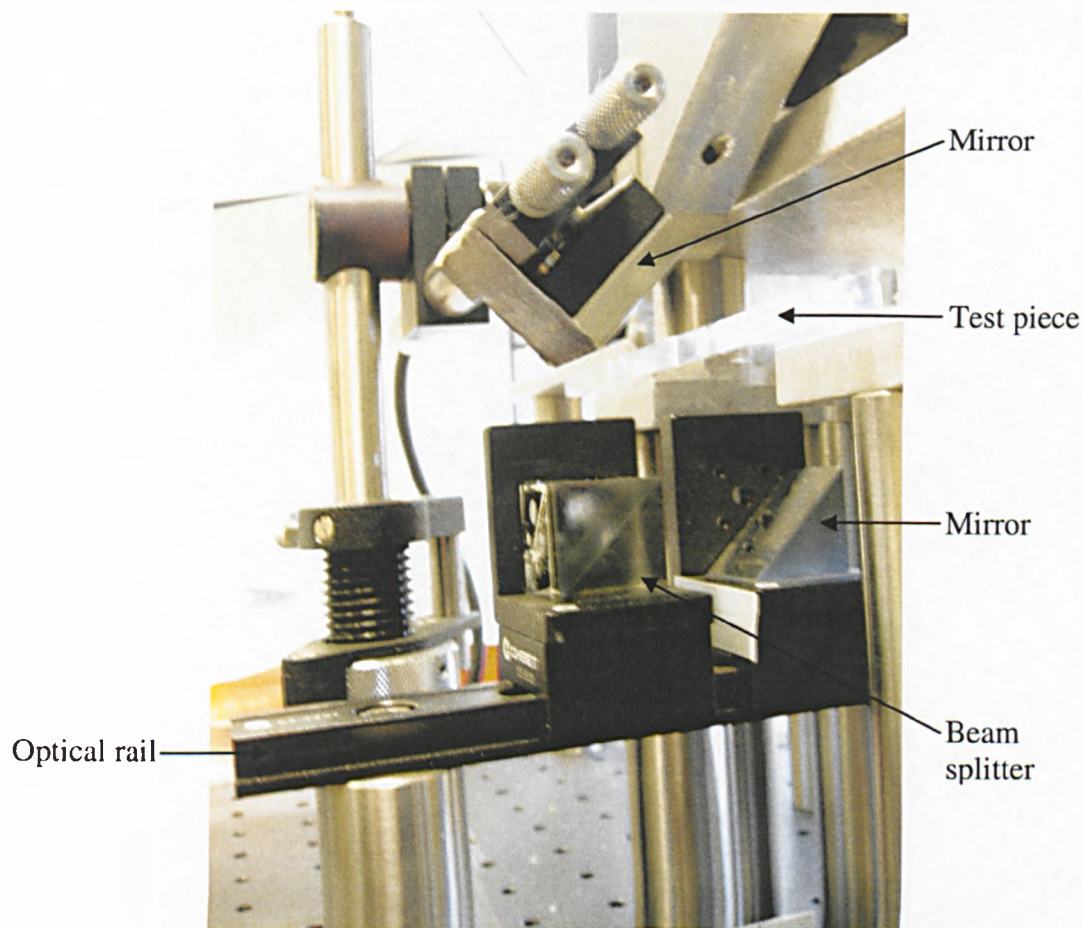


Figure 2.13: Graph for converting motor voltage to equivalent linear blade speed.

### 2.3.5 Optical Viewing system



*Figure 2.14: Photograph of the optical system – an adjustable angled mirror, a beam splitter and a right angled mirror.*

The optical system of the rig was designed to allow two concurrent images of the cell. The components included two mirrors and a beam splitter (as shown in Figure 2.14). These were mounted to an optical rail or directly to the breadboard. The mounting system enabled the three components to be aligned correctly and direct images to be recorded. The view from under the cell and the view from the side of the cell were captured simultaneously. To avoid the images directly overlying each other, an adjustable mirror was used to match the focal lengths and minimise blurring (see chapter 6 for schematic of the optical arrangement). However, this resulted in unavoidable distortion of the side view; the effect appeared to extend the cell depth. This allows good quality images to be obtained without blur, and post-image editing



can easily rectify the captured false extension. Improved quality of the captured images was also achieved by placing image blockers on the beam splitter: to prevent unnecessary (effectively noise) detail from one view overlapping and reducing the clarity of key filling behaviour observed in the other view.

The mirrors and beam splitter were cleaned using oil-free compressed air; if further cleaning was necessary, lint-free cleaning cloth with propan-1-ol was used ensuring each piece of cloth is used once only to minimise risk of scratching optical surfaces.

## 2.4 Image capturing

This section describes the equipment used to capture images of the experiments described in the thesis. A selection of cameras, microscopes and lighting were chosen for recording the specific events.

### 2.4.1 High speed camera and illumination

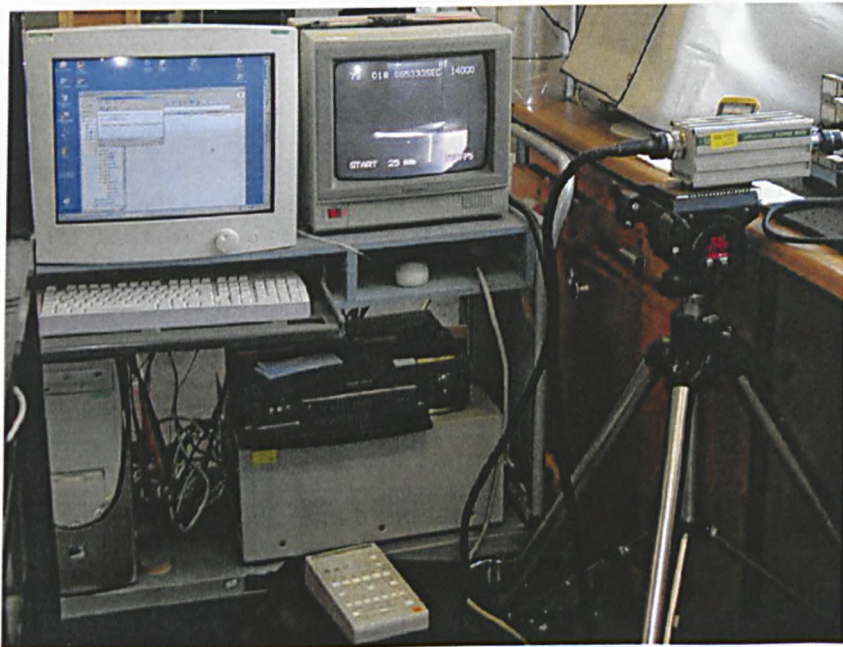


*Figure 2.15: Photograph of the high speed camera connected to two recordable output devices: PC and video.*

The Kodak EKTAPRO Motion Analyzer 4540mx Imager, shown in Figure 2.15, comprises of an imager (camera), a processor unit, and a handheld control unit keypad. It was used to capture images at high speed (i.e. to observe subtle changes inherent in quick meniscus movement). This camera records at exceptionally high speeds: achieving up to 4500 full frames (256×256 pixels) per second or 40500 partial frames (16×16 pixels) per second. The exposure time is the reciprocal of the recording rate, and so exposure is essentially continuous; at 4500 frames per second exposure time is  $\frac{1}{4500}$  seconds. The processor stores up to 16384 full frames in memory. This, in combination with the frame rate, determines the available recording time length. Therefore, for these experiments, to ensure a sufficient recording length to capture experimental events, the frame rate is significantly reduced from the maximum. A further benefit of reducing frame rate is the improvement of image clarity when the camera operates in combination with available light sources.

The processor was connected to a SVHS video unit and TV monitor to provide a live display of the image output and also a means to capture the images. A second connection to a PC enabled digital images to be downloaded (using Readcam 4540mx software) as bitmap (.bmp) or tagged image (.tif) filetypes, each of resolution size 256×256 pixels. Captured images are not colour but 256-greyscale.

The camera mounts to a tripod and was levelled using spirit levels. It is fitted with a monocular Meiji Techno Co lens combination (×0.7 lens and adjustable ×0.7-4.5 lens) which generates a fixed focal length of approximately 95mm. Using a fixed focal length is a disadvantage when setting up the camera, since both camera and tripod must be moved to obtain focused images (even for fine adjustments).

The camera functions are operated using the control unit keypad: setting frame rate, trigger type, ID number, live/playback/record mode etc. The camera system electronics require an initial calibration, to avoid production of image noise (observed as unwanted shaded black regions). The calibration procedure involves recording a sequence of images with no light at a high frame rate: the lens is covered with matt black card eliminating light, and frame rate of 4500 frames per second is selected. The recording mode AUX MEM is used for the calibration.

RECORD READY mode is used to capture experimental images. The START TRIGGER function was used to initiate image recording (other trigger variations included END, RANDOM, and CENTRE). The recorded image sequences were tagged with an ID number (1-100) to aid identification (during analysis) of images, relating to the experimental setup.

Two illumination sources were available for use with the camera: a 500W halogen light; and an Olympus Highlight 3000 with twin fibre optic output of adjustable brightness (max 200W combined).

#### **2.4.2 Microscope, camera and illumination**

A Nikon microscope (with lenses M Plan 5 9.1 210/0 [ $\times 5$  magnification], M Plan 10 DIC 0.25 210/0 [ $\times 10$  magnification], M Plan 20 0.4 END 210/0 [ $\times 20$  magnification]) was connected to a PC via a Pixelink PL-A662 camera (model 03956-02) to obtain digital colour images using Pixelink Capture software. The captured image could be saved as a bitmap file (.bmp) or a tagged image file (.tif) with a resolution size up to 1280 $\times$ 1024 pixels. The software controlled the exposure time of the camera (0-0.300s) and the brightness of the viewed image. An example screen shot of the control features of the software is shown in Figure 2.16.

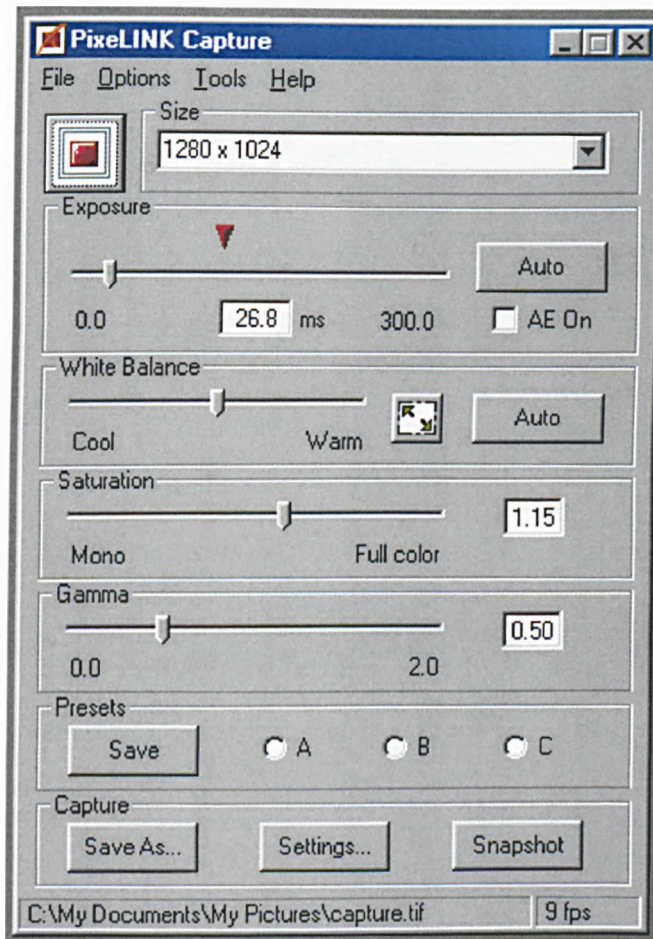


*Figure 2.16: Screen shot image of Pixelink Capture software control parameters.*

A Nikon power supply (model 10101AF) with a 150W halogen bulb enabled the light to be directed to the top of the investigated surface. The intensity of the light could be adjusted by varying an aperture. The microscope was mounted to the arm of a support stand enabling both lateral and vertical movement. Fine variation in the height was used for focusing the viewed image. The overall arrangement of the unit is shown in Figure 2.17. This image capture arrangement was suited to capturing still images rather than video images since the camera only had a low frame rate.

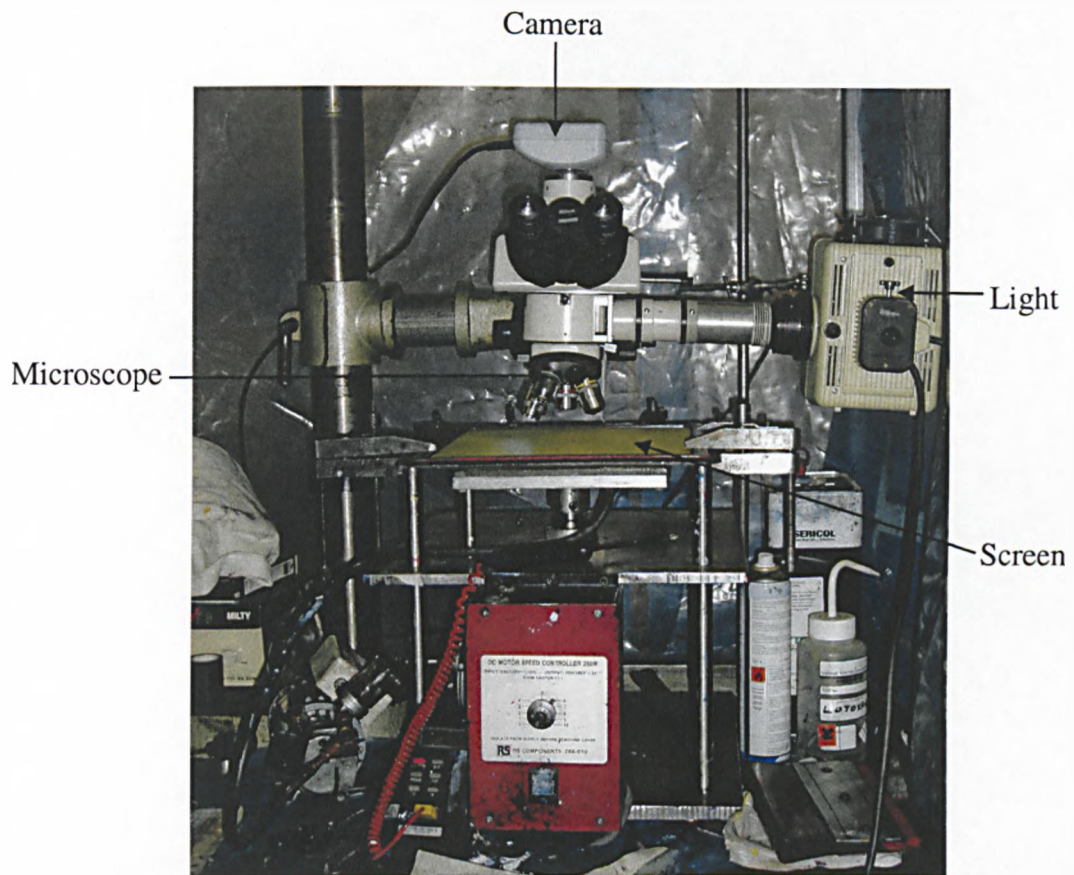


*Figure 2.17: Photograph of the Nikon microscope, mounted to the support stand arm, viewing a mesh on the manually operated screen printing rig. Also connected to the microscope is the light supply and Pixelink camera.*

The scale of the captured images were calibrated using a 1mm rule marked with  $10\mu\text{m}$  increments focused with the same set-up (i.e. at the same focal distance as the experimental images, for each of the three available lenses) of the Nikon microscope and Pixelink camera.

## 2.5 Measuring mass



*Figure 2.18: Photograph of the top loading mass measuring balance used to measure masses to a limit of 410g.*

The top loading balance, shown in Figure 2.18, (manufactured by Philip Harris Scientific, model 403 Status ST-series) measures mass with an accuracy of  $\pm 0.001\text{g}$ . The maximum load is 410g. An inbuilt spirit level was used to level the unit before use. To minimise the effect of air currents, the scales were placed within an air shield. The scales are calibrated annually by the manufacturers. The operational set-up was the “normal” mode of weighing sensitivity and speed of displayed reading. Daily checks of the scales measuring accuracy were performed using 6 weights (in the range of 3-11g) checked against an additional (externally calibrated) set of measuring scales (Mettler Toledo AT21 Comparator) capable of finer accuracy ( $\pm 0.00001\text{g}$ ). The same environmental conditions (temperature monitored  $\pm 1^\circ\text{C}$ , and use of air shields) were used for the comparison check between both balance units.

## 2.6 Measuring dimensions and surface profiles of screen meshes and substrates

### 2.6.1 Single dimension measurement – Co-ordinate measuring machine KEMCO 400

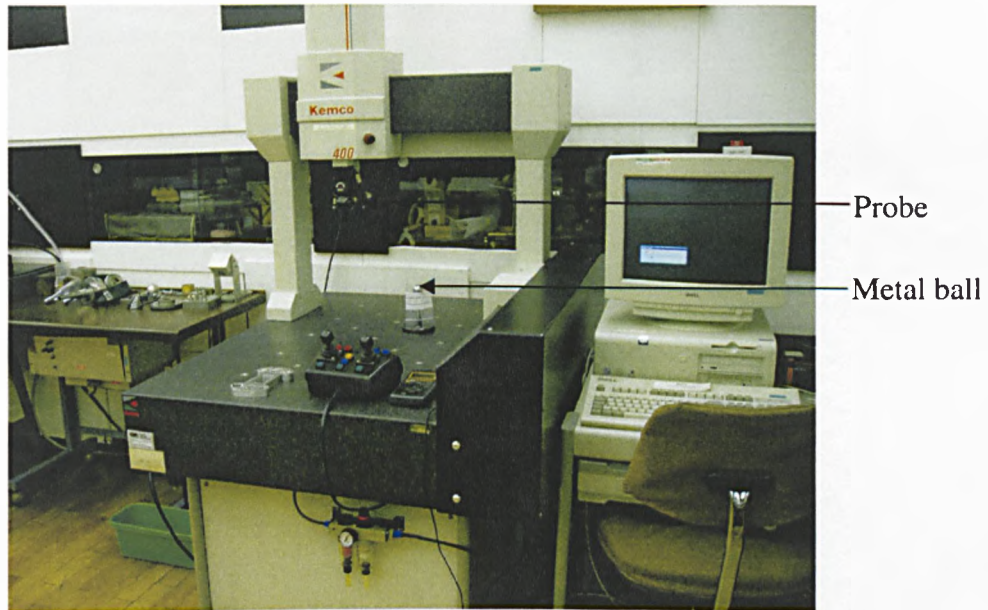


*Figure 2.19: Photograph of the co-ordinate measuring machine KEMCO 400.*

The co-ordinate measuring machine (CMM), shown in Figure 2.19, has the ability to measure in all 3 co-ordinate directions ( $x$ ,  $y$  and  $z$ ). The machine consists of: a highly manoeuvrable unit to which a probe is fitted; a dual joystick control to probe position; a work bench; and a linked PC using WinQCT software. The probe used had a spherical 2mm tip. The WinQCT software was used to display the co-ordinate position of the probe.

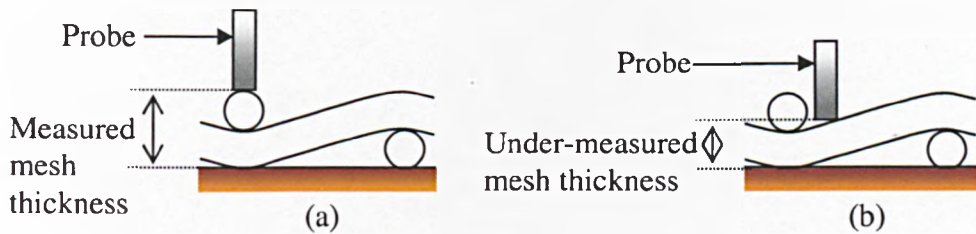


*Figure 2.20: Sketches highlighting how probe size can affect measured mesh thickness: (a) thickness correctly measured when positioned directly on the peak of the knuckle; (b) under-measurement of thickness occurs if probe is placed anywhere else on the surface of the mesh.*

The CMM was used to measure the thickness of screen meshes, utilizing just one of the three dimensions (z). Figure 2.20 shows how placing the probe directly on the mesh may affect the registered thickness. To avoid this occurring, the fabric (not the frame) of the screen mesh was sandwiched between metal blocks, see Figure 2.21. The blocks were checked separately, and in the combined sandwiched form, for consistent material height and flatness. This was achieved by bringing the probe into contact with the top surface to measure material thickness; repeating this process at multiple point locations on this surface confirms flatness. The mesh thickness was established by the difference in height between the individual block heights and the combined sandwiched mesh heights. The accuracy of the measurements was  $\pm 2\mu\text{m}$ . Calibration checks were performed using the metal ball each time the probe was replaced (featured in the photograph of Figure 2.19).



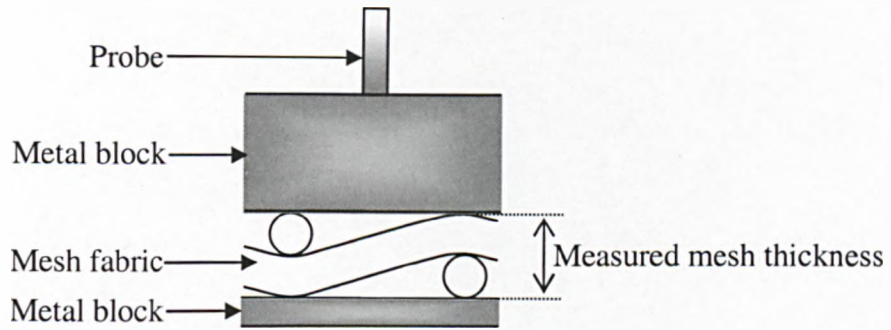


*Figure 2.21: Diagram of the mesh sandwiched by metal, removing the need for precise probe positioning on peaks of thread knuckles, whilst ensuring measured thickness is not comprised.*

### 2.6.2 2-dimensional measurement – Nikon Profile Projector Model V-16D

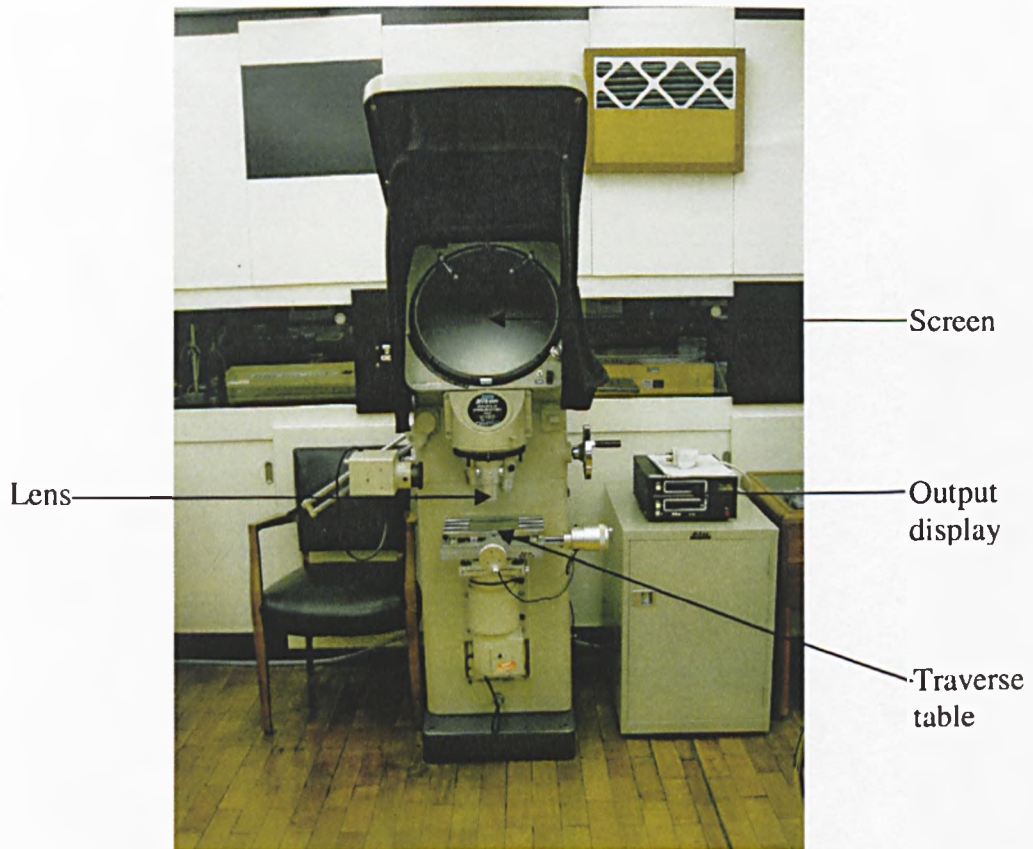


*Figure 2.22: Photograph of the Nikon Profile Projector Model V-16D.*

The microscope described in section 2.4.2 provides visual 2D information of the investigated surface. In addition to this, the Nikon Profile Projector (shown in Figure 2.22) was used (measuring dimensions in  $x$  and  $y$  directions) to measure screen mesh thread diameters and spacing in warp and weft directions. The projector consisted of:  $\times 50$  lens, a projector screen with  $x$  and  $y$  grid axis, a manually controlled traverse table, and a digital output display. The piece to be examined was placed flat on the traverse table, which was raised to within the focal length of the lens without viewing through the screen, so as to avoid collision of lens with the piece. The projection screen is used to refine the focus of the viewed image with fine height adjustments to the platform.

Dimensional measurements, of features of the piece, were obtained by controlled movements of the traverse table (using the two micrometer head dials) relative to the axes grid lines of the chart that overlays the screen. The distance the table moved was shown on the digital display. The accuracy of the measurements was  $\pm 2\mu\text{m}$ . Calibration checks were performed with the incremented ruler used in section 2.4.2.

### **2.6.3 Surface profiling**

The machines described in this section measure surface parameters, which provide information of the overall 3D surface profile and other features including roughness. The WYKO 3300NT machine uses non-contact interferometry and the Talysurf Taylor-Hobson machine uses contact stylus profilometry. These techniques were applied to investigate the surface geometry of meshes and substrates during screen printing stages.

### 2.6.3.1 Interferometry



*Figure 2.23: Photograph of the WYKO NT3300 machine in use.*

A Veeco WYKO NT3300 interferometer was used to investigate surface profiles via a non-contact method, and so can measure the surfaces of ink filled meshes without the need for curing. The machine consisted of: a CCD camera; a multiple magnification detector; an automatic filter assembly; a joystick controlled sample stage; a PC; and an illumination lamp (white light). The lenses available were  $\times 2$ ,  $\times 10$  and  $\times 50$ , with a pre-magnifier of  $\times 0.5$ ,  $\times 1.0$  or  $\times 2.0$  used in combinations to generate a greater number of available magnifications. WYKO Vision32 software controlled the operation of the interferometer.

The interferometer could operate using two different measuring methods. Phase-shifting interferometry (PSI) calculates the surface height by varying the optical length of the beams creating a shift in fringe pattern and generating interferograms; this method is more accurate for very smooth polished surfaces (roughness less than  $0.160\mu\text{m}$ ). The calibration is performed on a flat mirror surface to obtain height measurements and then the system shifts the fringes correctly. Vertical scanning interferometry (VSI) moves the lens unit downwards scanning for single focused points within the image from which the surface height is calculated; this method can

be used for surfaces with roughness up to 2mm. Calibration for VSI was done using step heights of  $10\mu\text{m}$ . VSI was used throughout this thesis for the measurements.

The set-up of the measurement stage included ensuring the test surface was visibly flat. The presence of fringes on the screen indicates focus of the corresponding surface features. The next stage was to null the fringes (i.e. maximize the spacing between the fringes) by tilting the microscope section. The illumination intensity was set as bright as possible without causing any saturation on the CCD receiver (displayed as red pixels on the screen). The lens objective was raised to focus just above the maximum surface height. Initiation of VSI lowers the objective, scanning down to the minimum surface height (determined previously during the focusing stage).

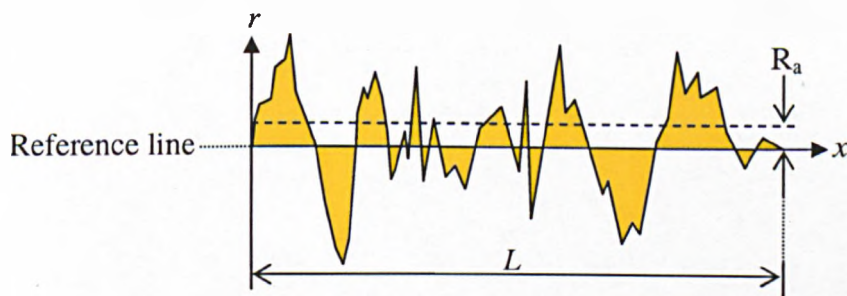


*Figure 2.24: Surface profile and  $R_a$  roughness parameter.*

The software also analysed the raw measured height data to graphically display the information as: contour plots, 2D  $x$  and  $y$  “slice” profiles, and 3D surface plots etc. Numerous roughness parameters were calculated by the system including the arithmetic mean roughness,  $R_a$ . The measured height data displays peaks and troughs. A reference line is positioned between the extremes so that the integrated distance deviating above the line equals that of below (shown in Figure 2.24); the reference line is therefore essentially an average of the height data.  $R_a$  is the average absolute distance the surface profile deviates from the reference line (see equation (2.3)); it does not describe surface peak/trough shape or spacing.

$$R_a = \frac{1}{L} \int_0^L |r(x)| dx, \quad (2.3)$$

where  $L$  is the evaluation length,

$r$  is the roughness (deviation distance from the reference line).

Some other software features include: the creation of databases (instead of individual datasets) to detect surface trends over time; filtered histogram – enables the elimination of individual false heights from the data using a masking feature; data restoration based upon interpolation of neighbouring points (not to be used for large restoration areas, created by factors such as poor material light reflectance, due to great reduction of accuracy); stitching – increases the viewing area.

#### 2.6.3.2 Stylus profilometry

A Form Talysurf 120L Talyor-Hobson stylus profilometer (shown in Figure 2.25) was used to measure surface roughness and generate 2D (and potentially 3D) surface profiles. The machine consists of: joystick controls and a PC; a laser 120L traverse unit; an adjustable height column; a traverse table; and a 6mm stylus (with a 2.5 $\mu$ m radius conical diamond tip) fitted to a solid stem (beam length 60mm). The column adjusted the height of the traverse unit and therefore the location height of the stylus tip. The traverse unit moved in the  $x$  direction; the traverse table moved in both  $x$  and  $y$  directions.

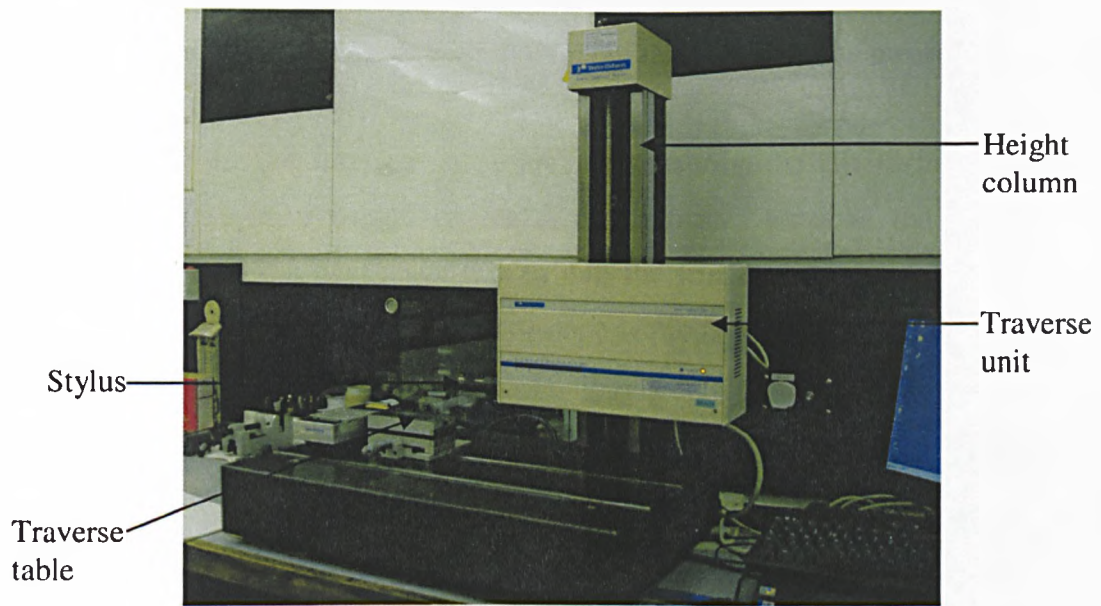


*Figure 2.25: The Form Talysurf 120L machine used to measure surface roughness parameters.*

The PC software ( $\mu$ ltra) controlled the position of the stylus tip above the surface under investigation. The software was used to define the locations where the stylus tip was to be moved to record the surface height. Single track measurements generated 2D surface profiles; multiple tracks (obtained by moving the traverse table with equal spaced increments) generated 3D profiles. The straightness of the track was within  $\pm 0.5\mu\text{m}$  over a 120mm length, with a measurement speed of  $0.5\text{mms}^{-1}$ . Defining the measurement set-up included the stylus start position, the track length, the number of readings, and the spacing between tracks. The stylus tip was then lowered to be in contact with the surface, initiating the measurement process.

The software incorporated surface roughness analysis of the collected raw data. In common with the WYKO machine (section 2.6.3.1) many roughness parameters are calculated, including  $R_a$ . Wavelength filters could be used to remove high wavelengths that relate to lack of surface flatness rather than the surface roughness.

The shape and size of the stylus may result in measured data differing from that of the actual surface, in a similar way to the previous note in section 2.6.1 (Figure 2.20) for use with the KEMCO 400 probe. Figure 2.26 highlights that the stylus shape and size

enforces measuring limits, in particular at the base of troughs; undercuts are not detectable. Although the diagram depicts the stylus shape as rectangular (i.e. cylindrical), the available cone shaped stylus is also susceptible to geometric error.

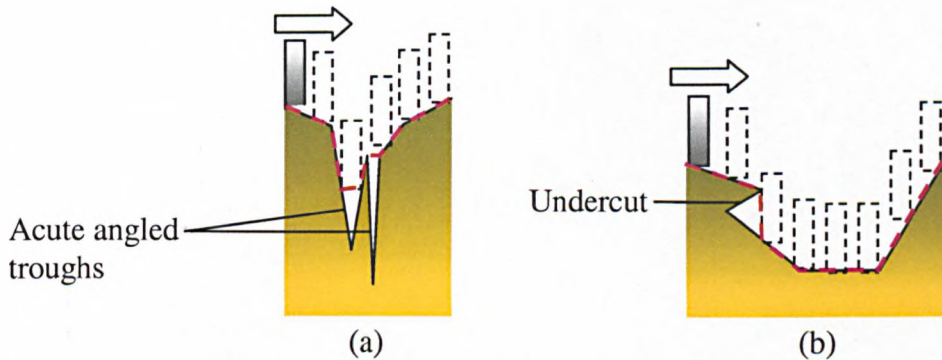


*Figure 2.26: Sketch highlighting two limit situations of the stylus for surface measurements: (a) acute angles; (b) undercuts. The red dashed lines depict the path followed by the stylus.*

A highly polished Tungsten Carbide precision ball (22mm radius) was used to calibrate the Form Talysurf unit every time the stylus was replaced. A standard test piece of 3 step height grooves ( $4\mu\text{m}$  deep) was used only as a calibration check.

Multiple track runs can construct a 3D surface profile, which (in theory) would provide much insight into the complex geometry of woven thread structured screen meshes. However due to the delicate structure, this contact profile measuring method was avoided to prevent damage (stylus tip sticking in mesh openings or catching at knuckles etc.) to either meshes or the profilometer. In addition, with ink filling the screen meshes (wet or cured), the stylus is susceptible to scratching the surface and so the recorded profile data would be inaccurate.

The stylus profilometer was used to measure surface profiles of the substrates, which are significantly less complex than the meshes. The substrate samples were mounted to flat steel blocks with tape and then placed on the traverse table. The measured data shown in Table 2.3 is the average roughness of two sample readings for each substrate type.

Substrate	$R_a$ ( $\mu\text{m}$ )
MA10 transparency	0.045
PPC1 transparency	0.058
Hello Gloss paper	0.216
Hello Matt paper	0.414

*Table 2.3: Measured roughness data of the available substrates performed on the Taylor Hobson Talysurf machine.*

Figure 2.27 shows graphically the difference in surface profile for two of the sample data readings of the substrates: MA10 and matt paper. This visually highlights the rougher surface matt paper has compared to MA10.

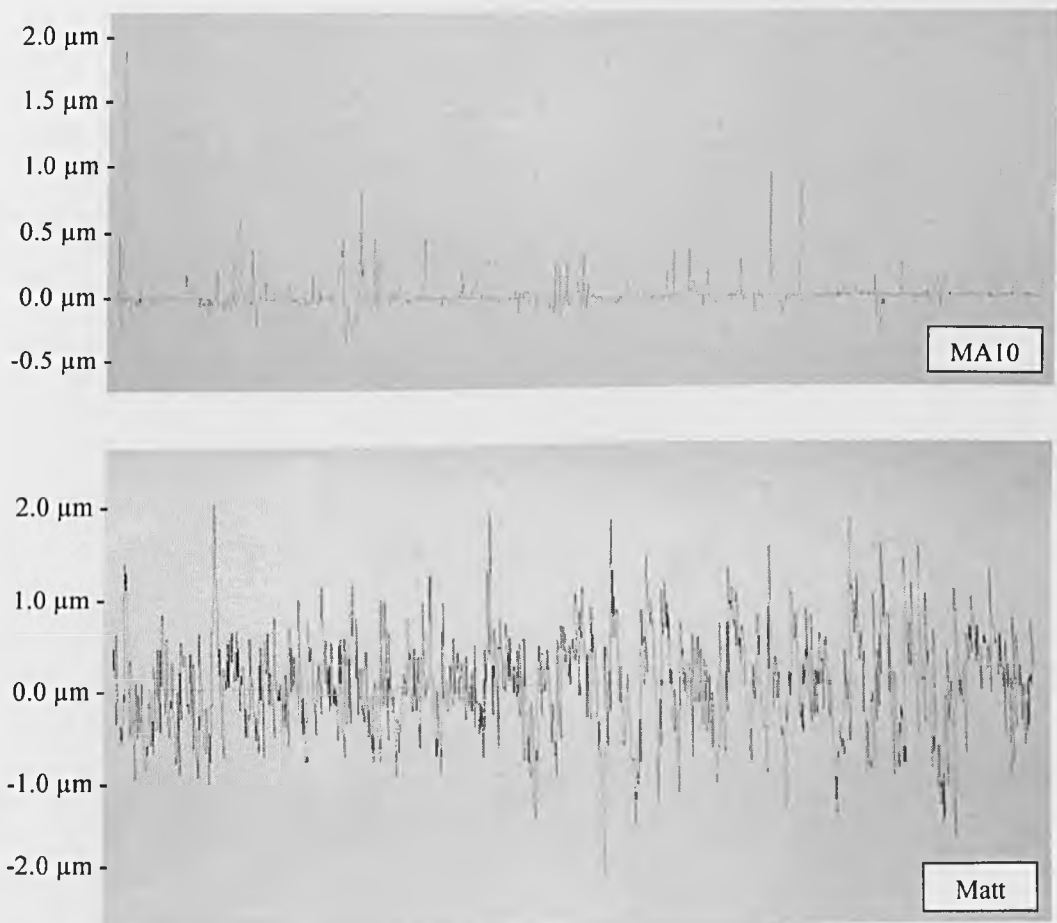


*Figure 2.27: 2D surface profiles of MA10 and matt substrates.*



## 2.7 Fluid properties

The fluids used in the printing experiments were typical of those used in industry. Two sets of UV inks were available in CMYK colours. Sericol Seridisc trichromatic set included: cyan (UR 215), magenta (UR 135), yellow (UR 052), and black (UR 004); NAZDAR 3200 half-tone set included: cyan (32101), magenta (32102), yellow (32103) and black (32104). Also available was Sericol UViplast Opaque White (UP 025 - 433875) ink and Shell Alvania R3 Grease. HVI 60 and HVI 160 oils were used in small percentages to vary the viscosity of the fluids without affecting the shape or size of particles in the test fluid. Diluting glycerine with water also provided a range of Newtonian viscosities to be tested.

A selection of pure oils is used in the experimental work of chapter 6; the methods detailed below are used to measure the fluid properties of these and are summarised in chapter 6.

### 2.7.1 Viscosity



Figure 2.28: A Bohlin rheometer.

A Bohlin CVO 120 high resolution rheometer (shown in Figure 2.28) was used to measure fluid viscosity. This instrument consists of 2 stainless steel plates, one of which remained stationary and the other that rotated when the test fluid was present. By rotating one plate at a known angular velocity the shear stress could be measured and the corresponding viscosity was calculated. There were 4 available geometries of the upper rotating plate. These were a cone of 4° with a diameter of 40mm; a cone of 1° with a diameter of 60mm; a flat plate with a diameter of 20mm; and a flat plate with a diameter of 40mm. (See Appendix A1 for further notes on the geometry types and calculations performed by the rheometer.)

For non-Newtonian fluids the typical shear rate of the fluids in the experimental system is required so that the viscosity can be measured over an appropriate range. Orders of magnitude estimations of the shear rates ( $\frac{\Delta u}{\Delta z}$ ) of the inks were calculated for the 3 stages of printing (that is cell filling, excess ink removal, and peel-off). The value  $\Delta u$ , for cell filling and ink removal was equivalent to the speed of the squeegee blade; whilst  $\Delta u$ , for the peel-off was approximated using the vacuum platform lowering rate as shown in Figure 2.5. The value used for  $\Delta z$  was the printed film thickness since it was not possible to accurately measure the gap between the squeegee blade tip and mesh.

Therefore the fluids, used on the manually operated screen printing rig, experienced the greatest shear rates in the cell filling squeegee stroke process. These shear rates were approximately in the range of 3000-5000s<sup>-1</sup>. Unfortunately this exceeded the measuring limit of the Bohlin rheometer with the available plate geometries. However the approximate shear rate that occurred in the process of transferring fluid to the substrate is lower (80-2000s<sup>-1</sup>) and the Bohlin rheometer was used to measure the viscosity of the fluids at the slow peel-off rates that the screen rig operated at. The data could also be used as a guide for the higher shear rates that the printing fluids also experience.

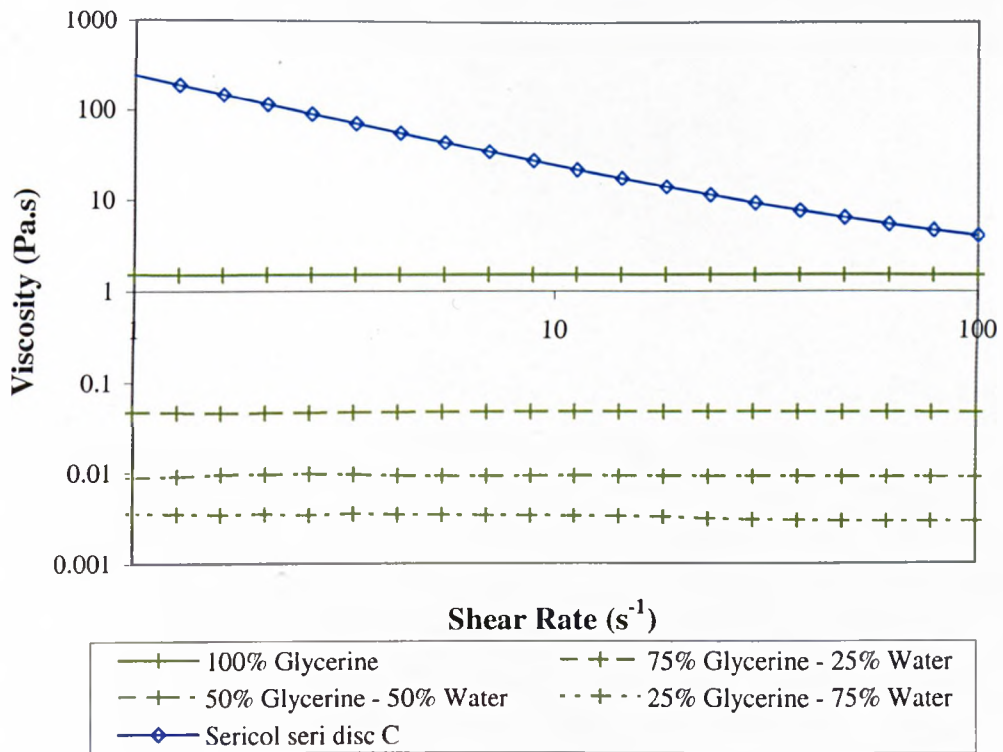
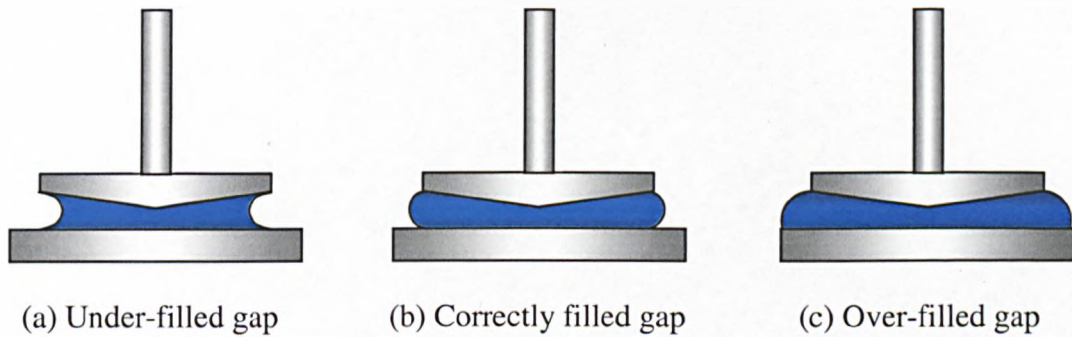


Figure 2.29: Effect of shear rate on viscosity, measured using cone ( $4^\circ$   $\text{\O}40\text{mm}$ ) and plate geometry, for a non-Newtonian ink (Sericol seri disc cyan) and a Newtonian fluid (Glycerine).

Figure 2.29 shows the measured viscosity of the glycerine/water mixtures and the Sericol seri disc cyan ink at  $20.0^\circ\text{C}$  up to  $100\text{s}^{-1}$ . The glycerine/water mixtures exhibit Newtonian behaviour as the viscosity remained constant irrespective of the shear rate. Power-law estimations were implemented for the non-Newtonian fluids, such as the inks, to extrapolate viscosity values to higher shear rates.

The rheometer also controls the temperature of the test fluid.

Due care was taken to ensure the gap between the 2 plates was correctly filled as shown in Figure 2.30, so that the geometry of the system is well characterised.



*Figure 2.30: Sketches demonstrating the correctly filled gap between the rheometer plates.*

Annual calibration of the Bohlin apparatus is performed by the manufacturer. Standard calibration oils (Newtonian) are used to measure the performance of the rheometer compared to the standards from the Paint Research Association (PRA). The calibrated viscosity results are used monthly in the calibration checks, using the same oils. For the calibration oil of viscosity 1.010 Pas (25°C) the accepted calibration checking measurement is to be within  $\pm 5\%$ , when varying the shear stress 0.024-240.0 Pa and using the 4° diameter 40mm cone and plate geometry.

### 2.7.2 Density



*Figure 2.31: Photograph of the cup used for density measurement of inks.*

The density was calculated by using the measuring scales described in section 2.5 with a small metal cup – diameter of 21mm and an approximate depth of 6mm, shown in Figure 2.31. The filleted corners at the bottom of the cup prevented air bubble entrapment. The mass of the empty cup was measured. The volume of the cup was established measuring the mass of distilled water required to fill it.

Figure 2.32 highlights that the shape of the meniscus without levelling would overestimate the volume of the cup. The cup was initially filled like this but then levelled by pressing firmly a flat steel sheet (40×40mm of a pre-measured recorded mass) onto the top of the cup. This process expelled the excess water, which was removed by absorbing it with a cleaning cloth. The mass of water within the cup is determined and combined with density of water ( $1000\text{kgm}^{-3}$ ): the cup volume is established. The density of other fluids was calculated by overloading the cup and then removing excess with a metal blade edge to fill the cup correctly; any fluid spread to the cup's outer surfaces was removed with cleaning cloth. The measured densities (calculated combining the liquid mass and volume) for the available fluids are displayed in Table 2.4.



Figure 2.32: Photograph of water filled density cup highlighting potential calculated volume error due to the meniscus shape.

Fluid	Density, $\rho$ (kgm <sup>-3</sup> )
Sericol cyan	1226.1
Sericol magenta	1214.6
Sericol yellow	1258.1
Sericol black	1244.9
Sericol white	1432.4
NAZDAR cyan	1056.8
NAZDAR magenta	1050.7
NAZDAR yellow	1070.6
NAZDAR black <sub>[1]</sub>	1046.9
NAZDAR black <sub>[2]</sub>	1066.2
NAZDAR black <sub>[2]</sub> (92.5%) and HVI 160 (7.5%)	1035.9
NAZDAR black <sub>[2]</sub> (90.0%) and HVI 60 (10.0%)	1024.8
Shell R3 grease	892.4

Table 2.4: Densities of the test fluids.

## Chapter 3

### Printed film thickness

---

#### 3.1 Introduction

In this chapter, contact screen printing experiments were performed to investigate the printed film thickness. The rig used for this is operated manually, unlike the automated rigs used by industry. The printing type is contact printing enabling the peel-off stage to be controlled separately from the squeegee stroke and printing stages, and hence providing better parameterization of the process.

Off-contact printing is considered to have a combined print stage where ink establishes contact with the substrate and simultaneously separates to enable transfer from the mesh, producing a print. No transfer occurs until the mesh is pressed (with the squeegee blade) to contact the substrate. After contact is achieved mesh release is initiated by the blade pass, enabling transfer to begin. The fundamental process, on a localised scale, is therefore the same as for contact printing (although the latter has a distinct separation of the print stages), enabling the work of this chapter to be applied to the broader field of screen printing, incorporating both contact and off-contact methods of application.

The aim of the present work is to establish how the print factors i.e. peel-off speed, choice of substrate (roughness) and ink, and mesh geometry affect the final printed film thickness.

### **3.2 Experimental method**

The experiments of this chapter were carried out on the screen printing rig, described earlier in section 2.2. As stated previously, this type of rig was used since it enabled independent control of the three printing stages: filling, metering, and printing (as described in chapter 1).

The temperature during the printing operation was monitored and in all cases was between 17.5-20.5°C. During testing of an individual ink there was a much smaller variation of  $\pm 0.5^\circ\text{C}$ . The fume cupboard extractor was operating throughout the experiments.

#### **Printing good quality images**

Before the apparatus was used, dust particles were removed from the vacuum platform and all rig components using lint-free cleaning sheets. The screen frame under test was secured to the main frame support of the printing rig, after ensuring there were no dust or ink particles in the mesh. The print ink was stirred with a metal application blade, in case any separation of the ink components had occurred, before being introduced to the system.

A substrate (of a size greater than the printable area of the mesh) was placed on the vacuum platform whilst it was stationary and in the lowered position, and this was held in position by activating the vacuum pump. The peel-off rate was set with the motor control unit. The main motor was briefly operated to raise the vacuum platform to the maximum height causing the substrate and mesh to create tensioned contact. At this stage, the main motor was stopped, and the ink was applied along the edge of the



mesh using the application blade. This was then distributed over the printable area of the mesh with a manual forward stroke of the squeegee blade. A reverse squeegee stroke then removed excess ink from the printable area of the mesh.

The final stage of generating a print was the lowering of the vacuum platform at the selected motor speed (by separating the substrate from the mesh) thus allowing the final stage of printing to occur. After this, de-activating the vacuum pump permitted the printed substrate to be removed from the rig. The process was then repeated to obtain more prints, with additional ink being introduced as required. The initial prints were discarded until a good quality print was obtained when the mesh became satisfactorily pre-wetted. This is in line with what is done in industry. Signs of poor quality prints included:

- Substrate not separating from the mesh surface
- Presence of circular regions with no ink deposited, caused by particles trapped between the mesh and the substrate, or on the vacuum platform
- Uneven printed surface, due to the mesh not being properly wetted
- Regions with no ink, due to the mesh not being properly wetted
- Streaks, caused from ink forming on the rear edge of the squeegee blade

It typically took between 5 and 10 initial prints to reach a state where good quality prints were generated. Each further print produced was inspected to ensure quality was not degraded.

Directly after completing prints with one mesh, or if a change in ink was required, cleaning was initiated as described in section 2.2.4 to prevent ink curing within the mesh. The squeegee blade unit and metal application blade were also cleaned as described in section 2.2.5. Before reuse of the mesh or squeegee blade a visual check was made to ensure that the cleaning solvent had fully evaporated.

## Film thickness variables and experimental method

The fluids available for printing were the Sericol CYMK ink set, NAZDAR CYMK<sub>[1]</sub> ink set, Sericol white ink and R3 grease described in section 2.7. The measured viscosities of these 10 fluids are shown in Figure 3.1.

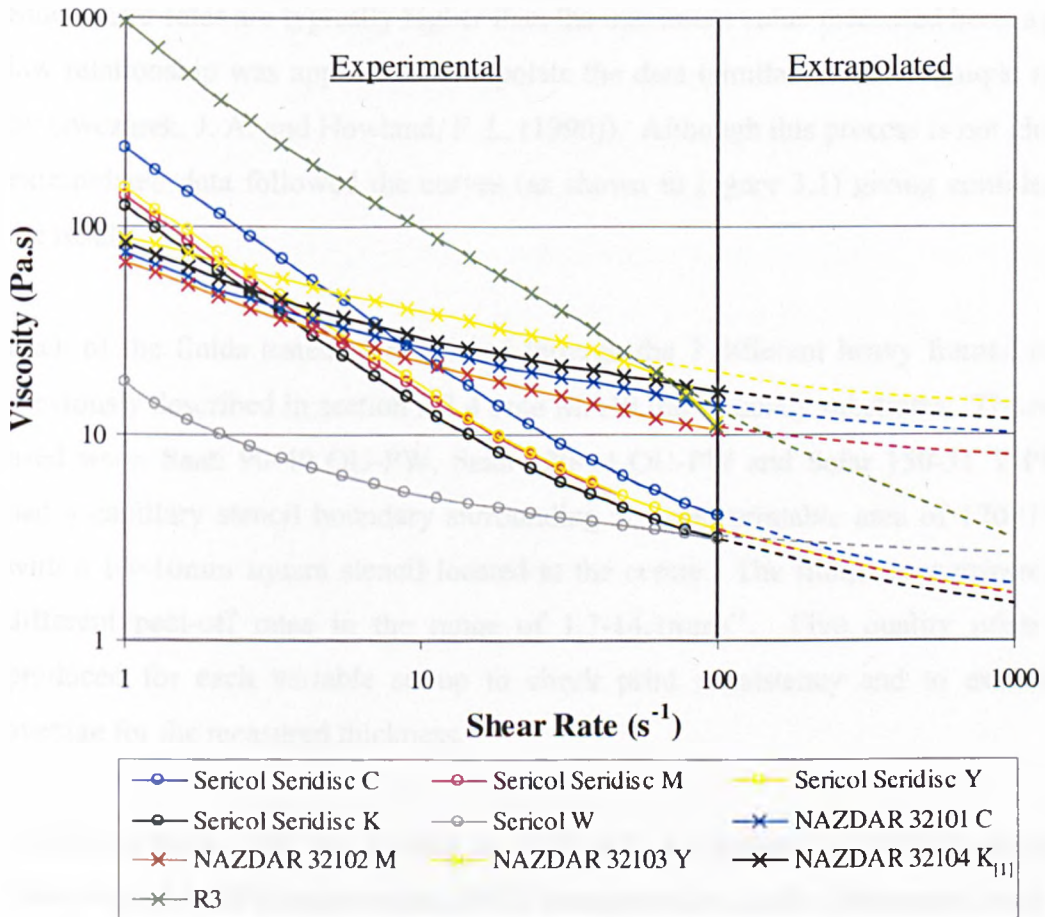


Figure 3.1: Graph showing the measured viscosity of the 10 test fluids in the shear rate range of  $1\text{-}100\text{s}^{-1}$  at  $20.0^\circ\text{C}$ ; viscosities extrapolated to shear rates of  $1000\text{s}^{-1}$ .

The maximum shear rate limit that the rheometer (described in section 2.7.1) fitted with cone-plate geometry ( $4^\circ$  cone of 40mm diameter) could reach was  $100\text{s}^{-1}$  for the inks used in these tests. Fitting the rheometer with the other available geometries did not improve the limit range. A larger cone geometry in theory enables higher shear rates to be achieved. However, when fitted with a cone of  $1^\circ$  and a diameter of 60mm, shear rates above approximately  $80\text{s}^{-1}$  could not be exerted on the printing inks, since the torque required by the motor to generate the shear rates exceeded its maximum

value. Tests performed using a parallel plate arrangement could obtain higher shear rates, but with the disadvantage of ink expulsion from the sides reducing the volume being sheared, which is required to remain constant. Therefore applying shear rates greater than  $100\text{s}^{-1}$  generates unreliable and unrepeatable results for these printing fluids.

Since shear rates are typically higher than the maximum value measured here, a power law relationship was applied to extrapolate the data (similar to the technique applied by Owczarek, J. A. and Howland, F. L. (1990)). Although this process is not ideal, the extrapolated data followed the curves (as shown in Figure 3.1) giving confidence in the results.

Each of the fluids tested were printed through the 3 different heavy framed meshes previously described in section 2.2.4 onto MA10 transparency substrates. The meshes used were: Saati 90-40 OU-PW, Saati 120-34 OU-PW and Sefar 150-31 Y-PW; all had a capillary stencil boundary surrounding an open printable area of  $170\times 170\text{mm}$  with a  $10\times 10\text{mm}$  square stencil located at the centre. The fluids were printed at 10 different peel-off rates in the range of  $1.7\text{-}14.1\text{mms}^{-1}$ . Five quality prints were produced for each variable set-up to check print consistency and to establish an average for the measured thickness.

NAZDAR black<sub>[1]</sub> ink was printed as above onto 4 substrates of different roughness. These were MA10 transparencies, PPC1 transparencies, Hello Gloss paper, and Hello Matt paper. The substrate roughness values are shown in section 2.6.3.2.

The average film thickness on the prints was calculated by measuring the mass of ink transferred to the substrate. This was established by calculating the difference (see equation (3.2)) between the substrate mass directly before and after printing (without curing) using the balance described in section 2.5. Equation (3.1) below was used to obtain the average film thickness for each print.

$$\text{Average film thickness, } h_{av} = \frac{m_{ink(on\_substrate)}}{\rho_{ink} A_{print}} \quad (3.1)$$

$$\text{where, } m_{\text{ink(on\_substrate)}} = m_{\text{substrate(after)}} - m_{\text{substrate(before)}} \quad (3.2)$$

The actual printed film thickness was also converted into a non-dimensional term using the theoretical maximum thickness of ink in the initial filled mesh. For clarity of reading, this parameter is calculated using a model that simplifies screen mesh geometry, but maintains a woven structure. The model essentially focuses on a single mesh cell, and through calculating the area and volume of the cell, the volume of thread material, the maximum ink volume occupying the cell is determined. From these parameters the maximum ink thickness is established (assuming 100% transfer from mesh to substrate occurs). For a detailed definition of the model see section 4.4.1; equation (4.8) of this section defines the theoretical maximum printed thickness ( $h_{\text{max}}$ ). The non-dimensional thickness was therefore calculated as follows:

$$\text{Non-dimensional thickness, } H = \frac{h_{\text{av}}}{h_{\text{max}}}, \quad (3.3)$$

where  $h_{\text{av}}$  is the average printed film thickness, and  $h_{\text{max}}$  is the theoretical maximum printed thickness.

### 3.3 Theoretical Ink Transfer Model (ITM) method

The mathematical ITM model (developed by Abbott, S., Gaskell, P. and Kapur, N. (2001, private communication)) predicts the printed film thickness through a mesh using off-contact screen printing principles. Surface forces dominate the behaviour; as the mesh separates from the substrate, ink transfers to the substrate, and a film of fluid remains on the mesh threads. The initial state of the system is shown in Figure 3.2. Figure 3.3 shows the development of a liquid bridge, occurring as the mesh rises, transferring ink from the mesh.



Figure 3.2: Schematic of the initial state of the mesh filled with fluid.

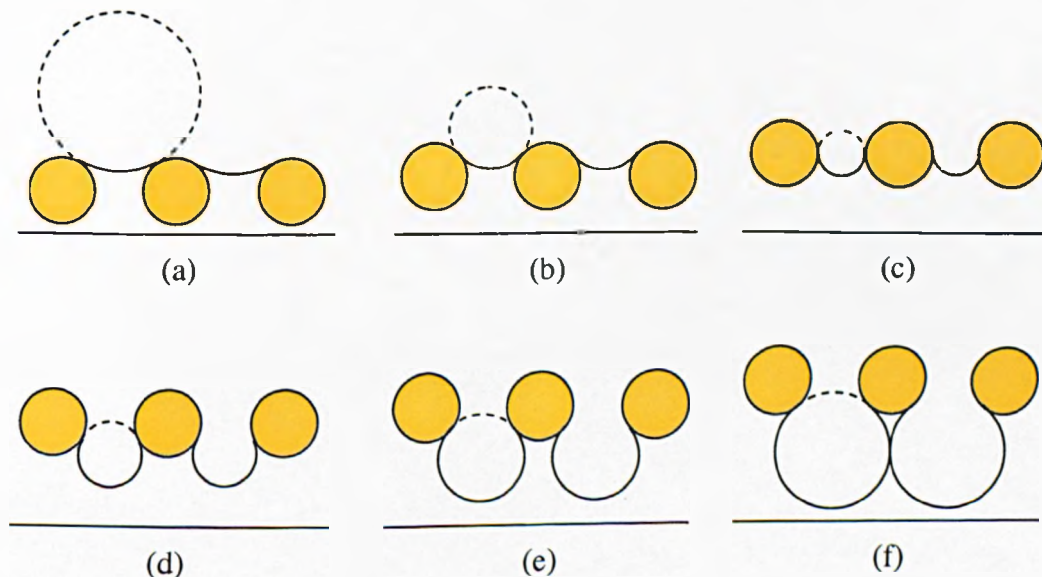


Figure 3.3: Schematic development of the liquid bridge as the separation between substrate and threads is increased (Abbott, S., Gaskell, P. and Kapur, N. (2001, private communication)).

### Assumptions of the model

The mesh geometry is simplified by considering it to be 2-dimensional. The threads are circular with radius of  $R_{thread}$ ; aligned at a constant height in the same orientation, with no woven formation. The distance between consecutive threads is  $2H_o+2R_{thread}$ , with a minimum space between threads of  $2H_o$  as shown in Figure 3.4.

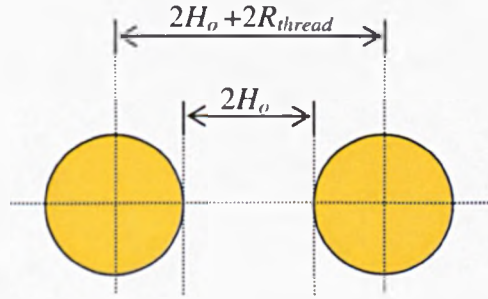


Figure 3.4: Diagram of adjacent threads in cross-section.

The fluid is assumed to be incompressible with negligible body and inertia forces. A no-slip boundary condition is applied where there is contact with threads and substrate. The shape of the fluid free surfaces (i.e. between mesh threads) is modelled by an arc of varying radius dependent upon the separation distance between the threads, a conservation of fluid volume and the residual film left on the threads. Snap-off completes as 2 adjacent arcs meet, as illustrated in the final image of Figure 3.3.

The snap-off speed is dependent on the distance of the squeegee blade from the screen edge, and the linear squeegee speed. The speed of the meniscus is approximated by maintaining conservation of fluid volume.

The capillary number,  $Ca$ , a ratio of viscous forces to surface tension, is calculated as follows:

$$Ca = \frac{\mu U}{\sigma} \quad (3.4)$$

The fluid meniscus  $Ca$  is typically of order 1 to 10, primarily due to the viscous nature of the ink. Under these conditions the film thickness remaining on the thread asymptotically reaches a limit. The model does not consider substrate properties or composition.

### Calculations to estimate the film thickness

The following equations are used to predict the printed film thickness. Figure 3.5 defines the system dimensions relative to the parameters of the equations. The two parameters that are used to describe the mesh are the thread diameter and spacing.

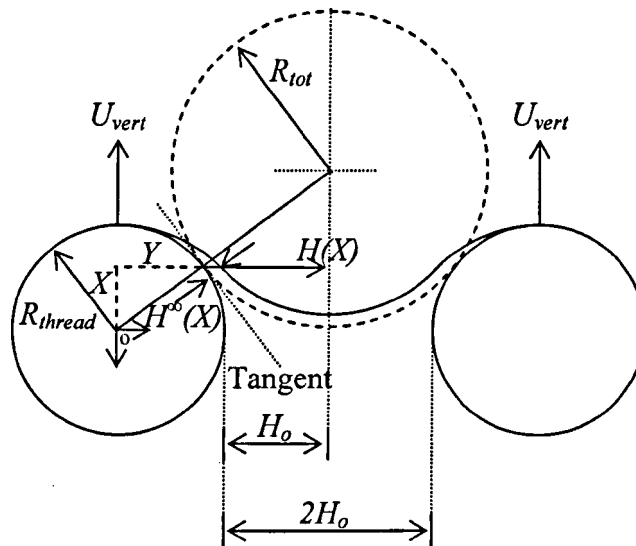


Figure 3.5: System used to solve the problem (Abbott, S., Gaskell, P. and Kapur, N. (2001, private communication)).

The distance the thread surface is from the centre of the space in the  $Y$ -direction is termed  $H(X)$ , for all  $X$  values:

$$H(X) = H_o + R_{thread} - \sqrt{R_{thread}^2 - X^2} \quad (3.5)$$

The gradient of the thread is defined as:

$$\frac{dY}{dX} = -\frac{X}{\sqrt{R_{thread}^2 - X^2}} \quad (3.6)$$

$R_{tot}$  is determined for each  $X$  value by setting the tangent equal to the thread gradient. This provides the following equation:

$$R_{tot} = H(X) \sqrt{1 + \left(\frac{dY}{dX}\right)^2} \quad (3.7)$$

From this the film thickness that remains on the mesh and the meniscus radius are defined using the relation:

$$R_{tot} = H^\infty(X) + R_{men} \quad (3.8)$$

To establish the film thickness, the meniscus speed and hence capillary number are still required, determined using the analytical relationship:

$$\frac{H^\infty}{R_{men}} = a \times Ca_{men}^b \quad (3.9)$$

since  $Ca$  is typically high (i.e. greater than 2) the values of  $a$  and  $b$  were set as:  $a = 0.66$ ;  $b = 0$  in accordance with Ruschak, K. J. (1982).

The model divides the thread into 100 equally spaced points in the  $X$  direction to perform the iterative calculation process, terminating when adjacent free surfaces of the fluid meet (i.e. the liquid bridge breaks). For each  $X$  location, the local meniscus speed and capillary number are evaluated. Numerical integration is applied to calculate the fluid volume remaining on the threads,  $V_{remain}$ . Combined with the initial volume,  $V_{initial}$ , the percentage of transfer to the substrate is given by:

$$\text{Percentage transfer to substrate} = \frac{V_{initial} - V_{remain}}{V_{initial}} \times 100\% \quad (3.10)$$



The model returns to the 3-dimensional screen mesh geometry to calculate the theoretical printed film thickness by multiplying the maximum theoretical thickness the mesh can print (equation (4.8)) by equation (3.10). The definition of the maximum theoretical printed thickness is described in section 4.4.1. The non-dimensional thickness value is calculated using equation (3.3).

### **3.4 Experimental results and discussion**

The experimental results displayed in this section, highlight the effect of the studied variables on both the generated film thicknesses and the non-dimensional thicknesses.

Confidence limits are determined to highlight observed thickness ranges. The thickness variations between experiments did not seem systematic; squeegee pressures varying from light to hard had no significant affect on the thickness – also observed by Abbott, S. (2003, private communication). Small variations in the squeegee operation may create a degree of variation, between prints, for the final printed thickness. Due to the limits of handheld squeegee operation, the pressure, speed and angle have not been studied further in this work. Lateral movement of the vacuum platform (minimised with the anti-rotation post) was not eliminated and so may also affect the fluid transfer to the substrate.

#### **3.4.1 Effect of the mesh-substrate separation rate on the film thickness**

Parikh, M., et al. (1991) previously reported that increased printing speed reduces the printed film thickness (based on previous work by Sergent, J. (1985)). Riemer, D. E. (1988) notes that there is a printing speed limit above which ink ceases to be transferred correctly to the substrate. Work done by Mannan, S. H., et al. (1993, 1994) suggests increased speed produces thicker films (via stencil printing) which agrees with the screen printing results performed over a greater printing speed range by Hunt, D. and Hohl, D. (1996a). The experimental work by Lomas, M. and Short, I. (1999) conflicts with these results, producing greater ink consumption (film thickness) at low

speeds. Printing speed refers to the squeegee speed, which affects the peel-off rate; for off-contact printing the peel-off rate is significantly harder to control than here.

The results shown in Figure 3.6 highlight that there is a small degree of fluctuation for the printed film thickness, obtained for each test fluid using the 150-31 mesh, for the peel-off range investigated. There is no consistent evidence that increasing the rate reduces the printed film thickness. The effect of mesh-substrate separation rate on the film thickness was similarly observed to be negligible when printing using the 90-40 and 120-34 meshes. These graphs are provided in appendix A2.

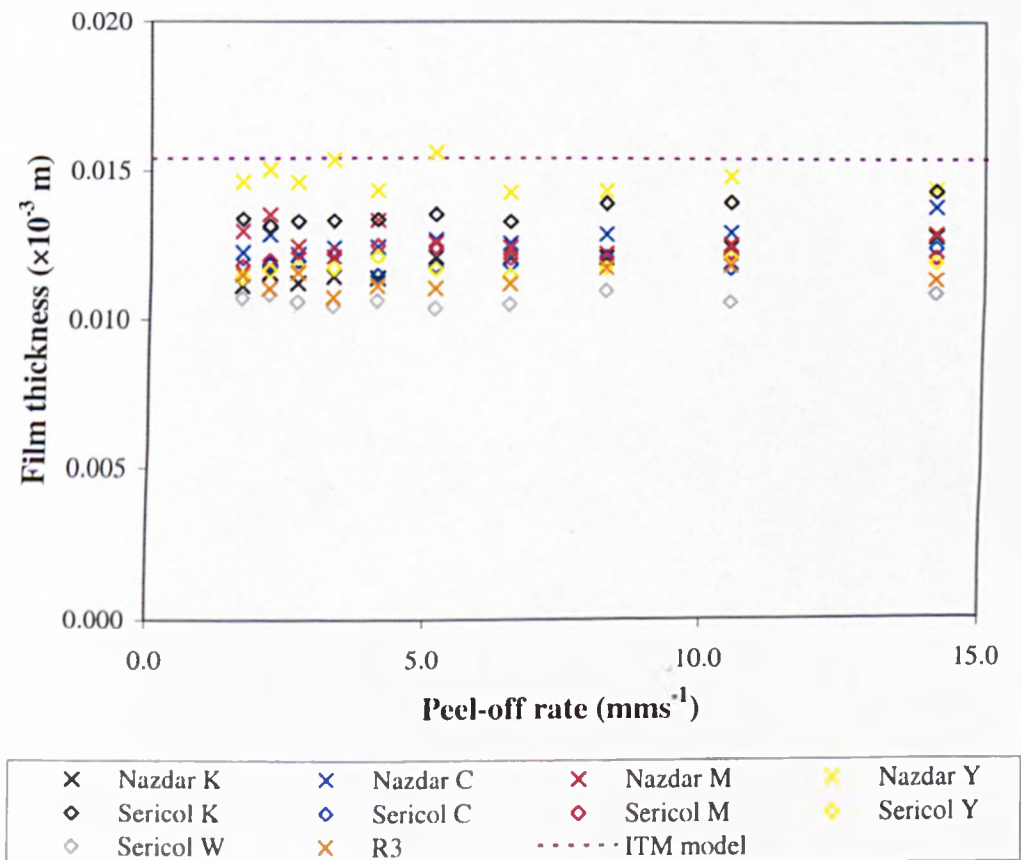


Figure 3.6: The printed film thickness of the tested inks and grease for peel-off rates in the range 1.7-14.1mms<sup>-1</sup> using the 150-31 mesh. Each point on the graph is the average of 5 prints with the same set-up conditions.

### 3.4.2 Effect of mesh geometry on the film thickness

Since peel-off rate (as demonstrated previously in section 3.4.1) has no significant influence on the print, the data from Figure 3.6 can be collapsed down so the printed film thickness can be simply given as a function of the mesh open area. Figure 3.7 shows the experimental printed thickness of these meshes. Increasing the open area fraction per mesh cell increases the observed printed film thickness and a larger mesh thickness causes a thicker film to be printed.

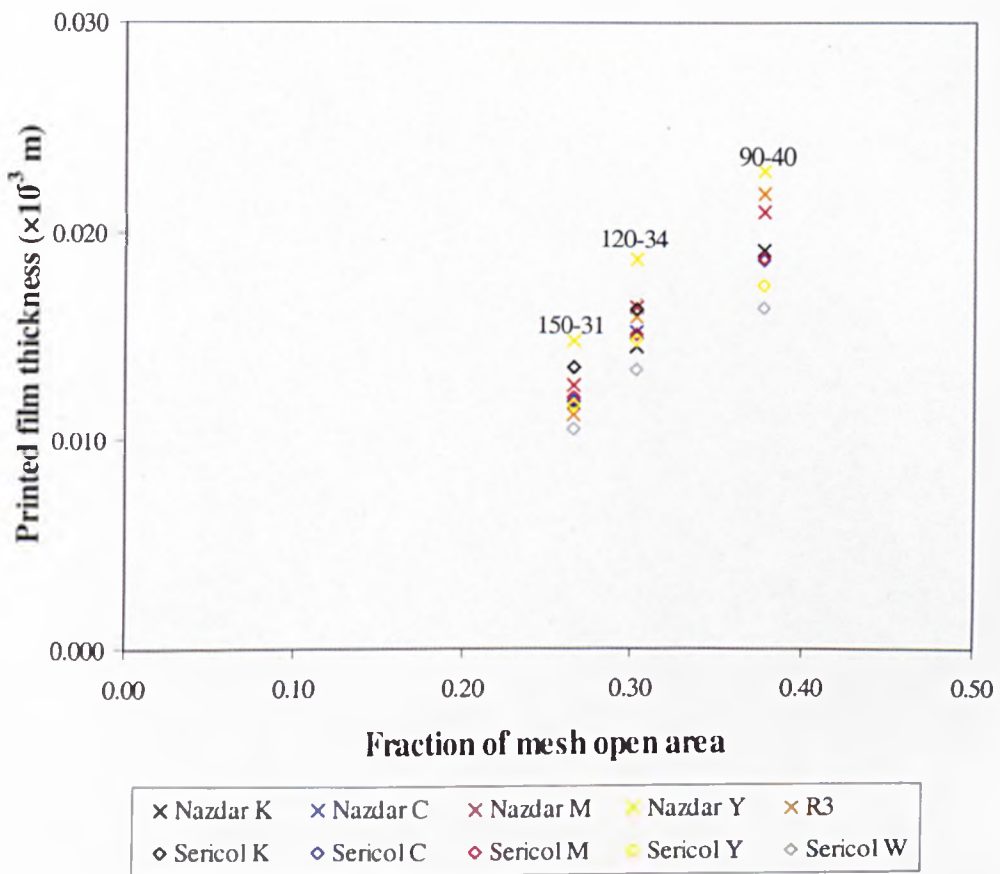


Figure 3.7: Graph showing the printed film thicknesses for the 3 meshes using the 10 tested fluids. The fraction of mesh open area is established from the dimensional measurements of the meshes, rather than using manufacturer's values.

Figure 3.8 shows the printed film thicknesses as non-dimensional values – equation (3.3) using the theoretical maximum initial ink thickness in each mesh – equation (4.8). Considering all the inks, there is no overall correlation between this value and the open area fraction per mesh cell. Some inks show a positive correlation whilst others display a negative one.

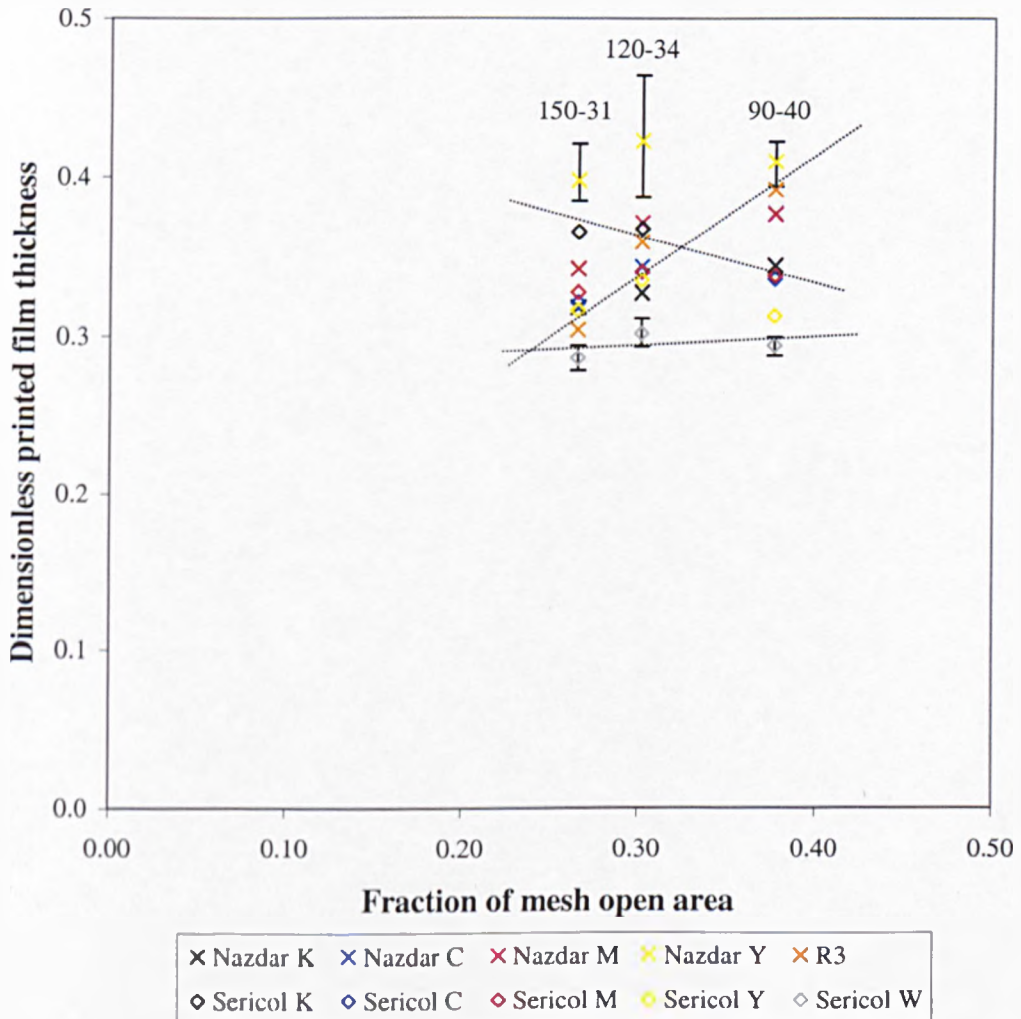


Figure 3.8: Graph showing the non-dimensional printed film thickness for the 3 meshes using the 10 tested fluids. The confidence limits for the meshes' two extreme fluid printing thicknesses are also displayed. The best fit lines relate to: R3 grease (positive correlation), Sericol black ink (negative correlation) and Sericol white ink (no correlation).

### 3.4.3 Effect of the fluid type on the film thickness

As shown in Figures 3.6-3.8 the ink type affects both the actual printed film thickness and the non-dimensional thickness value. In Figure 3.6, a thickness distribution of  $5.0\mu\text{m}$  was observed using the 150-31 mesh for the different inks. Using the 90-40 and 120-34 meshes this distribution increased to  $7.5\mu\text{m}$  – see Appendix A2. The NAZDAR yellow ink printed thickest, and the thinnest printed film was produced with the Sericol white ink.

Figure 3.7 shows that the printed thickness varied significantly for the different fluids. The percentage deviation of the film thicknesses are within 28-34%, for the 3 meshes, highlighting that the ink type is an important print factor.

Figure 3.8 highlights that the non-dimensional film thickness for a specific printed fluid remains constant, independent of the mesh used. There is a small positive correlation shown on the graph with the NAZDAR black, cyan and magenta inks, with a small negative correlation with the Sericol black ink. Since apparently there is little variation in the non-dimensional film thickness for a given ink, this could be used to predict the experimental printed thickness with other mesh geometries.

Increasing the fraction of open cell area of the meshes caused the non-dimensional printed thickness to more significantly increase when printing the R3 grease than with the inks – this is highlighted with a line of best fit in Figure 3.8.

Figure 3.9 displays confidence limits to highlight the range of thicknesses for each fluid; the ranges decrease as the fluid density increases. The non-dimensional film thickness for NAZDAR yellow ink is 0.410 (within the range of 0.385-0.464), and for Sericol white ink it is 0.294 (with a smaller range of 0.278-0.311). The R3 grease exhibited the greatest non-dimensional film thickness range; resulting from the observation that increased open mesh cell fraction affected the thickness for this fluid more than the inks, rather than having significant large ranges for the individual meshes.

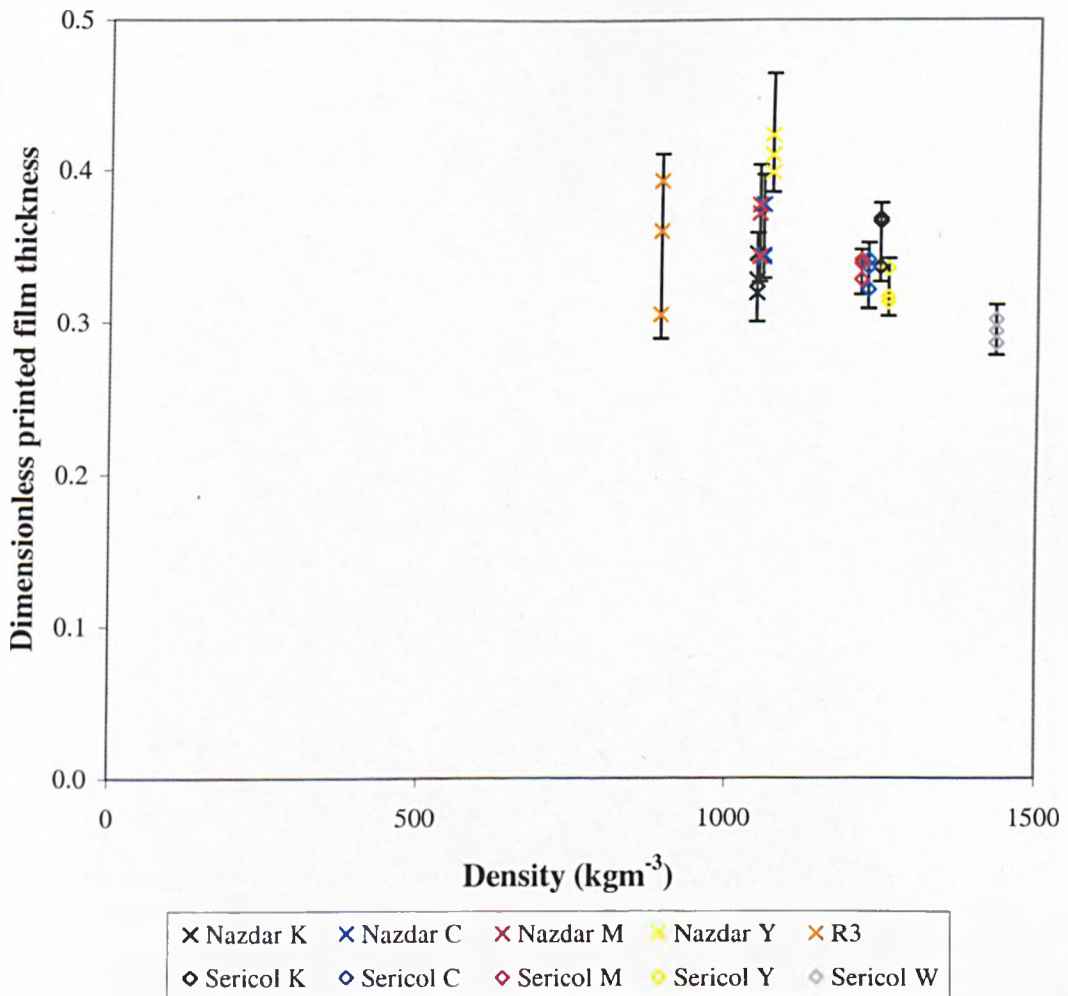


Figure 3.9: Comparison of the non-dimensional printed film thickness range with the density of the 10 test fluids. The confidence limits shown apply for the 3 meshes used.

The CMYK inks have similar densities within their respective Sericol or NAZDAR groups. Sericol white ink is denser, and R3 grease is less dense, than both ink groups. Focusing on any of these 4 density groups, shows there is a noticeable range of non-dimensional film thicknesses; fluid density has little effect on the parameter.

The test fluids are non-Newtonian; varying the rate of shear experienced in the print stage (achieved by varying peel-off rates) gives a range of different effective viscosities during this part of the process. Section 3.4.1 showed that the peel-off rate had negligible effect on the printed film thickness, and so implies that viscosity is not the controlling variable within the process.

A meaningful comparison between different fluids' viscosities and the printed film thicknesses cannot be directly made due to the different composition of each fluid since the inks are laden with particles. The shape, size and concentration of particles are specific to each ink, and therefore introduce uncontrolled variables to the study. The observed relationship between viscosity and the printed film thickness may have been affected by the fluid composition variables not being constant between inks. Chapter 4 investigates further the effect of viscosity on the film thickness (without variation of the peel-off rate variable), by using a range of ink dilutions with an appropriate oil creating a viscosity range. This enables the viscosity variable to be studied independently.

### 3.4.4 Effect of the substrate type on the film thickness

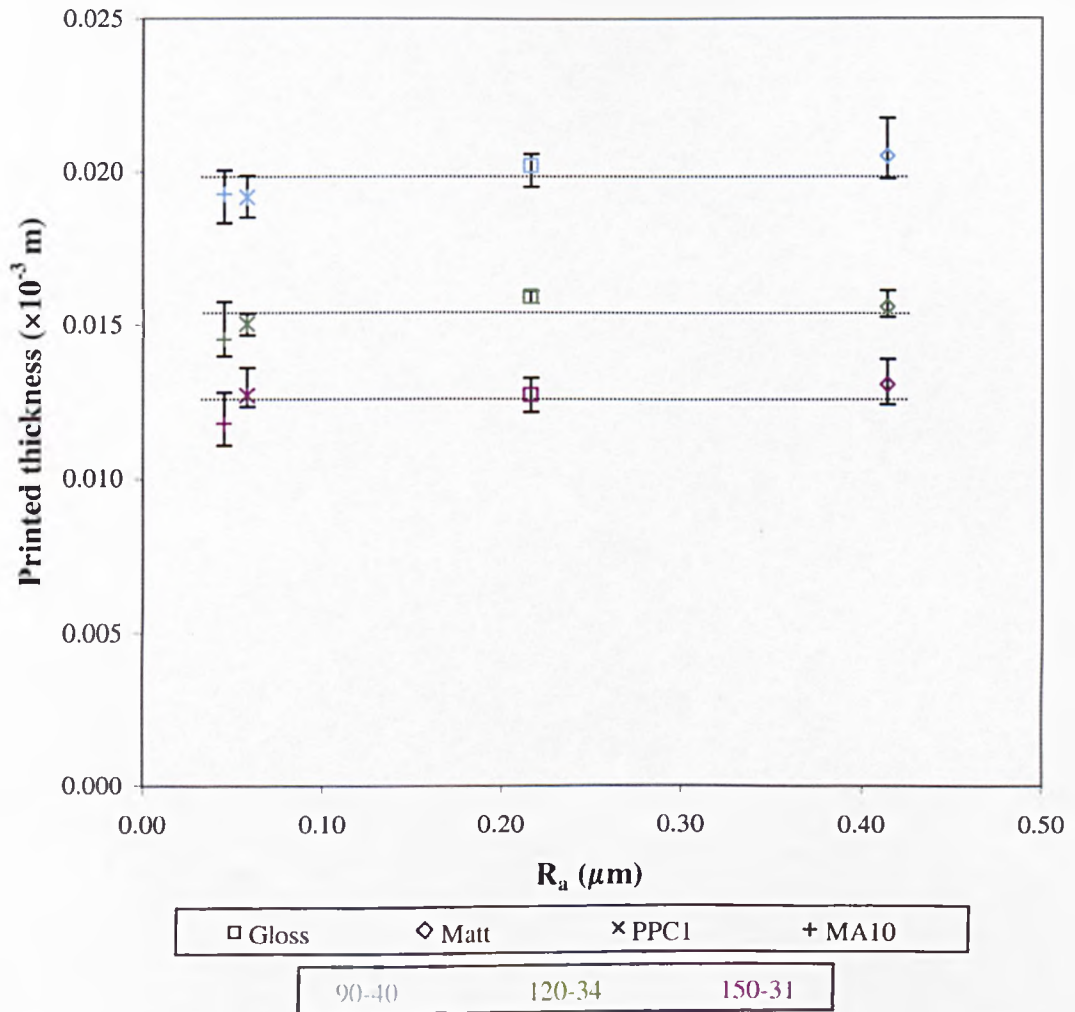
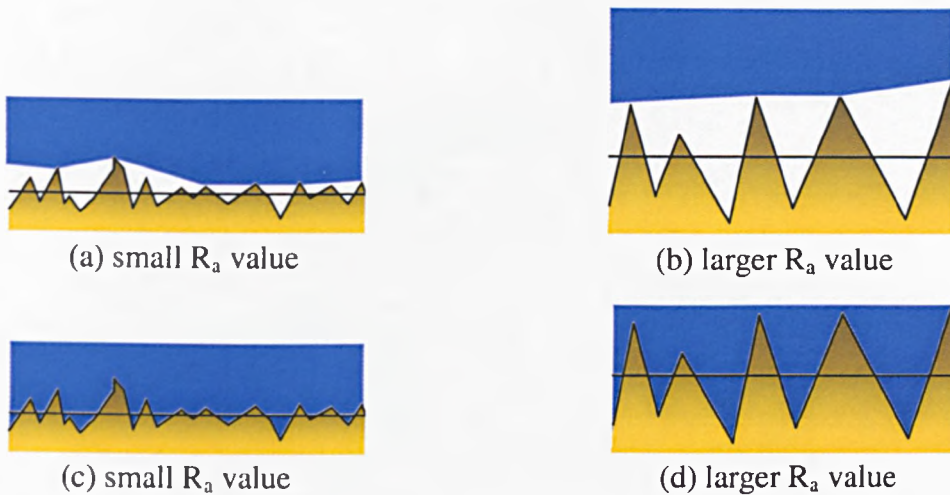


Figure 3.10: The effect of substrate roughness on the printed film thickness of NAZDAR black ink.

Figure 3.10 indicates that the printed film thickness remains approximately constant irrespective of the substrate roughness, remaining greatly dependent on the mesh geometry used. It is the volume of ink transferred to the substrate which must be a constant factor. It is initially unclear whether film thickness may also be constant as shown in Figure 3.11.





*Figure 3.11: Diagram illustrating how the surface roughness may affect the actual film thickness even if the same volume of ink is deposited.*

Figure 3.11 illustrates how  $R_a$  and filling behaviour may influence the actual obtained film thickness, which is the height of film above the substrate peaks. Figure 3.11(a)-(b) indicate the lower surface of the ink in contact with the peaks of the substrate roughness resulting in little difference of final film thicknesses for the two differing  $R_a$  values. Figure 3.11(c)-(d) show differing film thicknesses since the ink fills the surfaces troughs. This behaviour would be similar to how porosity influences film thickness by absorbing ink into capillary-like holes within the substrate.

The range of  $R_a$  values for the test substrates is  $0.045\text{-}0.414\mu\text{m}$ . This is significantly smaller than the transferred ink volume per area of print (i.e. the average film thickness). Considering the magnitude of ink transferred to the substrate the difference between Figure 3.11(a) and (c) (and Figure 3.11(b) and (d)) is insignificant. Therefore the substrate surface roughness has negligible influence on the printed film thickness, which remains constant.

### 3.5 Theoretical model results and discussion

Table 3.1 shows the theoretical predictions from the Ink Transfer Modeller (Abbott, S., Gaskell, P. and Kapur, N. (2001, private communication)) for the three meshes used in the experimental work. The model shows the mesh geometry affects the calculated printed thickness. The non-dimensional printed thickness values (equal to the fluid transfer fraction the ITM calculates) are very similar (within  $0.40 \pm 0.02$ ) and the maximum initial ink thickness in the mesh can be multiplied by  $0.40 \pm 0.02$  to calculate a theoretical dimensional thickness of the printed film, irrespective of the actual mesh geometry. However, the mesh geometry does affect the actual printed ink thickness since the initial maximum thickness of ink in the mesh is calculated from the geometry of the mesh (section 3.3).

Mesh geometry	Theoretical printed thickness ( $\mu\text{m}$ )	Theoretical non-dimensional printed thickness
90-40	21.7	0.39
120-34	17.7	0.40
150-31	15.4	0.42

*Table 3.1: Results of the ITM theoretical printed thickness for the meshes used experimentally.*

### 3.6 Comparison of experimental and theoretical results

The ITM model calculates film thickness from the percentage fluid transfer of a 2-dimensional system. This transferred fraction is then scaled, using the theoretical maximum amount of ink in the mesh to give an equivalent film thickness. The work of chapter 4 develops the experimental printing rig and method so this value is determined, by establishing initial ink volume in the meshes.

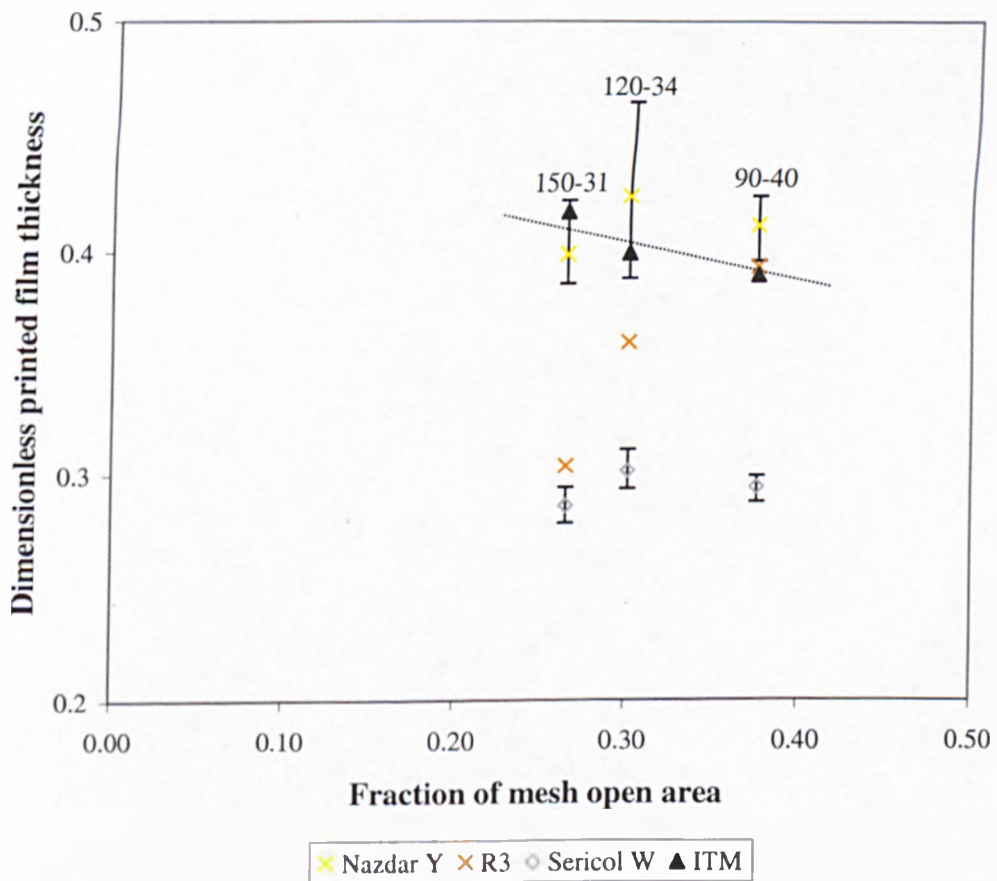


Figure 3.12: The ITM non-dimensional film thickness results compared to the 2 extremes of experimentally observed film thicknesses of the inks and grease, for the 3 screen meshes.

Figure 3.12 shows that the thickness predictions from the ITM are comparable to the experimentally observed results using NAZDAR yellow ink. However the ITM model calculates significantly greater thicknesses than those printed with the other inks (28-

51% over-calculation for the situation using Sericol white ink, based on the average thickness for each mesh).

The experimental non-dimensional ink thickness results are independent of the fraction of open mesh area (for the tested meshes). The ITM model calculates a slight negative correlation (shown in Figure 3.12), which is essentially also insignificant.

The ITM generates one printed film thickness per mesh geometry, but experimentally a range of thicknesses was observed using different fluid types. The non-dependence of the ITM on fluid viscosity and density is appropriate since experimental results found these variables had little effect on the print.

The simplified 2-dimensional model will never capture the true nature of the 3-dimensional process. The ITM has no inclusion of the woven mesh structure present in experimental meshes. It assumes there is initial contact between the substrate and whole length of the thread. However, experimentally the initial contact would only be at the threads knuckles due to the weave structure. Another difference relating to the thread geometry is that the ITM assumes a constant circular cross-sectional thread, but in practice the mesh threads flatten with variable cross-sectional shape (shown in Figure 2.8) because of the required screen tension and weave formation. The geometry effects will result in a more complex transfer of fluid than highlighted in the simple model.

Nevertheless, the ITM does provide confidence in the suggested mechanism involved in the ink transfer of screen printing, capturing a simplified understanding of the physics underpinning the process.

### 3.7 Summary

The conclusions that can be drawn from the work reported in this chapter are:

- Peel-off rate has negligible effect on the printed thickness using the contact printing technique. With off-contact printing, the peel-off rate is difficult to control, but the results obtained here indicate that this rate has little effect on the final film thickness.
- The roughness of the substrate does not influence either the transferred volume of ink to the substrate or the printed film thickness. This result is also useful since it indicates that any localised variations of substrate roughness would not affect the printing capability of ink transfer.
- The mesh geometry does significantly affect the actual printed film thickness, and therefore to obtain a desired wet film thickness the correct geometry needs to be selected for the particular ink. The mesh geometry however, has negligible affect on the non-dimensional thickness value, remaining approximately constant for an individual printing ink.
- The type of fluid used is a major influencing variable (from this study) affecting the printed film thickness. However there is no direct relationship between the studied fluid properties, density or viscosity, with the film thickness. Properties that were not assessed include: surface tension, solid content, particle size and shape, viscoelastic properties, and contact angle on mesh threads.
- The ITM modeller predicts thicker printed films than those generated experimentally for most inks used, however the calculations coincidentally compare well with NAZDAR yellow ink prints. The mesh geometry has little effect on the calculated (non-dimensional) thickness value of the ITM, which remains approximately 0.40.

## **Chapter 4**

# **Initial ink volume in the mesh and the percentage ink transfer to the substrate**

---

The focus of previous screen printing ink transfer research has been the final film thickness, whilst the percentage ink transfer to the substrate has generally been overlooked. This may be partly due to the industrial focus of the work, highlighted in chapter 3, including: total ink consumption governing the cost of a print run; obtaining required transparency of inks used in halftone printing; production of specified film thicknesses to meet design requirements of magnetic strength or electrical conductivity.

### **4.1 Introduction**

In this chapter, the ink transfer process of screen printing is investigated. The increased knowledge gained through the collection of experimental data is used to improve existing mathematical models established within industry and the ITM model (described in chapter 3). It can also assist in a theoretical approach for designing screen printing inks and meshes.

The previous mathematical models of chapter 3 over estimated the initial ink in the mesh. The aim of this present work is to further understand this pre-print state and therefore improve the models' accuracy. Establishing the initial ink in a mesh, together with post-print mesh measurements, leads to a greater insight of the ink transfer behaviour. This is achieved by collecting quantitative data using experiments based on those applied in chapter 3, and with qualitative visual images observed using a microscope.

The second aim of this work is to vary the viscosity of the printing ink without variation of pigment size or shape; printing fluids used in chapter 3 experiments did not isolate the viscosity variable. The work in this chapter independently determines the influence of this printing variable.

## 4.2 Experimental method

The following sets of experiments have been designed to investigate the initial ink volume in the mesh and percentage ink transfer to the substrate. The motivation is to test the commonly held assumption that the ink initially fully fills the mesh. Both the initial volume of ink in the mesh and the average transferred film thickness to the substrate are required to determine this. The experiments were carried out on the screen printing rig described in section 2.2. The rig set-up and method used to obtain quality prints is the same as performed in section 3.2.

For these sets of experiments the fluids available for printing were the Sericol CYMK ink set, NAZDAR black<sub>[2]</sub> ink (diluted with HVI 60, HVI 160, and undiluted), Sericol white ink, glycerine-water mixtures (25%, 50%, 75% and 100% glycerine dilutions) and R3 grease as described in section 2.7. The NAZDAR black<sub>[2]</sub> ink was diluted with the two oils so that the effect of changing the density and viscosity could be investigated without any variation to the components of the printed ink (such as pigment size and shape). The measured viscosity of the NAZDAR black<sub>[2]</sub> ink dilutions are shown in Figure 4.1.

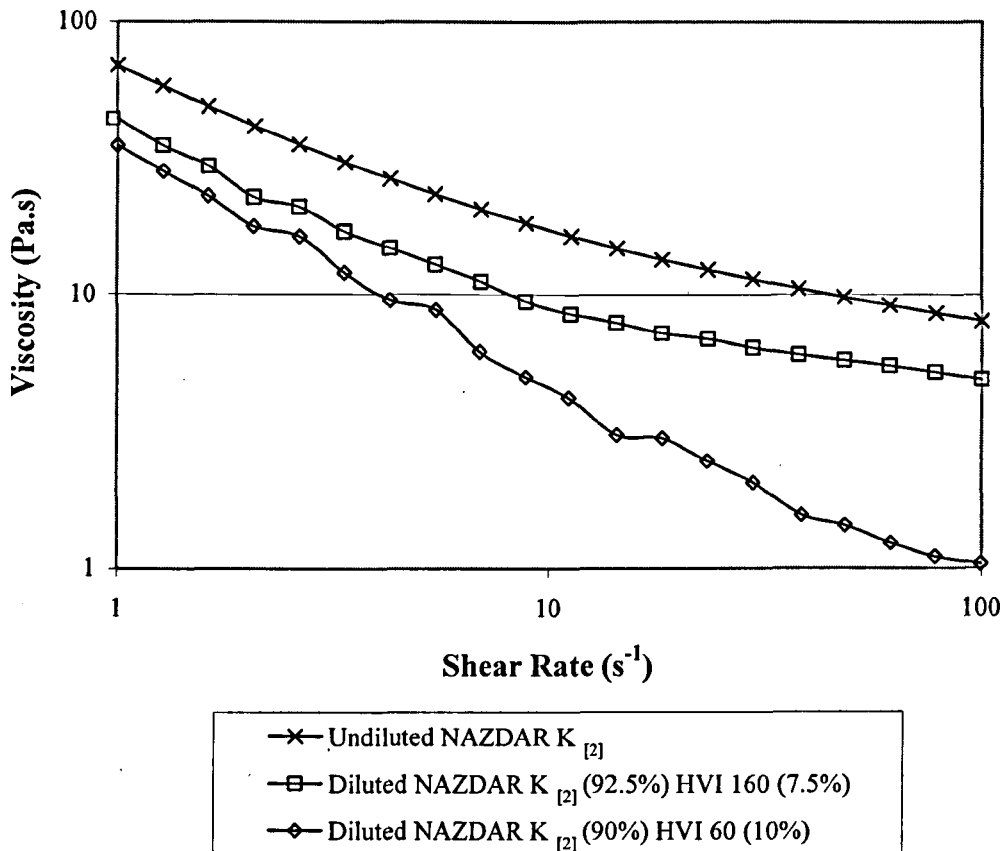


Figure 4.1: Graph of the measured viscosity of the NAZDAR black<sub>[2]</sub> dilutions in the shear rate range of  $1-100s^{-1}$ . Shear rate versus viscosity measured using a cone ( $4^{\circ}$   $\varnothing 40mm$ ) and plate geometry at  $20.0^{\circ}C$ .

#### Development of the method to establish the initial ink volume in the mesh

The aim was to design a reliable method of measuring the amount of ink occupying the mesh before printing occurs. Four different methods were tested to calculate the initial experimental ink volumes in the screen meshes, which are described below. The most appropriate of these methods is used to collect the data described in the results section of this chapter.



### **Method 1 – Cleaning**

After a quality print was obtained, the ink remaining within the printable region of the mesh was removed using Seriwash Universal Screen Wash with Tork Screen Wiper cleaning sheets. These cleaning sheets, laden with a mixture of ink and screen wash, were hung in a darkened cupboard, preventing ink cure while allowing the screen wash to evaporate from the cloth.

A major problem with this method is that components of the ink also evaporated, so the final recorded ink mass addition on the cloth was significantly less than the amount initially added. This was confirmed through depositing a known mass of ink on to a cloth and hanging it in the cupboard for the typical time required for screen wash evaporation to complete (dependent on how much screen wash is applied, this time ranged 45 minutes to several hours). Re-weighing the inked cloth highlighted ink evaporation occurrence (both with and without screen wash presence). Therefore this method, which assumes the additional ink mass to the cloth is equal to the ink mass remaining in the mesh, is unreliable. Other problems with the method include difficulties in removing ink only from the printable region especially near stencil edges.

### **Method 2 – Individual cell count**

A known mass of ink was added to the mesh, with a single blade movement, using a small length (approximately 30mm) of squeegee material; no excess ink remained on the mesh and the ink spread was confined to the mesh printable area. The area that the ink was added to was calculated by counting the number of mesh cells that contained ink – using a microscope linked to a PC. In this way the initial ink volume per mesh area was established.

Problems relating to this method include: accurately counting the number of ink filled cells and cells at the edge of the region only being partially filled.

### **Method 3 – Destruction of the mesh**

After obtaining a quality print, the mesh was cut removing the central open printing region of the mesh. The difference in mass between the removed section containing ink and the cleaned section (obtained using Seriwash solution) was used to calculate the ink volume remaining in the mesh. The initial ink volume was established by combining the post printing volumes of ink in the mesh with ink transferred to the substrate (using the method of chapter 3).

Problems with this method include: accurate cutting of the mesh along stencil edges, the unwanted ink transfer to the knife and the fact that the mesh cannot be reused.

### **Method 4 – Stencil removal**

Masking tape was used to form removable stencils (as described in section 2.2.4 – the light frames of each mesh had scale markings on to aid applying the tape) leaving an open printable region of 170×170mm. Tape was not applied to the underside of the mesh since ink leakage became unacceptable and it created an uncontrollable premature peel-off which occurred before the vacuum platform was lowered. This did not occur with capillary stencils since the stencil thickness from the mesh threads was significantly less than the tape thickness.

After the first quality image was obtained, the tape was removed. The mass of the frame and mesh were then measured using the scales described in section 2.5. Clean tape was then applied to the mesh at the outer edge of the previous printed printable area. It was ensured that the tape was securely fixed and did not overlap the print area since this resulted in an increased amount of ink leakage. This technique minimised the ink leakage at the tape boundary but could not totally eliminate it occurring since the tape was not applied within the mesh apertures like a capillary stencil. The actual printable area dimensions were measured using a mm incremented ruler.

The same experiment was repeated to produce further prints onto MA10 transparency substrates for data collection. For the Sericol black and yellow inks 10 quality prints were generated for all 3 light framed meshes: Saati 90-40 OU-PW, Saati 120-34 OU-PW and Sefar 150-31 Y-PW. (The actual mesh parameters were measured using a Co-ordinate measuring machine KEMCO 400 and a Nikon Profile Projector Model V-16D as described in section 2.6.1 and 2.6.2.) Due to the high level of repeatability, a reduction to 6 quality prints was made for the remaining inks tested.

Only one peel-off rate was selected since the previous experiments reported in chapter 3 had shown that this parameter did not affect the printed thicknesses. The selected peel-off rate was  $6.5 \pm 0.5 \text{ mms}^{-1}$  (main motor control unit setting of 7.0).

The printed film thicknesses were calculated using the method in section 3.2. The amount of ink remaining within the mesh after each print was calculated by measuring the mass after removing the tape (ensuring no excess ink contaminated the mesh). The difference between this mass and the mass of the clean dried mesh with no tape prior to any printing was the mass of the ink that remained in the mesh after a print (see equation (4.1) below). Combining this with the calculated printed ink mass enabled the initial ink volume in the mesh, the percentage of ink transferred to the substrate and percentage remaining in the mesh to be found using equations (4.2)-(4.4).

$$\text{Mass remaining in the mesh, } m_{ink(remaining)} = m_{mesh(post-print)} - m_{mesh(clean)} \quad (4.1)$$

$$\text{Initial ink volume in the mesh, } V_{ink(initial)} = \frac{m_{ink(on\_substrate)} + m_{ink(remaining)}}{\rho} \quad (4.2)$$

$$\% \text{ of ink transferred to the substrate} = \frac{m_{ink(on\_substrate)}}{m_{ink(on\_substrate)} + m_{ink(remaining)}} \times 100\% \quad (4.3)$$

$$\% \text{ of ink remaining in the mesh} = \left( 1 - \frac{m_{ink(on\_substrate)}}{m_{ink(on\_substrate)} + m_{ink(remaining)}} \right) \times 100\% \quad (4.4)$$

The non-dimensional printed thickness was established using equations (3.3) and (4.8), generating a ratio between the actual print thickness and the maximum theoretical thickness of ink in a mesh (described in section 4.4.1).

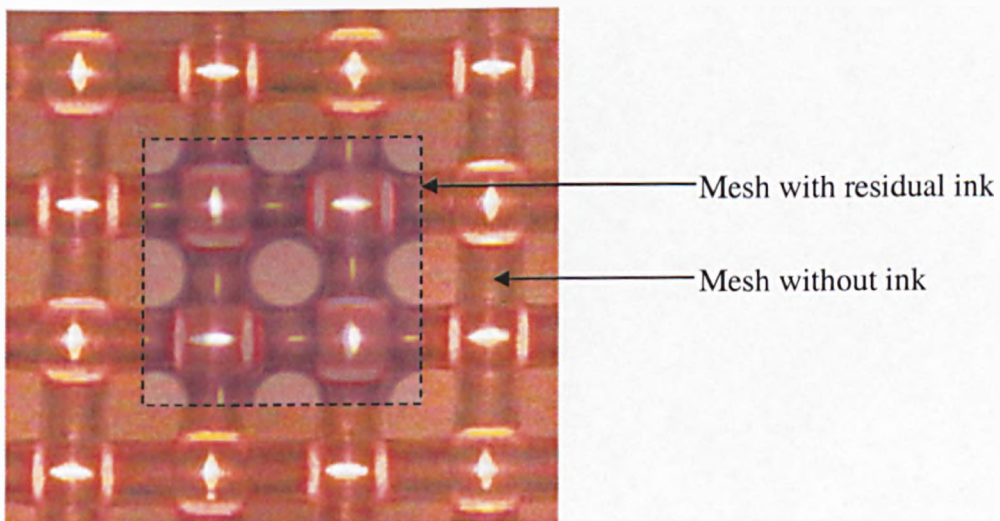
The microscope, described in section 2.4.2 was positioned directly above the mesh to capture images at different print stages. The  $\times 5$ ,  $\times 10$  and  $\times 20$  lens were used for each recorded feature. Images were collected of the clean mesh, and the wetted mesh after quality prints were generated – prior to printing, but after the print stroke; and finally after the print stage. This method was used for all the volume measurements.

### 4.3 Experimental results and discussion

This section reports experimental results determining three print values for each setup: the initial amount of ink in the mesh, the amount of ink printed to the substrate, and the percentage transfer of ink.

#### 4.3.1 Mesh images of the printing process

To gain a greater understanding of the print process, a series of images of the ink in the mesh were recorded using the microscope, to highlight particular features of the ink transfer behaviour through the screen meshes.



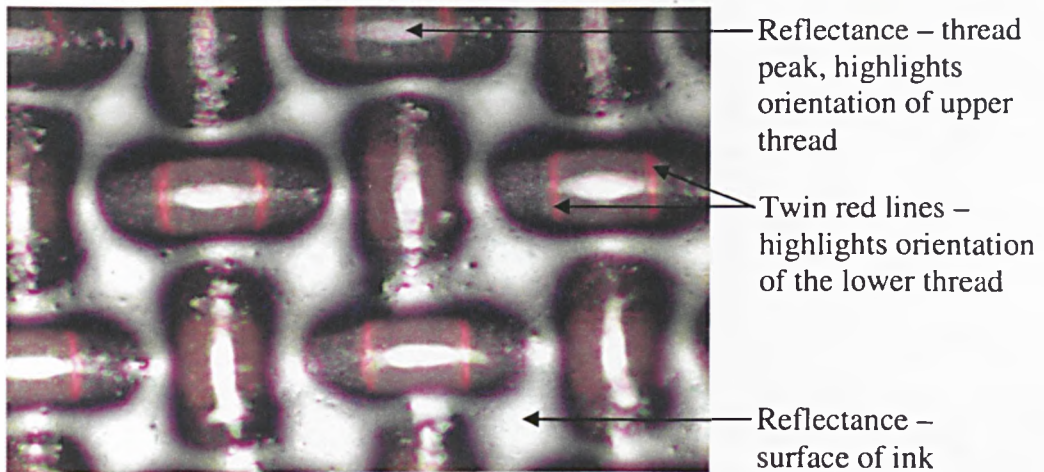
*Figure 4.2: Image of the clean 120-34 mesh (outer region) overlaid with the image of the mesh just after printing with NAZDAR black<sub>[2]</sub> ink (inner region).*

Figure 4.2 overlaps two images of the 120-34 mesh: the clean mesh and the mesh after printing. Correct alignment was achieved by matching the reflectance lines shown in both images. This combined image illustrates that it is possible to identify both the threads and the ink from just the final image. The need to generate combined images like Figure 4.2 is not necessary for identifying the thread location and orientation with images containing ink.

#### **Initial state of mesh filled with ink, after metering stroke and prior to peel-off**

Figures 4.3-4.5 are images taken of the mesh just after the metering squeegee stroke. They indicate that the ink profile is neither flat nor level with the tops of the threads, as previously assumed in descriptions of the process and in the models used within the industry. The reflectance in the images highlights regions that are perpendicular to the microscope viewing angle. This is particularly useful for identifying the orientation of the threads – i.e. using the reflectance from the peak of the thread.

The maximum height the ink reaches in the cells is significantly lower than the mesh thickness and appears to be closer to only half the mesh thickness. The ink fills above the thread uppermost surfaces only for the lower thread at the vicinity of the knuckles, on which a small film channel of ink exists. This was observed for each mesh with all the tested print fluids. Figure 4.3 shows the peaks of the threads are the same colour as the ink and not the threads, possibly suggesting that a thin layer of ink has coated the threads. However on further investigation this was attributed to the presence of ink underneath the thread rather than ink on the surface; Figure 4.5 shows this where there is a better contrast between ink and mesh.



*Figure 4.3: The initial 90-40 mesh state filled with Sericol black ink. N.B. the main features of the image are labelled to assist with identifying features in the following images (i.e. up to Figure 4.5): white regions are light reflectance from surfaces perpendicular to the microscope.*

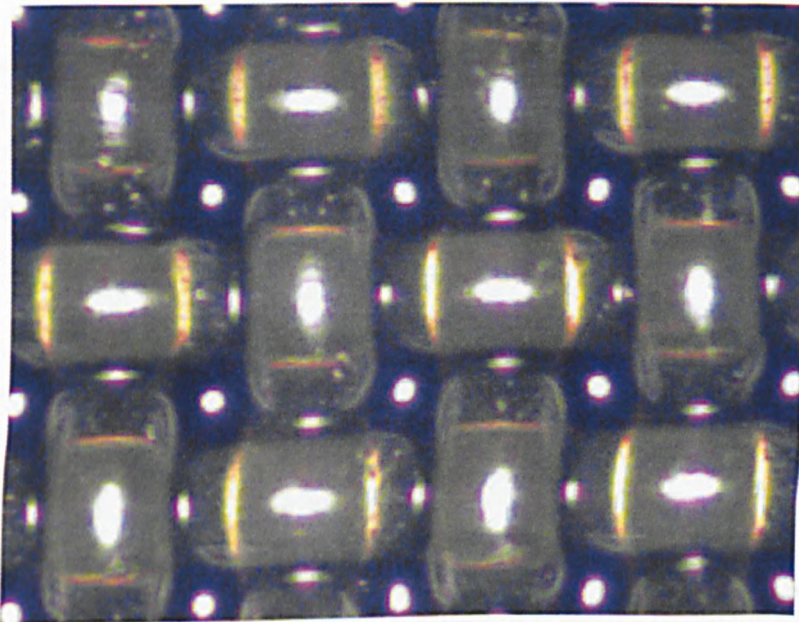


*Figure 4.4: 150-31 mesh filled with Sericol black ink. N.B. The twin line feature, highlighting the orientation of the lower thread, is yellow for the 150-31 mesh. The white circular regions at cell centres are caused due to reflectance from the ink (as described in Figure 4.3).*

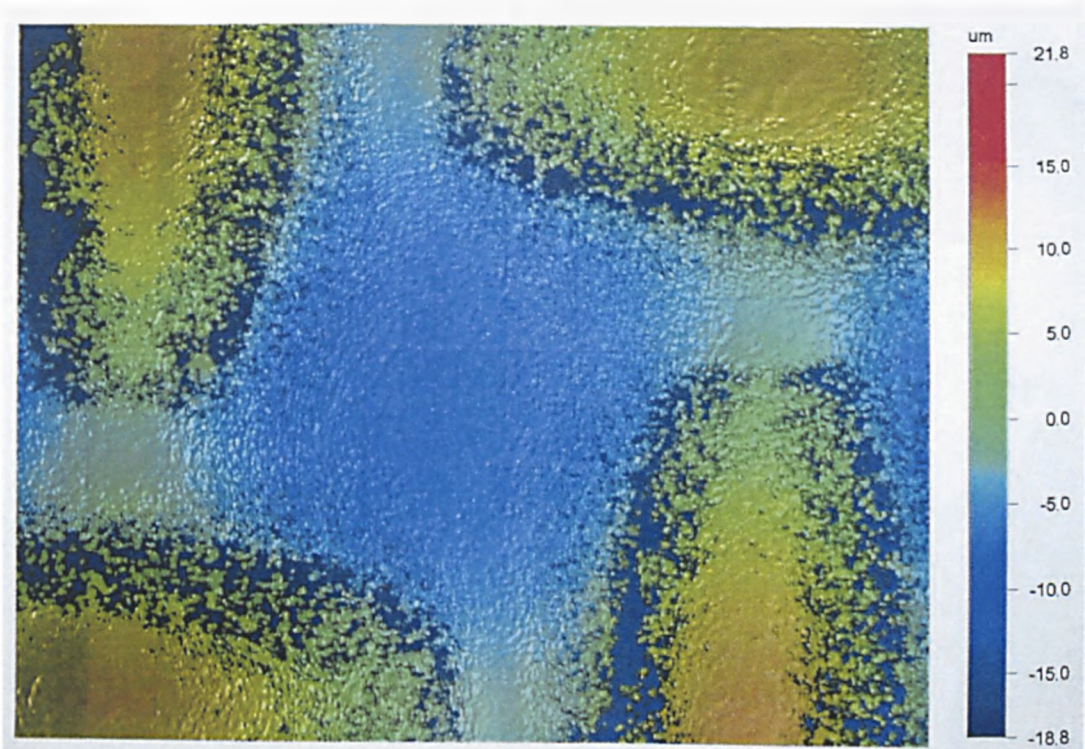


*Figure 4.5: The initial 90-40 mesh state filled with Sericol white ink.*

Since the microscope images only provide qualitative results, the WYKO interferometry apparatus was used to explore quantitative results. The ink-filled mesh was transferred to the WYKO with the substrate held in place (using masking tape positioned outside the squeegee blade path region) preventing printing. The frame rested on two level precision metal blocks. The area investigated was the squeegee side of the mesh in the middle of the printing region.

Due to the principle of the WYKO requiring detection of the reflected beams from the surface of investigation, certain inks generated high levels of noise and blank data; this problem was also observed for clean meshes (i.e. containing no ink). The only ink which generated good quantitative results was Sericol white ink, due to its high reflectance.

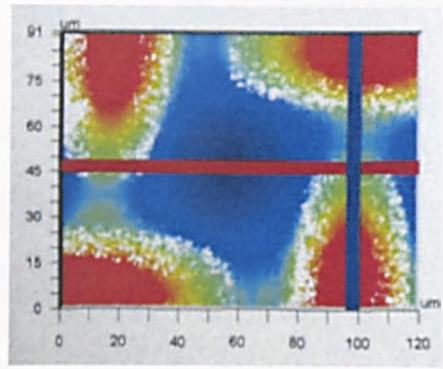
The meshes were returned to the microscope to confirm the ink profile in the mesh had not been affected during removing the screen from the printing rig.



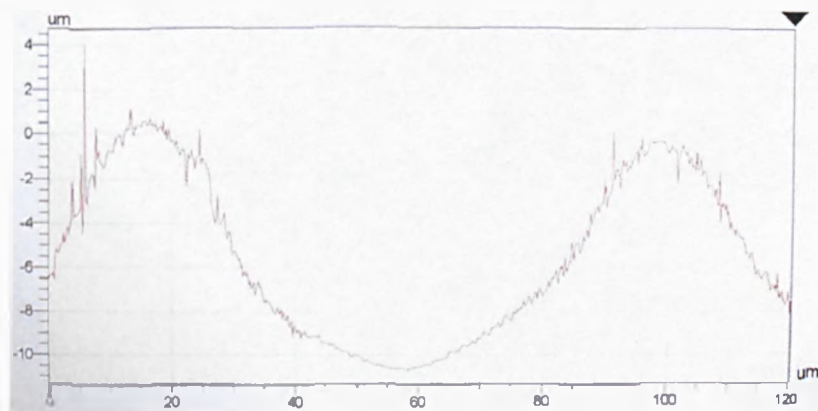
*Figure 4.6: Interferometry surface results taken using WYKO machine of the 120-34 light framed mesh filled with Sericol white ink just after the metering squeegee stroke.*

Figure 4.6 shows the central region of the Sericol white ink filled 120-34 mesh cell; as can be seen it fills below the height of the thread peaks. Figure 4.7 shows the ink meniscus is of an inverted dome shaped with the lowest point being  $22\mu\text{m}$  below the thread peaks (fills 57.1% of the mesh thickness).





x-profile – red line above



y-profile – blue line above

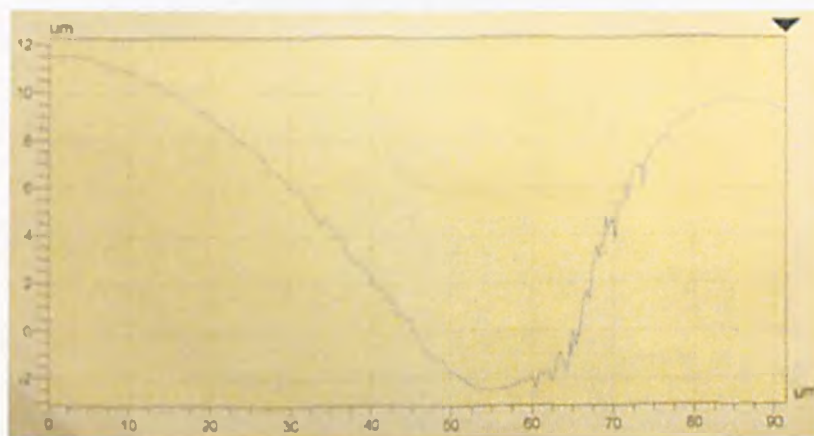


*Figure 4.7: Two slice profiles of the squeegee side surface of the Sericol white ink filled 120-34 light framed mesh, measured with the WYKO apparatus.*

There are several possible explanations as to why the meshes do not fully fill:

1. The blade involvement in the filling process may cause the blade edge to follow the local thread geometry, rather than just passing over knuckle peaks, and so a “dug-out” effect occurs resulting in less ink introduced into the mesh.
2. The mesh deforms further (than the already compressed tensioned mesh state) due to the pressure experienced by the ink and blade. The mesh temporarily compressing further as the blade passes, reduces the available space for ink to occupy. After the blade passes, it is reasonable the mesh would return to its previous tensioned state, and so the amount of ink would be insufficient to occupy this mesh space. This explanation however is unlikely to be the reason why the mesh only partially fills since it was observed that applying soft and hard squeegee pressure had no noticeable variation on the mass of ink introduced into a mesh (also observed as having negligible effect on the printed thickness in section 3.4).

The final shape of the ink surface within a screen mesh will tend to a curved shape (Figure 4.7) in equilibrium state. The surface tension is responsible for the curvature, since it dominates the meniscus to maintain an equilibrium state requiring least energy.

Further work is required to explain why the meshes do not fully fill. An insight into the filling behaviour of cavities (cells) is included in the study of chapter 6.

### **Image of the mesh after printing**

Anything less than 100% ink transfer to the substrate would leave some residual ink within the mesh. The following photographs (Figures 4.8-4.9) were taken just after printing occurred to illustrate that this does happen in practice. These images highlight that ink is trapped within the mesh, especially at knuckles. The shape of the meniscus varies depending upon both the ink and the mesh geometry (see Table 4.1).

The Sericol CYMK inks produced very square-like menisci with rounded corners (a typical image shown in Figure 4.8); the Sericol white and NAZDAR black<sub>[2]</sub> ink dilutions had circular menisci (as shown in Figure 4.9); R3 grease had square menisci, but also had more irregular shapes than the other tested fluid (highlighted in Figure 4.11(c)).

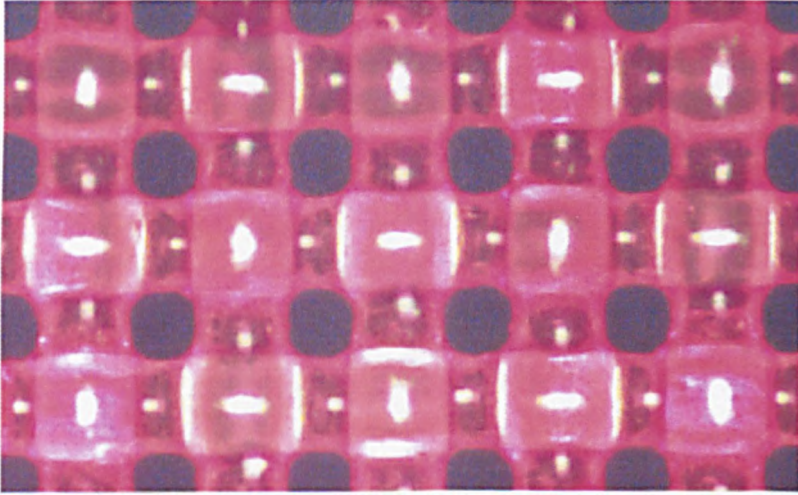


*Figure 4.8: Photograph showing the square-like shape with rounded corners of the Sericol magenta ink menisci remaining in the 150-31 mesh after printing.*

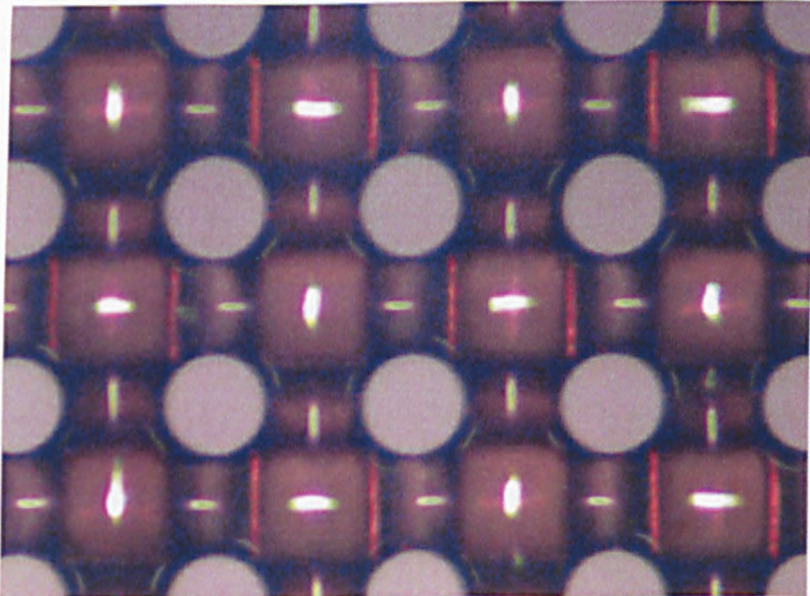


*Figure 4.9: Photograph showing circular menisci of NAZDAR black<sub>[2]</sub> ink remaining in the 120-34 mesh after printing.*

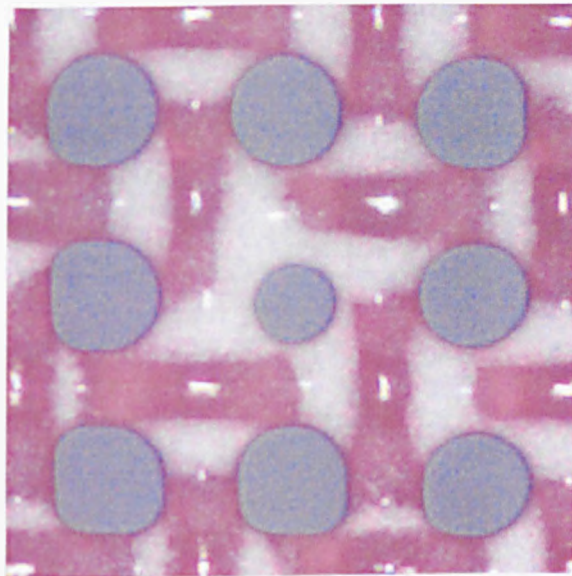
Ink	90-40	120-34	150-31
Sericol C	Square-like with rounded corners	Square-like with rounded corners	Square-like with rounded corners
Sericol M	Square-like with rounded corners	Irregular – rounded corners	Square-like with rounded corners
Sericol Y	Square-like with rounded corners	Square-like with rounded corners	Irregular - Square-like with rounded corners
Sericol K	Square-like with rounded corners	Square-like with rounded corners	Square-like with rounded corners
Sericol W	Circular	Circular	Circular
NAZDAR K <sub>[2]</sub>	Circular	Circular	Circular
NAZDAR K <sub>[2]</sub> 92.5% HVI 160 7.5%	Circular	Circular	Circular
NAZDAR K <sub>[2]</sub> 90% HVI 60 10%	Circular	Circular	Circular
R3	Square	Square-like with rounded corners	Irregular

 "Closed" cells observed

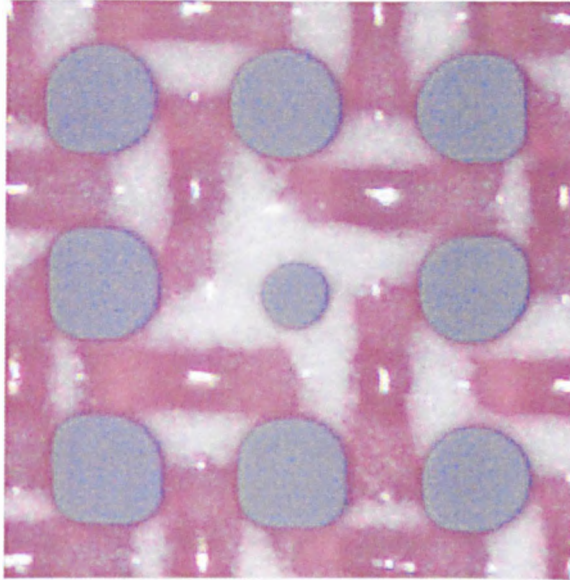
*Table 4.1: The meniscus shape of the fluids remaining in the mesh after printing. "Closed" cells are highlighted.*

### Presence of “closed” cells

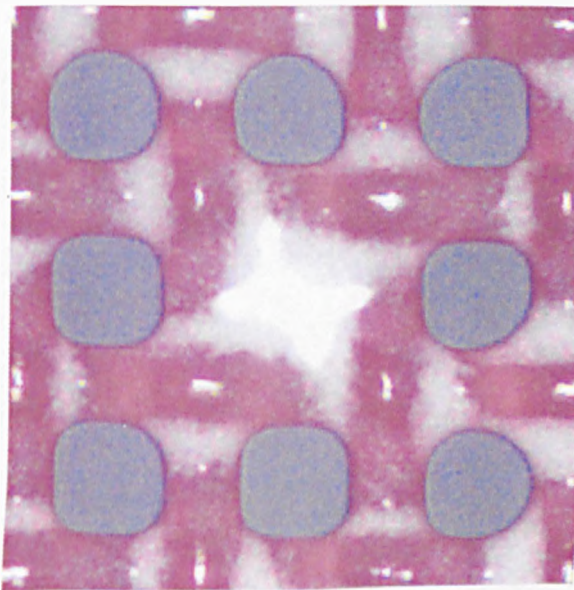
Sericol white ink and R3 grease appear to produce “closed” cells in the mesh after printing. The following series of images (Figure 4.10(a)-(c)) however show that fluid transfers through these particular cells to the substrate. After printing, surface tension forces cause the meniscus radius to decrease; eventually the “hole” disappearing and the appearance of the cell falsely implying no ink transfer occurred. The location of “closed” cells varies for successive prints, and so is not a feature relating to a particular mesh cell, but to the fluid type.



*Figure 4.10(a): Photograph just after printing occurred using 90-40 mesh and Sericol white ink.*

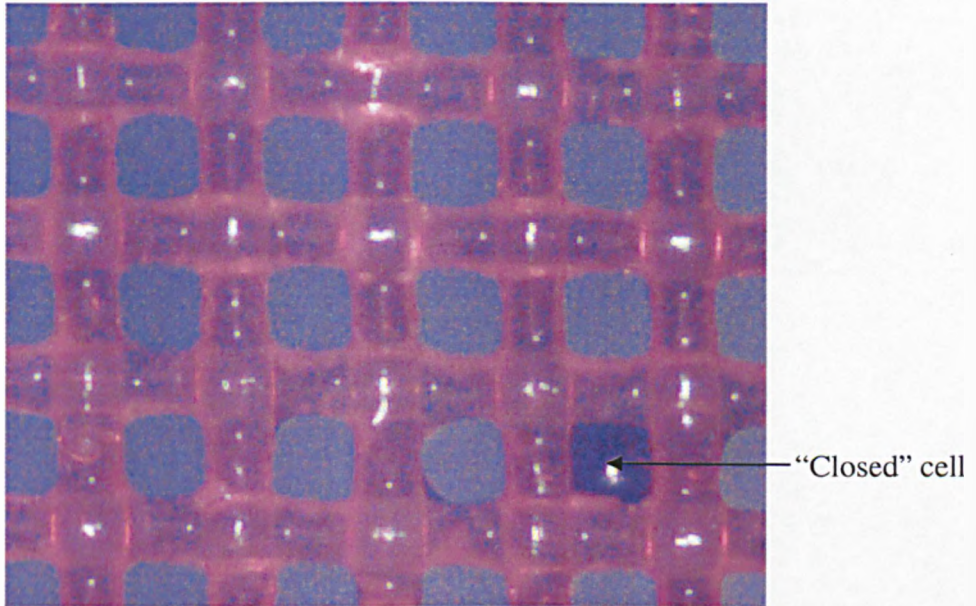


*Figure 4.10(b): Photograph taken 5 seconds after image in Figure 4.10(a), highlighting the reduction of meniscus radius in the central cell causing progression of a “closed” cell.*

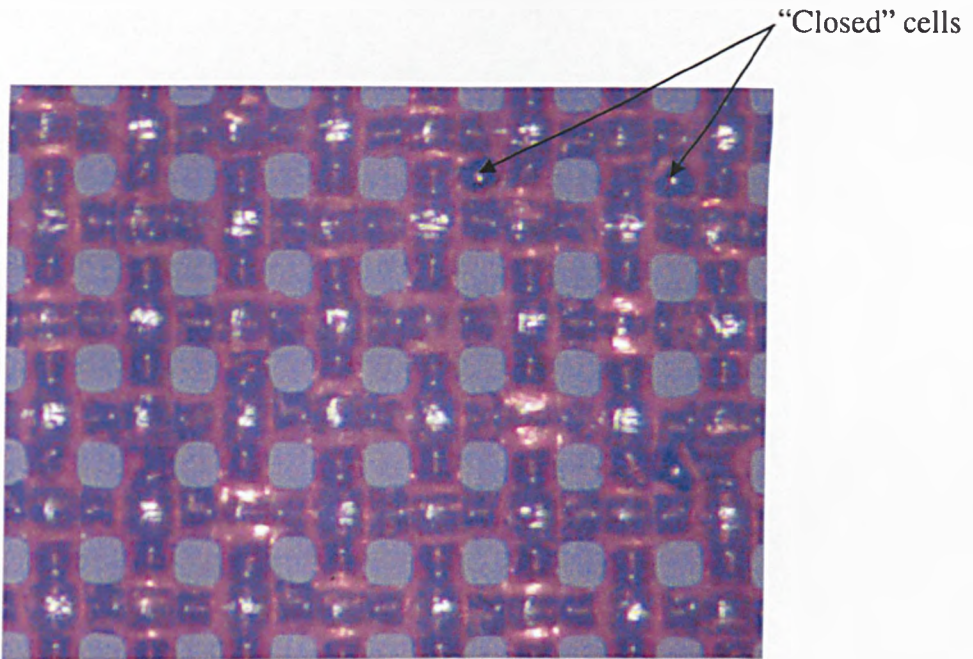


*Figure 4.10(c): Photograph taken 5 seconds after image in Figure 4.10(b), showing a fully developed “closed” cell.*

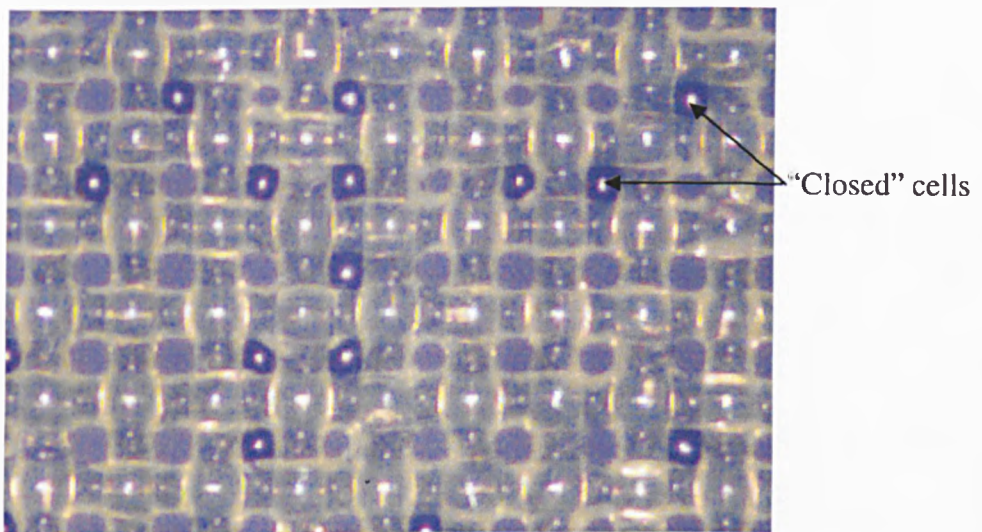
Due to vibrational movement of the mesh, at peel-off, the time taken to focus the microscope (after printing) was greater than the time required for some “closed” cells to form. The formation of “closed” cells with R3 grease was not observed because of this. The proportion of observed “closed” cells varies with R3 (more present in 150-31 than 120-34 than 90-40 – shown in Figure 4.11(a)-(c)); the proportion for Sericol white ink is approximately the same for each mesh.



*Figure 4.11(a): Photograph of 90-40 mesh after printing R3 grease, showing a “closed” cell.*



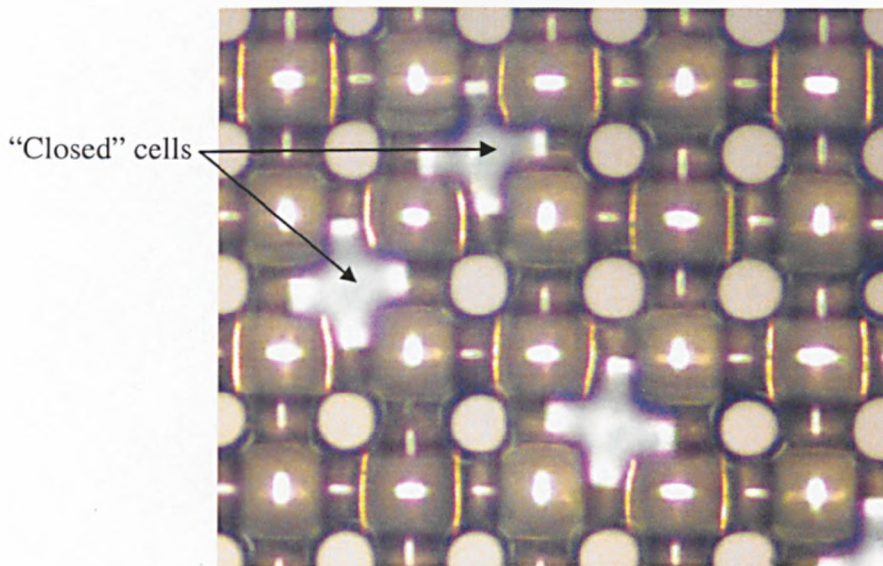
*Figure 4.11(b): Photograph of 120-34 mesh after printing R3 grease, showing "closed" cells.*



*Figure 4.11(c): Photograph of 150-31 mesh after printing R3 grease, showing a higher proportion of "closed" cells than with the other meshes.*

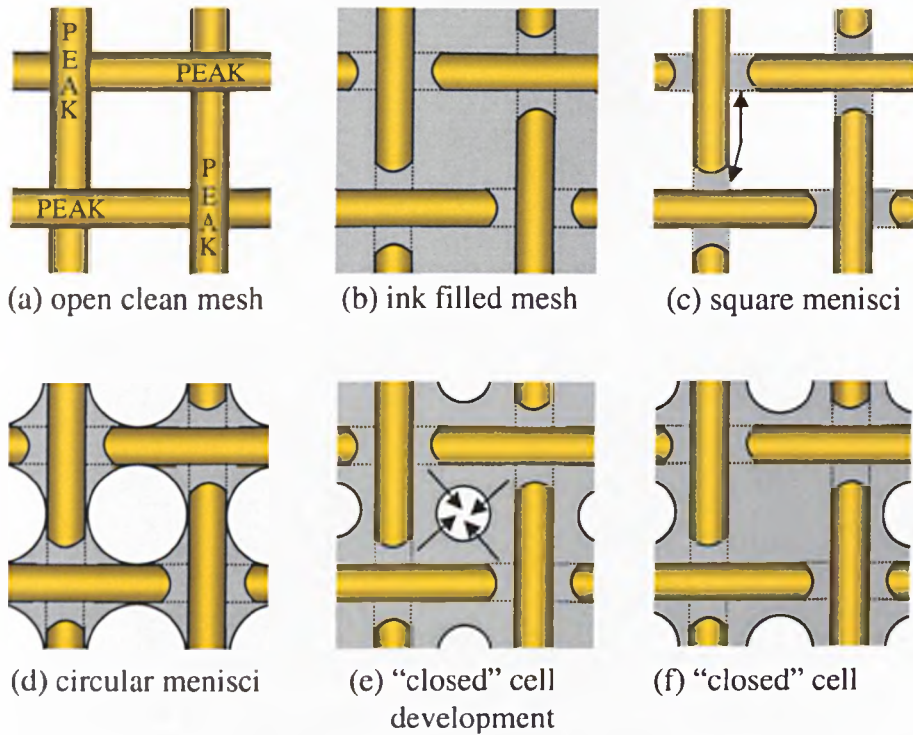


“Closed” cells were also observed with the 3 dilutions of NAZDAR black<sub>[2]</sub> ink, but only using the 150-31 mesh (as shown in Figure 4.12).



*Figure 4.12: Presence of “closed” cells also observed with the NAZDAR black<sub>[2]</sub> ink, but only with the 150-31 mesh.*

The localised effect of “closed” cells on final prints is difficult to determine using the current experimental setup, due to small-scale translation which occurs at peel-off. Visual checks suggested there was no overall degradation in print quality. One possible explanation for the presence of “closed” cells results in more ink remaining (locally) in the mesh and less transferring to the substrate producing a thinner film in this region.



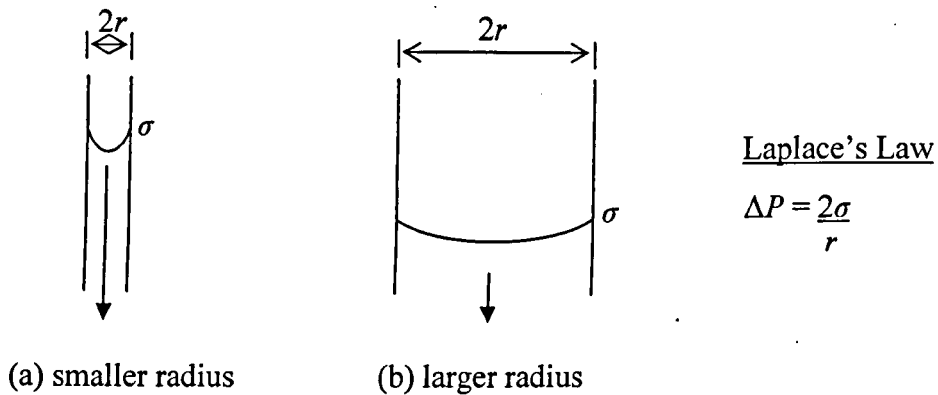
*Figure 4.13: Sketches of various stages of the mesh during the printing process.*

Figure 4.13 shows sketches of the mesh during the different print stages. This figure highlights a residual ink path must exist between all corners of the unit cell for the cell to potentially “close”; hence circular menisci are more likely to develop “closed” cells than square menisci. The lack of residual ink path for the square menisci is shown with the arrow in Figure 4.13(c).

Prior to mesh release ink contacts both mesh threads and the substrate. The ink contact with both materials incurs adhesive forces, which at the onset of mesh release initiates ink transfer to the substrate. Ink resides at the knuckle sites on the upper surface of the lower thread, observed for both square and circular menisci types (shown in Figure 4.13).

The knuckles of a mesh consist of regions where thread surfaces are extremely close together. The action of capillarity draws the fluid into these regions, advancing further than if the gap is increased (illustrated in Figure 4.14). From Laplace’s Law, the pressure difference across the fluid surface within a narrow tube is much greater than

for a wider tube. This makes it harder to remove fluid from such regions in proximity to the knuckles. Larger gaps between solid surfaces enable a greater proportion of fluid to be removed (with greater ease). Therefore the ink held within the opening of the filled mesh cells is removed from the region with greater success than at the knuckle sites (as noted in Figure 4.13).



*Figure 4.14: Diagrams of capillary sections used to illustrate Laplace's Law.*

The flow path of ink from the open regions to the substrate is explored in more detail in chapter 5 – one observation is that high spots on the print correspond to knuckles under the mesh.

### 4.3.2 Experimental printed thicknesses and ink transfers

The actual percentage ink transfer was obtained by comparing the volume of printed ink with the initial amount of ink in the mesh.

A conclusion of the previous chapter was the printing fluid affected both the dimensional and non-dimensional film thickness. To confirm that this is the same for the lighter screens used here, Figure 4.15 shows the dimensionless film thickness as a function of mesh open area. Therefore the replacement of a permanent stencil material with the masking tape has little effect on the prints.

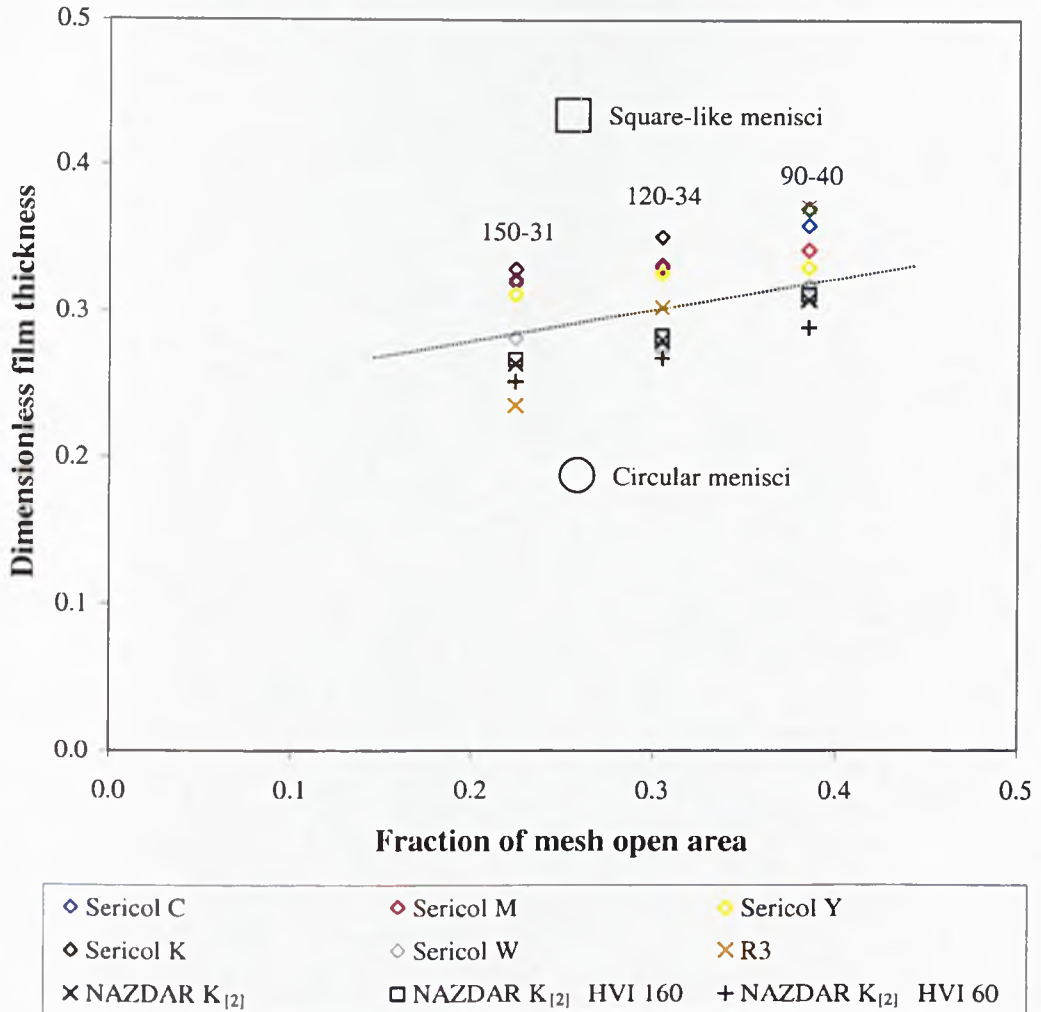


Figure 4.15: A comparison of the open area of 3 light framed meshes with the non-dimensional film thickness for the fluids printed. The dividing line on the graph highlights that the region above generated square-like menisci with the ink remaining in the mesh, and the region below exhibited circular menisci.

Table 4.2 shows both the dimensional and non-dimensional thickness of fluid initially deposited in the mesh for each of the 3 meshes using the 9 fluids. The dimensional initial ink thickness in the mesh is calculated from the measured ink mass introduced to the mesh combined with the printable area. The choice of fluid does not significantly affect the initial mesh filling for any of the meshes, the greatest range ( $3.1\mu\text{m}$ ) was observed with the 90-40 mesh. The non-dimensional thickness range is approximately the same for each mesh, the 90-40 mesh generating the greatest range of 0.45-0.50.

Fluid	Initial fluid thickness in mesh ( $\mu\text{m}$ )			Dimensionless fluid thickness initially in mesh*			% transfer to substrate		
	90-40	120-34	150-31	90-40	120-34	150-31	90-40	120-34	150-31
Sericol C	26.9	21.0	16.6	0.48	0.47	0.45	74.4	69.9	70.9
Sericol M	25.9	20.4	16.3	0.46	0.46	0.44	73.8	72.2	73.1
Sericol Y	25.0	20.2	16.0	0.45	0.45	0.43	73.9	71.8	71.7
Sericol K	28.1	21.5	16.5	0.50	0.48	0.45	73.6	72.7	73.6
Sericol W	27.7	20.1	17.2	0.49	0.45	0.46	64.1	60.5	60.6
NAZDAR K <sub>[2]</sub>	26.4	21.1	16.9	0.47	0.47	0.46	65.2	59.2	57.8
NAZDAR K <sub>[2]</sub> 92.5% HVI 160 7.5%	27.3	21.4	17.2	0.49	0.48	0.46	63.9	58.9	57.5
NAZDAR K <sub>[2]</sub> 90% HVI 60 10%	26.0	20.7	16.9	0.47	0.46	0.46	62.0	57.7	55.1
R3	27.2	21.1	15.5	0.49	0.48	0.42	76.4	63.6	56.0

\* calculated using equation (3.3), ratio between experimental thickness and maximum theoretical fluid thickness in mesh.

*Table 4.2: Table showing the percentage fluid transfer and the initial ink thickness for the 3 light framed meshes.*

As identified in chapter 3, the fluid type has a greater effect on the amount transferred to the substrate, shown in Table 4.2. The actual printed thickness ranges for all the fluids are approximately  $6.0\mu\text{m}$  for each mesh – similar to the range observed for the heavy framed meshes in chapter 3. The percentage deviation of the film thicknesses are within 32-54% (slightly greater than those in chapter 3) for the 3 meshes, highlighting again that the ink type is an important print factor.

The Sericol CMYK ink group print the same as each other having very little transfer difference between the 3 meshes. Sericol white ink and the NAZDAR black dilutions all have greater percentage of ink remaining within the meshes after printing.

For the R3 grease, the percentage fluid transfer to the substrate varies greatly for the 3 meshes. With the 90-40 mesh, the grease prints a similar amount to the Sericol

CMYK ink group, but as the open fraction area of the mesh decreases (i.e. for the 150-31 mesh) the grease behaves more closely to the ink transfer of Sericol white ink. This is also highlighted in Figure 4.15, where the R3 graph point lies in the region that has square-like menisci using the 90-40 mesh (like the Sericol CYMK ink range), the 120-34 point is on the boundary between the two regions, and the corresponding R3 point using the 150-31 mesh lies in the region that has circular menisci (observed however to have an irregular menisci, see Table 4.1).

The fluids that produce circular menisci, remaining in the mesh, transfer less fluid to the substrate than the square-like menisci inks. 69.9% is the lowest observed fluid transfer from the mesh for the square-like menisci inks, whereas the greatest transfer for the circular menisci inks is 65.2%.

In section 4.3.1, it was also shown that inks generating circular menisci were prone to develop “closed” cells in the mesh. The presence of this feature highlights a greater amount of ink remaining in the mesh. For the “closed” cells to form there must be a greater amount of ink remaining in the individual unit cell, than square-like menisci generating fluids, to allow the surface tension forces to “refill” the hole.

A smaller open mesh fraction suggests that the menisci shape (post print) will be of a smaller radius than with the same condition for a larger open mesh fraction, and so more likely to form a “closed” cell. This is confirmed with the printing results using R3 grease where decreasing the open mesh fraction increased the proportion of “closed” cells, and with the 3 NAZDAR black<sub>[2]</sub> ink dilutions where “closed” cells were observed only with the lowest available open mesh fraction.

The mechanism creating “closed” cells with fluids of predominantly square-like menisci (such as the R3 grease) is unclear since their formation occurred during the very early stages of mesh release and was not able to be observed. It is possible the presence of these cells containing residual fluid, with the apparent appearance of “closed” cells, could actually be “unprintable” cells where no ink transfer occurred, resulting in a poor print quality.

### 4.3.3 Effect of varying fluid viscosity

This work involved printing glycerine-water solutions and NAZDAR black<sub>[2]</sub> dilutions to obtain a range of viscosities without variation of fluid composition.

#### Glycerine solutions

The 4 glycerine solutions proved inappropriate for printing. The squeegee action, required for filling the mesh with the 100% glycerine solution, caused air entrapment within the fluid degrading the quality of the prints. The 25% glycerine – 75% water solution displayed drainage behaviour through the mesh, which is a different type of fluid transfer than that associated with screen printing. Consequently the print quality was poor. The 75% glycerine – 25% water solution exhibited both drainage and air entrapment features, causing this fluid (and also 50% glycerine – 50% water solution) to be unsuitable for printing.

#### NAZDAR black<sub>[2]</sub> dilutions

The measured viscosity results of the NAZDAR black<sub>[2]</sub> dilutions are in the shear rate range of 1-100s<sup>-1</sup>, shown previously in Figure 4.1. Using the power law estimation method (introduced in section 2.7.1) the range can be increased to the higher shear rates experienced in printing, which is shown in Figure 4.16. For each printing setup, the shear rate ( $\frac{\Delta u}{\Delta z}$ ) at fluid transfer is approximated as described in section 2.7.1: the value “ $\Delta u$ ” approximated as the peel-off rate, 6.5×10<sup>-3</sup> ms<sup>-1</sup>; the value “ $\Delta z$ ” defined as printed film thickness. Table 4.3 shows the shear rate results.

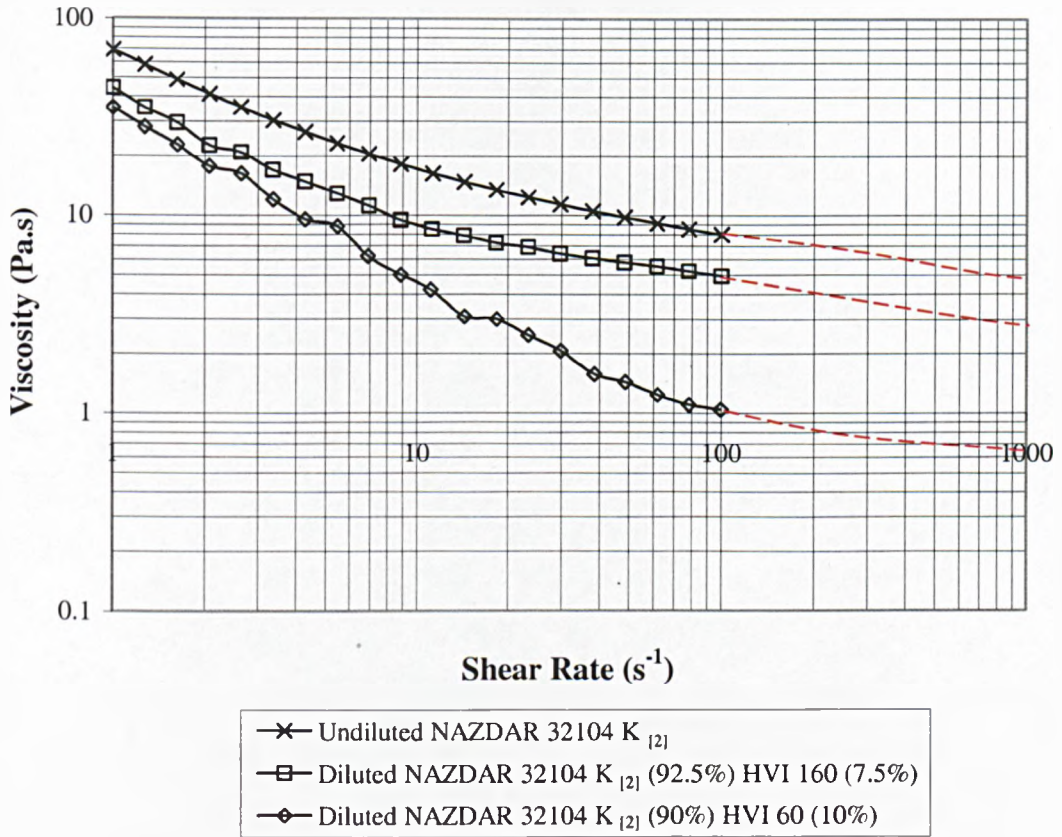


Figure 4.16: Effect of shear rate (in the range of  $1-100s^{-1}$ ) on viscosity measured using a cone ( $4^{\circ}$   $\varnothing 40mm$ ) and plate geometry at  $20.0^{\circ}C$ . Graph is extended for shear rates up to  $1000s^{-1}$ , using power law assumptions to estimate the corresponding viscosities.

	90-40	120-34	150-31
NAZDAR K <sub>[2]</sub>	376	520	664
NAZDAR K <sub>[2]</sub> 92.5% HVI 160 7.5%	372	516	657
NAZDAR K <sub>[2]</sub> 90% HVI 60 10%	401	544	696

Table 4.3: Calculated shear rates ( $s^{-1}$ ) of the NAZDAR black<sub>[2]</sub> dilutions for the three meshes at peel-off operating at motor rate 7.0.

The print results of the 3 NAZDAR black<sub>[2]</sub> dilutions have been briefly discussed in sections 4.3.1 and 4.3.2. It was observed that the menisci were circular for all the dilutions (shown in Table 4.1). Figure 4.15 showed a small positive correlation between the non-dimensional film thickness and the fraction of open mesh area. In



Figure 4.17 the dependence of the non-dimensional film thicknesses with viscosity is shown. Overall the viscosity has negligible effect on the non-dimensional printed film thicknesses.

Figures 4.17 and 4.18 show that the approximated viscosity of each dilution varies slightly between the 3 meshes. This is inherent from the spread of calculated shear rates for each dilution (shown in Table 4.3), originating from “dz” (printed film thickness) varying between meshes: shear rate is calculated inversely proportional to printed thickness. Increasing the film thickness decreases the calculated shear rate, but increases the approximated viscosity value due to the negative correlation shown in Figure 4.16. The best fit lines of Figures 4.17 and 4.18 highlight this for each dilution; the positive correlation shown for each dilution is due to both non-dimensional printed thickness and approximated viscosity values having positive relations with corresponding measured film thicknesses. The confidence limits shown in Figure 4.17 highlight good repeatability of results.

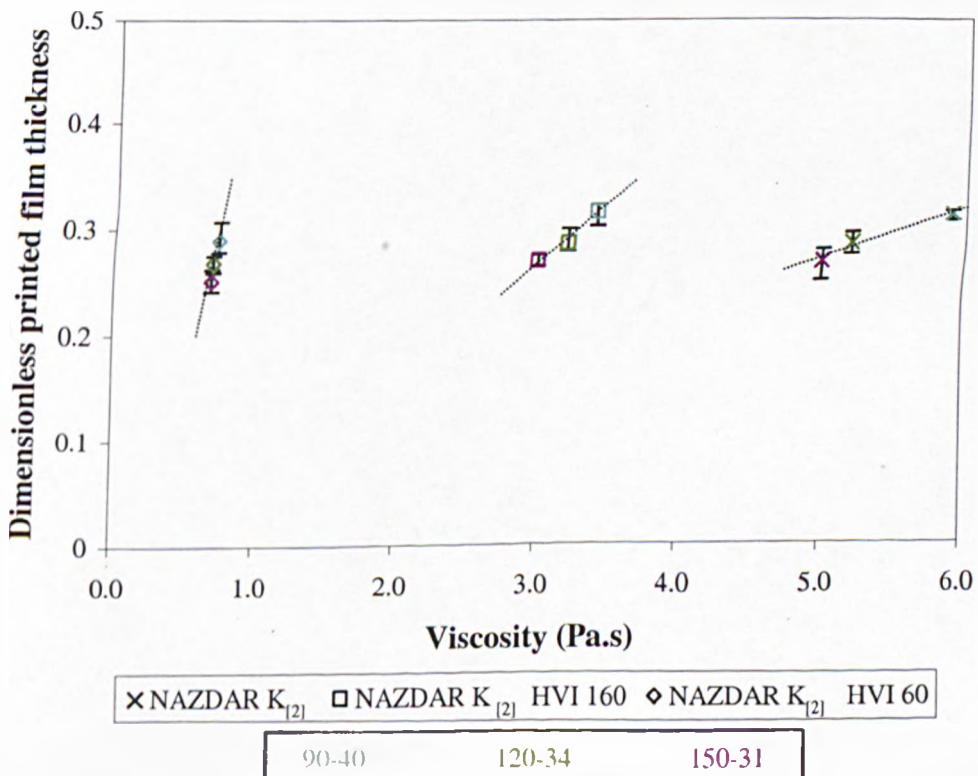


Figure 4.17: Comparison of the viscosity of 3 NAZDAR black<sub>[2]</sub> ink dilutions with the non-dimensional film thickness.

Table 4.1 showed the percentage fluid transfer of the dilutions. Figures 4.17 and 4.18 show that the overall effect of viscosity on the printed thickness and percentage ink transfer is negligible. These results demonstrate the correlations between non-dimensional thicknesses and viscosity are the same for percentage fluid transfer and viscosity.

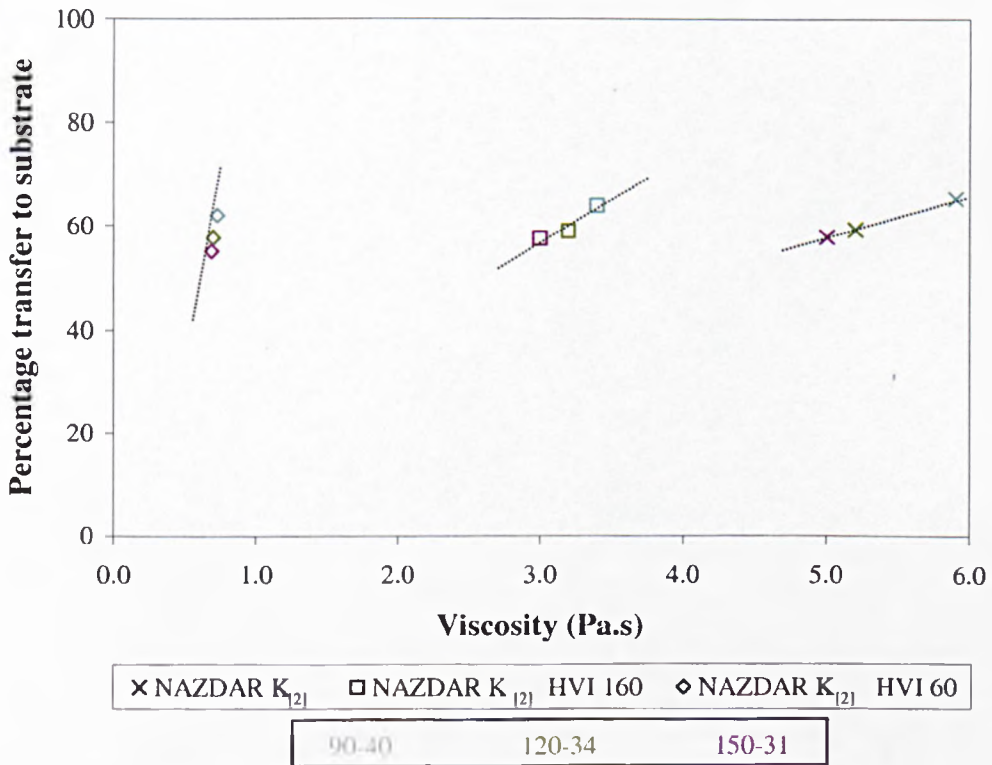


Figure 4.18: Graph showing the effect of viscosity on the percentage fluid transfer to the substrate, for the 3 NAZDAR black<sub>[2]</sub> dilutions.

#### 4.3.4 Effect of varying fluid density

The density range for the NAZDAR black<sub>[2]</sub> ink dilutions was 1024.8-1066.2kgm<sup>-3</sup> (as shown in section 2.7.2). Section 4.3.3 revealed little printing difference between the dilutions. Since the density range is relatively small, the effect on printing behaviour cannot be determined.

#### 4.4 Development of theoretical models of the mesh

Up to this point, the non-dimensional printed film thicknesses have currently been scaled with the maximum volume of ink in the mesh (section 4.4.1). The motivation here is to generate an improved representation of the mesh volume and consequently a better understanding of the fraction of ink transferred in the printing process.

A series of models have been developed to predict the volume of the mesh. The models do not offer a predictive way of calculating the fluid transfer through the mesh, since the hydrodynamic process is not considered – this is beyond the scope of this work. The simple model of the mesh described in section 4.4.1 is often used by industry to predict the maximum printed thickness by dividing the initial volume of fluid in the mesh by the printable area, assuming all ink is transferred to the substrate. The model is based on the geometric properties of the threads (data provided by the manufacturer - Saati (2002b), Sefar (1999a)) rather than the actual measured geometry of the woven mesh. Consequently the mesh thickness used for the calculations is greater than actual meshes and therefore a second model was developed, described in section 4.4.2. In this adapted model the thickness used for the calculations is that taken from the actual mesh measurements, and hence is similar to the model defined by Hunt, D. and Hohl, D (1990) which also extends the use of actual dimensional measurements to the thread diameter and spacing.

Section 4.4.3 shows a further development considered here for the first time, where the cross-sections of the mesh threads need not be circular. The model assumes they remain of a constant elliptical cross-section, requiring the major diameter of the threads in both warp and weft directions to be measured from the actual mesh, and the minor diameter to be established as half the measured mesh thickness.

All three of the models consider one unit cell to calculate the theoretical ink volume the overall mesh holds. The theoretical results from these models were generated using the mesh parameters of the experimental meshes described in section 2.2.4. Table 4.4 shows the geometric mesh parameters, measured using a Co-ordinate measuring machine KEMCO 400 and a Nikon Profile Projector Model V-16D.

Mesh	Used by model	90-40	120-34	150-31
Manufacturers' $M$ ( $\mu\text{m}$ )	1, 2, 4, 5	111.1	83.3	66.7
Manufacturers' $D$ ( $\mu\text{m}$ )	1, 2, 4, 5	40	34	31
Measured $M$ – warp ( $\mu\text{m}$ )	3, 4	111.2	82.3	67.7
Measured $M$ – weft ( $\mu\text{m}$ )	3, 4	111.7	84.4	67.2
Measured $D$ – warp ( $\mu\text{m}$ )	3, 4	43.0	38.0	36.7
Measured $D$ – weft ( $\mu\text{m}$ )	3, 4	41.7	36.7	34.3
Measured thickness ( $\mu\text{m}$ )	2, 3, 4	64.3	51.3	46.3

*Table 4.4: The measured mesh dimensions of the light-framed meshes.*

The measurements in Table 4.4 show that the thread spacing,  $M$ , are approximately equal in both warp and weft directions comparing well with the manufacturers' data (Saati (2002b), Sefar (1999a)) for each of the 3 meshes. Due to the thread woven structure, it may be expected that the mesh thickness will be equivalent to twice the thread diameter (as this will generate the maximum thickness observed at knuckles). The measured mesh thicknesses however are significantly less than  $2D$ . The measured values relating to the thread major diameter are greater than the manufacturer's data. These two geometrical differences suggest that the mesh threads do not maintain cross-sections that are circular, but must deform: compressing in height (to reduce mesh thickness) and expanding in width (to increase the thread diameter parameter) – also noted in Table 4.4.

The fourth and fifth models have been developed to consider more accurately the initial state of the ink filled mesh. The fourth model was developed as a consequence of experimental observation (section 4.3.1) that the mesh cells do not completely fill: evidence from WYKO measurements and microscope images of the initial ink filled meshes highlighted that the ink level is not to the level of the thread peaks, but significantly lower. This model can be adapted from any of the three previous models. The fifth model is an extension of the earlier models, incorporating the concept of

incomplete filling the fourth model introduces, and also mimics the geometry of the actual mesh threads more faithfully.

The results of the models are shown in section 4.5.

#### 4.4.1 Model 1 – Circular cross-sectional thread

This basic model is similar to that defined by Hunt, D. and Hohl, D. (1990). Hohl's model however includes thread compressibility, which section 4.4.2 considers.

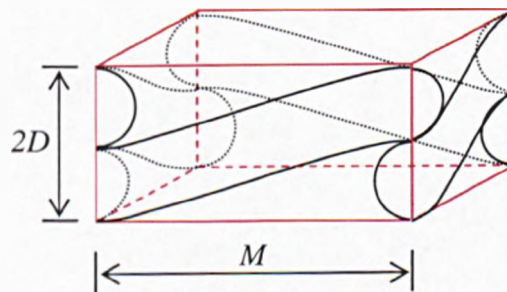


Figure 4.19: 3-dimensional illustration of the woven thread structure of the unit cell ( $M \times M \times 2D$ ).

#### Assumptions

- Fluid fills independent of the fluid properties
- Fluid fills independent of surface energies
- Ink fills the unit cube completely
- Threads are of a circular cross-section
- The length of the thread within a unit cell is approximated to  $L$  (as shown in Figure 4.20)
- There is no geometric difference between warp and weft threads
- All knuckle peaks are at the same height
- Threads contact at a single point in knuckles (not over an area)

- There is no thread deformation or compression, therefore the thickness of the mesh is  $2D$

Figure 4.19 is a 3-dimensional representation of a unit cell, highlighting the thread woven feature; Figure 4.20 below shows a unit cell 2-dimensionally from above and side views. The open region is central to the unit cell. There are 4 threads involved, although it is just half of each thread volume in the unit.

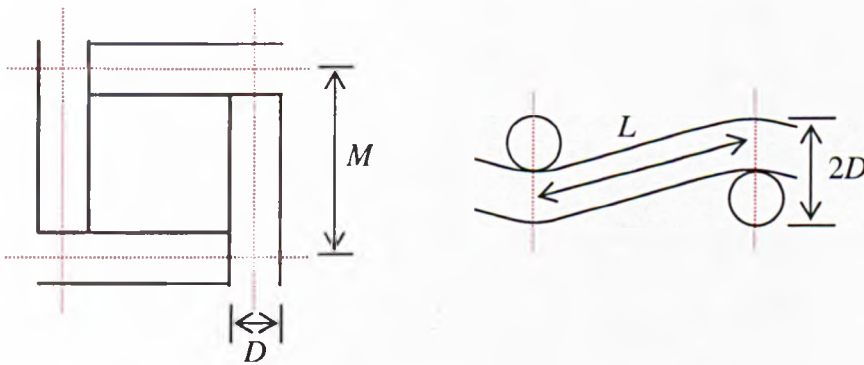


Figure 4.20: The geometric variables of the mesh unit cell.

$M$  is the thread spacing, and  $D$  is the diameter of the threads. The approximation of the thread length,  $L$ , within the unit cell is calculated using equation (4.5).

$$L = \sqrt{M^2 + D^2} \quad (4.5)$$

The total volume of the unit cell is calculated using equation (4.6). The volume of the threads within the unit cell is established by treating the threads as prisms, length  $L$ , with semi-circular cross-sectional area equivalent to  $\pi D^2/8$ . Deducing the thread volume from the unit cell volume deduces the empty space within the unit. Assuming all this empty space fills with ink after the metering squeegee stroke, it equals the initial ink volume in the unit cell (equation (4.7)). The printable area of the cell unit is  $M^2$ , and not the open area  $(M-D)^2$ , since threads do not act as stencil which blocks ink transfer. Equation (4.8) shows the theoretical maximum printed thickness of the ink assuming 100% transfer to the substrate.

$$\text{Total unit cell volume} = 2DM^2 \quad (4.6)$$

$$\text{Theoretical ink volume in the unit cell} = 2DM^2 - \frac{\pi D^2 L}{2} \quad (4.7)$$

Theoretical maximum printed thickness,

$$h_{\max} = \frac{\left(2DM^2 - \frac{\pi D^2 L}{2}\right)}{M^2} = 2D - \frac{\pi D^2 L}{2M^2} \quad (4.8)$$

#### 4.4.2 Model 2 – Adapted circular cross-sectional thread

This model includes the concept of thread compressibility for establishing mesh thickness; but unlike the model of Hunt, D. and Hohl, D. (1990), it uses the manufacturers' data (Saati (2002b), Sefar (1999a)) for defining all other mesh geometry. Section 4.4.3 progresses the model to include actual measured geometry observed from tensioned meshes, like Hohl's model.

#### Assumptions different from those of model 1 in section 4.4.1

- There is thread compression, and the mesh thickness is not considered to be  $2D$  but  $2D_{comp}$ , which is an actual measured thickness of the mesh after completion of all tensioning stages. Figure 4.21 highlights that the mesh thickness is  $2D_{comp}$ .

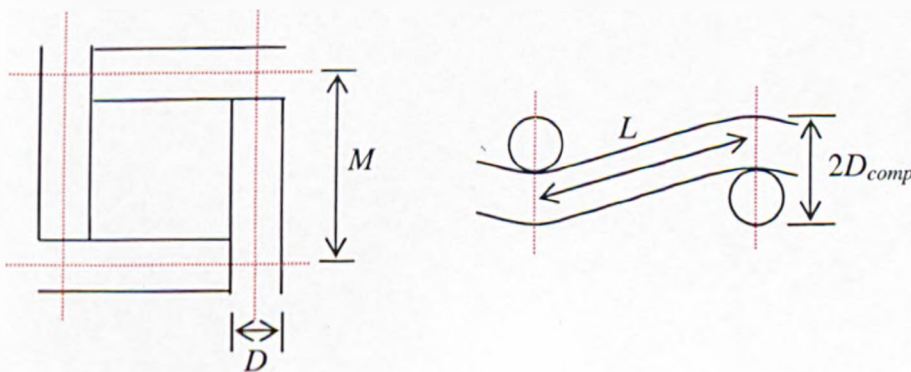


Figure 4.21: Unit cell mesh parameters for the adapted circular cross-sectional thread model.

There is only a slight difference between this model and the previous one (as highlighted above). Since the mesh thickness is different, this leads to a difference in the calculated unit cell volume (equation (4.9)). The thread volume within the unit cell is considered to be unchanged, despite compression. Therefore the initial ink volume of the unit cell, which is equivalent to the available empty space, is found using equation (4.10). Equation (4.11) is used for obtaining the theoretical maximum printed thickness (assuming 100% ink transfer to the substrate).

$$\text{Total unit cell volume} = 2D_{comp}M^2 \quad (4.9)$$

$$\text{Theoretical ink volume in the unit cell} = 2D_{comp}M^2 - \frac{\pi D^2 L}{2} \quad (4.10)$$

Theoretical maximum printed thickness,

$$h_{max} = \frac{\left(2D_{comp}M^2 - \frac{\pi D^2 L}{2}\right)}{M^2} = 2D_{comp} - \frac{\pi D^2 L}{2M^2} \quad (4.11)$$

#### 4.4.3 Model 3 – Elliptical cross-sectional thread

This model is the most similar to the Hunt, D. and Hohl, D. (1990) model, since only measured mesh geometry is applied rather than manufacturers' data – used in the previous 2 models. It follows from Hunt, D. and Hohl, D. (1990) to more closely represent the true thread geometry in a mesh, and includes differentiation between warp and weft thread dimensions (introducing separate thread diameter parameters for each). This model also removes the assumption that the tensioned threads in a screen mesh maintain of circular cross-section.

#### Assumptions different from those of model 2 in section 4.4.2

- Threads are not of a circular cross-sectional, but are considered to be elliptical
- There is a geometric difference between warp and weft threads as experimentally measured (see Table 4.4)



These assumptions are introduced due to the significant compression of the measured mesh thickness, and increase of thread diameter (width), which suggests a substantial change in cross-sectional thread shape deviating from circular. Implicit in this is the assumption the compression of a cylinder will give a body that is elliptical in shape. Selecting elliptical thread cross-sections is more suitable than polygon geometry, justified with the WYKO measurements in Figures 4.6-4.7 that exhibit no corner edges (a distinct property of a polygon).

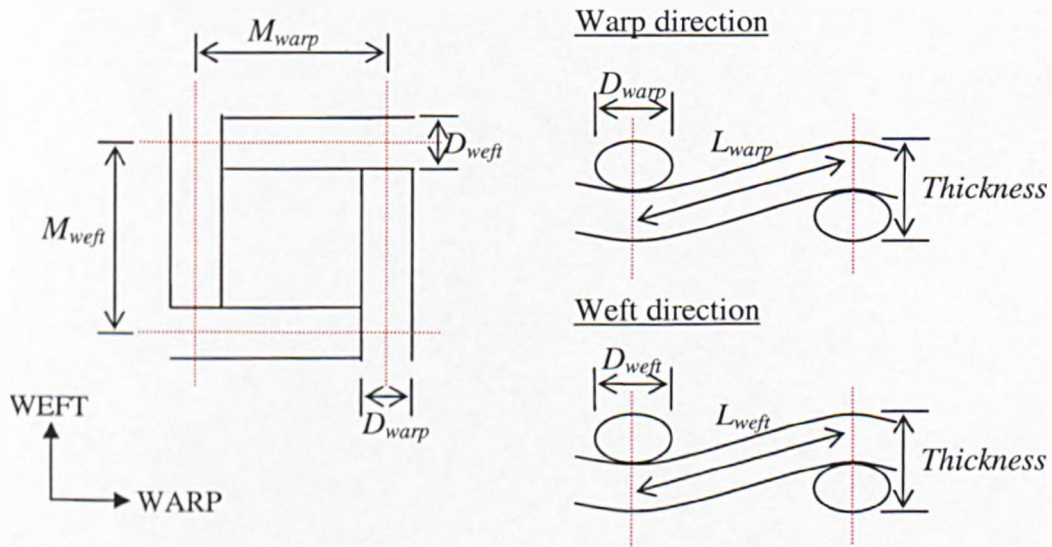


Figure 4.22: The unit cell parameters involved for considering elliptical cross-sectional threads. N.B. The warp and weft labelling is in the “direction of” and is not specific to the thread type.  $D_{warp}$  (and  $D_{weft}$ ) refer only to the major diameter of the thread width, and not the minor diameter in the mesh thickness direction.

Figure 4.22 above highlights that the dimensions of the threads in warp and weft directions are considered in this model. The same principle of calculating the thread volume and deducting it from the unit cell volume is used to find the theoretical initial ink volume in the unit cell and also the maximum printed ink thickness (see equations (4.12-4.17)).  $L_{warp} \neq L_{weft}$  and therefore needs to be considered calculating the volume of the threads in the unit cell.

$$L_{warp} = \sqrt{M_{warp}^2 + (Thickness / 2)^2} \quad (4.12)$$

$$L_{weft} = \sqrt{M_{weft}^2 + (Thickness/2)^2} \quad (4.13)$$

$$\text{Total unit cell volume} = Thickness \times M_{weft} M_{warp} \quad (4.14)$$

Thread volume in the unit cell

$$= \frac{\pi \times Thickness}{8} [D_{weft} L_{warp} + D_{warp} L_{weft}] \quad (4.15)$$

Theoretical ink volume in the unit cell

$$= [Thickness \times M_{weft} M_{warp}] - \left[ \frac{\pi \times Thickness}{8} [D_{weft} L_{warp} + D_{warp} L_{weft}] \right] \quad (4.16)$$

Theoretical maximum printed thickness,

$$h_{max} = \frac{[Thickness \times M_{weft} M_{warp}] - \left[ \frac{\pi \times Thickness}{8} [D_{weft} L_{warp} + D_{warp} L_{weft}] \right]}{M_{weft} M_{warp}} \quad (4.17)$$

#### 4.4.4 Model 4 – Incomplete mesh filling

Assumptions different from those of models 1-3 in sections 4.4.1-4.4.3

- The assumption that ink completely fills the cell is relaxed

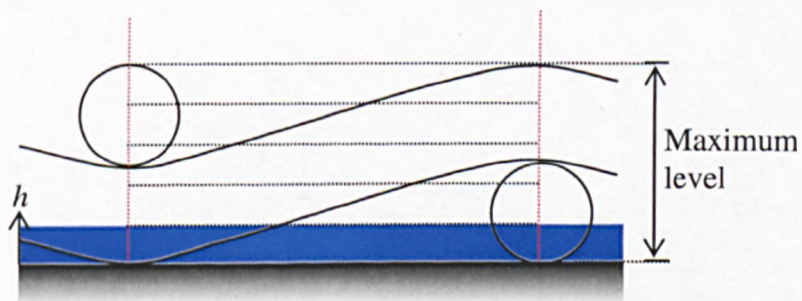


Figure 4.23: Illustration of ink levels introduced for incomplete mesh filling.

The ink is present from the base of the lower thread to a predefined height of the ink level ( $h$ ); the maximum possible level of ink is the upper thread knuckle surface (as shown in Figure 4.23). The volume of the partially filled unit cell is calculated using:

$$\text{Partial unit volume} = M_{\text{weft}} M_{\text{warp}} h \quad (4.18)$$

The ink volume in the cell and the theoretical maximum printed film thickness is established by subtracting the thread volume below the ink height level from the partial unit volume (equation (4.18)).

### Calculation of thread volume within the partially filled unit cell

Three sub-models are derived here, for different assumptions of the thread cross sections. The thread geometry is simplified as a cylinder, of either circular or ellipse cross-sectional area. These are shown in Figure 4.24.

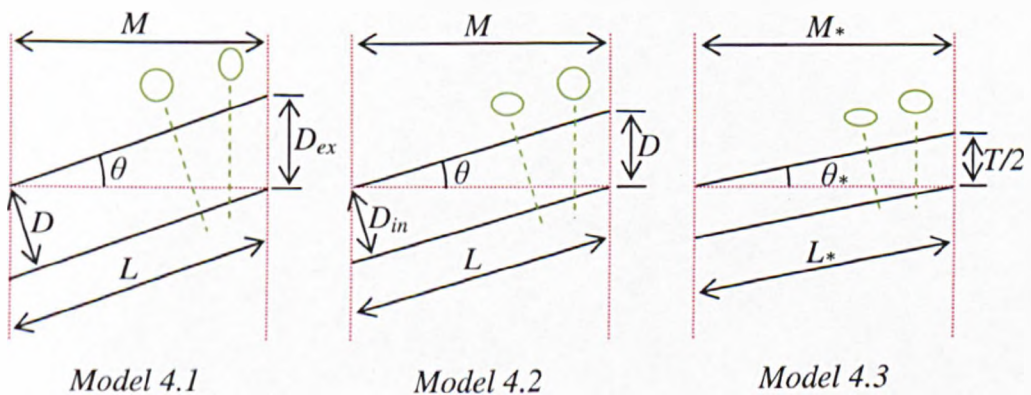


Figure 4.24: The main thread dimensions for each model 4 version, highlighting the cross-sectional area shape. Model 4.3 incorporates the geometrically measured difference between weft and warp threads, indicated by \*.

The thread considered in model 4.1 is essentially a cylinder positioned at an angle of  $\theta$ . The shape at the ends, due to this sloped angle, is not circular but elliptical. The thread geometry of model 4.2, is generated so the shape at the ends remains circular – this continues through the length. In order to achieve such geometry, the cross-sectional shape of the cylinder must be elliptical. For these sub-models (4.1 and 4.2), the manufacturers' data of mesh thread spacing ( $M$ ) and thread diameter ( $D$ ) is applied

(Saati (2002b), Sefar (1999a)). The mesh thickness (shown in Figure 4.24) is defined as  $2D_{ex}$  for model 4.1, and  $2D$  for model 4.2.

Model 4.3 however uses the measured mesh data to treat weft and warp threads separately, as done in the previous model 3 (section 4.4.3). The calculations are performed for both the heavy and light framed meshes used experimentally.

The model 4 versions all assume contact at the knuckle between the woven threads. The geometrical simplification of the experimental mesh weave does lead to the geometries of both threads overlapping, but is ignored in these models since this volume is negligible.

The method used to calculate the thread volume in the partially filled unit involves (numerically) taking fine horizontal slices of the thread. When the ink height is equal to half the mesh thickness of the particular model 4 version then the cross-sectional area is an ellipse; all other slice cross-sectional areas are segments of this ellipse as highlighted in Figure 4.25.

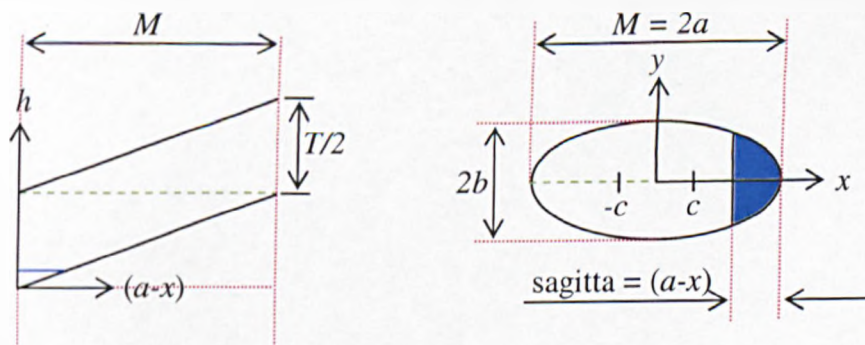


*Figure 4.25: Diagram of the ellipse and an example segment cross-sectional area generated from horizontal thread slicing. The points labelled  $-c$  and  $c$  are the ellipse foci, occurring on the centre-line of the minor axis.*

The equation of the ellipse shown in Figure 4.25 is:

$$\frac{x^2}{a^2} + \frac{y^2}{a^2 - c^2} = 1, \quad (4.19)$$

where  $a = \frac{M}{2}$ , and  $c = \sqrt{\left(\frac{M}{2}\right)^2 - b^2}$ .

$$\Rightarrow y = \sqrt{\left(1 - \frac{4x^2}{M^2}\right)} \times b, \quad (4.20)$$

where  $2b$  is the horizontal diameter of the thread.

Using congruent triangle theory, the value of  $x$  for each horizontal slice increments of  $h$  to the desired ink height is established with equation (4.21).

$$\frac{T}{2M} = \frac{h}{(a-x)} \Rightarrow x = a - \left(\frac{2Mh}{T}\right) = M\left(\frac{1}{2} - \frac{2h}{T}\right) \quad (4.21)$$

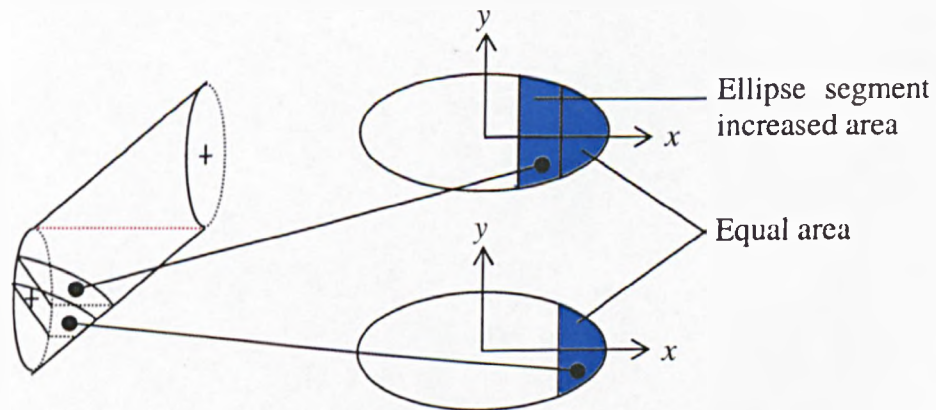


Figure 4.26: Diagram highlighting the equal ellipse segment area for successive horizontal slices.

Figure 4.25 highlights that  $(a-x)$  is the sagitta length of generated ellipse segments. Numerical approximation of the ellipse segment area is implemented by calculating the  $y$  values for the respective  $x$  values. The difference in area between successive ellipse segment slices is established by considering only the area between the

difference of sagitta limits of  $x$  values for each slice segment (Figure 4.26). The total slice area is this area added to the previously calculated total segment area. The required thread volume is established by multiplying each slice area by slice thickness.

The accuracy of the numerical approximation method can be found by calculating the percentage difference between the total single thread volume of this method and the expected value using the formula in Table 4.5. Using fine slices of  $0.01\mu\text{m}$  thickness and 20 slice calculations for each "ellipse segment increased area", between each successive horizontal slice (as shown in Figure 4.26), results with an overall accuracy within  $\pm 0.05\%$  compared with Table 4.5.

Parameter	Model 4.1	Model 4.2	Model 4.3
Cell unit volume	$2M^2 D_{ex}$	$2M^2 D$	$T \times M_{warp} M_{weft}$
Single thread volume	$\frac{\pi D^2 L}{4}$	$\frac{\pi D^2 M}{4}$	Weft: $\frac{\pi T D_{warp} L_{weft}}{8}$ Warp: $\frac{\pi T D_{weft} L_{warp}}{8}$
Total thread volume in cell unit	$\frac{\pi D^2 L}{2}$	$\frac{\pi D^2 M}{2}$	$\frac{\pi T (D_{warp} L_{weft} + D_{weft} L_{warp})}{8}$
$L$	$\sqrt{M^2 + D_{ex}^2}$	$\sqrt{M^2 + D^2}$	Weft: $\sqrt{M_{weft}^2 + \frac{T^2}{4}}$ Warp: $\sqrt{M_{warp}^2 + \frac{T^2}{4}}$
$D_{ex}$	$\frac{D}{\cos \theta}$	n/a	n/a
$D_{in}$	n/a	$D \cos \theta$	n/a
$\theta$	$\sin^{-1} \left( \frac{D}{M} \right)$	$\tan^{-1} \left( \frac{D}{M} \right)$	Weft: $\tan^{-1} \left( \frac{T}{2M_{weft}} \right)$ Warp: $\tan^{-1} \left( \frac{T}{2M_{warp}} \right)$

Table 4.5: Table of equations used to calculate the main model 4 geometrical thread parameters.

#### 4.4.5 Model 5 – Refined estimation of the thread geometry

##### Assumptions different from those of model 4 in section 4.4.4

- The geometry of the thread knuckle is not approximated to a cylinder, a torus is used
- The length of the thread within a unit cell is no longer approximated to  $L$

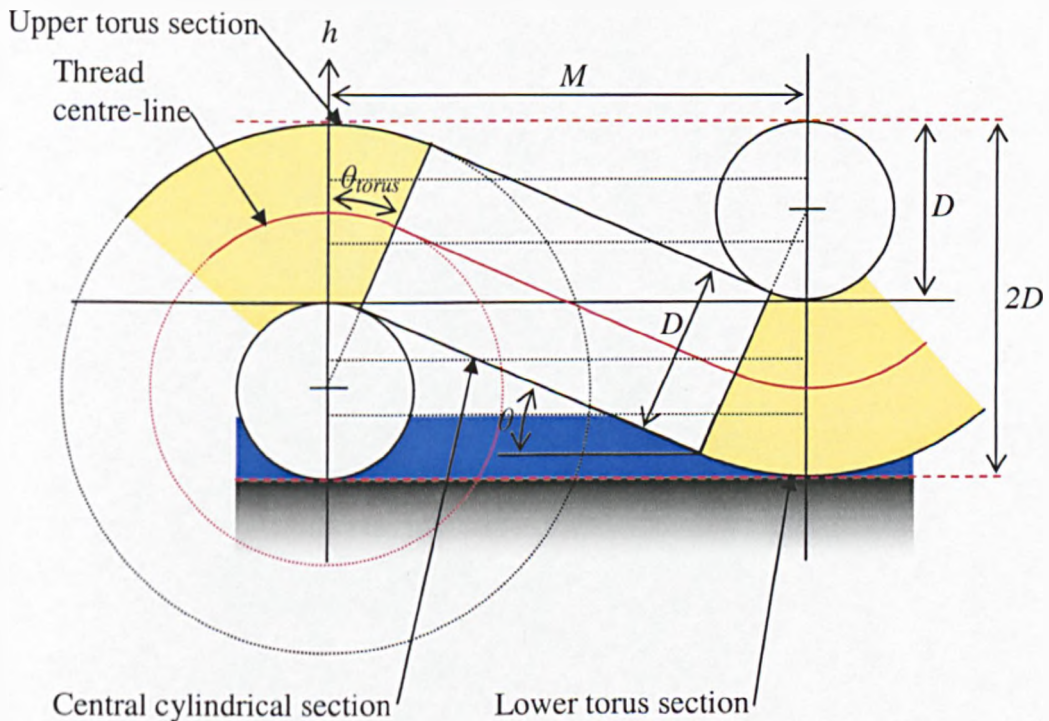


Figure 4.27: Illustration modelling the thread using torus and cylinder geometry.

The thread volume is established by assuming geometry as a combination of a cylindrical section and a ring torus (shown in Figure 4.27). The cross-sectional shape of the thread is circular (development of model 1). The model includes the concept of partially filled cells (introduced in model 4).  $D$  and  $M$  are the manufacturers' values of thread diameter and spacing respectively (Saati (2002b), Sefar (1999a)). These two parameters define the value of  $\theta$  (equations (4.22) and (4.30)).

$$\theta = \theta_{torus} \quad (4.22)$$



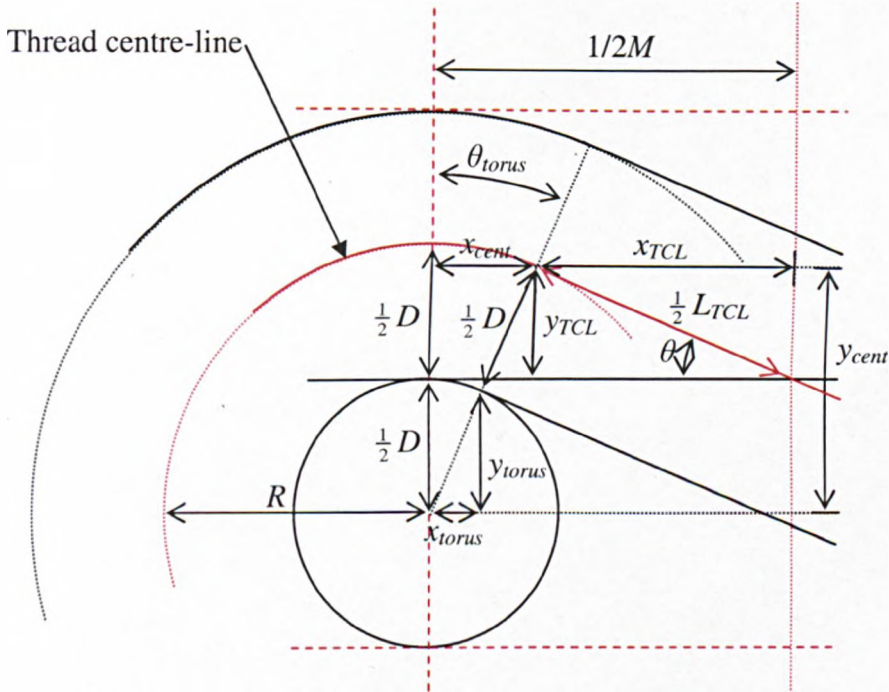


Figure 4.28: Diagram focusing on the centre-line of a thread of diameter  $D$  and thread spacing  $M$ , to establish the value of  $\theta$ .

Figure 4.28 shows schematically the relationships between the parameters defined in equations (4.23-4.30), used to establish the value  $\theta$  for a given  $D$  and  $M$  mesh geometry. The dimensions of the torus affect the value of  $\theta$ . The thread centre-line of the torus is defined as  $R$  (shown in Figure 4.29), which is equal to  $D$  (shown in Figure 4.28). Increasing  $R$ , greater than  $D$ , has the effect of essentially slackening the knuckle contact, which physically implies a reduction of mesh tension. Defining  $R$  less than  $D$  implies an overlap of threads. Therefore  $R$  equalling  $D$  is the simplified optimum value for the torus that is most equivalent to the experimental screen meshes (without incorporating compression factors).

$$\frac{1}{2} L_{TCL} = \sqrt{y_{TCL}^2 + x_{TCL}^2} \quad (4.23)$$

$$x_{cent} = D \sin \theta \quad (4.24)$$

$$y_{cent} = D \cos \theta \quad (4.25)$$

$$x_{torus} = \frac{1}{2} D \sin \theta \quad (4.26)$$

$$y_{torus} = \frac{1}{2} D \cos \theta \quad (4.27)$$

$$x_{TCL} = \frac{1}{2}M - x_{cent} \quad (4.28)$$

$$y_{TCL} = y_{cent} - \frac{1}{2}D \quad (4.29)$$

$$\theta = \tan^{-1}\left(\frac{y_{TCL}}{x_{TCL}}\right) = \tan^{-1}\left(\frac{y_{cent} - \frac{1}{2}D}{\frac{1}{2}M - x_{cent}}\right) = \tan^{-1}\left(\frac{D \cos \theta - \frac{1}{2}D}{\frac{1}{2}M - D \sin \theta}\right) \quad (4.30)$$

Using equation (4.30) the following values of  $\theta$  are established for the selected mesh geometries of Table 4.6:

Mesh description	$D$ ( $\mu\text{m}$ )	$M$ ( $\mu\text{m}$ )	$\theta$ (degrees)
90-40	40	111.1	22.85
120-34	34	83.33	26.88
150-31	31	66.67	32.55

*Table 4.6: Table of the calculated  $\theta$  values for the mesh geometries.*

The numerical approximation slice method, used in model 4 calculations, is applied for calculating the thread volume to specific ink heights for partially filled cells; the volume of the partially filled unit cell is calculated using equations (4.18) of model 4.

### **Calculation of thread volume within a partially filled unit cell**

Thread volume below a specified ink height is calculated by initially establishing the volume of the thread which is part of the torus section and that which is of the central cylindrical section. The combination of these sectional volumes is the required thread volume.

### The torus section volume

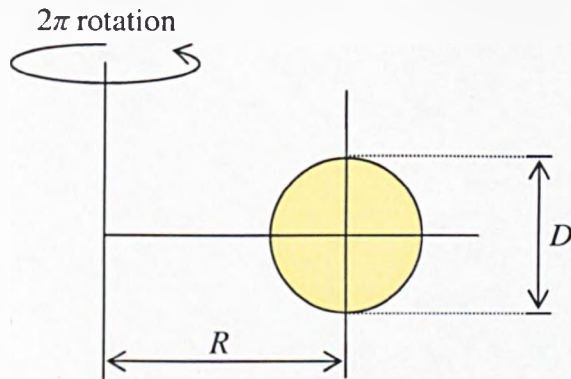


Figure 4.29: Diagram showing how rotation of a circle forms a torus.

The full volume of the torus is formed by rotating a circle through  $2\pi$  radians, as shown in Figure 4.29. Therefore the volume is calculated using Pappus's centroid Theorem (volume by revolution) generating these equations:

Volume = Area of circle  $\times$  rotation path length

$$\Rightarrow \text{Full torus volume} = \frac{\pi D^2}{4} \times 2\pi R = \frac{\pi^2 D^3}{2} \quad (4.31)$$

(since  $R = D$ )

The thread considered in the unit cell however consists of two torus sections: an upper and a lower section (shaded in Figure 4.27). The total volume of each torus section is:

$$\text{Upper torus section} = \text{Lower torus section} = \frac{\pi^2 D^3 \theta}{4\pi} \quad (4.32)$$

### Calculation of torus section volume within the partially filled unit cell

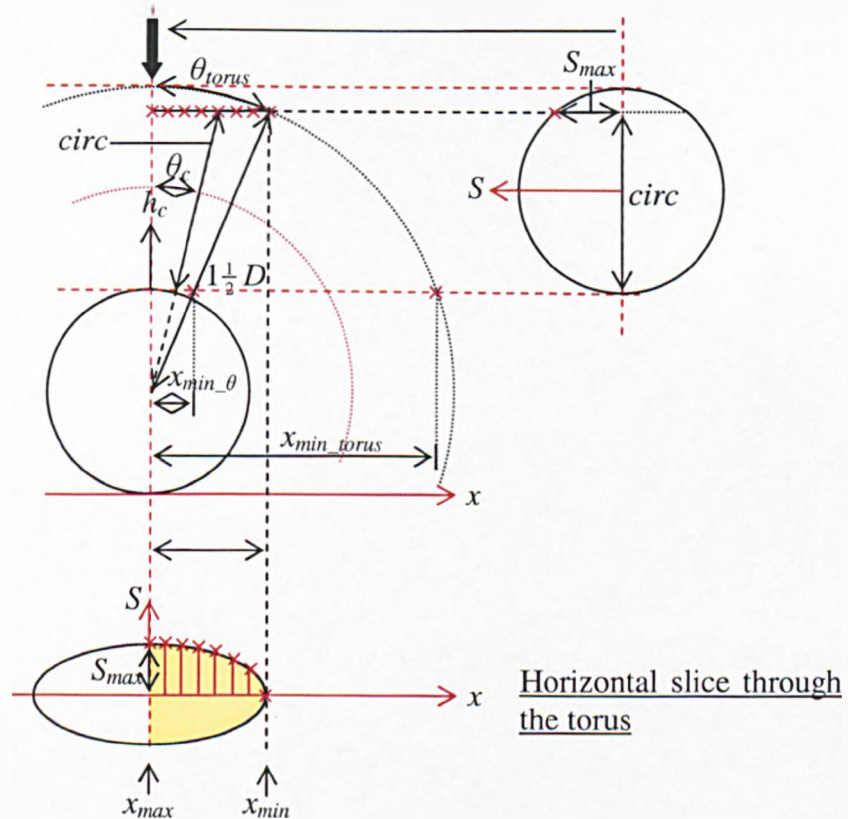


Figure 4.30: Diagram showing a horizontal slice through the torus highlighting the parameters involved to calculate the slice area.

The numerical approximation used previously in section 4.4.4, is adapted to calculate the horizontal slice areas of the torus section. Figure 4.30 shows an example horizontal slice; the  $x_{min}$  point for this example slice is located where the torus section and central cylindrical section of the thread meet. The geometric shape of the slice is not elliptical. The height above the peak of the lower mesh thread to the slice is termed  $h_c$ .

The horizontal slice is subdivided to establish the lengths between the slice surface and the  $x$  axis for the limits within the torus section. These limits will be  $x_{max}$  ( $x_{max}$  equals 0 except when calculating the additional torus section described at the end of this section) to whichever is the smaller of  $x_{min_\theta}$  and  $x_{min\_torus}$  for the horizontal slice (determined using equations (4.35) and (4.36)).  $\theta_c$  (shown on Figure 4.30) is used to

calculate  $x_{min\_torus}$ .  $\theta_{torus}$  is a constant value for a specific mesh geometry, but  $\theta_c$  varies depending upon  $h_c$  and the  $x$  value of the slice. Setting the  $h_c$  value leads to  $x_{min}$  (shown on Figure 4.30) and  $\theta_c$  being defined by equation (4.34) which is named  $\theta_{c(xmin)}$  to correspond with the  $x_{min}$  point.

$$h_c = \frac{3D \cos \theta_{c(xmin)}}{2} - \frac{D}{2} \quad (4.33)$$

$$\Rightarrow \theta_{c(xmin)} = \cos^{-1} \left[ \frac{2(h_c + \frac{1}{2}D)}{3D} \right] \quad (4.34)$$

$$x_{min\_torus} = \frac{3D \sin \theta_{c(xmin)}}{2} \quad (4.35)$$

$$x_{min\_theta} = \left( h_c + \frac{D}{2} \right) \tan \theta_{torus} \quad (4.36)$$

$$x_{min} = \min \{ x_{min\_torus}, x_{min\_theta} \} \quad (4.37)$$

For the slice example in Figure 4.30,  $x_{min\_theta}$  equals  $x_{min\_torus}$  since the limit point coincides with the point where the torus section meets the central cylindrical section of the thread. Horizontal slices with  $h_c$  values less than this example will apply limits of  $x_{max} \rightarrow x_{min\_theta}$ ;  $h_c$  values greater than the example limits of  $x_{max} \rightarrow x_{min\_torus}$  will apply. The limit length in the  $x$  direction is equally divided into subdivisions required for calculating the horizontal slice area.

The value of  $S$  is calculated for each of the subdivision points, by calculating the corresponding  $x$  value, *circ* length and then  $S$ , using equations (4.38) and (4.39) defined in Figure 4.30. The  $x$  value is between the limits of  $x_{max}$  and  $x_{min}$ , and is determined by the number of sub-slices used in the calculation.

$$circ = \sqrt{x^2 + \left( h_c + \frac{D}{2} \right)^2} - \frac{D}{2} \quad (4.38)$$

$$S = \sqrt{\left( \frac{D}{2} \right)^2 - \left( circ - \frac{D}{2} \right)^2} \quad (4.39)$$

The additional torus section

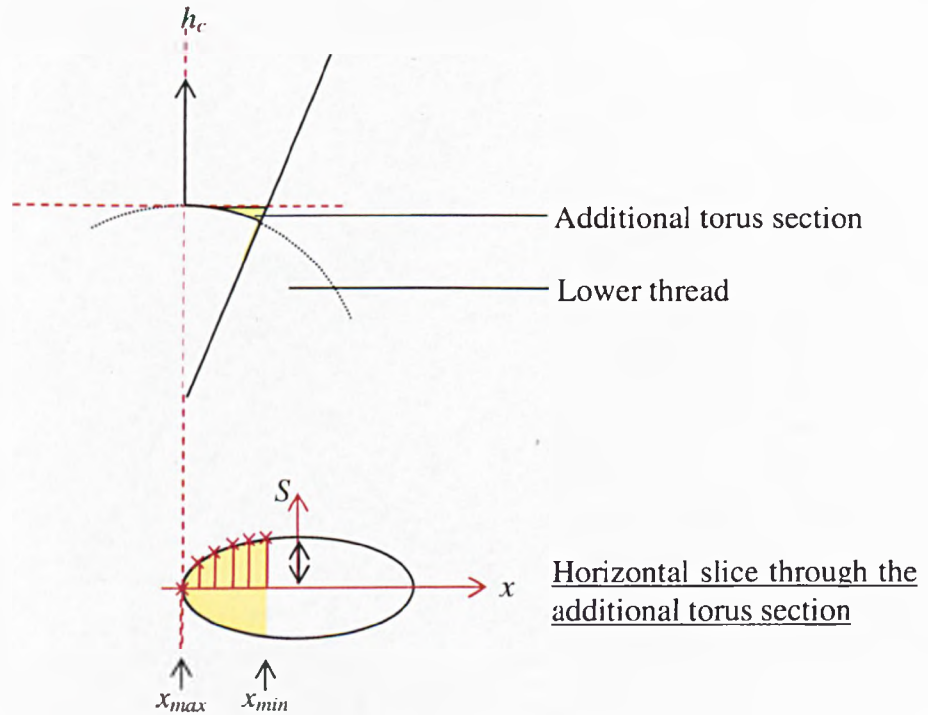


Figure 4.31: Diagram showing a horizontal slice through the additional torus section highlighting the limits  $x_{min}$  and  $x_{max}$  involved for calculating slice area.

The additional torus section value of  $x_{max}$  does not equal 0 but is defined as the position where  $S$  equals 0 (equation (4.40));  $x_{min}$  is determined from the location where the torus meets the central cylinder (equation (4.41)) for each  $h_c$  level.

$$x_{max} = \sqrt{\left(\frac{D}{2}\right)^2 - \left(\frac{D}{2} - |h_c|\right)^2} \quad (4.40)$$

$$x_{min} = \tan \theta_{torus} \left(\frac{D}{2} - |h_c|\right) \quad (4.41)$$

The values of  $circ$  and  $S$  are calculated using the method applied previously with equations (4.38) and (4.39).

The horizontal slice area is established by multiplying each calculated  $S$  value by the sub-strip width (the distance between successive  $x$  value calculations); the slice volume equals slice area multiplied by slice thickness.

The ink height in relation to  $h_c$  is defined in equation (4.42).

$$\text{Ink height, } h = h_c + D \tag{4.42}$$

The cumulative volume of horizontal slices generates the volume of thread to the desired ink height.

**The central cylindrical section volume**

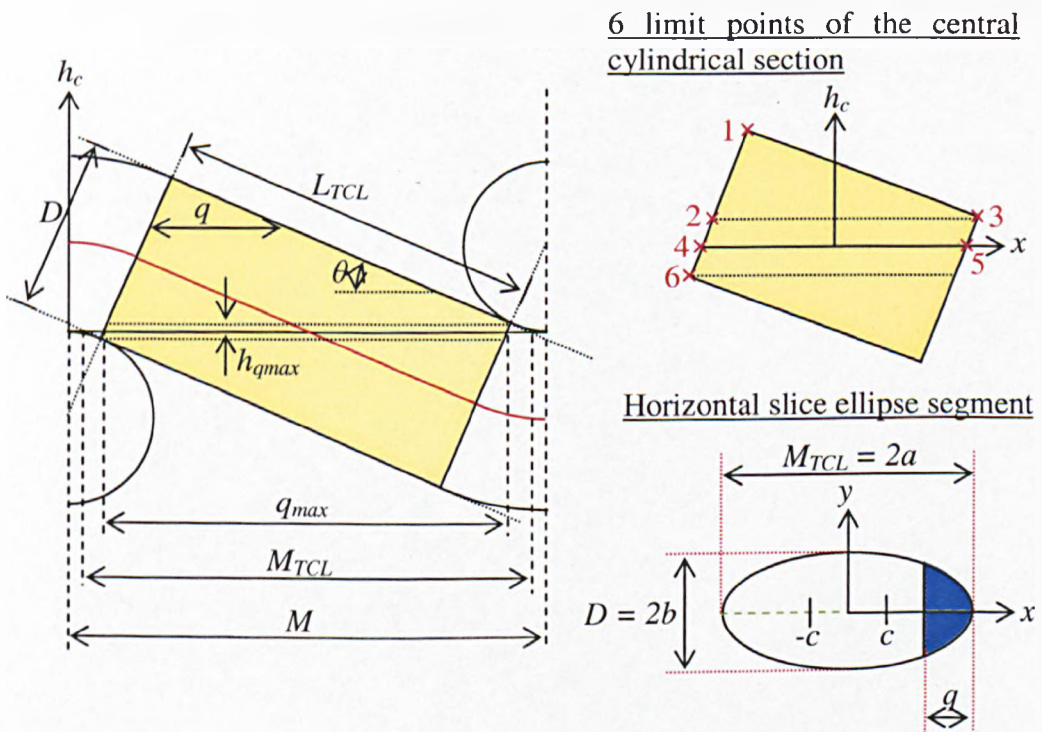


Figure 4.32: Diagram showing the ellipse segment of a horizontal slice through the central cylindrical section of the thread highlighting the parameters used to calculate slice area. The points labelled  $-c$  and  $c$  are the ellipse foci.

The full volume of the central cylindrical section is calculated using equation (4.43).

$$\text{Full central cylindrical volume} = \frac{\pi D^2 L_{TCL}}{4} \quad (4.43)$$

The numerical approximation method is adapted to calculate the horizontal slice areas of the central cylindrical section. The horizontal slices through the central cylindrical section have elliptical section geometry (as shown in Figure 4.32), all from the same ellipse. The equation of the ellipse is defined with equations (4.44) and (4.45).

$$\frac{x^2}{a^2} + \frac{y^2}{a^2 - c^2} = 1, \quad (4.44)$$

$$\text{where } a = \frac{M_{TCL}}{2}, \text{ and } c = \sqrt{\left(\frac{M_{TCL}}{2}\right)^2 - b^2}.$$

$$\Rightarrow y = \sqrt{\left(1 - \frac{4x^2}{M_{TCL}^2}\right) \times b^2}, \quad (4.45)$$

where  $2b$  is the horizontal diameter of the thread.

Figure 4.32 shows 6 limit points which are used in the following calculations. The co-ordinates of these points are shown in Table 4.7 below (N.B. the  $x$  co-ordinate system is zeroed at the centre of the unit cell):

Limit point	$x$ co-ordinate	$h_c$ co-ordinate
1	$1 \frac{1}{2} D \sin \theta - \frac{1}{2} M$	$1 \frac{1}{2} D \cos \theta - \frac{1}{2} D$
2	$\frac{1}{2} M - \frac{1}{2} D \sin \theta - q_{max}$	$\frac{1}{2} D - \frac{1}{2} D \cos \theta = h_{qmax}$
3	$\frac{1}{2} M - \frac{1}{2} D \sin \theta$	$\frac{1}{2} D - \frac{1}{2} D \cos \theta = h_{qmax}$
4	$\frac{1}{2} M - \frac{1}{2} D \sin \theta - q_{max} - h_{qmax} \tan \theta$	0
5	$\frac{1}{2} M - \frac{1}{2} D \sin \theta - h_{qmax} \tan \theta$	0
6	$\frac{1}{2} D \sin \theta - \frac{1}{2} M$	$\frac{1}{2} D \cos \theta - \frac{1}{2} D$

Table 4.7: The co-ordinates of the 6 limit points of Figure 4.32.



In Figure 4.32,  $q$  is the sagitta length of the ellipse and can be established for each  $h_c$  value of the respective horizontal slice.  $q$  is a constant value between the range of:  $-h_{qmax} \leq h_c \leq h_{qmax}$  as shown in equation (4.46) and is calculated with equation (4.47).

$$q = q_{max} \text{ when } |h_c| \leq h_{qmax} \tag{4.46}$$

$$q_{max} = \frac{L_{TCL}}{\cos \theta} = \frac{2\sqrt{(\frac{1}{2}M - D \sin \theta)^2 + (D \cos \theta - \frac{1}{2}D)^2}}{\cos \theta}, \tag{4.47}$$

when combined with parameters of equations (4.23-4.29).

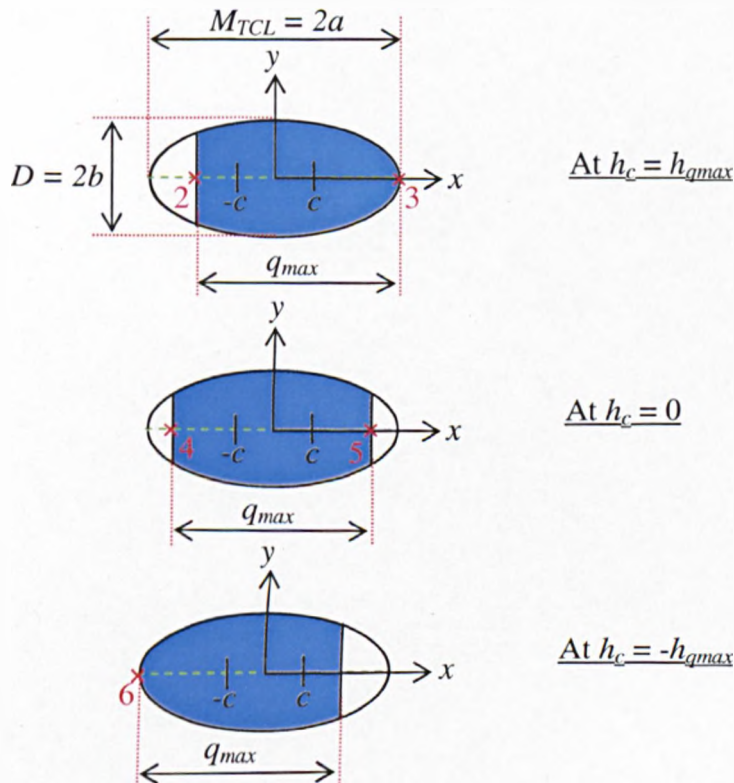


Figure 4.33: Diagram showing the “progression back” of the ellipse segment limits through the range of  $h_c$  when  $q$  is constant and equal to  $q_{max}$ ; the limit points of Figure 4.32 are labelled.

The limit points of Figure 4.32 are used to establish the ellipse segment limits for  $h_c$  values with  $q$  equalling  $q_{max}$  (as shown in Figure 4.33). The “progression back” of the limits occurs at a constant rate of  $h_c$ . The  $x$  direction difference in limit points 2 and 4 is shown in equation (4.48).

limit point 2 – limit point 4 =

$$\left[\frac{1}{2}M - \frac{1}{2}D \sin \theta - q_{max}\right] - \left[\frac{1}{2}M - \frac{1}{2}D \sin \theta - q_{max} - h_{qmax} \tan \theta\right] = h_{qmax} \tan \theta \quad (4.48)$$

$$\therefore \text{progression back} = h_c \cdot \frac{h_{qmax} \tan \theta}{h_{qmax}} = h_c \tan \theta \quad (4.49)$$

Hence the  $x$  co-ordinates of the ellipse segment limits will be:

$$\left[\left(\frac{1}{2}M_{TCL} - q_{max}\right) - h_c \tan \theta\right] \rightarrow \left[\left(\frac{1}{2}M_{TCL}\right) - h_c \tan \theta\right] \quad (4.50)$$

The difference in ellipse segment limits between successive horizontal slices is used to apply the sub-slice numerical method used in section 4.4.4 for calculating horizontal slice area and volumes.

For the  $h_c$  range of  $h_{qmax} < |h_c| \leq 1\frac{1}{2}D \cos \theta - \frac{1}{2}D$

$$q = \left(1\frac{1}{2}D \cos \theta - \frac{1}{2}D - h_c\right) \cdot \frac{q_{max}}{L_{TCL} \sin \theta} \quad (4.51)$$

The difference in  $q$  for successive horizontal slices is calculated so that the same numerical procedure (used in section 4.4.4) of calculating the extra ellipse segment area between slices is established to calculate the final thread volume to the selected  $h_c$  slice at the desired ink height.

### Combination of the geometric shapes

The volume of the torus and central cylindrical sections are summed to the ink height to calculate the thread volume. The accuracy of the numerical method is established by calculating the percentage difference of the thread volume in the unit cell between the numerical method and the expected volume of the geometric shapes (equation (4.52)). An accuracy within  $\pm 0.30\%$ , is achieved by the numerical approximation using: slice thickness of  $0.01\mu\text{m}$ , 20 sub-slice calculations for the “ellipse segment

increased area” that occurs between successive horizontal slices of the central cylindrical section, and 20 sub-slice calculations for each torus section slice.

The theoretical ink volume is established by subtracting the calculated thread volume from the partial cell volume (equation (4.18)). The theoretical maximum film thickness is found using equation (4.53).

$$\text{Thread full volume in unit cell} = 4 \left( \frac{\pi^2 D^3 \theta}{4\pi} \right) + 2 \left( \frac{\pi D^2 L_{TCL}}{4} \right) \quad (4.52)$$

$$\text{Theoretical film thickness} = \frac{\text{ink volume}}{M^2} \quad (4.53)$$

#### 4.4.6 Ink Transfer Model (ITM)

The ITM model was previously described in section 3.3. It models the maximum thickness of ink in the mesh which can easily be converted into the initial ink volume in the mesh by multiplying with the printable area. It also calculates the percentage ink transfer to the substrate. A combination of these parameters enables the printed ink thickness to be established.

The same mesh input data was used as in section 3.3.

## 4.5 Results and discussion of the geometric mesh models

The following results used the manufacturers' and actual measured mesh dimensions of the light framed meshes (shown in Table 4.4).

### Models 1-3

To calculate the theoretical maximum printed thicknesses using models 1-3 it is assumed that 100% fluid transfer occurs from the mesh. Implicit within these models is that the mesh is completely full.

	90-40		120-34		150-31	
Model	Ink vol. ( $\times 10^5 \mu\text{m}^3$ per cell)	Max. film thickness ( $\mu\text{m}$ )	Ink vol. ( $\times 10^5 \mu\text{m}^3$ per cell)	Max. film thickness ( $\mu\text{m}$ )	Ink vol. ( $\times 10^5 \mu\text{m}^3$ per cell)	Max. film thickness ( $\mu\text{m}$ )
1	6.91	55.96	3.09	44.47	1.65	37.03
2	4.97	40.29	1.93	27.80	0.95	21.36
3	5.51	44.36	2.25	32.43	1.19	26.08

Table 4.8: *Mathematical results for models 1-3.*

Model 1 (circular cross-sectional thread model commonly used in industry) predicts the greatest ink volume in the unit cells and correspondingly the greatest maximum theoretical film thickness (shown in Table 4.8). The equivalent calculated values are less when using model 2 (adapted circular thread model) due to the thinner measured mesh thickness; the corresponding values of model 3 (elliptical model) lie between those of model 1 and 2.

Figure 4.34 displays the calculated maximum film thickness results using model 1. It highlights that the model is not sensitive to the thread spacing at low values of the thread diameter, but this parameter has more effect when used for thicker threads. The dominant parameter affecting the sensitivity of model 1 is clearly shown to be the

thread diameter. Similarly this also occurs for models 2 and 3. The (hashed) region to the right of the dotted line in Figure 4.34 can be ignored since physically this implies adjacent threads overlap due to the thread diameter exceeding the unit spacing ( $D > M$ , where  $M = 10^4 \div \text{thread count per cm}$ ).

The mesh parameters used to construct the model 2 unit cell was previously defined in Figure 4.21 of section 4.4.2. Figure 4.35 highlights the effect of thread compression, using model 2, on the predicted maximum film thickness. The (hashed) region to the left of the dotted line (for each graph) can be ignored since physically this implies an expansion of the thread thickness (i.e. ignore situations where  $D_{comp} > D$ ) rather than compression. The bottom graph of Figure 4.35 does not include thread diameters greater than  $55\mu\text{m}$  since these exceed the thread spacing (180 threads per cm) – physical implication is the same as for the ignored region in Figure 4.34.

For the low mesh counts, model 2 is very sensitive to the thread compression factor regardless of the original thread diameter. For example, if the compressed thread thickness is  $40\mu\text{m}$  (in a mesh of 30 threads per cm) and the original thread thickness was just  $50\mu\text{m}$  then the calculated film thickness is  $70.5\mu\text{m}$ ; but if the original thread thickness was  $100\mu\text{m}$  (implying greater compression factor) the calculated film thickness is  $60.3\mu\text{m}$ . However, if the compressed thread thickness value is varied, there is significantly greater change to the calculated film thickness. For example using original thread thicknesses of  $100\mu\text{m}$ , and thread count of 30, a compressed thread thickness of  $80\mu\text{m}$  generates a calculated film thickness of  $120.6\mu\text{m}$ ; whereas compression of the same thread to a thickness of  $20\mu\text{m}$  calculates a film  $30.2\mu\text{m}$  thick. This illustrates the model is greatly sensitive to the compressed thread thickness.

For model 2, the mesh thickness is equivalent to  $2D_{comp}$ , and therefore highlights that this also has significant sensitivity within the calculations. At the higher mesh counts this sensitivity significantly reduces for thicker original thread dimensions, but remains true for the thinner threads.

Figures 4.36 and 4.37 depict the influence of the variables of model 3 (defined previously in Figure 4.22 of section 4.4.3) on the calculated film thickness. Model 3

uses two sets of separate variables to distinguish between warp and weft threads. Figure 4.36(a) highlights that both  $D_{warp}$  and  $D_{weft}$  parameters contribute equally to the calculated film thickness. The average of  $D_{warp}$  and  $D_{weft}$  generate the same film thickness result as calculating each separately – for example, a warp of 50 $\mu\text{m}$  and weft of 50 $\mu\text{m}$  has the same mesh volume as a warp of 80 $\mu\text{m}$  and weft of 20 $\mu\text{m}$ . Figure 4.36(b) displays a similar result for when the thread counts of both warp and weft directions are varied – therefore  $M_{warp}$  and  $M_{weft}$  have equal influence. This justifies previous models usage of a single value for  $D$  and  $M$ , which should use the measured averages from the mesh rather than the manufacturers' provided data.

Figure 4.36(c)-(d) show that thread count has little effect on the calculations of mesh volume and that mesh thickness has the greatest influence regardless of the thread count. The (hashed) region above the dotted lines can be ignored since physically this implies thread expansion (ignore situations where mesh thickness  $> 2D$ ). Therefore with  $D_{warp}$  and  $D_{weft}$  threads measured as 40 $\mu\text{m}$ , the mesh thickness cannot exceed 80 $\mu\text{m}$ . The dotted lines on the graphs depict this maximum mesh thickness, however in practice the measured thickness is likely to be significantly less than 80 $\mu\text{m}$ .

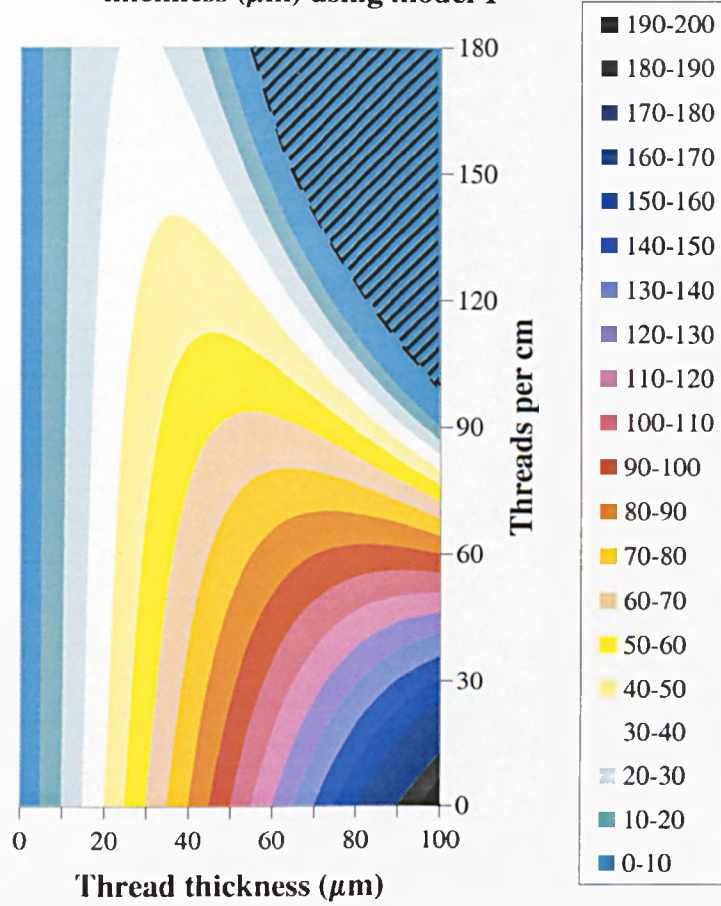
Figure 4.36(c) shows the effect of varying only one of the thread count variables (warp). In Figure 4.36(d) thread counts (i.e.  $M_{warp}$  and  $M_{weft}$ ) are set equal. Both graphs remain comparable up to thread counts of 90 threads per cm. Above this thread count, Figure 4.36(d) highlights that the combination of equal  $M_{warp}$  and  $M_{weft}$  (and hence both variables decreasing with the increased thread count) result with calculations of thinner films. For example, a mesh of a 60 $\mu\text{m}$  thickness and thread counts of 90 and 150 threads per cm, in weft and warp directions respectively, gives a maximum film thickness of 36.1 $\mu\text{m}$ , whereas an equivalent mesh constructed of 150 threads per cm (in both directions) calculates a thinner film of 29.0 $\mu\text{m}$ .

Figure 4.37(a)-(b) confirm the mesh thickness is the most dominating variable in model 3. The (hashed) regions above the dotted lines can be ignored to ensure the mesh thickness is less than both  $2D_{warp}$  and  $2D_{weft}$ . Figure 4.37(a) shows that an individual thread width (in this case  $D_{warp}$ ) has little effect on film thickness, especially at lower values. Figure 4.37(b) however displays that the results

significantly differ with  $D_{warp}$  and  $D_{weft}$  being equal: increasing both  $D$  variables results in greater sensitivity (with respect to the thread width,  $D$ ) and overall thinner films; similarly to the effect of setting  $M_{warp}$  and  $M_{weft}$  equal in Figure 4.36(d). For example, if the mesh thickness is  $60\mu\text{m}$  and the thread width is  $40\mu\text{m}$  (relatively low value), the maximum film thickness results simplified in Figure 4.37(a) is  $42.4\mu\text{m}$ , whereas Figure 4.37(b) calculates the same thickness of  $42.4\mu\text{m}$ . Increasing the thread width to a higher value of  $80\mu\text{m}$ , introduced a difference in the calculated film thickness:  $33.6\mu\text{m}$  from Figure 4.37(a), and a thinner film of  $24.9\mu\text{m}$  from Figure 4.37(b).

Figure 4.37(c) shows the effect of varying the thread count and thread diameter in the warp direction. The (hashed) region to the right of the dotted line is ignored to ensure the thread width,  $D$ , is less than the distance between adjacent threads,  $M$ . The influence of both variables is comparable for generating the film thickness. Small values of either variable increase the calculated thickness; reduction of both combines the effect resulting in substantially thicker films.

**The effect of the mesh geometry on the calculated maximum film thickness ( $\mu\text{m}$ ) using model 1**



*Figure 4.34: A graphical representation of the calculated maximum film thicknesses using model 1 – the key depicts 10 $\mu\text{m}$  ranges of these film thickness values ( $\mu\text{m}$ ).*



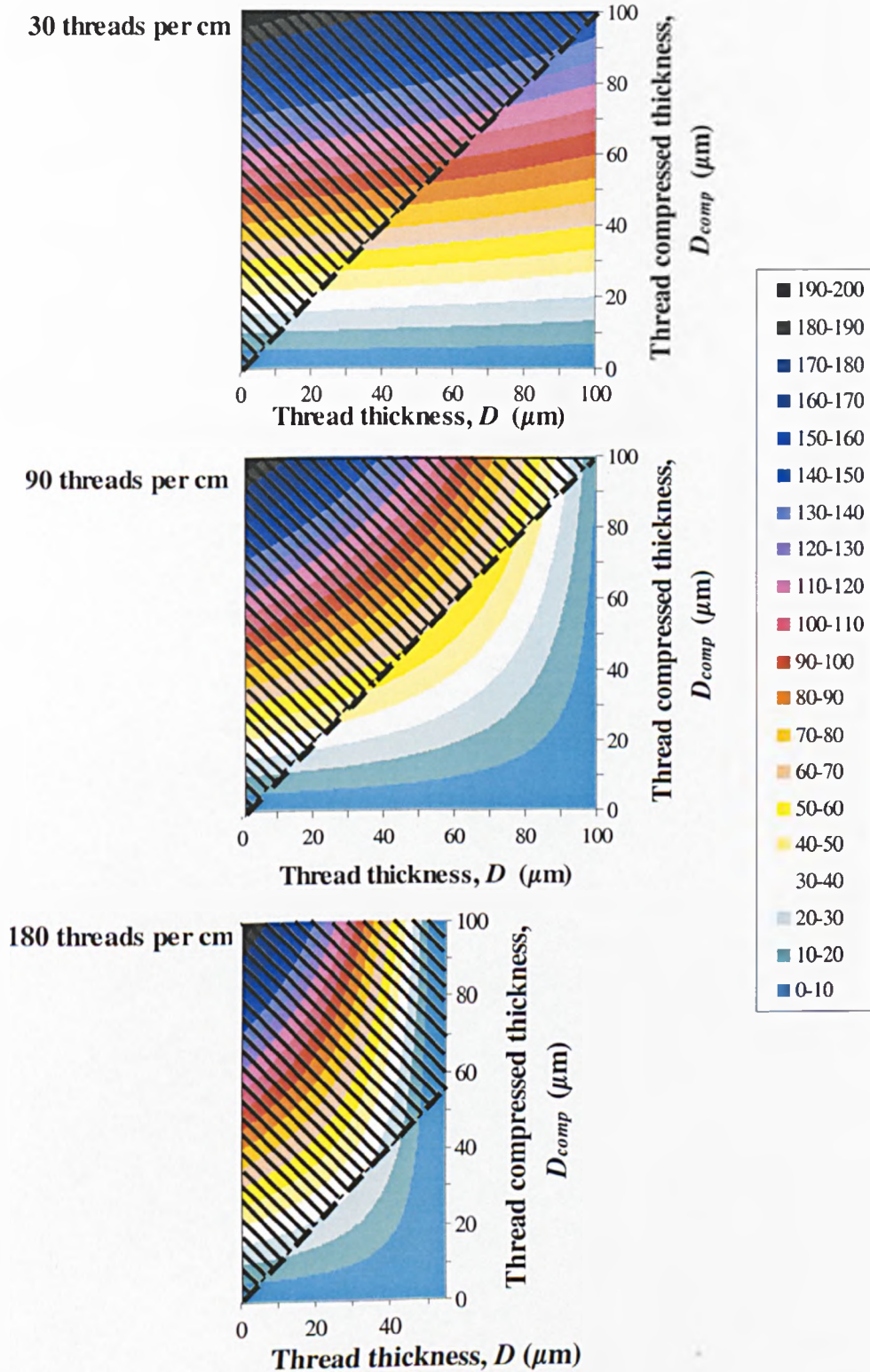


Figure 4.35: A graphical representation of the effect of thread compression on the calculated maximum film thickness ( $\mu\text{m}$ ) using model 2.

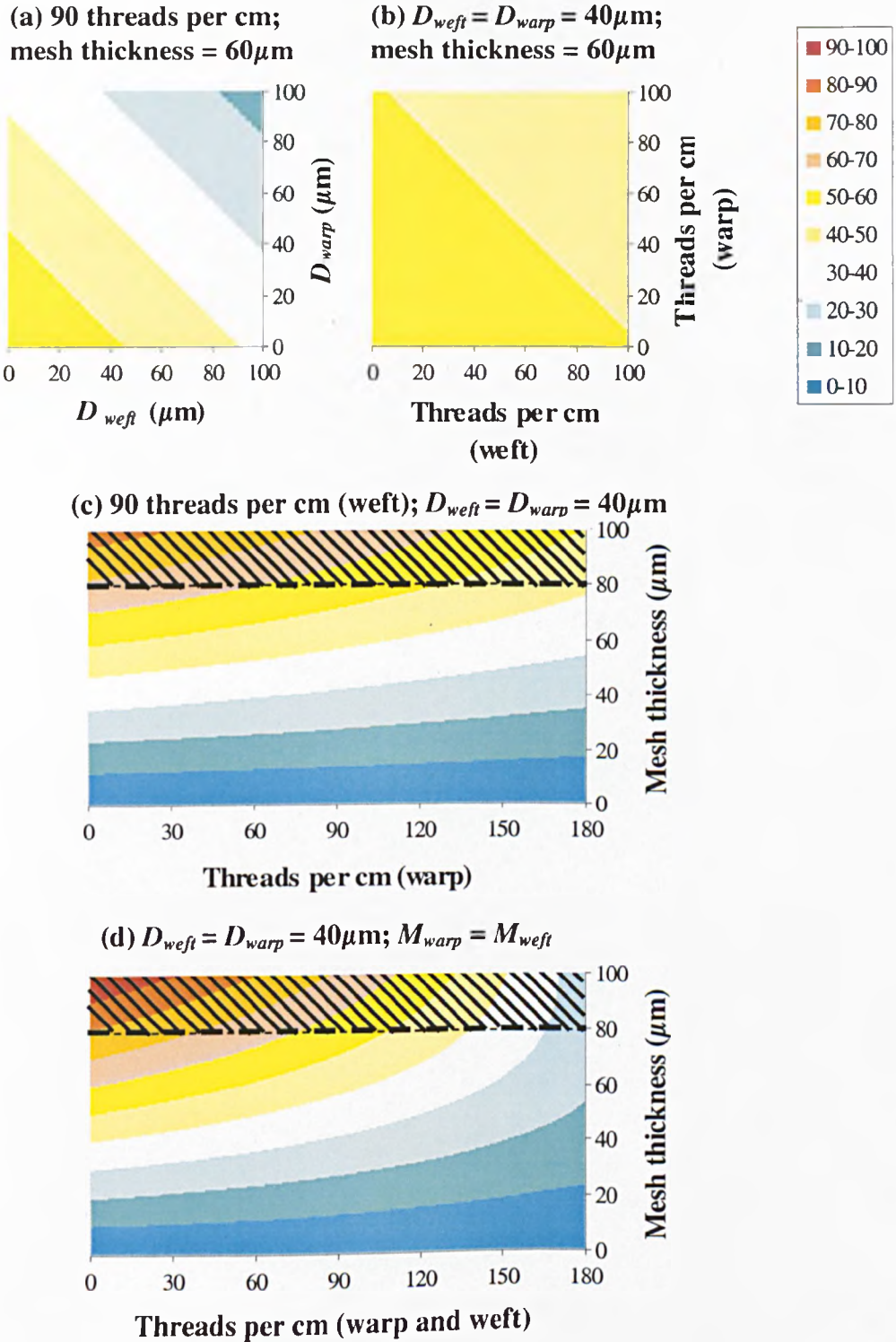


Figure 4.36: Graphical representations of model 3 variables on the calculated maximum film thickness. The key depicts the calculated maximum film thickness values ( $\mu\text{m}$ ).

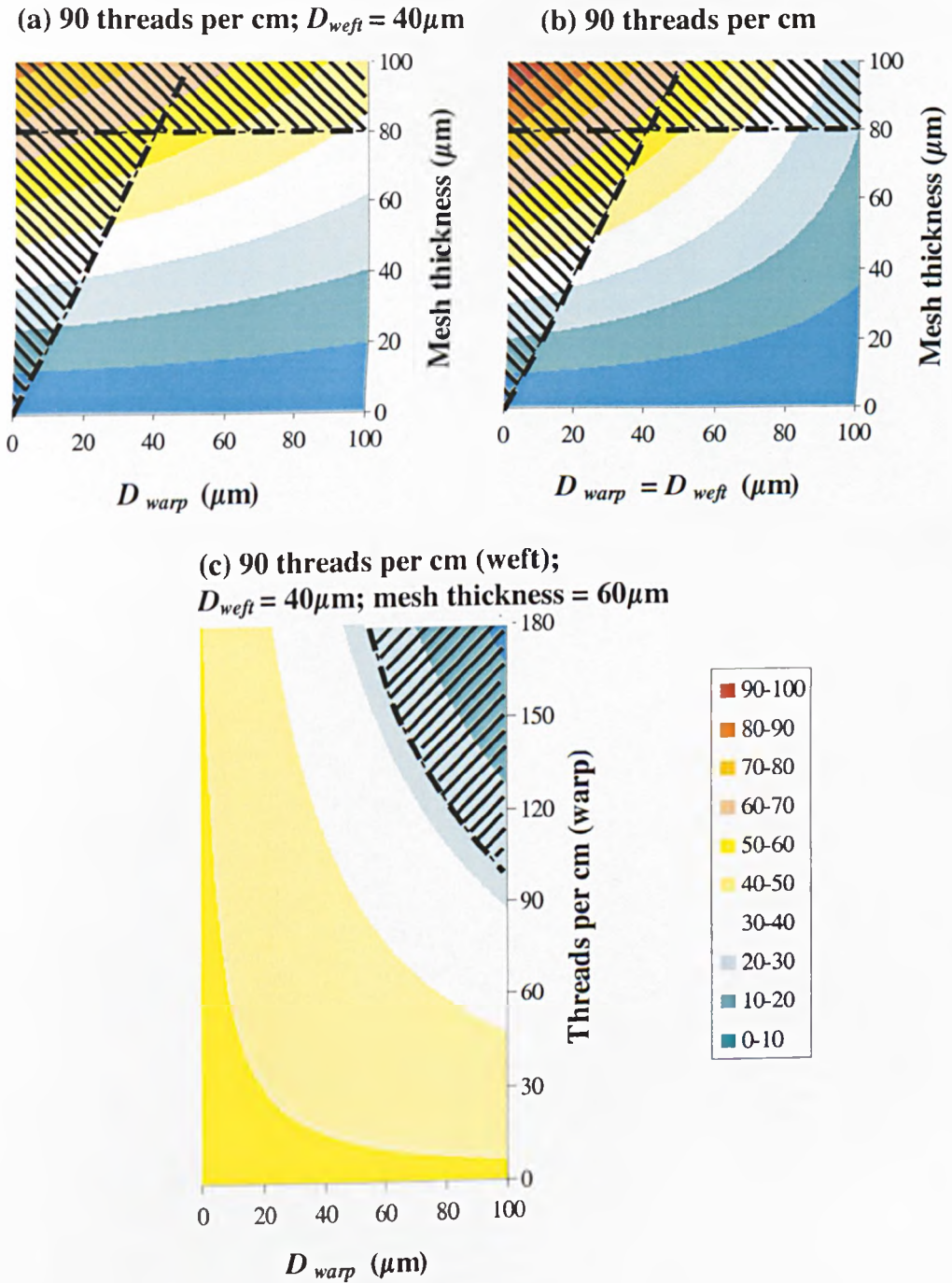


Figure 4.37: Graphical representations of model 3 variables on the calculated maximum film thickness. The key representing ranges of the calculated maximum film thickness values ( $\mu\text{m}$ ).

## Model 4

Model 4, as previously described in section 4.4.4, has three sub-models that include the theory that the ink fills to a predefined level, partially filling the mesh. Models 4.1 and 4.2 used the manufacturers' data of thread diameter and spacing. The difference between these two models is the cross-sectional shape: in model 4.1 the thread is represented as an angled cylinder with a circular cross-section throughout the length, whereas in model 4.2 the angled cylinder has a circular cross-section only when viewed from the ends. Model 4.3 used the measured data from the meshes of thread width, mesh thickness, and mesh spacing in both warp and weft directions.

A series of successive horizontal slices, of thickness  $0.01\mu\text{m}$ , were used to calculate to overall thread volume. This gave an overall accuracy within  $\pm 0.05\%$ , calculated by comparing against the thread volume in the full mesh.

Table 4.9 highlights the variation in the theoretical maximum film thicknesses calculated with each model 4 version.

Mesh	Model 4.1 (uses manufacturers' thread data)	Model 4.2 (uses manufacturers' thread data)	Model 4.3 (uses measured thread data from light framed mesh)	Model 4.3 (uses measured thread data from heavy framed mesh)
90-40	61.50	57.37	45.10	44.15
120-34	50.60	46.20	33.23	34.04
150-31	44.45	39.35	27.15	27.68

*Table 4.9: Theoretical maximum printed film thickness ( $\mu\text{m}$ ) results for 100% filled cells calculated using model 4.*

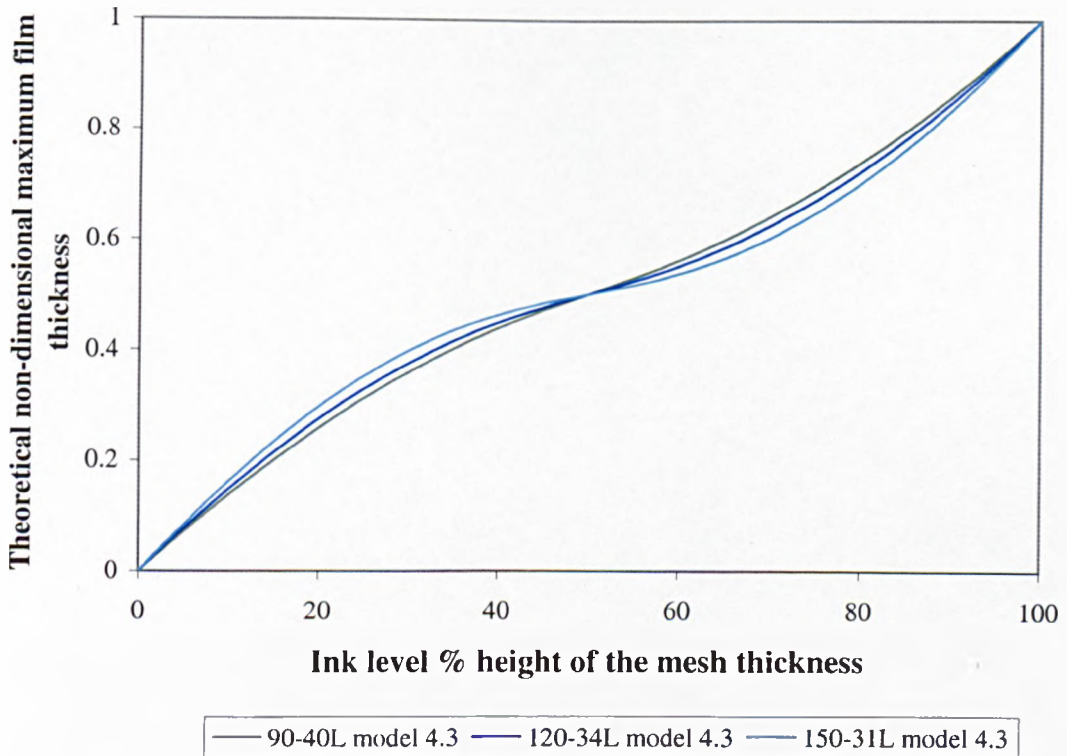
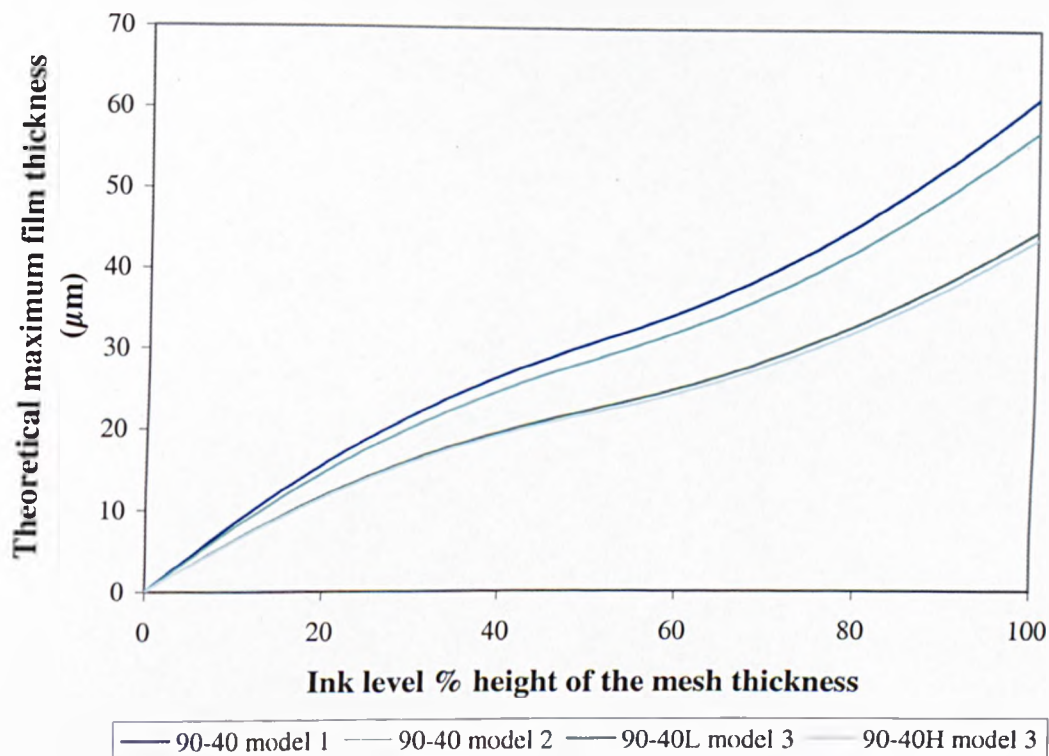


Figure 4.38: Relation between the level the ink fills to in the mesh cells and the calculated theoretical dimensionless maximum film thickness for model 4.3. (L indicates light framed mesh.)

The dimensionless maximum film thicknesses of Figure 4.38 were established using the respective maximum value for 100% filled cells in Table 4.9. The results for the each mesh geometry are approximately the same regardless of which version of model 4. The greatest percentage difference of dimensionless film thicknesses, between the models, occurs with low for values of  $h$ . The percentage difference is considerably reduced between models focusing in the ink height range of 40-60% height of the mesh thickness: 90-40 geometry has a difference of  $\pm 0.42\%$ ; 120-34 geometry has a difference of  $\pm 0.76\%$ ; 150-31 geometry has a difference of  $\pm 1.25\%$ .

The thread geometry influences the calculations of maximum film thickness in model 4, highlighted in Figure 4.38, since the calculated film thicknesses are not directly proportional to the ink height in the cells.

Figure 4.39 shows the maximum film thickness as a function of how full the mesh is (expressed as a percentage height of the mesh thickness) for the three sub-models.



*Figure 4.39: Comparison of the calculated theoretical maximum film thicknesses for the 90-40 mesh geometry, when the cells are partially filled. (L – light framed mesh; H – heavy framed mesh.)*

Although the models predict very similar dimensionless results, Figure 4.39 shows that the dimensional thicknesses differ for the three mesh geometries. The two meshes used in model 4.3 generate essentially the same results. Models 4.1 and 4.2 predict thicker films due to these models assuming thicker meshes (due to the use of the provided manufacturers thread data) for equivalent geometry when compared with model 4.3, which uses actual measured mesh thickness data.

## Model 5

Model 5 combined cylinder and torus sections to construct the simplified geometry representing the thread (previously described in section 4.4.5). Like model 4, it allows the ink level to be predefined as a height of the mesh thickness. A series of fine increments ( $0.01\mu\text{m}$ ) were used between successive horizontal slices to calculate the thread volume below the ink level. This led to accuracy within  $\pm 0.30\%$ , when comparing the total slice volume of thread with the total geometric thread volume (derived in equation (4.52)).

Mesh	Model 5
90-40	55.83
120-34	44.27
150-31	36.69

*Table 4.10: Theoretical maximum printed film thickness ( $\mu\text{m}$ ) results for 100% filled cells calculated using model 5.*

Table 4.10 shows the theoretical maximum film thicknesses calculated with model 5. These results are very similar to those from model 1; due to the simplified mathematics the calculation of the maximum theoretical film thickness from model 1 is significantly more convenient. However, for situations involving mesh filling of less than 100%, model 5 provides data that model 1 does not include (shown in Figure 4.40).

Figure 4.40 shows the maximum dimensionless film thickness as a function the ink level fills to in the mesh (characterised as a percentage height of the mesh thickness) for the three meshes used experimentally. The manufacturers' thread data was used to describe the geometry, rather than using the measured data.

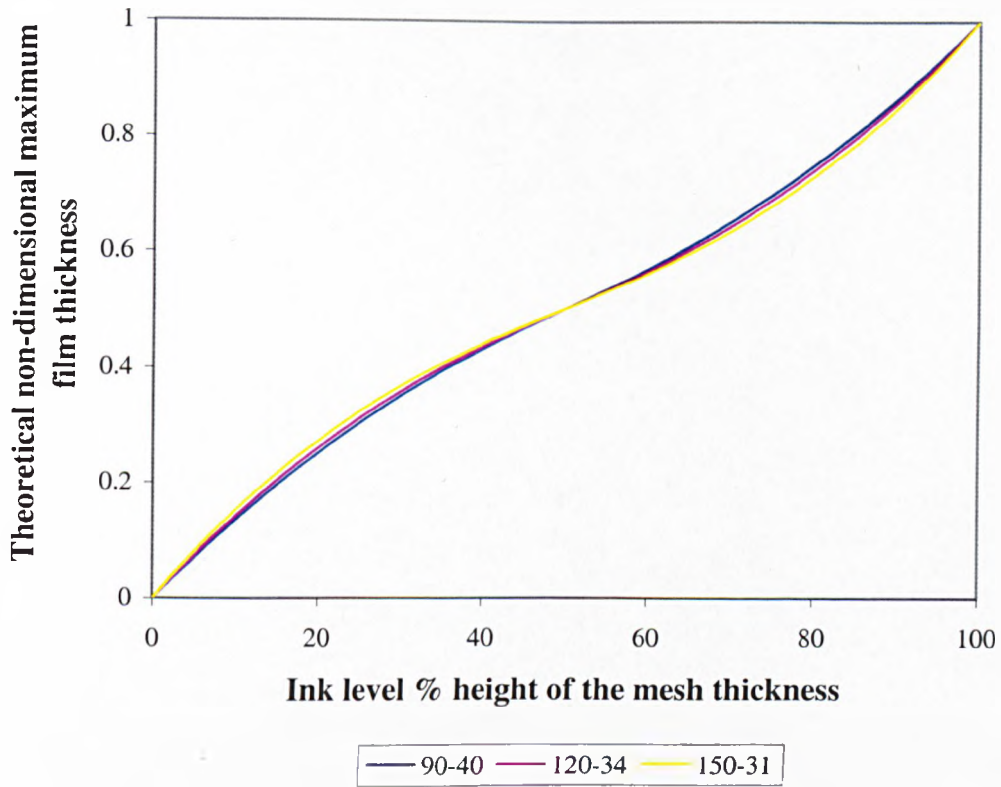
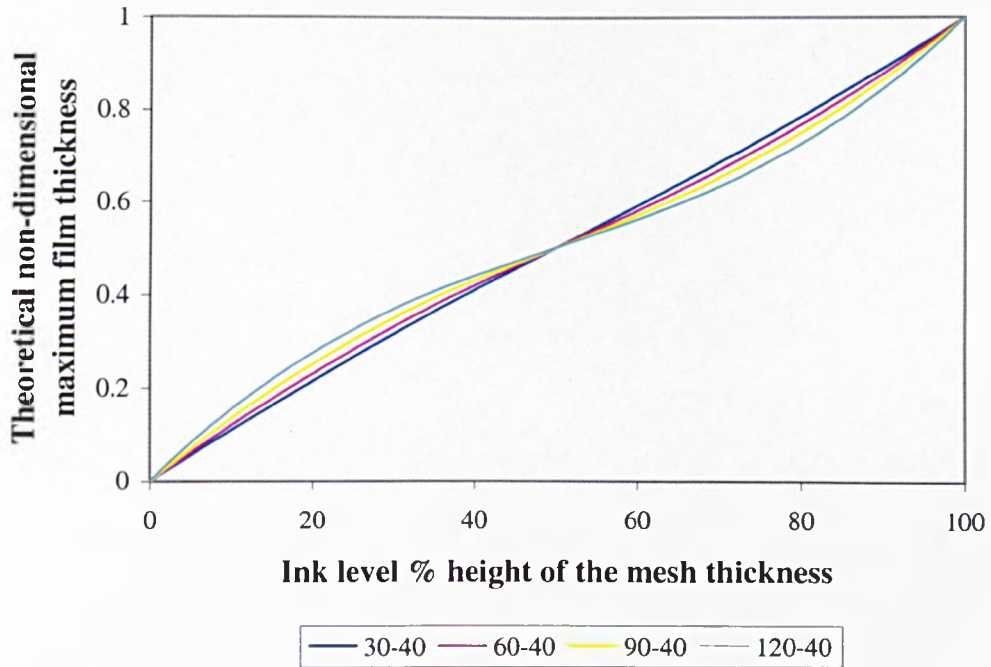


Figure 4.40: Graph showing the relation between the level the ink fills to in the meshes and the calculated theoretical dimensionless maximum film thickness.

Figure 4.40 shows that the mesh geometry affects the predicted maximum thicknesses less with this model than with model 4. However, the model does exhibit sensitivity to mesh geometry as shown in Figure 4.41.





*Figure 4.41: Theoretical non-dimensional maximum film thicknesses for incomplete mesh filling, observing the influence of the mesh count.*

Figure 4.41 highlights that decreasing the mesh count causes the relation between the dimensionless film thickness and the ink level percentage height of the mesh to tend to direct proportionality; although this becomes less true at high mesh counts. This is due to the thinner maximum film thicknesses for 100% filled cells that the high mesh counts predict using model 5.

The model is also greatly sensitive to the thread diameter since this parameter greatly influences the maximum film thickness for 100% filled cells and therefore also affects the dimensionless results for the range of partially filled cells.

Figure 4.42 shows the dimensional variation of the film thickness calculations for the three mesh geometries used experimentally.

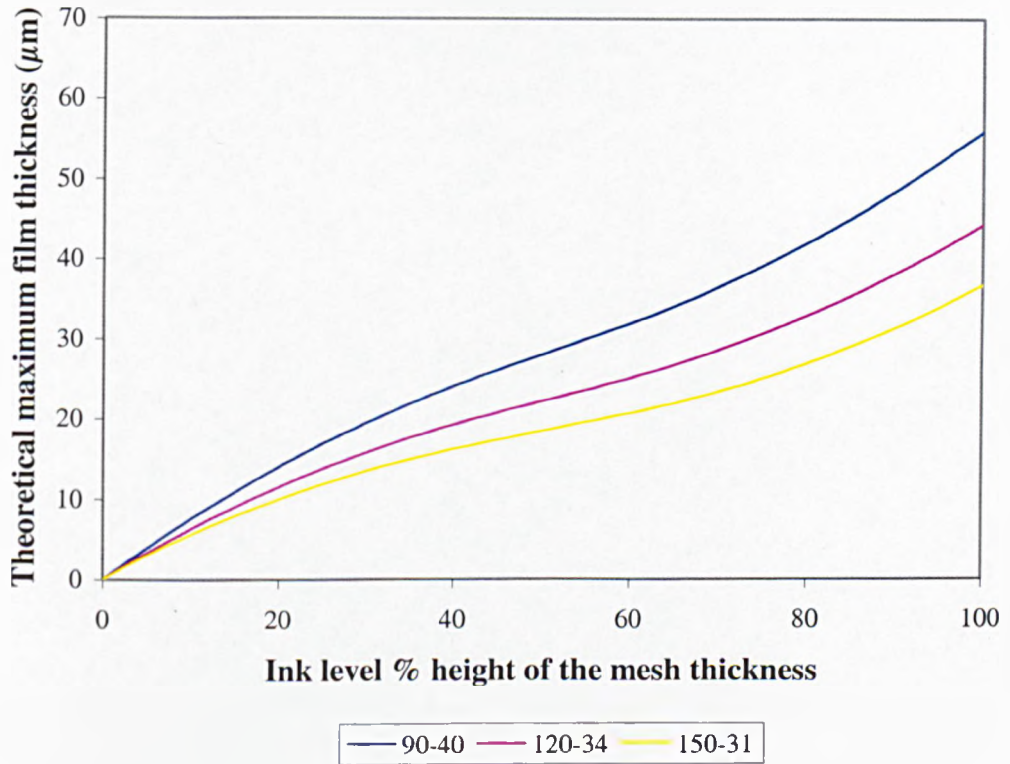


Figure 4.42: Theoretical maximum film thickness for incomplete mesh filling for the mesh geometries.

### Results from the ITM model

Table 4.11 shows the ITM results for the three experimental mesh geometries. Increasing the open mesh fraction only slightly decreases the calculated ITM non-dimensional printed thickness; the dimensional ITM printed thickness increases. The calculated range for ink transferring to the substrate (for the 3 meshes) is 38.8-41.6%. The model assumes the initial state of the mesh fills 100% of ink and the non-dimensional initial ink thickness is 1.0 for all meshes.

Mesh geometry	Maximum thickness in mesh ( $\mu\text{m}$ )	% ink remaining in the mesh	% ink transferred to the substrate	Printed thickness ( $\mu\text{m}$ )	Non-dimensional thickness
90-40	56.0	61.2	38.8	21.7	0.39
120-34	44.5	60.2	39.8	17.7	0.40
150-31	37.0	58.4	41.6	15.4	0.42

*Table 4.11: The ITM calculated results established by solving the percentage fluid remaining in the mesh after printing.*

## 4.6 Comparison of experimental and theoretical results

The accuracy of the theoretical models is highlighted by comparison with experimental observations from this chapter and chapter 3. Models 1-5 compare how much ink is initially in the mesh system, with models 4 and 5 considering partial cell filling; the ITM model compares the percentage fluid transfer, the initial state, and the printed film thicknesses.

Good agreement between the models and experimental data leads to potential application of the models to a wider printing field. Since all the models focus on the mesh geometry, a natural extension is to use the models as a predictive tool to calculate film thicknesses with mesh geometries not considered here. The predictive thicknesses would be applicable to both on- and off-contact printing types.

### Models 1-3 and experimental results

Figure 4.43 compares the experimental initial ink parameter with equivalent results generated using models 1-3. The initial ink thicknesses in the theoretical meshes (shown in Table 4.8) are converted into non-dimensional thickness values using the theoretical maximum printed thickness of the corresponding mesh (as done previously for the experimental thicknesses). Model 1 calculates a maximum theoretical thickness value of 1.0 for the non-dimensional thickness of ink in the mesh. All the models significantly over-calculate the amount of ink in the actual meshes, since each assumes that meshes are 100% full; the experimental results in section 4.3.1 shows that this is not a valid assumption.

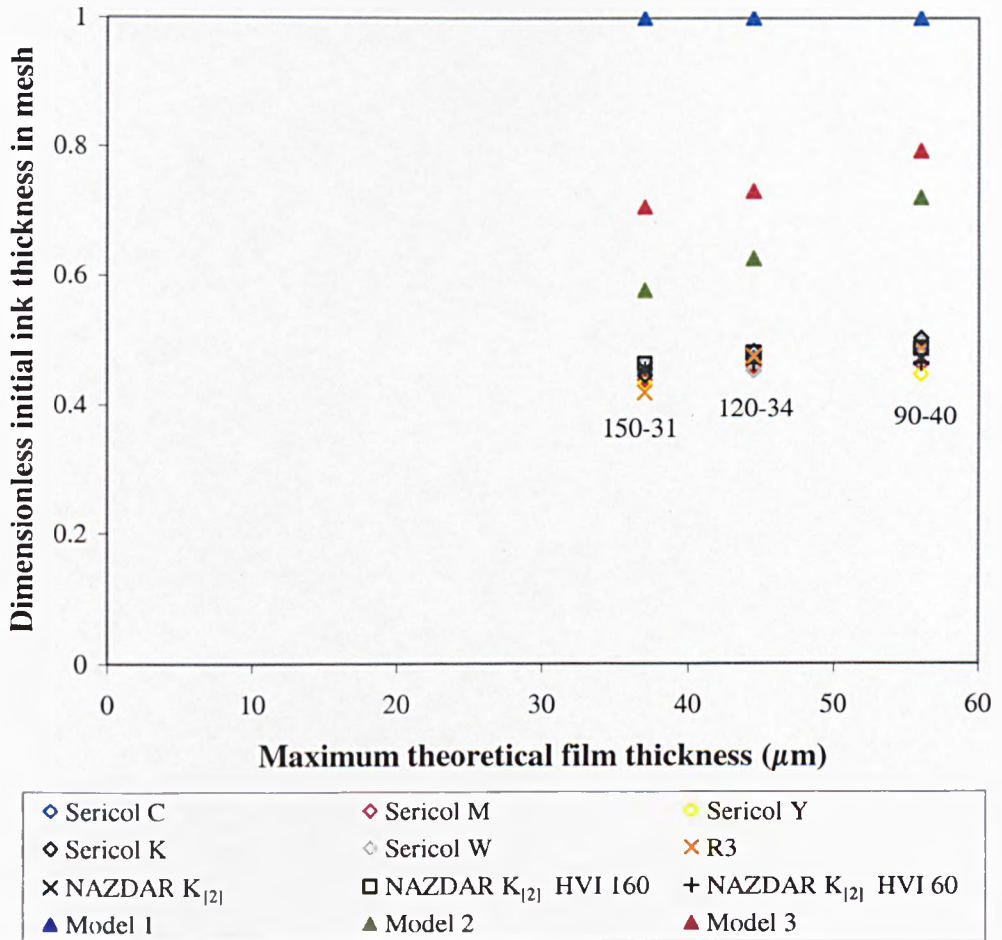
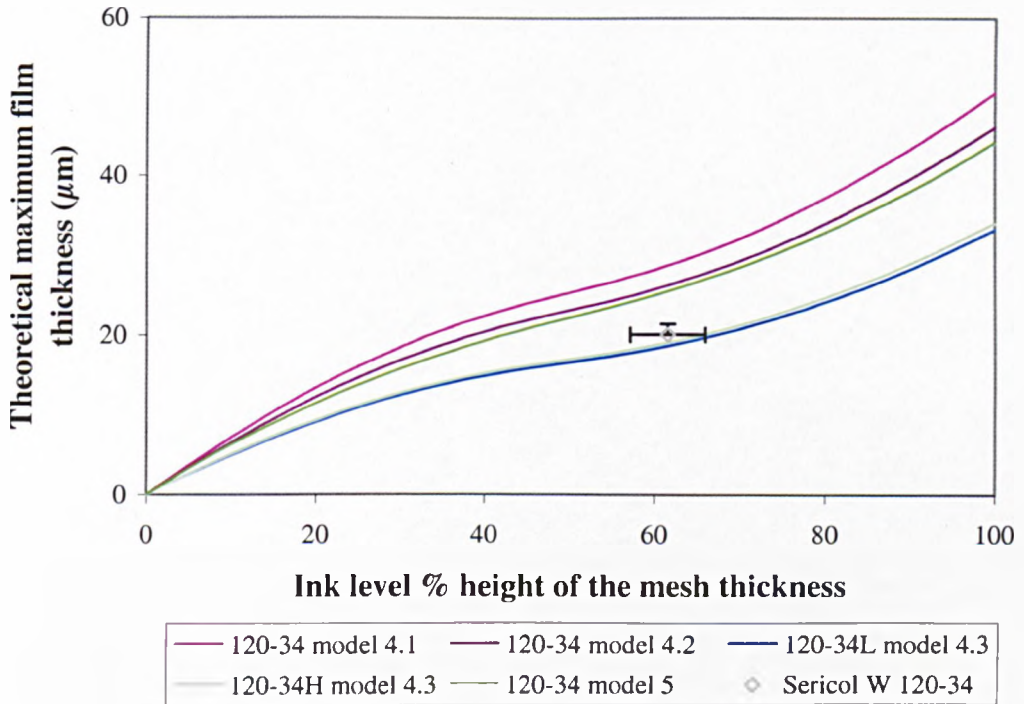


Figure 4.43: Comparison of the non-dimensional initial ink thicknesses in the meshes for the experimental data and the theoretical models using equivalent meshes.

### **Models 4-5 and experimental results**

The non-dimensional film thickness results from models 4 and 5 were previously found to be essentially the same in section 4.5. Each model uses the corresponding maximum theoretical film thickness value to non-dimensionalise the initial calculated dimensional values. The experimental results cannot be represented as non-dimensional values using this method since the true maximum film thickness, assuming both 100% filled mesh cells and 100% ink transfer, is unknown. All previous experimental non-dimensional thicknesses have used the maximum theoretical thicknesses calculated from model 1.

It was found previously, in section 4.3.2, that each experimental mesh filled approximately the same independent of ink type. The surface profile data from the WYKO machine (section 4.3.1) of the Sericol white ink filled cell (120-34 mesh) is used to calculate the ink level percentage height of the mesh thickness; this individual point is plotted on the graph of Figure 4.44. The *y*-confidence limits represent the volume range of the ink introduced initially to the 120-34 mesh for the different ink types used. This was calculated previously in section 4.3.2 from the measured ink mass held initially in the mesh combined with the print volume, so is expressed as a thickness (equivalent to the maximum print thickness achievable if 100% ink transfer to the substrate occurred) – summarised in Table 4.2 for each ink. The *x*-confidence limits refer to the surface profile data of Figure 4.7: the lower limit corresponds to the lowest level of the ink surface; the upper limit corresponds to the approximated ink level generated if the ink surface could be levelled.



*Figure 4.44: Comparison of the amount of ink initially in the experimental mesh, represented as a thickness (equivalent to the maximum film thicknesses obtained assuming 100% ink transfer from the mesh to the substrate), with the mathematical models developed to incorporate partially filled cells.*

Figure 4.44 shows the dimensional maximum film thickness results calculated using models 4 and 5 for the partially filled 120-34 mesh. Model 4.3 results compare most closely with the experimental data point. The mesh thickness calculated by models 4.1, 4.2 and 5 predict greater thickness than the measured experimental mesh thickness (used in model 4.3), which results in significant over-calculation of the volume of initial ink in the mesh and therefore also thicker theoretical films than the experimental printed films encountered with 100% ink transfer from the mesh cells to the substrate.

Since the use of the provided manufacturers' thread data in models 4.1, 4.2 and 5 led to over-prediction of both the mesh thickness and of the initial ink in the mesh, the results can be reduced by essentially scaling the calculated mesh thickness (from each model) such that it is equal to the measured value. This adaptation of the models multiplies the corresponding original calculated non-dimensional maximum

thicknesses (expressed as a function of the percentage ink height) by the measured mesh thickness. The results of the adapted models, incorporating this scaling to match model with experimental mesh thicknesses are shown in Figure 4.45.

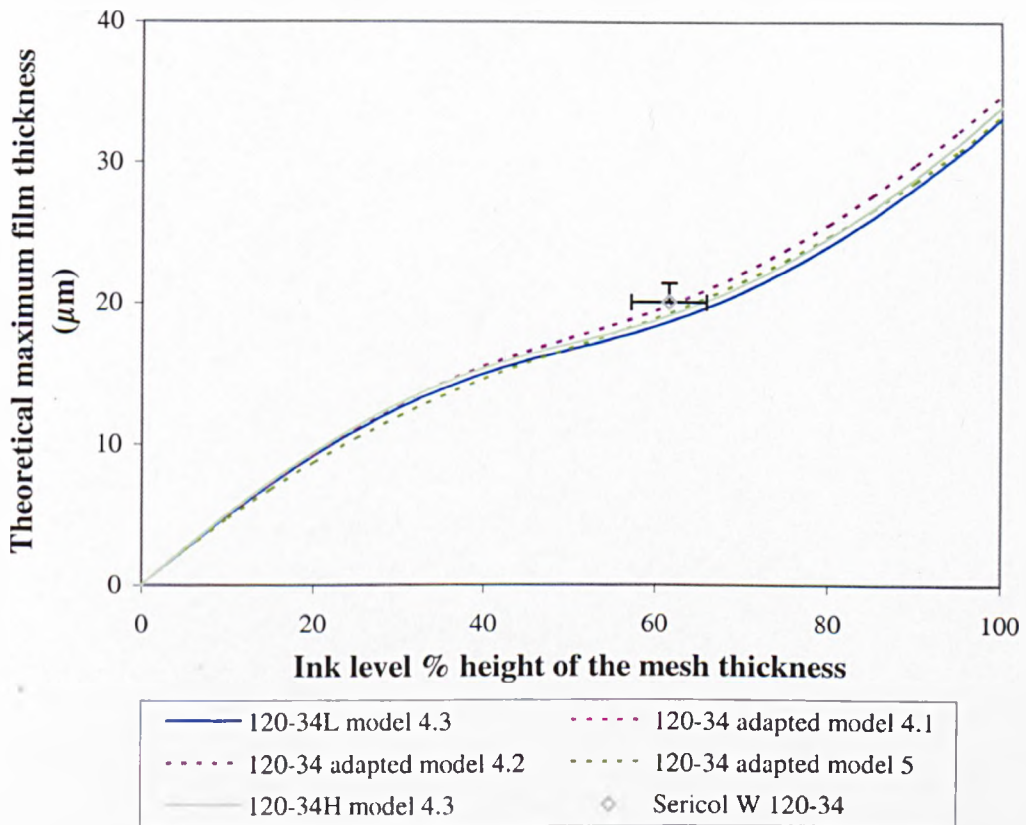


*Figure 4.45: Theoretical maximum film thickness results for incomplete mesh filling calculated from the adapted models 4 and 5 that limit the maximum mesh thickness to the measured experimental mesh thickness.*

This last stage calculation process not only reduces the theoretical maximum film thickness throughout the height of the mesh thickness, as shown in Figure 4.45, but also generates results that correspond well with the experimental data, and fall within the confidence limit range. Figure 4.45 also highlights a significant improvement in accuracy of these adapted models (4.1, 4.2 and 5) with model 4.3 results.

As previously suggested, these models may be used as a predictive tool for other mesh geometries not considered here. Mesh thickness is the most important parameter, as confirmed by the mesh thickness amendments of the adapted models resulting in



calculated data significantly closer to the experimental results. To a lesser extent the fine detail of the thread geometry within the mesh appears to have influence on the ink volume within the mesh. Therefore, model 4.3 (which uses the measured mesh thickness directly in the calculations) is not only most suitable at generating comparable results with experimental, but also uses a relatively simple mathematical method compared with the other models that consider ink filling level in the mesh to be a percentage of the mesh thickness.

### **Future model developments**

The geometry of model 5 can be further developed to consider threads of elliptical cross-section rather than circular, to more closely model the threads of the experimental meshes. However this development is not expected to significantly improve the accuracy generated from the existing adapted models 4.1, 4.2 and 5, and model 4.3. It would significantly complicate the mathematics involved in the problem.

Models 1-5 only consider the initial state of the ink filled mesh. A further development could fully predict the amount of fluid entering the mesh (through the inclusion of hydrodynamics etc.). Another possible extension is to model the printing stage by incorporating percentage ink transfers from the mesh cells.

## ITM and experimental results

Outputs from the ITM model are: the initial ink state in the mesh, the printed film thickness and the percentage fluid transfer to the substrate. Chapter 3 compared the experimental printed thicknesses with the equivalent ITM results, establishing that the ITM over-calculated the actual film thicknesses with most of the printed inks. The ITM model also over-predicted the film thicknesses when compared with all the fluids tested using the light screens.

The ITM model calculates the percentage fluid transfer for the specified mesh geometry. These calculated percentages are significantly lower than actual fluid transfers (not exceeding 41.6%, as shown in Table 4.12). Results in chapter 3 showed that printing different ink types led to a range of film thicknesses using a particular mesh whilst the ITM model calculates a single value. A range of percentage fluid transfers (for each mesh) is similarly observed in Table 4.12 with the experimental fluids, but not with the ITM model. The ITM model is good at explaining the printing process mechanism, but is not currently capable of capturing all the physics involved of the process.

	% transfer to substrate		
	90-40	120-34	150-31
Experimental range	62.0-76.4	57.7-72.7	55.1-73.6
ITM	38.8	39.8	41.6

*Table 4.12: Comparison of the experimental percentage fluid transfer with the calculated ITM value for equivalent meshes.*

The ITM model assumes the initial ink thickness in the mesh is equal to the maximum theoretical printed thickness, which is the same thickness model 1 calculates. Figure 4.43 showed that this initial ink thickness was considerably greater than experimentally filled meshes. The ITM model incorrectly assumes the 100% mesh filling condition (illustrated in Figure 4.46(a)), leading to the initial ink thickness also being too large. Figure 4.46(b) shows the ink height initially lowered within the mesh so that it is comparable with experimental observations. This adjustment to the initial

filled mesh state in the ITM model would result in the calculated film thicknesses being thinner since there is less ink within the mesh – therefore likely to improve the predictive results of the ITM.

The effect of lowering the initial ink level will also affect the percentage transferred to the substrate – this will increase, since the reduction of residual ink on the thread occurs from both the bulk zone and the region highlighted with the red dotted lines, as shown in Figure 4.46.

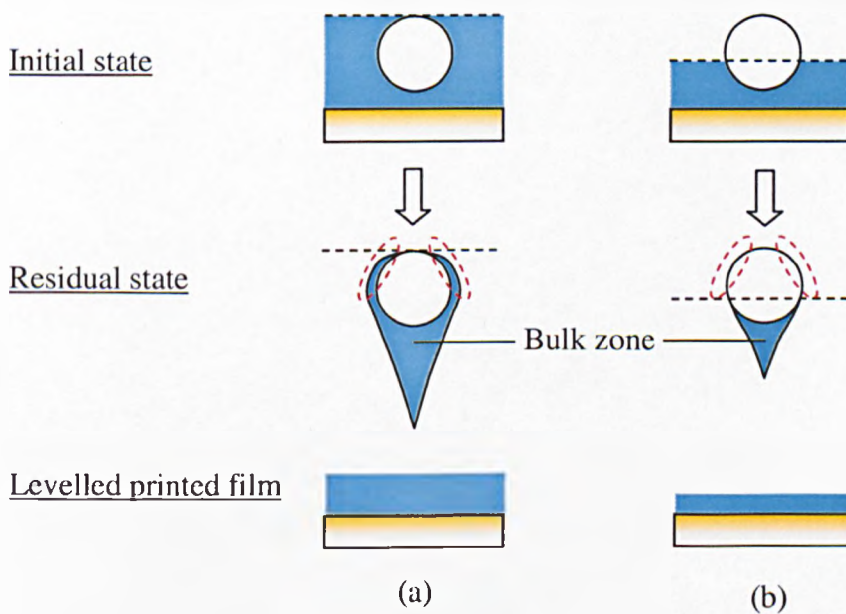


*Figure 4.46: Illustration of the effect of lowering the initial ink level: (a) 100% ink filled mesh; (b) initial ink level lowered comparable to experimental.*

## 4.7 Summary

The following conclusions are made from the work of this chapter:

- The volume of ink that initially fills the mesh is very similar for the ink types.
- “Closed” cells were observed forming only after printing, so ink transfer does occur through such cells. The location of “closed” cells varies and so is not a feature relating to the local thread of the mesh.
- The greatest percentage fluid transfers occurred for the Sericol group of inks and the R3 grease, where the menisci shape of the remaining ink in the mesh was square-like. Circular forming menisci significantly transfer lower percentages of fluid from the mesh.
- Viscosity has negligible effect on the film thickness or the fluid percentage transfer.
- The space (unoccupied by thread) within a screen mesh does not fully fill with ink after the metering squeegee stroke, as assumed previously by many models used in industry. This assumption has led to models 1-3 and the ITM greatly over-calculating the initial ink within meshes.
- The development of models 4 and 5 to include the concept of partially filled cells greatly improved the accuracy of the calculated initial ink within meshes compared with the experimental data. The development to the adapted models further increased the accuracy due to reduction of the overestimated mesh thickness to be equal to the measured mesh thickness. The adapted models 4.1, 4.2 and 5, and model 4.3 all generated results within the experimental confidence range. This improved accuracy is achieved at a sacrifice since it considerably complicates the mathematics of the problem from the original model 1.
- The models are all greatly sensitive to the thread diameter. The introduction of thread compression in model 2 highlights that the mesh thickness is the most dominant parameter influencing model sensitivity; confirmed as the dominating parameter also in model 3.

- Development of models to investigate partially filled cells highlights that an increase in mesh count reduces the direct proportionality between theoretical non-dimensional maximum thicknesses and the ink level percentage height of the mesh thickness. Model 5 is very sensitive to the thread diameter, particularly since the mesh thickness is equal to twice the thread diameter. The improvement of model accuracy, generated by scaling the overestimated mesh thickness ( $2D$ ) with measured mesh thickness data, to produce the adapted version of model 5 highlights that mesh thickness remains effectively the most dominant parameter influencing sensitivity.
- The ITM model predicts a significantly higher ink percentage remaining in meshes after printing than found experimentally. Despite this the ITM model still over-predicts the non-dimensional film thicknesses when compared with the experimental values, due to the difference between initial ink states of theory and experimental data.

## Chapter 5

# CFD study into the ink transfer process

---

### 5.1 Introduction

Previous observations in the experimental work of chapter 4, shows ink resides within the mesh after printing, particularly in the cell corners of the knuckle regions. This evidence highlights that mesh threads do interact with the ink transfer process. The existence of thread interaction forming an imprint on the surface of printed ink was not determined: due to unavoidable lateral movement incurred in the printing stage with the manually operated screen printing rig, and a lack of a mapping technique to relate the thread locations with the obtained print image.

Therefore the occurrence of ink peaking on the print surface – caused by the raising of the mesh threads in the peel-off stage, or the prevention of ink flow to the substrate – due to the threads occupancy of space and behaving as stencil material, remained undetermined experimentally (chapter 4). The experimental work by Fox, I., et al. (2003) indicates that there is an interaction between threads and the print surface (observed printing with halftones of 100% open regions). However, despite the existence of peaks and troughs on the printed surface (measured using interferometry), there is no identification of which of these surface features relates to the interaction from the thread.

Abbott, S. (2005, private communication) has provided the printed image (Figure 5.1(a)) and a second image of this print overlaid with the corresponding mesh and stencil (Figure 5.1(b)). Figure 5.1(a) shows that Abbott also observed peaks on the printed surface, identified by darker regions of the ink. A green dotted line is introduced to Abbott's image to highlight an apparently regular pattern of these peaks. The overlaid image of the print with corresponding mesh and stencil (Figure 5.1(b)), shows that in general the position of the peaks on the print relate with the location of the thread of the mesh. Markers are introduced to Abbott's image (Figure 5.1(b)) to correspond with the location of the peaks more clearly shown in Figure 5.1(a): green markers highlight the peaks that align with the mesh threads, and red markers are used if the alignment with threads is unclear. This raises the question as to whether this research fully answers the issue of an interaction in the ink transfer between the threads (in particular the knuckles of the threads) and the printed surface, but it does provide a good indication that the threads do create peaks on the print surface.

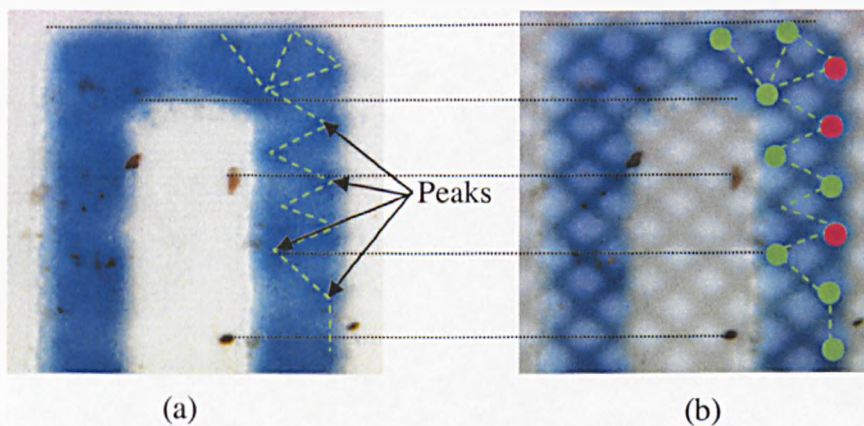


*Figure 5.1: (a) Image of the printed surface obtained printing Sericol UV speed blue ink through a 120-20 mesh. The darker regions in the print indicate a higher concentration of ink due to a local increase of film thickness i.e. peaks (Abbott, S. (2005, private communication)).*

*(b) Image (a) overlaid with the corresponding mesh image, aligned using the edges of the stencil (Abbott, S. (2005, private communication)).*

In this chapter, the process of screen printing is investigated using numerical simulations. Simulations have numerous advantages compared to purely obtaining

experimental data, particularly for printers in early stages of the design work. Developing simulations can save costs incurred for experimental “trial and error” data collection. They can provide a “feel” for how a certain setup will print without having to invest in equipment such as mesh fabric, tensioning to make the screen, and inks. Simulated results need to be validated to gain confidence of the accuracy, achievable by comparison with actual experimental data. Simulations therefore should be used as tools alongside experimental work. The experimental work of chapter 3 and 4 is used for comparison purposes.

Obtaining experimental images of the peel-off stage proved to be infeasible due to the inaccessibility of the region, and so obtaining numerical simulations assist the understanding of the printing process. This can be used to highlight potential sites in a print which may be more susceptible to fluctuations of surface level, such as peaking, in relation to mesh threads. Investigation into thread interaction could lead to improvements in mesh and stencil design – could also affect the ink design, since if the threads cause a peaked effect in the film this is almost certainly an unwanted feature for most printing designs (especially for electronic circuits) where a constant film thickness needs to be applied.

The aim of this work is to develop a simulation based upon the physics experienced in the screen printing process. The accuracy of the simulations is determined comparing with the experimental process, between the calculated and measured values of percentage ink transfer to the substrate (chapter 4) and the average film thickness applied to the substrate (chapters 3 and 4). The effect of the variables investigated experimentally is simulated: mesh geometry, fluid properties (viscosity, density), and peel-off rate. The effect of the following variables (not considered in the experimental work of the thesis) is also investigated in the simulations of this chapter: surface tension, contact angles, and initial ink height level within the mesh.



## 5.2 Computer simulation method

Computational fluid dynamics (CFD) is a simulated method used to calculate fluid behaviour, based upon the underlying physics. There are numerous CFD codes available, either commercial or tailored for specific fluid events. The robustness of the codes determines the reliability of the generated data. The suitability of the code is also selected considering the problem setup and running time costs. The potential savings to gain good data for a fluid problem through simulations as opposed to experiments makes the tool attractive particularly for industrial usage. As highlighted previously though, the calculated data needs to be validated experimentally.

In this chapter, the commercial code FLOW3D was made available for the simulations. The separation of the thread and substrate, for an ink filled mesh, is investigated to simulate the situation of ink transferring from mesh to substrate as experienced in the print stage of screen printing.

### 5.2.1 FLOW3D software

FLOW3D is commercially available CFD software, developed by Flow Science Inc. The fluid speciality of the simulations is of modelling free-surface behaviour. The software is available for multi-platform usage: either using a UNIX operating system or through X-windows, FLOW3D can be operated on a PC.

The Graphical User Interface (GUI) is the software display used to define the problem setup and enable overall control of the software operation. The GUI is used for the three operational stages of the software: pre-processing (defining the problem), solver (calculations performed), and post-processing (analysis of results). The main display (a basic button and tab display arrangement) of the GUI enables the user to quickly setup the problem, introducing obstacles, fluid properties, boundary conditions, and overlay a grid mesh. This generates a prepin file, which can be further edited by accessing the file directly using a text format to display the setup program file –

necessary for introducing less common variables not available directly with the button and tab display.

Initiation of the solver commences the calculations of the simulation defined by the prepin file. FLOW3D can continue to be operated whilst the solver is in use. This provides intermittent results generated from the solver to be accessed and analyzed without the requirement of completion of the full simulation run.

Post-processing of the calculated data is accessed using the GUI. The GUI allows multiple specific time frames and regions of the calculation zone (selection of co-ordinate limits in 1D, 2D or 3D is available) to graphically display the fluid behaviour. A mirror function is available for the 2D display, which reduces the overall size (CPU time) of a symmetrical problem since the pre-processing stage can consider the problem as a half problem and convert it into a full problem in the post-processing stage. The results are also available in a text format (ASCII) to export for further analysis into other software packages, such as Excel. Exporting the fluid fraction results, relating to corresponding grid cells, enables closer identification of the fluid behaviour. This simulated data can be analyzed to determine the percentage transfer and the average thickness of fluid on the substrate.

### **Meshing and obstacle geometry**

The grid meshing applied for FLOW3D calculations consists of rectangular cells; generation is achieved without requirement of conforming the grid with obstacle geometry, and therefore significantly reduces the time required to construct the overall mesh compared with other CFD packages that apply deformable grids to align with obstacles surfaces. For 3D problems the rectangular grid cells are extruded to generate cuboid cells. The number of cells is selected depending on the fineness required in the problem (to maintain good accuracy of generated data results) and the overall time required to complete the calculation run. Additional reference lines and points may be applied, throughout the mesh to align cell edges with; the use of as little of these as possible is recommended by the software to avoid over-specification of the mesh

arrangement, which may lead to significant variation of adjacent cell sizes – smooth changes are most suitable.

Simple obstacle region geometries (e.g. planes, cuboids, cylinders) are easily defined using the GUI. The geometry dimensions and positions within the calculation zone need to be set; Cartesian or cylindrical axis systems may be applied. More complex geometry can be imported into FLOW3D, generated using CAD packages including: IDEAS, stereolithography, or from topographic data sources. Combinations of obstacle regions (addition and subtraction of geometries) are used to form the solid obstacles required in the problem. Properties relating to the obstacles (such as enabling motion) are also set.

FLOW3D uses a fractional area/volume method (FAVOR) to define obstacle geometries within the rectangular grid – obstacle surfaces intersect through grid cells and therefore the two systems remain defined independently. Since the grid does not deform to align grid cells edges with obstacle surfaces, the fractional area (or volume value) of the grid cell that is unoccupied by the solid geometry (i.e. the fluid fraction) is used to represent obstacles. This provides great flexibility for varying the location or dimension of the obstacles, or the number of cells used to construct the grid, without consuming significant setup time.

Maintaining rectangular cells makes using the FAVOR method simple to apply and relatively easy to compute. The fractional areas and volumes for each cell unit at each time frame are stored as fractions of the original setup values of the problem. The FAVOR method does not sacrifice numerical accuracy, but significantly improves setup time of the grid construction.

### **Free surface modelling**

The interface between a liquid and gas is called a “free surface”. There are several methods used by CFD packages to model a free surface: Lagrangian grid, surface height, marker and cell (MAC), surface marker, and volume of fluid (VOF) – the latter

is applied in FLOW3D. The VOF method stores a single value per grid cell for each calculated flow variable, such as velocity and pressure (Flow Science Inc. (2005)). This procedure significantly reduces the CPU time required to complete calculations (Hirt, C. W. and Nichols, B. D. (1981)). The proportion of fluid (fluid fraction) in each grid cell, defined as a value between 0 (void) and 1 (full), is calculated for each time frame to generate the corresponding fluid location – local combination of adjacent cells provides information of meniscus location.

In 2- and 3-dimensional calculations, the exact meniscus location is not established with the VOF method. FLOW3D sacrifices sharp edge (meniscus) accuracy in favour of efficiency. This results in smearing of the edges, inherent from the averaging process used (Hirt, C. W. and Nichols, B. D. (1981)). This particularly becomes a greater issue for fine interfaces, such as thin liquid threads (Fawehinmi, O. B., et al. (2005)). For example, the graphical results (in section 5.3.2) indicate breakage, whereas analysis of the fluid fractions of each cell (using Excel) shows a fine liquid exists bridging the supposedly “broken” region. The amount of fluid within the bridge is insignificant and can be essentially neglected. Therefore whether breakage occurs in the simulations, or not, is unimportant for calculating the percentage transfer and average thickness applied to the substrate.

The calculations performed with FLOW3D apply a single phase approach, based upon conservation of momentum equations of the fluid (Fawehinmi, O. B., et al. (2005)). This enables an accurate method for predicting the fluid motion within the calculation zone. The solver applies an implicit approximation technique, enabling convergence rates to be attained without causing instability or the requirement of extremely small time-steps between calculations – the overall effect is that it reduces the CPU time significantly (Hirt, C. W. and Nichols, B. D. (1981), Fawehinmi, O. B., et al. (2005)). The calculations are accurate to a first order approximation method.

### 5.2.2 2D problem setup

The 2D problem greatly simplifies the geometry of screen printing meshes removing the woven structure and so considers threads essentially laid parallel; this simplification is similar to the ITM thread arrangement. The problem focuses on an individual mesh cell with thread remaining stationary as the substrate lowers, to simulate the peel-off stage of printing. The 2D setups investigate the problem as either a full mesh unit (FMU) or a half mesh unit (HMU); applying FLOW3D post-processing symmetry function converts half unit into a full mesh unit, further reducing CPU calculation time.

The simulation was adapted to investigate these screen printing variables: thread geometry, peel-off rate, initial fluid level and fluid properties (viscosity, surface tension, contact angle, density).

#### Geometry, boundaries and obstacles

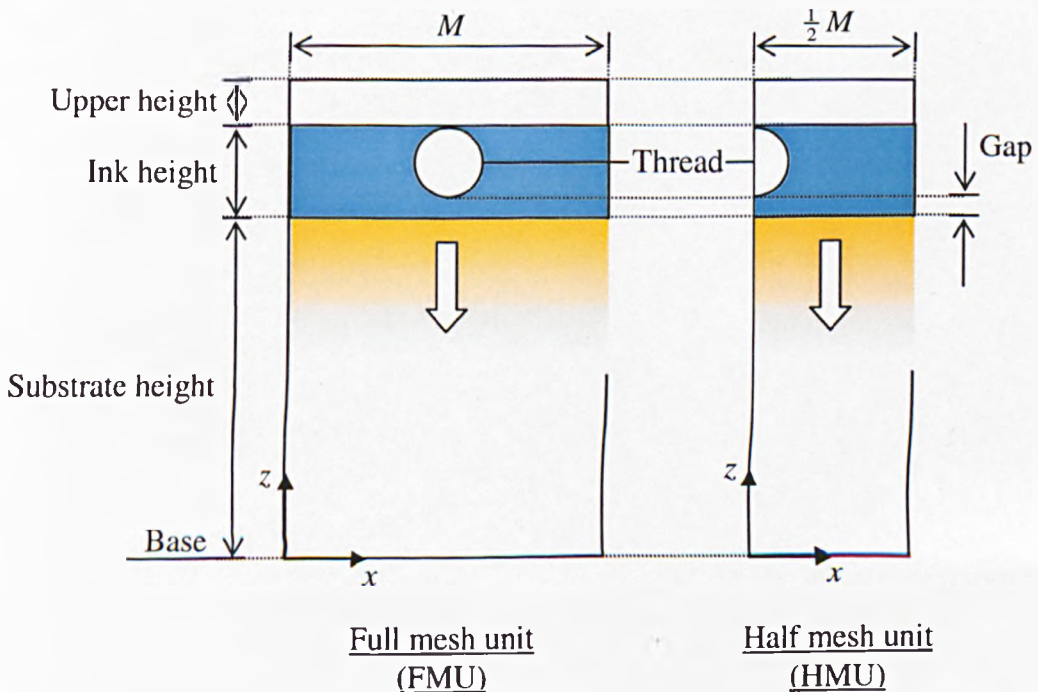


Figure 5.2: Arrangement of the geometries defined in the 2D problem using both a full mesh unit and a half mesh unit.

Figure 5.2 shows the initial location of two solid obstacles, representing the thread (stationary) and substrate (moving), within the calculation region. The thread obstacle is positioned centrally along the  $x$ -axis for FMU simulation, and centred at  $x = 0$  for HMU simulation. The cross-sectional dimensions of the thread obstacle are equivalent to manufacturers' data of threads used to construct screen printing meshes. The substrate is initially located at a height  $200\mu\text{m}$  above the base of the problem ( $z = 0$ ).

FLOW3D requires an initial gap of a height at least that of an individual mesh cell (defined later) to exist between the substrate and lowest thread point. Above the thread, a zone is used to introduce the existence of air into the problem – this is above the surface of the ink. Therefore the maximum height of the calculation region is set to  $250\mu\text{m}$ . To obtain a two dimensional problem, a single unit in the  $y$ -direction is applied. The calculation region dimensions for FMU are  $(0,0,0)$  to  $(M, 1, 250)\mu\text{m}$ , and  $(0,0,0)$  to  $(\frac{1}{2}M, 1, 250)\mu\text{m}$  for HMU.

The calculation region boundaries are defined as either symmetrical or rigid walls as shown in Figure 5.3. Symmetrical boundaries are applied to convert the individual screen mesh unit problem into an infinite problem of parallel threads. Rigid wall boundaries are primarily used to prevent in and out flow of fluid from the system.

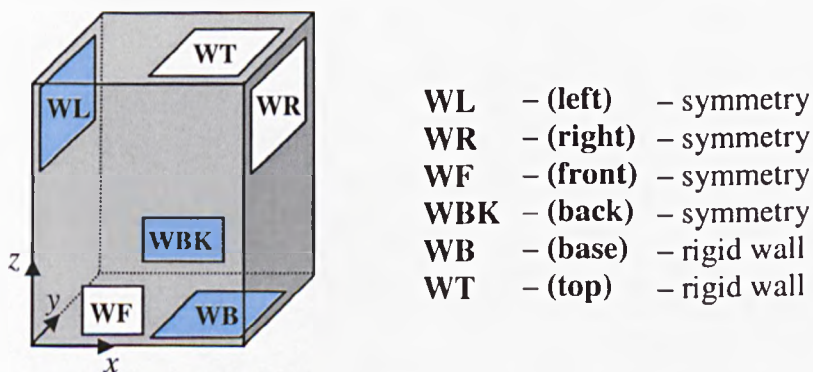


Figure 5.3: Diagram showing the boundary conditions and type.

The boundary types are set the same for both FMU and HMU simulations. The terms WL, WR, WF, WBK, WB, and WT (shown in Figure 5.3 above) are defined in the prepin file and relate to the specific boundary surfaces. Grid location point ( $p_x$  and  $p_z$

terms) are used within the prepin file dimensioning the calculation zone. The grid location points (essentially planes) are also used to align grid cell edges with the initial edge of the substrate.

## Meshing

Equally sized rectangular cells are positioned through the calculation zone. Two separate types of meshing are implemented, a relatively fine mesh and a coarser mesh to reduce CPU calculation time. Table 5.1 shows the number of cells used for the meshing arrangements.

Simulation type	Meshing	Number of cells			Dimension of the cell ( $\mu\text{m}$ )
		$x$	$y$	$z$	
FMU	Coarse	30	1	60	$(\frac{1}{30} M) \times 1 \times 4.167$
HMU	Coarse	15	1	60	$(\frac{1}{2 \times 15} M) \times 1 \times 4.167$
HMU	Fine	56	1	250	$(\frac{1}{2 \times 56} M) \times 1 \times 1$

*Table 5.1: Table of the number of cells in each  $x$ ,  $y$ ,  $z$  direction for the simulations run.*

Since the substrate and lowest thread part must be separated by the height ( $z$  length) of at least one cell, the initial gap is set to  $5\mu\text{m}$ .

## Calculation time settings

The nominal time step of the calculations is set to  $1 \times 10^{-5}$ s and the minimum time step is set to  $1 \times 10^{-7}$ s. Although increasing the minimum time step decreases the overall CPU calculation time required to solve the simulation, it tends to result in divergence of solution with stability not satisfied. Therefore these settings were accepted as a suitable optimum for enabling the calculations to be performed within a reasonable time.

The time length for the overall simulation is set to 0.150s. The available restart and output data is generated at 0.001s intervals.

## Variables

The effect that the thread geometry (the thread diameter and spacing) has on the separation behaviour was investigated. The manufacturers' geometry of previously used experimental meshes (90-40, 120-34, 150-31) was applied to the simulations to compare with the experimental behaviour of chapter 4. Thread spacing of a mesh unit was also investigated maintaining constant thread diameter: 110-34 and 150-34. Table 5.2 shows the values of thread diameter and thread spacing,  $M$ , applied for each simulated thread geometry.

Thread description	Thread diameter, $D$ ( $\mu\text{m}$ )	Thread spacing, $M$ ( $\mu\text{m}$ )
90-40	40	111.11
110-34	34	90.90
120-34	34	83.33
150-31	31	66.67
150-34	34	66.67

*Table 5.2: Thread diameter and spacing used in the calculations.*

FLOW3D enables the fluid properties (density, viscosity, surface tension and contact angle) to be varied. An initial setup using a typical screen ink, Sericol cyan (chapters 3 and 4), was chosen setting the fluid properties as: density, previously measured as  $1226.1\text{kgm}^{-3}$  (section 2.7.2); viscosity of  $4.9\text{Pa}\cdot\text{s}$  (section 3.2); surface tension approximated to be  $0.030\text{Nm}^{-1}$ ; and contact angles with the thread and substrate to be  $15^\circ$  and  $45^\circ$  respectively. The simulated fluid is assumed to be Newtonian.

In addition to solving this base case, each of the fluid properties (density, viscosity, surface tension and contact angle) were systematically altered, with the other parameters held at the initial setup values. This procedure enabled the effects, on the



deposited film thicknesses, of each fluid property to be investigated individually. The ranges of the fluid properties solved for are shown in Table 5.3 below.

Fluid property	Range
Density	500-2000kgm <sup>-3</sup>
Viscosity	0.001-100Pa.s
Surface tension	0.0035-0.15Nm <sup>-1</sup>
Thread contact angle	15-165°
Substrate contact angle	15-165°

Table 5.3: The ranges of solved fluid properties.

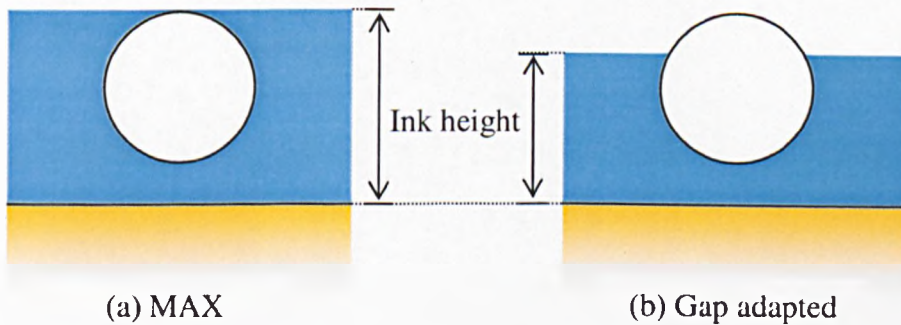


Figure 5.4: Initial ink height levels: (a) fills to the maximum thread height with the gap; (b) fluid volume is set filling to the thread peak with no gap, then the gap is introduced causing the ink height to be lower than the maximum height of the initial placement of the thread.

Two initial states were used to investigate the initial filled scenario. Figure 5.4 depicts the initial filling levels of the ink: one level achieving 100% coating of the thread, the second with 100% filling of mesh space. Figure 5.4(a) shows fluid above the substrate surface to the top of the thread, this filling type is referred to as MAX filling. Due to the initial gap between thread and substrate, MAX filling overestimates the fluid within an individual mesh unit, but coats the thread surface fully.

The overestimation of the ink in MAX filling situation resulted in a second “gap adapted” filling state being considered (Figure 5.4(b)). The fluid in the gap at the base of the thread was subtracted from the top of the fluid. Consequently the volume is correct for a unit cell.

Table 5.4 shows the calculated initial filling levels for both MAX and gap adapted filling.

Mesh	MAX filling ink level ( $\mu\text{m}$ )*	Gap adapted filling ink level ( $\mu\text{m}$ )*
90-40	245.0	238.91
110-34	239.0	232.74
120-34	239.0	232.57
150-31	236.0	229.14
150-34	239.0	231.96

\* Initial ink level = initial substrate height + ink height, where initial substrate height is  $200\mu\text{m}$

*Table 5.4: Initial ink levels for MAX and gap adapted filling.*

The speed that the substrate was lowered at was varied to correspond with the 10 peel-off rates investigated in chapter 3. (The rates for the 10 motor speeds were measured in section 2.2.3; an additional rate faster than the motor limit was also investigated to extend the range.) The acceleration that occurred between peel-off at the back and front of the vacuum platform is incorporated into the simulations. A gravitational term is also included in the simulation calculations acting in the direction of substrate motion. As the simulation time increases the substrate lowers to the base of the calculation region, mimicking peel-off.

### **The solver**

The solver is activated after completion of the problem setup. It is post-processed and analyzed to determine the effect of the variables on the process. The fluid fraction data is used to determine the percentage fluid transfer to the substrate and film

thickness on it using data calculated at the final time frame. The results from the 2D problems are included in section 5.3.1.

### 5.2.3 3D problem setup

As for the 2D problems described previously in section 5.2.2, the 3D problem is of a simplified screen printing mesh accomplished through removal of the woven structure of the thread (as shown in Figure 5.5). The problem is a progression from the general 2D model. The threads are represented by cylinders and like the 2D examples they remain stationary obstacles, whilst a plane lowers to simulate the peel-off stage of the substrate from the threads.

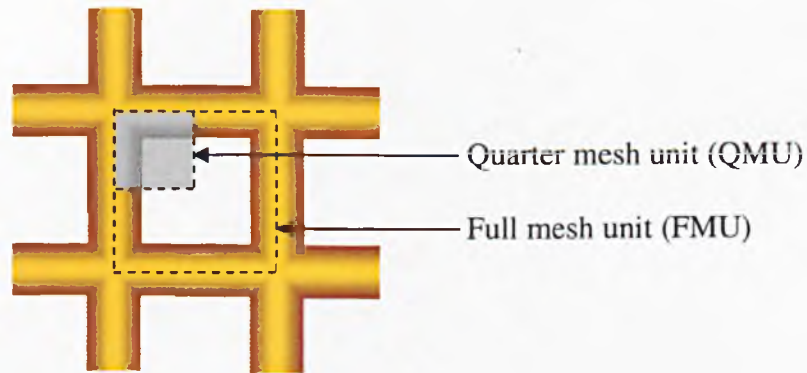


*Figure 5.5: Diagram of the simplified joins used in the 3D problem to replace true woven structure of screen printing meshes.*

To investigate the 3D problem, the calculations are performed on a quarter mesh unit (QMU), as highlighted in Figure 5.5, to reduce CPU time.

## Geometry, boundaries and obstacles

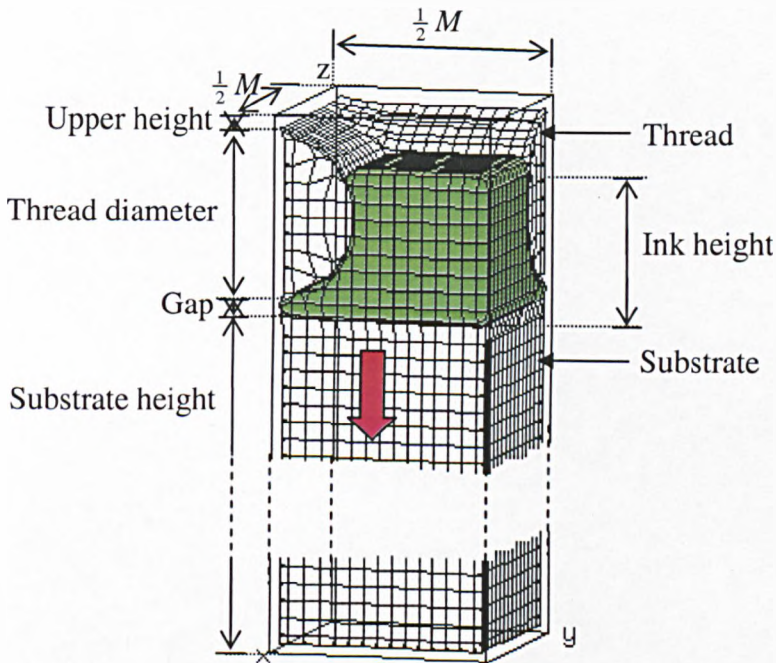


Figure 5.6: Initial setup of the thread and substrate geometry in a quarter mesh unit (QMU).

Figure 5.6 shows the general design of the QMU model. The threads are represented by two interlocking perpendicular cylinders, rotated and translated so only half of each is within the calculation region (therefore shapes used are actually two semi-circular prisms). Each is defined as a separate region, and combined together to represent a single obstacle which remains stationary throughout the simulation. The screen mesh modelled using the 3D QMU simulation is 90-40; therefore each cylinder section diameter is set to  $40\mu\text{m}$ , with a length equivalent to half a mesh unit ( $55.56\mu\text{m}$ ).

The second obstacle consists of one region defined to represent the lowering substrate. The obstacle is initially located at a height of  $200\mu\text{m}$  above the base (same as the 2D setup), spanning the  $x$ - $y$  plane.

The gap required between the thread and substrate obstacles within the 2D simulations, is still necessary for the 3D problem. The calculation region of the simulation is adapted from the 2D simulations to progress into the  $y$ -direction. The

defined dimensions for simulating 90-40 screen mesh using QMU is therefore (0,0,0) to (55.56, 55.56, 250) $\mu\text{m}$ .

The calculation region boundaries are kept the same as previously defined in Figure 5.3 of the 2D simulations.

## Meshing

The meshing applied through the calculation region consists of cuboid cells, developed from the 2D HMU coarse mesh cells, to extend into the  $y$ -dimension. The dimension and number of cells used for the QMU simulation are shown in Table 5.5. The  $x$  and  $z$  dimensions are the same as the 2D HMU coarse mesh setup.

Simulation type	Meshing	Number of cells			Dimension of the cell ( $\mu\text{m}$ )
		$x$	$y$	$z$	
QMU	Coarse	15	15	60	$\left(\frac{1}{\sqrt{2 \times 15}} M\right) \times \left(\frac{1}{\sqrt{2 \times 15}} M\right) \times 4.167$ $= 3.704 \times 3.704 \times 4.167$

*Table 5.5: Table of the number of cells in each  $x$ ,  $y$ ,  $z$  direction for the quarter mesh unit simulation run.*

The initial gap required between thread base and substrate is set to  $5\mu\text{m}$ , the same as 2D simulations.

## Calculation time interval

The time settings and overall simulation time length are maintained the same as the 2D simulations.

## Variables

The effect of the variables studied with the 2D problems is not investigated with the 3D problem setup due to the significant increase of time required to complete the calculations of a simulation. Consequently only one setup is designed for 3D simulation.

The thread geometry is based upon the 90-40 screen mesh. The fluid properties are set as those of the Sericol cyan ink (density of  $1226.1\text{kgm}^{-3}$ , viscosity of  $4.9\text{Pa}\cdot\text{s}$ , surface tension of  $0.030\text{Nm}^{-1}$ , and contact angles with the thread and substrate to be  $15^\circ$  and  $45^\circ$  respectively). The simulated fluid is Newtonian, like the 2D cases.

The initial fluid filling level was set the same as the gap adapted level applied for 2D simulations. Due to the change in geometries involved between 2D and 3D, the initial ink level is  $237.24\mu\text{m}$  above the base of the problem for the 3D case (initial substrate height remaining at  $200\mu\text{m}$ , with ink height  $37.24\mu\text{m}$ ).

The peel-off rate is based upon one motor speed setting: 7.0. The equivalent range of substrate speed during the 0.15s calculation time of the simulation is  $(6.0444-6.4050)\times 10^{-3}\text{ms}^{-1}$ .

The gravitational term applied in 2D simulations is applied for the 3D situation.

## The solver

The solver is activated after completion of the 3D problem setup. The calculated data can be assessed, post-processed and analyzed using the same procedure as described previously with the 2D simulations. The results for the 3D problem are included in section 5.3.3.

### 5.3 FLOW3D results and discussion

This section contains the calculated results for the 2D and 3D problems using FLOW3D. The CPU time to calculate the 2D problems was between 4-9 hours, whereas the 3D problem required significantly greater time to complete taking approximately 10 days. The calculations were done on a 32bit 2.4GHz Pentium processor using a Linux operating system.

Post-processing of the calculated results was partially done using FLOW3D. The software graphically displays the results at selected time frames and at desired planes in 1D, 2D or 3D. The mirror feature (for 2D problems) enables the results to be reflected horizontally, converting the half mesh unit (HMU) results into an equivalent full mesh unit.

The software stores the calculated results of each cell in an ASCII format, which may be accessed and converted via an "awk" command (within the unix shell) to separate the column text structure into a tab form. This tab separated file format enabled the fluid fractions of each cell (at specific time frames) to be imported into Excel for further analysis. Identification of fluid breakage is achieved using Excel, highlighted by a complete row of cells containing fluid fractions of 0, positioned between thread and substrate locations. If no row contains purely 0's then Excel is used to locate the thinnest section of the fluid, which indicates the most likely place breakage would occur. Fluid below this level is therefore expected to transfer to the substrate, and above resides attached to the thread.

The volume transferred is determined by summing the individual cell volumes multiplied by corresponding fluid fractions. The average film thickness is established by dividing this transferred volume by  $\frac{1}{2}M$  (for 2D HMU results),  $M$  (for 2D FMU results), or  $\frac{1}{4}M^2$  (for 3D QMU). The percentage transfer for each problem is calculated by combining the transfer volume with the initial fluid volume.

### 5.3.1 2D problem transfer and average thickness results

Two types of boundary dimensions were investigated: FMU and HMU. A summary of the results modelling a 90-40 screen mesh are shown in Table 5.6. There is very little difference between FMU and HMU, and similarly there is a relatively small difference between the results of coarse and fine meshing. Therefore to conserve CPU calculation time, the remaining 2D problems were solved using coarse meshing with HMU boundary setup (which was solved significantly faster than the other two setups).

Simulation	Meshing	Approx CPU time (hrs)	Average film thickness ( $\mu\text{m}$ )	Percentage transfer (%)
FMU	Coarse	8-9	21.7	75.7
HMU	Coarse	4	21.5	75.0
HMU	Fine	>60	21.3	74.1

*Table 5.6: Summary of FMU and HMU results, with coarse and fine meshing. The setup models 90-40 screen mesh, Sericol cyan ink fluid properties filled initially to the gap adapted level, with the substrate lowered at speed equivalent to motor setting 7.0 of the experimental rig used in chapter 3.*



### Thread geometry

The thread geometry and spacing within the screen mesh is observed to affect both the average film thickness and percentage transferred to substrate using the HMU simulations, as shown in Table 5.7.

Thread geometry	MAX filled initial ink level		Gap adapted filled initial ink level	
	Average film thickness ( $\mu\text{m}$ )	Percentage transferred (%)	Average film thickness ( $\mu\text{m}$ )	Percentage transferred (%)
90-40	24.4	72.3	21.5	75.0
110-34	20.7	71.4	18.1	75.5
120-34	19.4	69.2	17.0	73.5
150-31	16.6	67.3	13.7	69.8
150-34	16.6	65.4	13.4	65.8

*Table 5.7: Table of results for the simplified screen mesh geometries solved using the HMU simulation.*

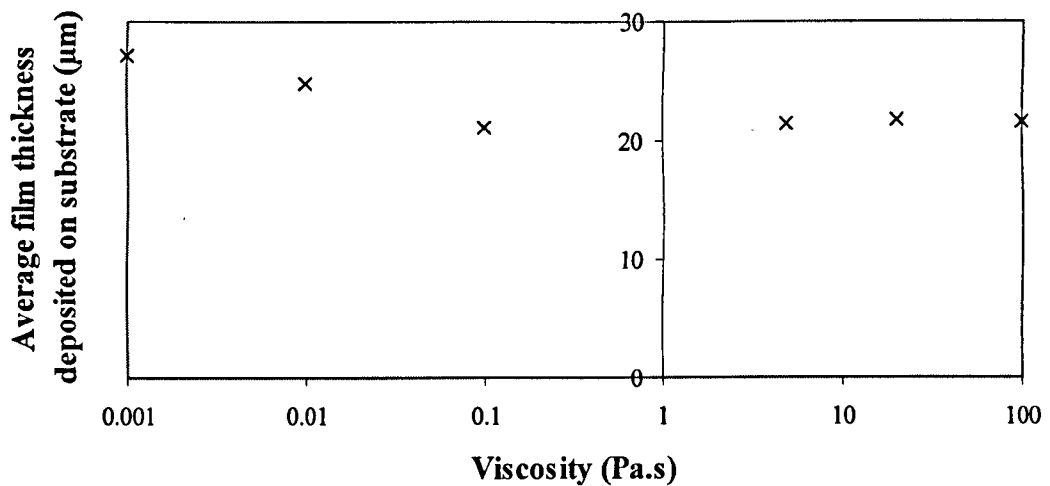
Regardless of which initial ink filling level was applied, increasing the thread spacing has the effect of increasing average film thickness and percentage transferred: high spacing between threads give larger initial ink volumes in the system; this in turn is more readily transferred to the substrate since there is less fluid drawn from the mesh by the thread surfaces in the separating process.

Initial filling to the level classified as MAX causes thicker simulated films to be printed than when applying the lower levels, adapted for the gap beneath the thread. However, the percentage transferred is less since the amount of thread surface initially covered is larger and more ink remains on the thread during the transfer process.

There is no direct relationship between the thread geometry and spacing with the resultant ink transfer or average film thickness.

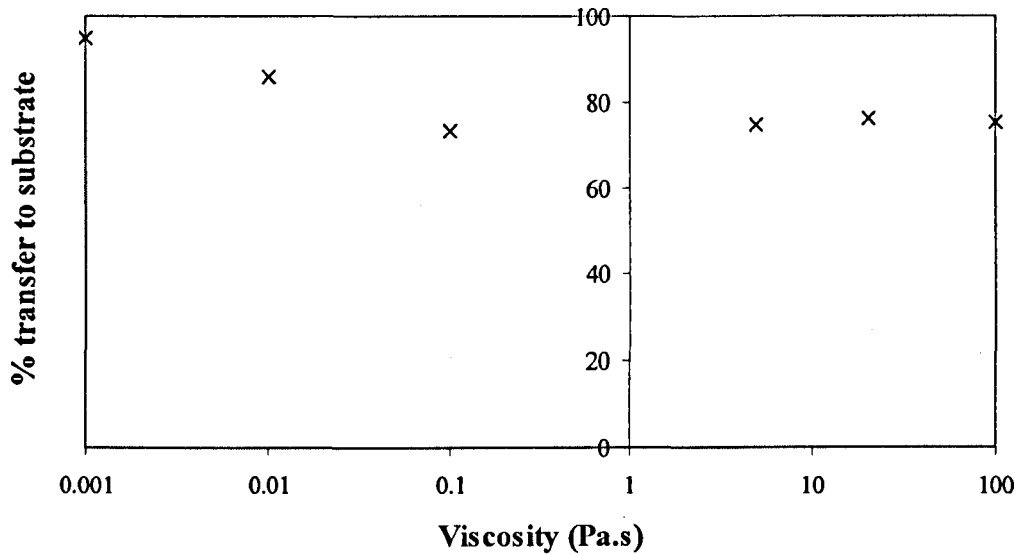
## Fluid properties

Figure 5.7 highlights that for the viscosity range 0.1-100Pa.s, the average film deposited is essentially constant ( $21.5 \pm 0.3 \mu\text{m}$ ), suggesting that viscosity is negligible in this range. The two simulations run at lower viscosities, however print thicker – in practice, such low viscosities (determined from glycerine dilutions observation in chapter 4) clearly exhibit drainage behaviour, making fluids such as these unsuitable for screen printing.



*Figure 5.7: The effect viscosity has on the simulated average film thickness deposit. Setup modelled 90-40 screen mesh, using Sericol cyan values of density, surface tension and contact angles, with a peel-off rate equivalent to motor setting 7.0. Initial filling level has been compensated for the gap.*

Since these simulations all contained the same initial ink volume, the percentage transferred to the substrate is shown (in Figure 5.8) to be greater for the lower viscosity setups (reaching 94.7% at viscosity of 0.001Pa.s). For the viscosity range 0.1-100Pa.s transfer to the substrate was  $74.9\pm 1.2\%$ .



*Figure 5.8: The effect viscosity has on the simulated percentage transfer to the substrate. The setup modelled is the same as that in Figure 5.7.*

Surface tension had little effect on either film thickness ( $21.6\pm 0.2\mu\text{m}$ ) or percentage transferred ( $75.1\pm 0.7\%$ ), as highlighted in Figure 5.9 and Figure 5.10.

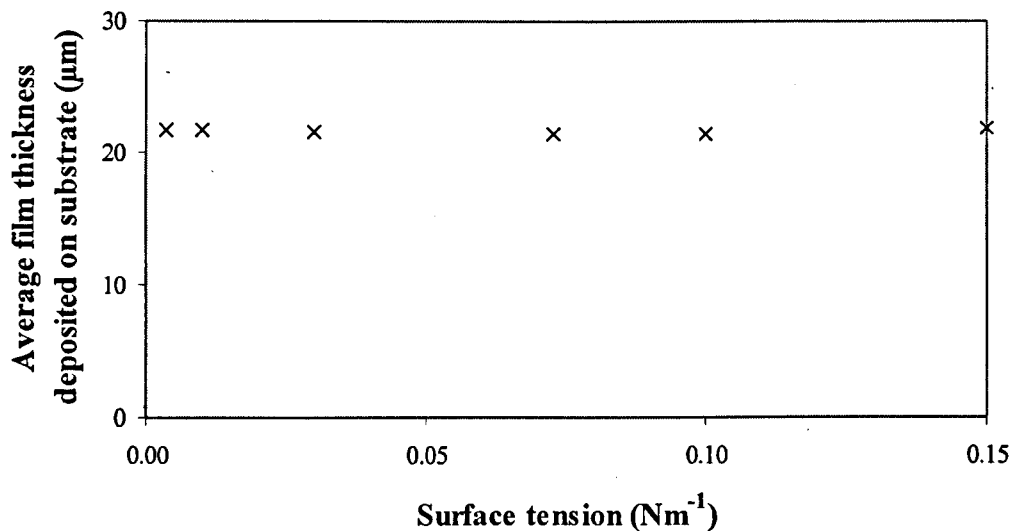


Figure 5.9: The effect surface tension has on the simulated average deposited film thickness. Setup modelled 90-40 screen mesh, using Sericol cyan values of density, viscosity and contact angles, with a peel-off rate equivalent to motor setting 7.0. Initial filling level was adapted for the gap.

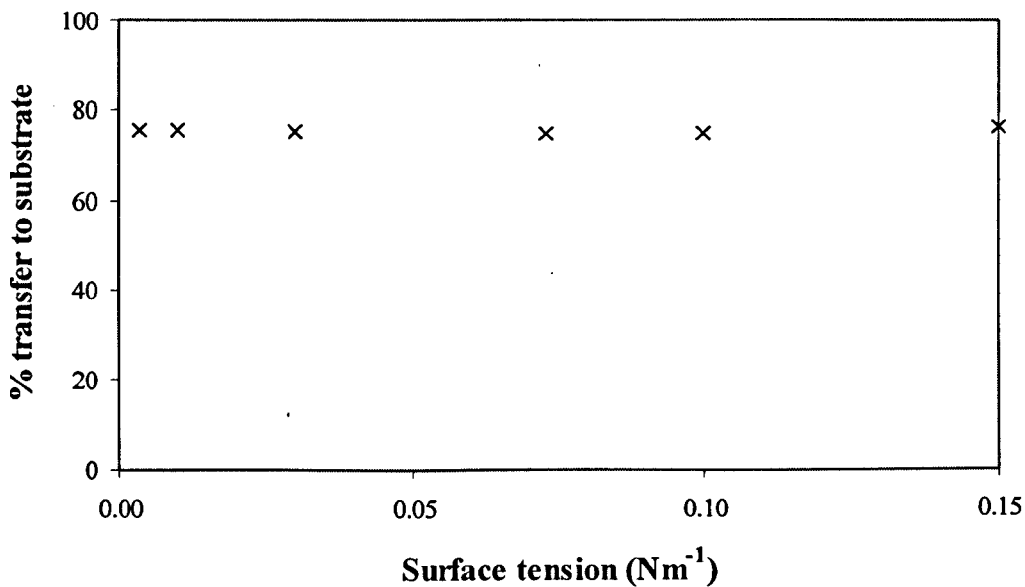
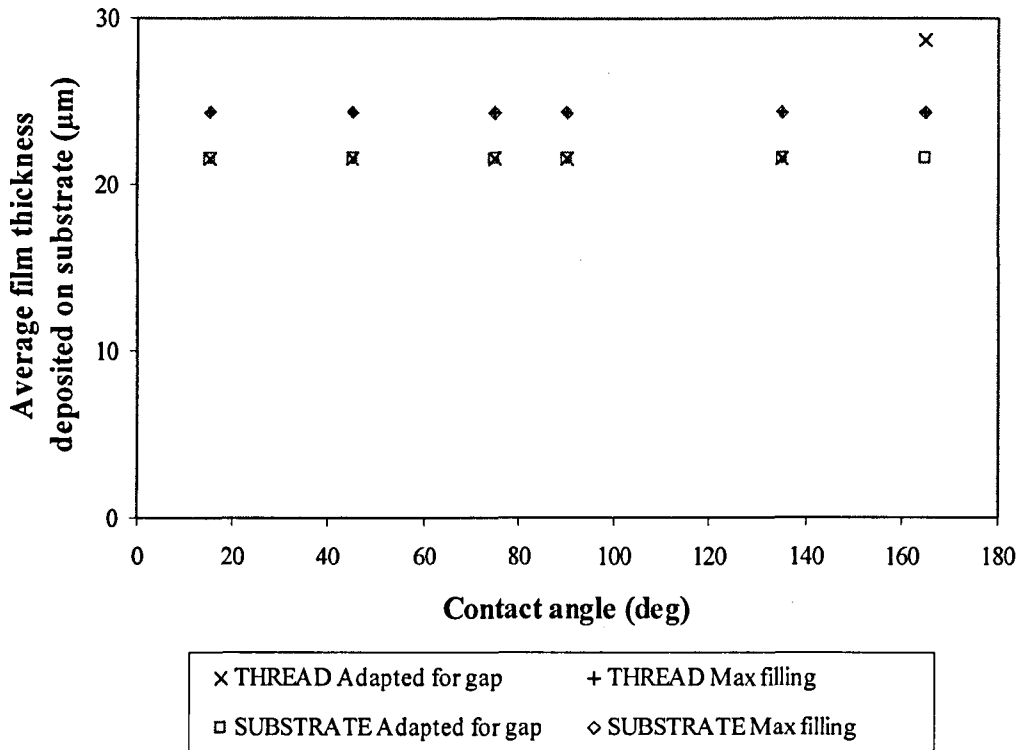


Figure 5.10: The effect surface tension has on the simulated percentage transfer to the substrate. The setup modelled is the same as that in Figure 5.9.

The influence of contact angle on either thread or substrate is also apparently negligible as suggested from the results shown in Figure 5.11 and Figure 5.12.



*Figure 5.11: The effect of the contact angle on the average film thickness for both gap adapted and maximum initial filling types. Setup modelled 90-40 screen mesh, using Sericol cyan values of density, viscosity, surface tension and contact angle (substrate contact angle maintained at 45° while thread contact angle is varied – labelled as THREAD in the key, and thread contact angle remaining constant at 15° for variation of substrate contact angle – labelled as SUBSTRATE in the key), with a peel-off rate equivalent to motor setting 7.0.*

Figure 5.11 highlights that the initial state of ink level filling has significantly greater dominating influence on the final average thickness of ink transferred than the contact angles experiencing both wetting and non-wetting setups. Setting the initial fluid level to gap adapted filling resulted in deposits of  $21.6 \pm 0.1 \mu\text{m}$  ( $\theta \leq 135^\circ$ ); raising the initial level to correspond with the maximum thread height increased the deposits to constant thicknesses of  $24.4 \mu\text{m}$ .

The contact angle was observed to affect transfer for the situation with less initial fluid in the system (i.e. applying adapted gap filling level rather than maximum filling) and thread contact angle behaving with strong non-wetting character ( $\theta=165^\circ$ ). The thread repels the ink resulting in thicker deposit to the substrate. Figure 5.12 confirms this is due to the maximum transfer of 100% being achieved, which is significantly greater than the other contact angle transfers of  $75.2\pm 0.2\%$  (gap adapted filling) and 72.3% (maximum filling).

Conversely for highly non-wetting substrates, the repelling action of the substrate may not oppose transfer with an effect of thinner average film deposits but may instead hinder fluid levelling due to a tendency of the fluid to form ball-like droplets on the substrate surface. However, neither a reduction of film deposit or droplet formations were observed in the simulations due to a lack of fluid edge existing on the substrate surface: the fluid is initially defined coating the substrate as a continuous layer, repeated infinitely from one calculation zone to the next.

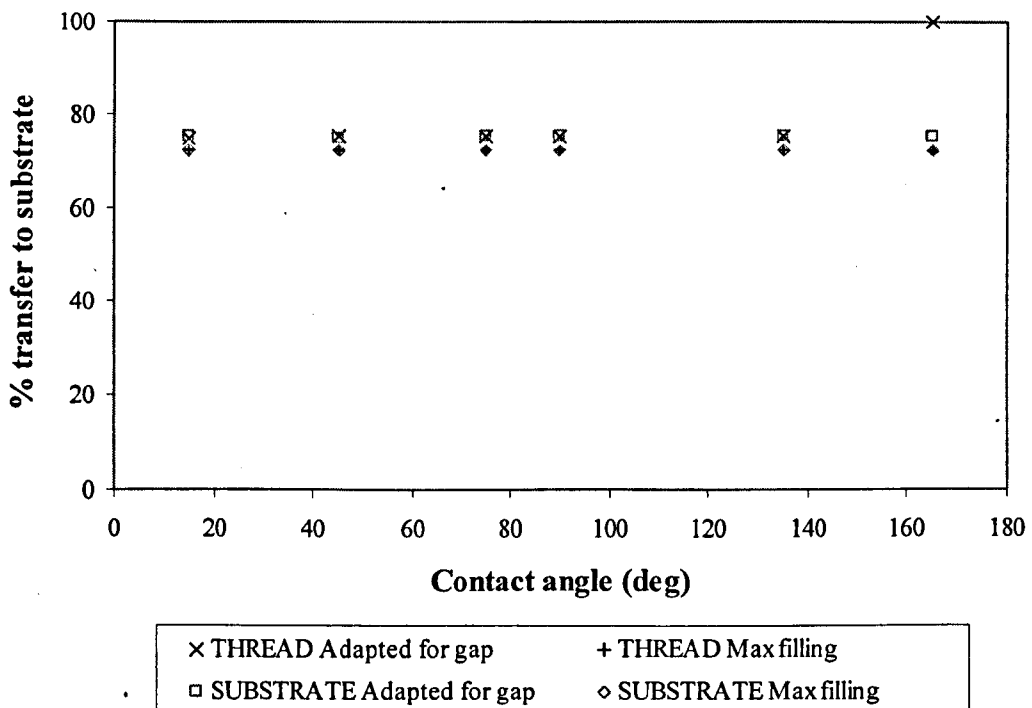


Figure 5.12: The effect of the contact angle on the percentage transfer for both gap adapted and maximum initial filling types. The setup modelled is the same as that in Figure 5.11.

Figure 5.13 and Figure 5.14 highlight fluid density had little effect on film thickness or percentage transferred, observing again that the initial filling level has a significantly greater effect: MAX filling resulting with transfers of  $24.1 \pm 0.2 \mu\text{m}$  and  $71.6 \pm 0.7\%$ , with gap adapted filling generating  $21.5 \pm 0.1 \mu\text{m}$  and  $75.1 \pm 0.3\%$  transfers.

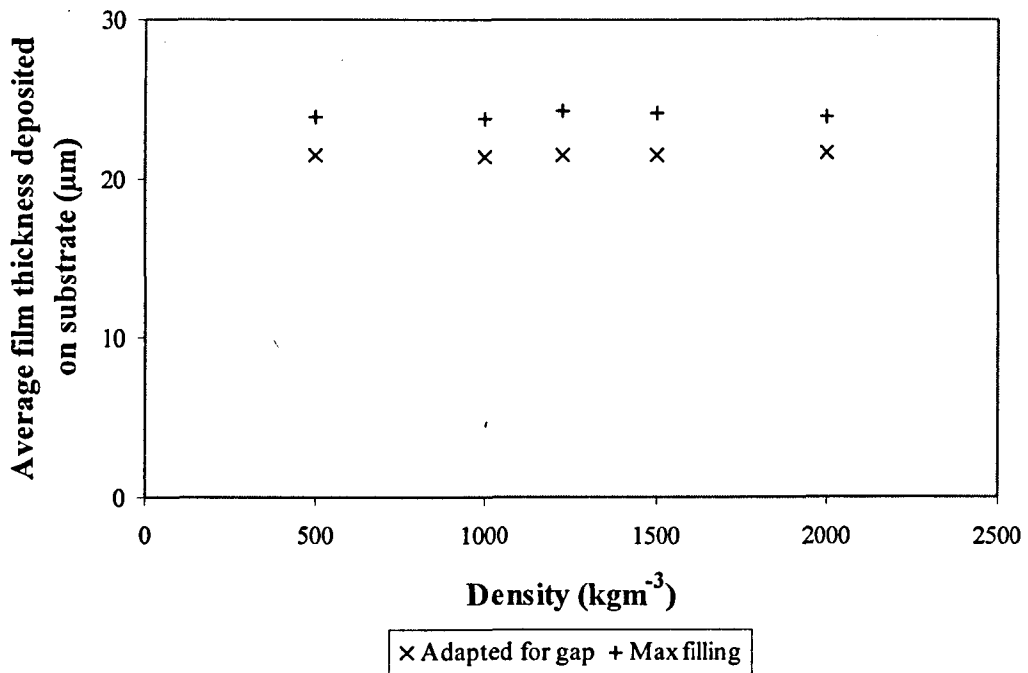
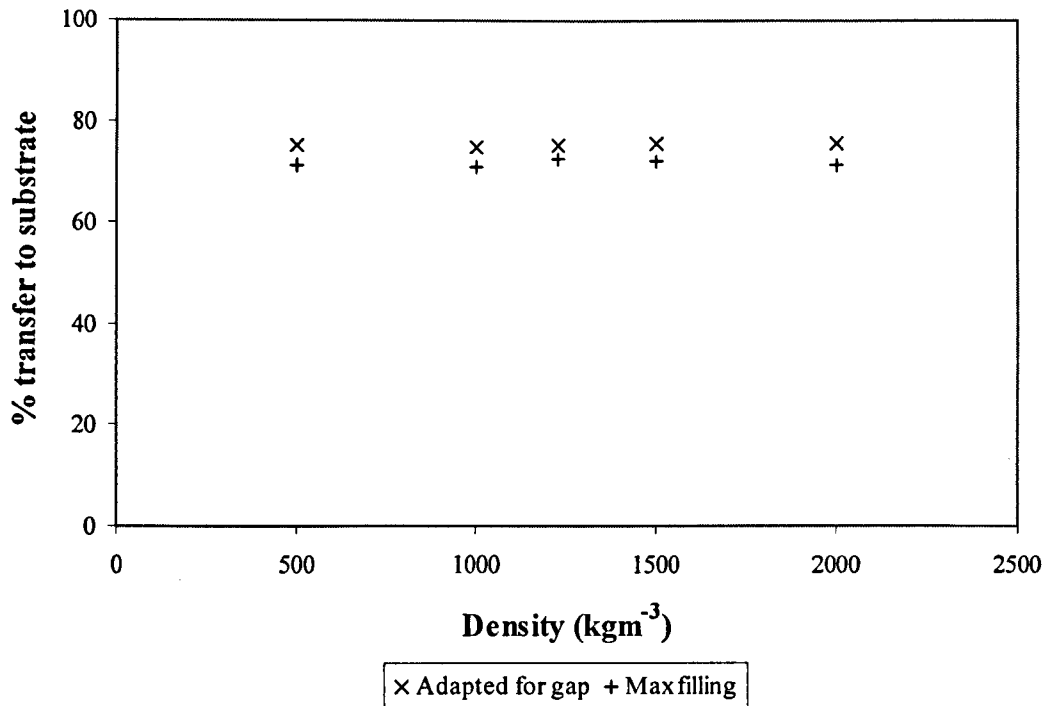


Figure 5.13: The effect fluid density has on the calculated average deposited film thickness for both gap adapted and maximum initial filling types. Setup modelled 90-40 screen mesh, using Sericol cyan values of viscosity, surface tension and contact angle, with a peel-off rate equivalent to motor setting 7.0.



*Figure 5.14: The effect density has on the percentage transfer for both gap adapted and maximum initial filling types. The setup modelled is the same as that in Figure 5.13.*



### Peel-off rate

Variation of the peel-off rate has negligible influence on deposited film thicknesses. Figure 5.15 highlights the constant average film deposit ( $21.6 \pm 0.1 \mu\text{m}$ ) generated from applying the initial adapted gap fluid level state. Setting the initial fluid level to the maximum thread height increases the observed range to  $\pm 0.6 \mu\text{m}$ , with slightly thicker deposits occurring under the conditions of slower peel-off rates.

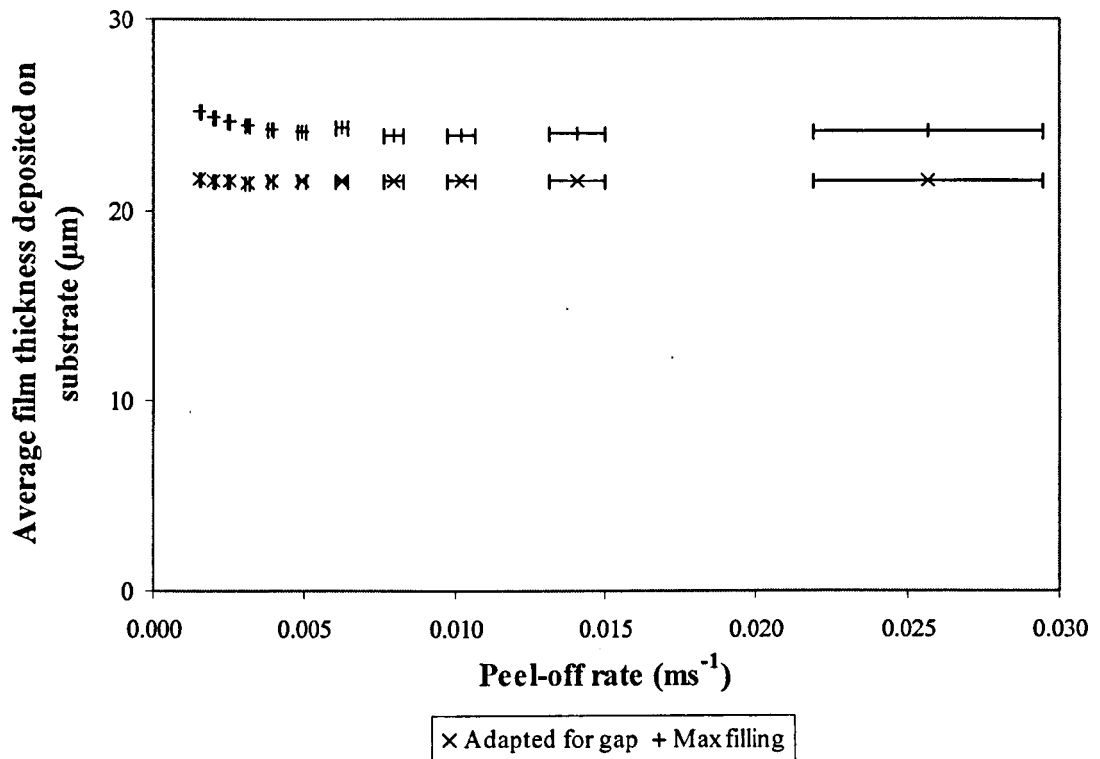


*Figure 5.15: Comparison of the peel-off rate and the calculated average film thickness for both gap adapted and maximum initial filling types. Setup modelled 90-40 screen mesh, using Sericol cyan fluid property values. Confidence limits depict the peel-off rate increase equivalent to experimental chapter 3 observations for time range 0-0.15s.*

Figure 5.16 highlights the similar percentage transfers for both initial fluid levels. The gap adapted level setup generated more consistent transfers of  $75.1 \pm 0.4\%$ , independent to the peel-off rate. The maximum fluid level setup resulted with transfers of  $73.0 \pm 1.9\%$ .

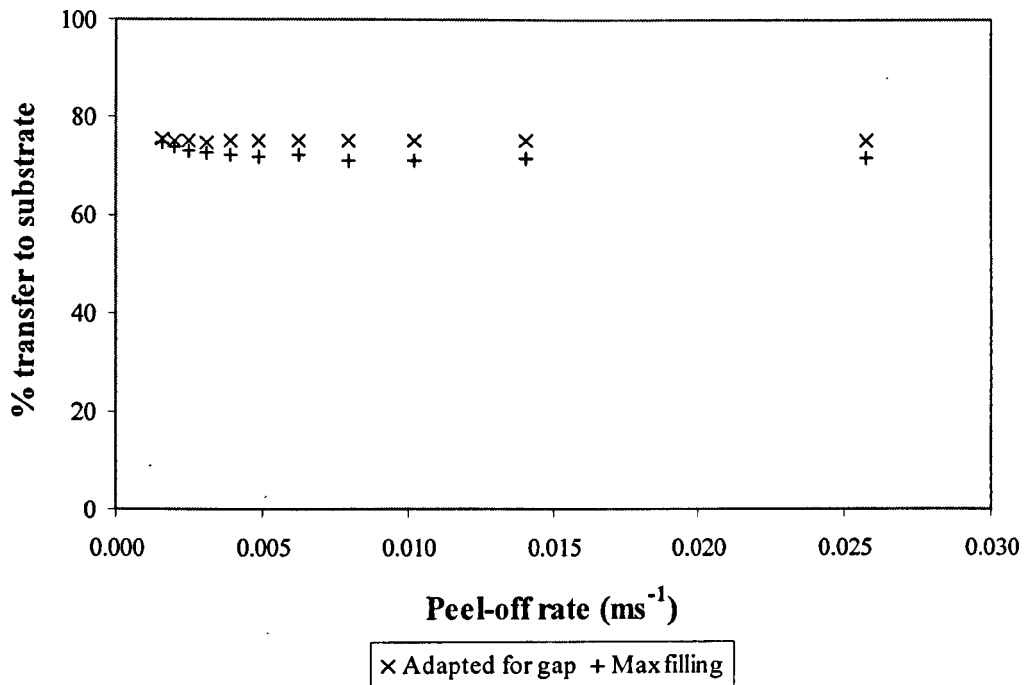
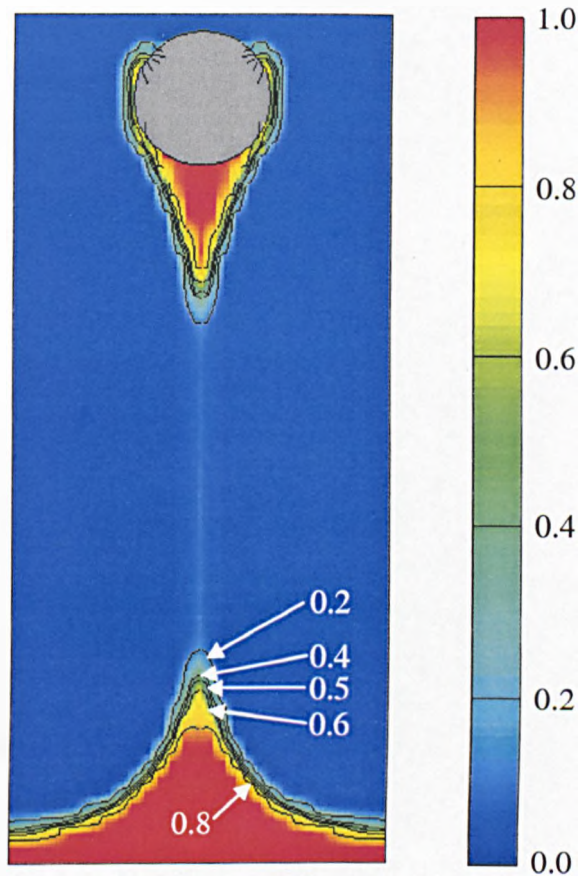


Figure 5.16: Graph showing the effect the peel-off rate has on the percentage transfer for both gap adapted and maximum initial filling types. The setup modelled is the same as that in Figure 5.15. Peel-off rate confidence limits are omitted for clarity.

### 5.3.2 2D simulation results graphically displayed with FLOW3D



*Figure 5.17: Image representing the fluid fractions between 0 and 1 in the calculation zone – indicated on the key. The contours for the lower section are labelled with the corresponding fractions.*

Figure 5.17 is an example image that corresponds with the final time of a 2D HMU simulation run (equivalent for  $t=0.150s$  for the simulation setup used in Figure 5.18). The colour shading and series of contours display the fluid fractions between 0 (void) and 1 (full). The contours are used to show the approximate location of the fluid meniscus, of which there is little variation particularly in the fluid fraction range  $0.5 \pm 0.1$ . Deviation of the contour position highlights the meniscus smearing.

The following results graphically display the  $z$ -velocity of the ink within the calculation zone. The meniscus position is highlighted in each image. Due to smearing of the interface (depicted in Figure 5.17), the meniscus is shown as a contour

through cells having a fluid fraction of 0.5 (as also recommended by Flow Science Inc. (2005)). A typical example of a half mesh unit model result is included for both initial gap adapted and MAX filling levels.

Figure 5.18 consists of a series of images from the HMU gap adapted simulations, graphically displaying the ink transfer through the simplified screen mesh. The ink remains in contact with both thread and substrate throughout the peel-off process. As the substrate lowers the formation of an elongated strand is produced. The images between 0.025s and 0.150s show separation between ink connected to the thread and ink on the substrate. However the separation presented in this figure does not indicate a breakage of ink, which is confirmed in Figure 5.17 where a fine bridge of fluid maintains a connection between the thread and substrate – the fluid fraction in this region is significantly less than 0.2, and hence is low.

Despite a lack of strand breakage, the key feature of the simulation is the generated peak directly below the thread on the film of the substrate (at 0.150s). The simulation also indicates that a thin layer of ink remains surrounding the thread, with significantly higher proportional remaining hanging from the base of the thread.

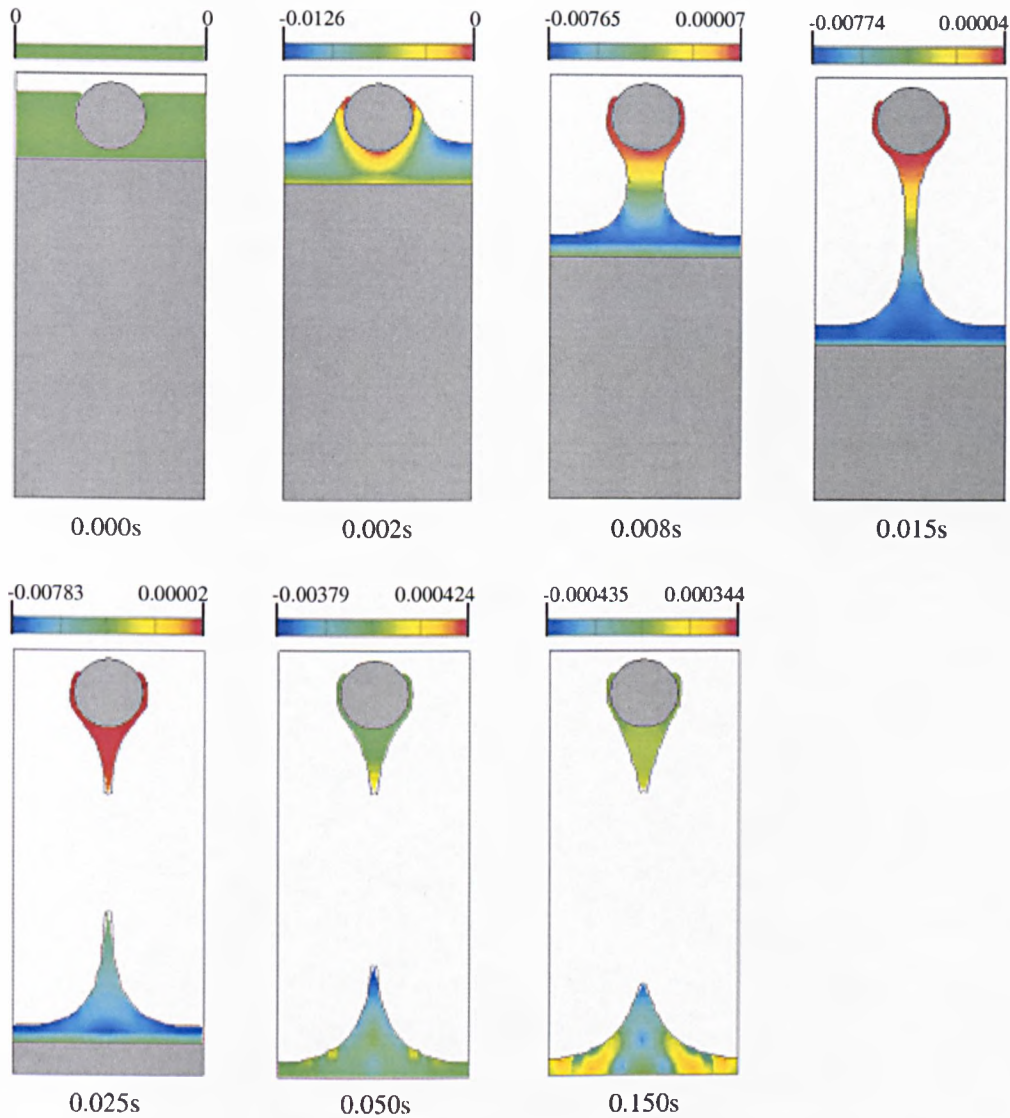
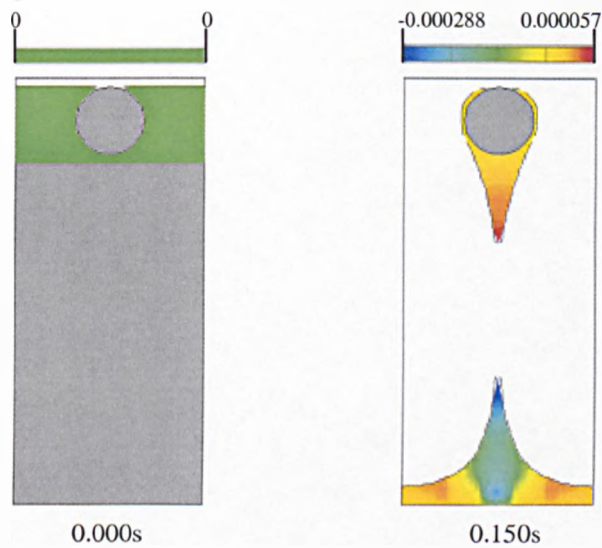


Figure 5.18: FLOW3D simulations graphically displaying a series of images of the 2D HMU problem, mirrored forming a full mesh unit. The colour coding represents  $z$ -velocity ( $\text{ms}^{-1}$ ) of each calculation cell, each simulation time having an individual key as shown. Problem setup: 90-40 screen mesh, using Sericol cyan fluid property values, with peel-off rate equivalent to motor setting 7.0. Initial filling level was adapted for the gap.

The initial fluid level setup of the Figure 5.18 image series was filled to the gap adapted level. Modifying the initial level to apply MAX filling generates the initial and final images shown in Figure 5.19. These images are essentially the same as those for adapted gap filling, but have greater amount of ink within the simulation. The thin layer of ink surrounding the thread, with unbroken elongated strand bridging the thread and substrate remain common features between both initial filling levels.



*Figure 5.19: Graphical display of the initial and end results for the same setup as Figure 5.18, but with MAX initial filling.*

### 5.3.3 3D problem results

With the 3D problem, for a 90-40 mesh, the percentage transfer to substrate was 60.6%, depositing an average film thickness of  $12.6\mu\text{m}$  for this geometry.

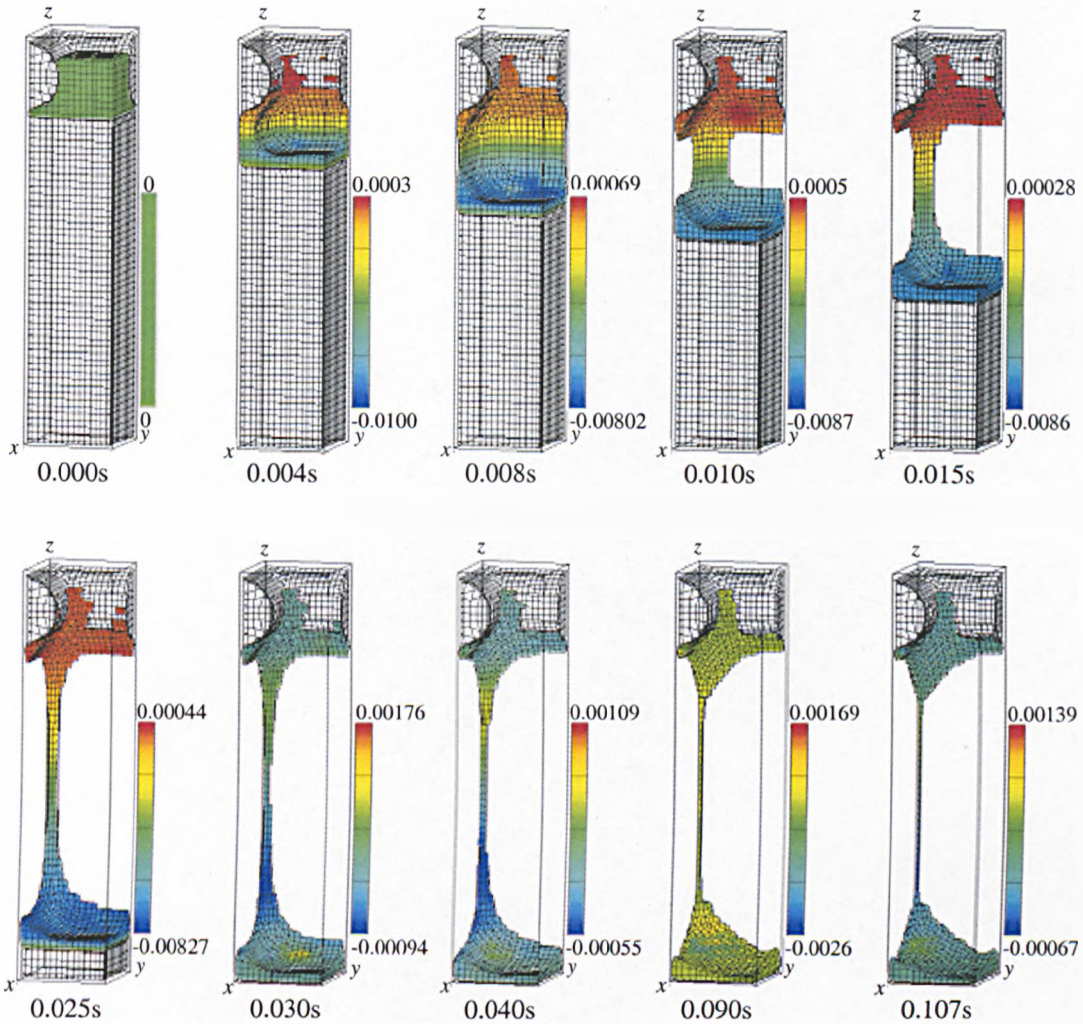


*Figure 5.20: FLOW3D simulations graphically displayed of the 3D problem for an idealised 90-40 mesh. Colour coding is the same as used in Figure 5.18.*

Figure 5.20 is a series of graphical displays representing the simulated ink transfer through the simplified screen mesh quarter unit. The features of the 3D simulation are very similar to those of the 2D simulations. This is shown by comparing the slice at  $y_{\text{max}}$  in the  $x$ - $z$  plane, and at  $x_{\text{max}}$  in the  $y$ - $z$  plane with the 2D simulations. The initial elongation of strand for all three of these cases behaves apparently the same with the lowering of the substrate. At 0.008s in Figure 5.20 the image shows the film

ruptures and the edges of the strands move inwards, to form the filament clearly seen in the 0.010s image. This is another similarity with the graphical display of the 2D simulations, confirmed through analyzing individual cell fluid fraction data. Performing this analysis on the data results of  $y_{max}$  in the  $x$ - $z$  plane, and  $x_{max}$  in the  $y$ - $z$  plane highlights a lack of breakage between the strand connecting thread and substrate. This was done for the final simulation time (0.107s). The fluid fractions of the cells at these extremities are very low, indicating the presence of the strand thickness being significantly less than the thickness of the cell ( $3.704\mu\text{m}$ ).

Figure 5.20 clearly shows how ink is pulled from the centre of the mesh opening, and that the film is thickest on the substrate under the mesh knuckle. The 3D thread geometry at the inter-link between the two cylinders is responsible for providing a more stable location for the ink to adhere to as the opposing motion of substrate lowering is initiated. The geometry in this area accounts for the lower transfer rate observed for the 3D simulation compared to the 2D simulations.

There is a lack of ink maintained at the central opening of the screen mesh. This is apparent from Figure 5.20, confirmed by applying individual cell data analysis (cells develop with fluid fractions of zero) at locations of both  $x_{max}$  and  $y_{max}$ .



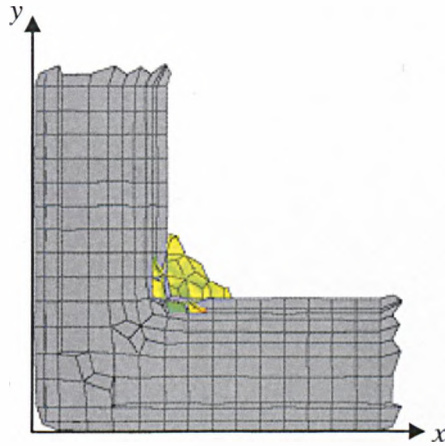


*Figure 5.21: QMU simulated view from above the threads ( $200 < z < 250 \mu\text{m}$ ) at  $0.107\text{s}$ .*

Figure 5.21 shows the 3D image of the simulation orientated to view from above, after the print has taken place. The view enables the presence of ink to be observed within the corner junction of the threads. Very little ink remains on the upper surface of the threads. This is similar to the post-print mesh photographic image results observed experimentally in chapter 4.

## 5.4 Comparison of simulated and experimental results

The initial gap between the thread and substrate obstacles of the simulations is a mathematical necessity to this problem and the results are not directly comparable to the experimental mesh where the knuckle initially touches the substrate. However, due to the woven structure of the experimental meshes, this contact is not sustained throughout the mesh; therefore the concept of a simulated gap is somewhat representative of the actual threads (excluding the knuckle sites).

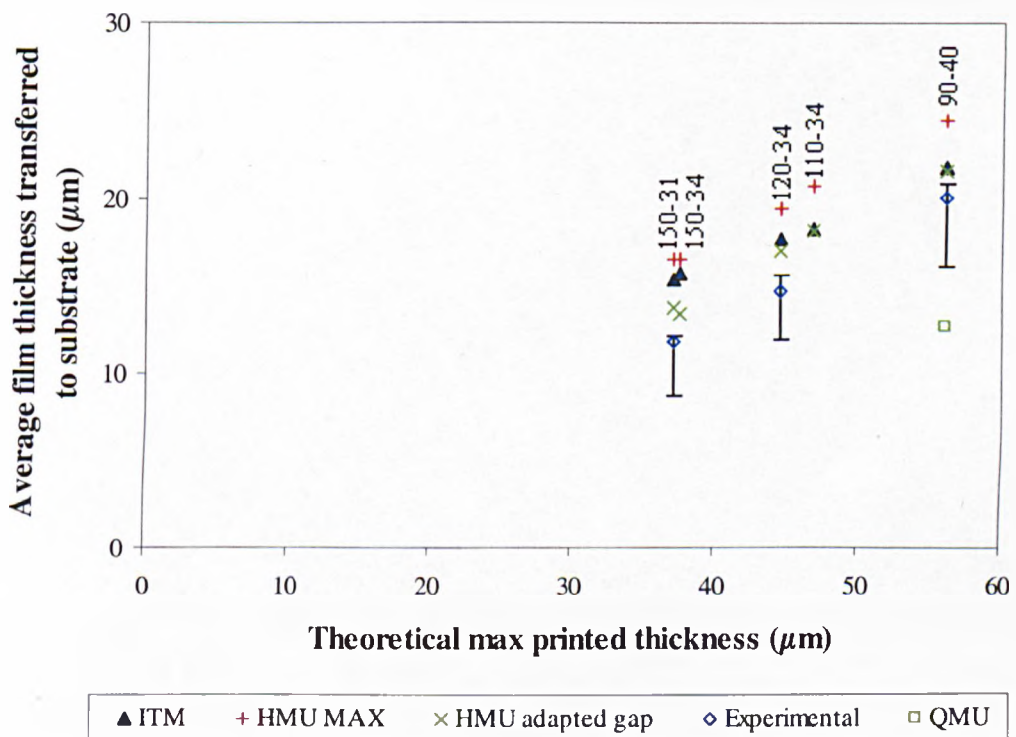


Figure 5.22: Average film thickness comparison of FLOW3D simulated results with equivalent experimental and ITM results of chapter 4.

Figures 5.22 and 5.23 compare the FLOW3D simulated results with the ITM and results from chapter 4 (Sericol cyan ink) for equivalent screen mesh geometries. The ITM was also used to model the two screen geometries also considered with FLOW3D that were not calculated previously: 110-34 and 150-34. The confidence limits relating to the experimental data points depict the printing range observed using the

other tested fluids. The theoretical maximum printed thickness is expressed from the screen mesh geometry (obtained with equation (4.8) in section 4.4.1) enabling meaningful comparison of results between experimental and simulated screens.

Figure 5.22 shows a comparison of the generated film thicknesses. The 3D model significantly under-predicts the average film thickness whilst the ITM and HMU gap adapted results agree well, both overestimate the experimental observations. Due to the greater amount of ink initially in the 2D MAX model, this calculates even thicker average film thicknesses significantly overestimating experimental results.

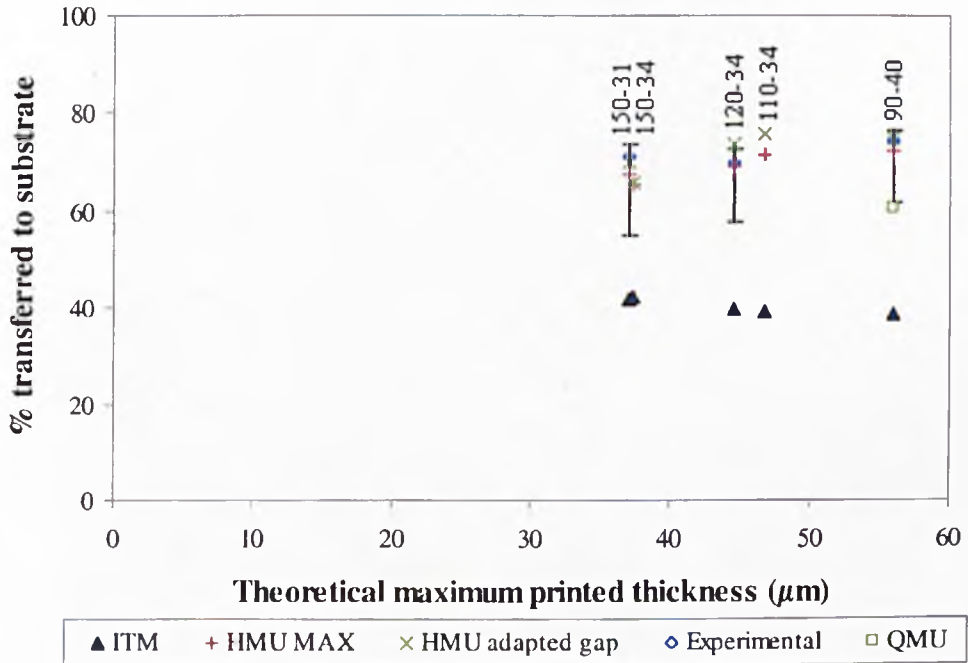
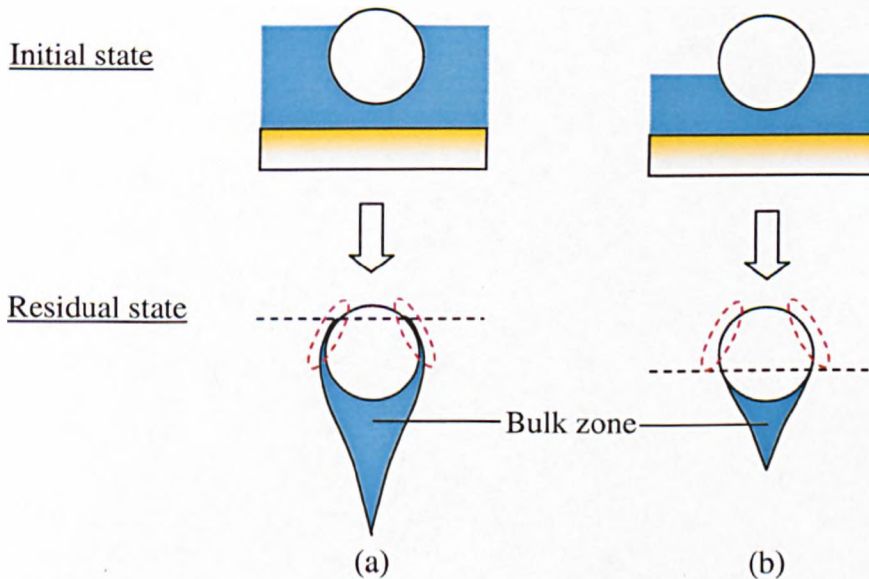


Figure 5.23: Percentage transfer comparison of FLOW3D simulated results with equivalent experimental and ITM results of chapter 4.

Figure 5.23 compares the percentage transfers. The ITM model estimates significantly lower percentage transfers than simulated and experimental. The 3D model also generates a low percentage transfer to the substrate but this compares well to the lowest percentage transfer obtained for a printing fluid in chapter 4, through equivalent mesh geometry (90-40).

Both 2D simulations relate well to the experimental results for Sericol cyan ink. This therefore indicates that the simulations are most accurate at describing the percentage transferred, rather than predicting the actual average film thicknesses. To improve the predictive accuracy of the simulations (HMU) the amount of ink in the system could be reduced; this amendment would also compare more faithfully with the experimental initial filled mesh state, which does not achieve 100% filling (noted in chapter 4). The percentage transferred will increase slightly (as reported when lowering the initial level from the MAX filling state to that of gap adapted level), since the reduction of residual ink on the thread occurs (as shown in Figure 5.24) from both the bulk zone and the thinner layer surrounding the thread – highlighted with the red dotted lines.



*Figure 5.24: Illustration of the effect of lowering the initial simulated ink level on the residual ink: (a) adapted gap initial level; (b) further reduction of initial ink to be comparable with experimental initial mesh filled state.*

Another possible extension of the simulation is to incorporate particles to more closely mimic printing fluids, which are densely populated with pigments and surfactants.

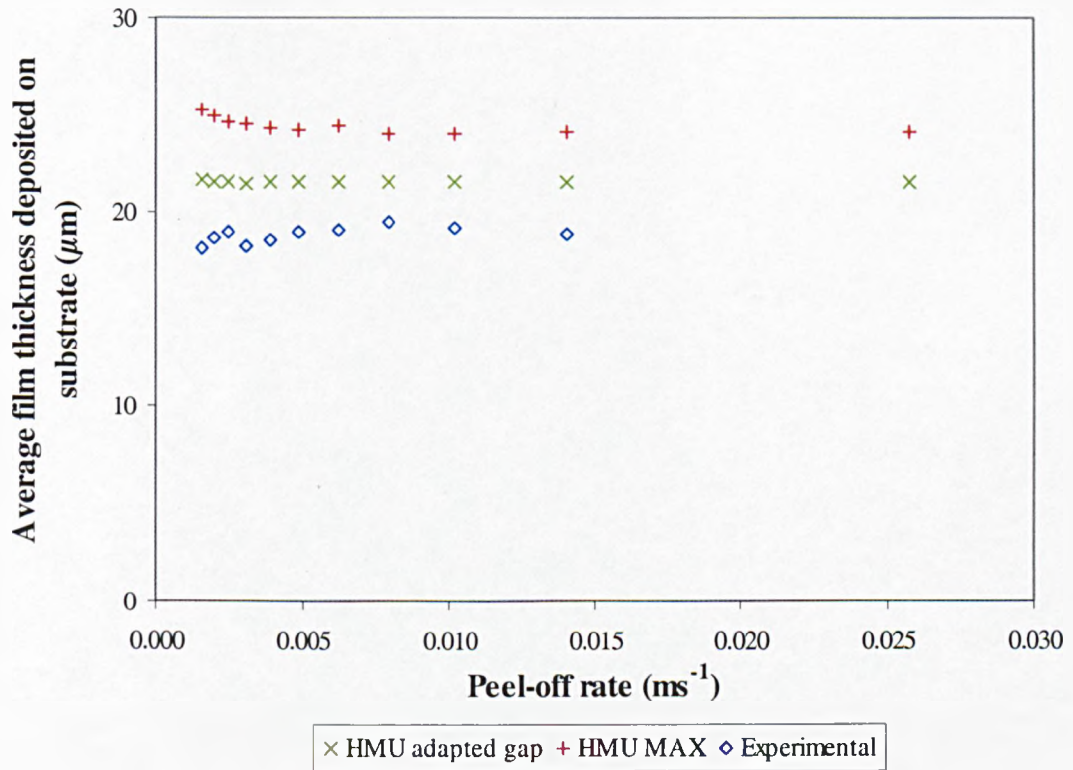


Figure 5.25: Average film thickness comparison of FLOW3D calculated results with equivalent experimental results (90-40) of chapter 3.

Figure 5.25 highlights that both simulated sets of data and the experimental results show little variation of the average film thickness for the investigated peel-off rates. The greatest variation occurs in the slower peel-off range for both the experimental Sericol cyan results (shown previously in chapter 3 and Appendix A2) and the 2D simulations. As noted previously from Figure 5.22, both initial filling levels applied in the simulations overestimate the experimental printed thicknesses.

## 5.5 Summary

These conclusions were made from the work of this chapter:

- The coarser mesh simulations generated comparable results to the significantly finer meshed simulation, without compromising accuracy.
- As observed in earlier chapters, both the thread diameter and spacing influences the final film thickness. Large spacing between threads introduces greater initial ink volume into the system and this results in more ink transferred to the substrate in the separating process.
- The initial filling level influences the transfer behaviour. MAX filling generated greater average film thicknesses, but slightly lower percentage transfers since more ink resided on the surface of the thread (due to the greater initial coverage of the MAX filling level, achieving complete coating of the thread).
- None of the investigated fluid properties (viscosity, surface tension, contact angle, density) had any significant effect on either the average printed thickness or the percentage transferred.
- 100% transfer was observed for highly non-wettable threads, which are not initially fully coated with fluid. Coating such threads fully enabled fluid to reside on the surface despite the repellent action introduced by the contact angle.
- The peel-off rate does not influence the transfer behaviour, and so is similar to the previous experimental finding of chapter 3 – simulations over-predict the average film thickness.
- The graphical simulated images highlight thread interaction occurring as the ink transfers to the substrate, creating a bridge between thread and substrate. This results with the printed surface containing peaks corresponding with the thread position. The 3D results (QMU) also produce the same behaviour at the knuckle (with the central opening of the screen mesh unit printing less thickly). The QMU simulation reveal a tendency for the ink to reside in the mesh at knuckle corners, the same as observed experimentally in chapter 4.

- The 2D HMU simulated setups generated most comparable results with the experimental data (chapter 4): adapted gap level closer approximation comparing to experimental work (both HMU methods over-calculate the average film thickness corresponding with actual screen printing meshes); MAX level compares particularly well regarding the percentage transfer.
- The QMU simulation results in under-prediction of both average transferred film thickness and the percentage transferred.

## Chapter 6

# Individual cell filling

---

### 6.1 Introduction

The cell filling process is an important stage in screen printing, and this has motivated the need for investigation of the fluid dynamics of the process. In this chapter, the fundamental behaviour of filling an aperture with fluid via blade application is considered. This knowledge is of importance for various processes including both screen and gravure printing. Little is known of the physical mechanisms involved in filling screen printing mesh cells with ink; investigations are difficult due to the small size of the cells and in gaining visual access of the cells.

The aim of the work in this chapter is to firstly design a specialised rig to perform experiments to visualise the filling behaviour. The complex screen printing process can initially be simplified to gain a general understanding of how cells fill. Using larger scale apertures than those found in screen meshes allows visual access to digitally record the events.

The geometry of the model cell (to be filled) is simplified as a single cylindrical hole, removing the complexity of woven threads – this greatly enhances visual access. The cylindrical shaped hole is used rather than a cuboid, since the typical cavity shape of a



pre-wetted screen mesh cell (observed in section 4.3.1 of chapter 4) contains residual ink supported in the corners forming a rounded open area.

Introducing an idealised aperture enables the filling of an individual basic cell to be studied as a closed system by preventing fluid moving between adjacent cells; unlike a woven meshed structure that provides numerous paths between cells where the thread does not block or seal such interaction. The cell is also idealised regarding the constraint of air flow: no air flow is allowed out at the cell base (due to the construction of cell walls and base formed from a single material block eliminating requirement of joins), and so models a perfect seal between the mesh and substrate.

This will help allow the mechanisms involved in replacing of air, with fluid, in the cell are observed. In particular, understanding how air is expelled is essential for printing techniques to avoid air remaining trapped within the cells, or ink layer, resulting in deterioration of print quality.

The results presented show the fundamental behaviour of fluid filling the idealised cells, allowing the influence of the following typical screen printing variables on how cells fill to be determined: blade angle, blade speed, gap between blade tip and surface, cell geometry, and fluid viscosity.

## 6.2 Design of the cell filling rig

This section details the design of the cell filling rig described previously in section 2.3. The design criterion was to enable experimental investigation of air displacement from a cell by liquid using a blade stroke.

The required rig functions were to:

- hold a test cell in position
- fill the test cell with a liquid by operation of a blade
- observe the filling procedure
- have a main frame structure for integrated component alignment

The system variables include: fluid type; blade angle and speed; gap between blade tip and surface of the test piece; and the cell geometry.

Figure 6.1 shows the alignment of rig components, constructed with IDEAS software – Appendix A3.6 includes a series of assembly drawings generating a gradual build-up of components located on the breadboard. The main rig sections are: a main unit; a test piece containing a cell; a blade drive unit; and an optical observation system.

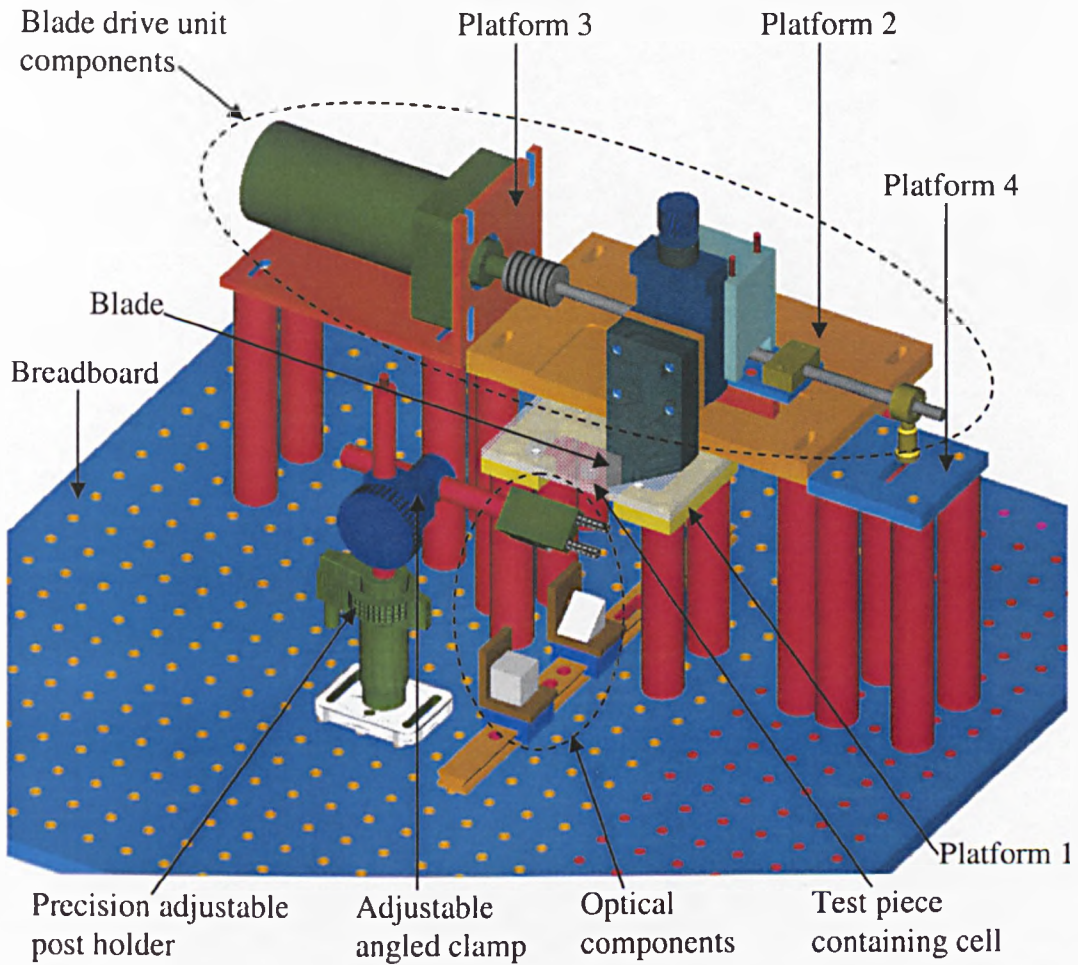


*Figure 6.1: 3D image of the cell filling rig designed with IDEAS software.*

### 6.2.1 Design of the main unit

The principle purpose of the main unit is to provide alignment, support and attachment locations for the other rig components. The base of the main unit is a 600×600mm aluminium breadboard with a matrix of equally spaced (25mm centred) tapped holes.

This allows great flexibility for approximate location sites (in the horizontal planes). Accurate alignment is achieved with equipment including rails, sliding components, slot holes etc. For vertical alignment, the supporting platform thicknesses' and the lengths of the support stands (connecting platforms with the breadboard) are accurately machined to within  $\pm 0.02\text{mm}$ . The platform levels of the main unit are:

Platform 1 – test piece mount

Platform 2 – blade drive slideway mount

Platform 3 – motor support

Platform 4 – end bearing support

The platforms and support stands were manufactured from steel, since a machined flatness of  $\pm 0.001\text{mm}$  can be achieved.

Each steel platform is mounted to the breadboard with 4 support stands. Platform 1 (mounts the test cell piece) is the component all other rig components align (directly or indirectly) to. Platforms 2 and 3 have 4 slot holes for assisting horizontal component alignment for mounting to the corresponding support stands; platform 4 has 4 thru-holes to locate on the support stands, but includes a central slot for connection of the end bearing on the platform providing necessary horizontal alignment with the lead screw. Platform 3 also has a set of 4 slots to mount the motor; these enable vertical alignment of the motor's output shaft with the opposite end of the lead screw.

The design of the main unit ensures no components interfere with the experimental observations of the test cell. Platform 1 is "C" shaped to permit viewing of the test cell from underneath. This design eliminates the requirement for the platform material to be transparent, with no subsequent reduction of optical quality. It allows additional light sources to be directed at the cell region, with the aim of improving captured images. The design drawings of the platforms, support stands, and the location of the stands on the breadboard are shown in Appendix A3.1-A3.2 and A3.5.

The optical components are mounted directly to the breadboard. The optical viewing system aligns with the test cell both horizontally and vertically, as described in detail in section 6.2.4.

### **6.2.2 Design of the test piece and cells**

The primary function of the rig is to hold a test cell rigidly in position. The design of the cell is based upon screen printing mesh apertures, but is greatly simplified. The cell is significantly larger (approximate dimension of  $1\times 1\times 1\text{mm}$ ). The geometric shape of the cell is also a simplified version of the woven thread unit cells; having solid walls that do not enable any ink flow between adjacent apertures. This simplification allows the filling of individual apertures to be investigated.

Another difference is that the screen mesh apertures are essentially thru-holes, but the cells in the test piece have a solid bottom to emulate the squeegee filling stroke when mesh and substrate are in contact. Assuming stencil material acts as a gasket sealing screen mesh cells when positioned contacting the substrate, then the perfect seal between the test piece cell base and walls is introduced as a first approximation of the physical boundary during filling. The approximation implies that no fluid leaks between the stencil base and substrate, therefore confining fluid transfer to the specific area of substrate defined by the open area geometry of the mesh cell.

The cross-sectional geometry of the cells was machined circular, based upon the shape of the pre-wetted unit cells of screen meshes, as observed in section 4.3.1.

The test piece is located on platform 1 (described in section 6.2.1). The blade passes it, so the piece cannot have any obstructions that would interfere with the blade path i.e. no raised bolt heads for mounting the test piece to the platform can be along the path of the blade or the drive unit.

The test piece block needs to be transparent to enable cell filling observations from multiple views. For the same reason the cell walls also have to remain transparent

after any chemical or physical treatment. Perspex proved a suitable material from which to manufacture the block.

The location of the cell within the test piece can affect the optical clarity of collected images. Consequently the volume of material between the cell and the image collection point is kept to a minimal by locating the cell as close to the viewing surfaces as possible.

A milled groove located 30.0mm upstream from the centre of the cell (1mm deep and length of approximately  $30\pm 5$ mm perpendicular to the blade path) is a design feature that aids control of the initial set-up onto the test piece. The groove limits the spread of the fluid prior to activating blade swipe. It also acts as a visible marker for positioning the blade tip ensuring a repeatable constant run-up length to the cell. The final draft design of the test piece and cell is shown in Appendix A3.3.

### **6.2.3 Design of blade unit**

The design of the blade unit enables independent study of these variables: blade angle and speed, and the gap between blade tip and test piece surface. The unit consists of a blade and a blade drive mechanism to control its movement. The blades are rigid, rather than the usual deformable polyurethane blades used in screen printing, to simplify the geometry for comparison to mathematical models. Three angled tips ( $10^\circ$ ,  $20^\circ$  and  $30^\circ$ ) were produced. These fit to the blade mount which has an alignment cut-away to ensure parallel location of the blade tip with the test piece, simplifying the setup procedure. The tips were made from steel and ground to ensure good quality surface finish.

The drive mechanism consisted of a lead screw to change the rotational motion of the motor to linear motion of the blade. The lead screw was indirectly connected to the output shaft of the motor via a flexible shaft coupling, which improves alignment and minimises vibration within the system. The other end of the lead screw couples with an end bearing to minimise vibration. A motor with variable and controllable output

shaft speed was necessary to allow the blade speed variation. The central section of the blade drive mechanism includes the blade.

The final design required 2 slideways, a mounting block (part 1.6), an adaptor plate (part 1.10), a blade spacer (part 1.11), a blade mount (part 1.8.4), and a blade. The chosen material for these components was steel since a high level of flatness could be obtained through grinding, which was necessary to ensure the blade tip travelled level and parallel to the surface of the test piece. Draft drawings of the designed components are included in Appendix A3.

It is important that the position of blade tip can contact the test piece upper surface and be driven along a path passing over the test cell. Slideway 2 was incorporated into the rig design so that the blade tip could be raised above the test piece surface, facilitating gap distance variable to be studied. (A displacement height gauge is fitted to the blade block to measure the distance between the blade tip and the test piece surface.) The dimensions of the blade block and other components of the blade drive mechanism were designed to enable successful location of the blade tip at the desired working site of the test cell.

Care was taken to ensure the blade drive did not obscure the optical path required for image views.

### 6.2.4 Design of optical viewing system

An optical viewing system is required to allow images from the cell region to be recorded enabling the filling behaviour to be studied. The image-recording equipment includes a high-speed camera, PC, video recorder and TV or display monitor. Multiple images (one from beneath the cell and another from the side i.e. at the same vertical height as the cell) can be simultaneously captured using a single camera. To achieve this, an arrangement of prisms and mirrors was required to direct both image beams to the camera. The first arrangement that was considered is shown below in Figure 6.2.

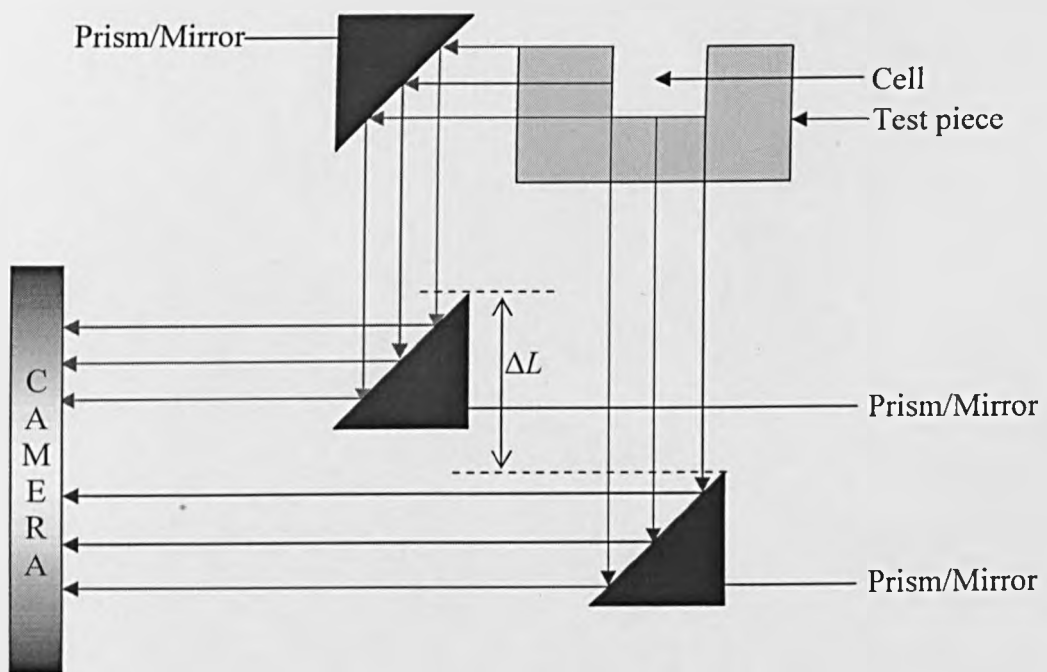


*Figure 6.2: Simple arrangement of prisms/mirrors used to direct two different simultaneous views of the cell to the camera.*

This arrangement creates different lengths the image light has to travel to reach the camera, resulting in focusing problems. The image that is reflected twice has a shorter path length; it is  $\Delta L$  shorter than the other beam. Figure 6.3 shows how the prism/mirror arrangement can be modified so that the two beams are of the same length, without the means of introducing lenses. This is achieved by varying the angle  $\beta$  so that the following equation is true:



$$\Delta L = L_1 + \frac{L_1}{\sin(2\beta)} - \frac{L_1}{\tan(2\beta)}$$

⇒ image light paths are equal and so the focal distance is the same for both images

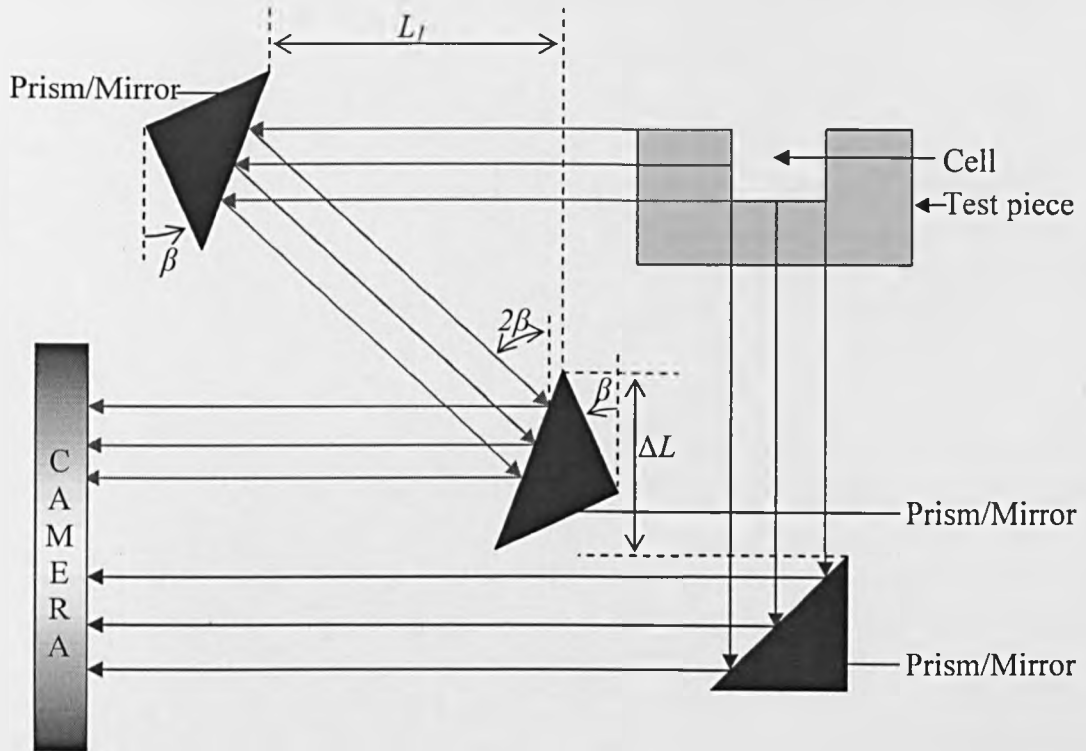
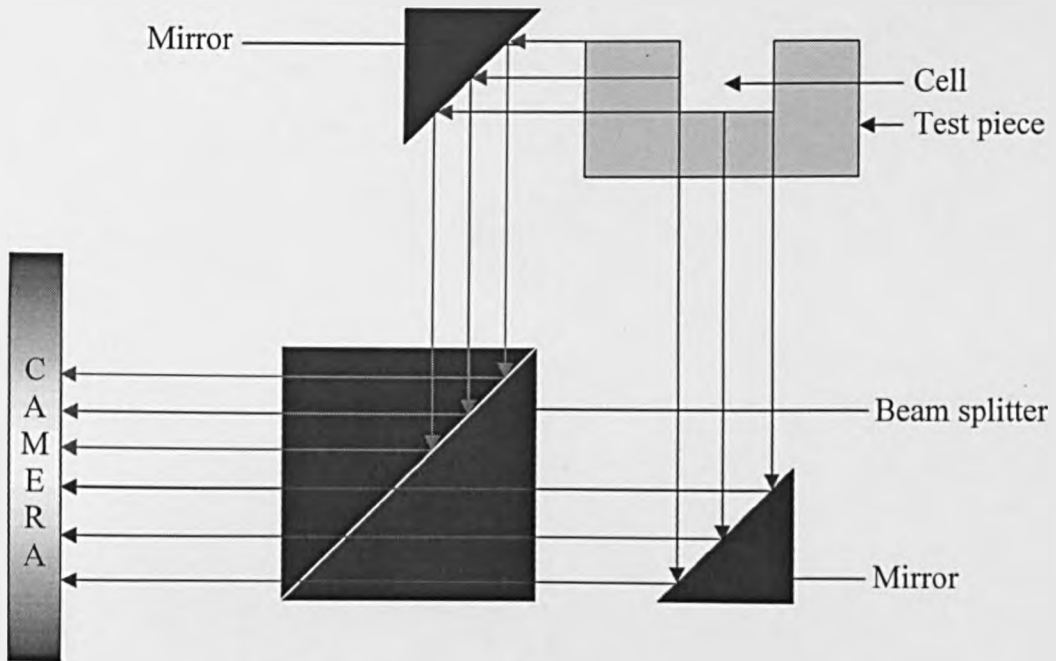


Figure 6.3: Arrangement of prisms/mirrors so that the two image beams have the same focal length.

Achieving accurate alignment of  $\beta$  angle complicates the set-up of the optical viewing system. This optical combination cannot be practically instigated due to the mirror backing length that creates a large “blocked” area in the captured image.



*Figure 6.4: Arrangement of mirrors with a beam splitter for directing the two images of the cell region to the camera.*

The final design of the optical viewing system is based on that shown in Figure 6.4 – this design significantly decreases the set-up time, whilst still enabling the generation of two equal focal lengths. A right-angled mirror is used for the single reflected beam. This beam then passes through the beam splitter to the camera. The other image beam is directed to the camera via a flat mirror and the beam splitter. The right-angled mirror and the beam splitter are mounted on an optical rail as shown in Figure 6.1 – labelled “optical components”. These two optical components are vertically aligned with each other. The right-angled mirror is located directly below the test piece cell; the beam splitter is positioned below the flat mirror, so it can receive the second image beam, on the optical rail to maintain horizontal alignment with the right-angled mirror’s first image beam.

The flat mirror is mounted to a holder that allows fine angle adjustments. This is then connected to a horizontal post and adjustable angled clamp, ensuring horizontal alignment and major angle adjustment. This enables the mirror to be positioned at the required angle directing the image beam to the beam splitter. The adjustable angled clamp is mounted to a precision adjustable post holder, which is connected to the

breadboard of the main unit (as shown in Figure 6.1). This component allows vertical alignment of the flat mirror with the test piece cell, completing the alignment of all rig components.

### 6.3 Experimental method

The rig was used to observe filling behaviour of test cells. The monitored rig temperature was  $18.5 \pm 0.5^\circ\text{C}$ . For these experiments, transparent fluids were appropriate to observe filling within the cell. Screen printing inks were not suitable and so a selection of oils were used: HVI 60, HVI 160, EP80 and EP90. The oil viscosities were measured using the Bohlin viscometer, described in section 2.7.1, fitted with a  $1^\circ$  angled cone of 60mm diameter operating on a flat plate geometry. The measurements at  $18^\circ\text{C}$  and  $20^\circ\text{C}$  are shown in Figure 6.5.

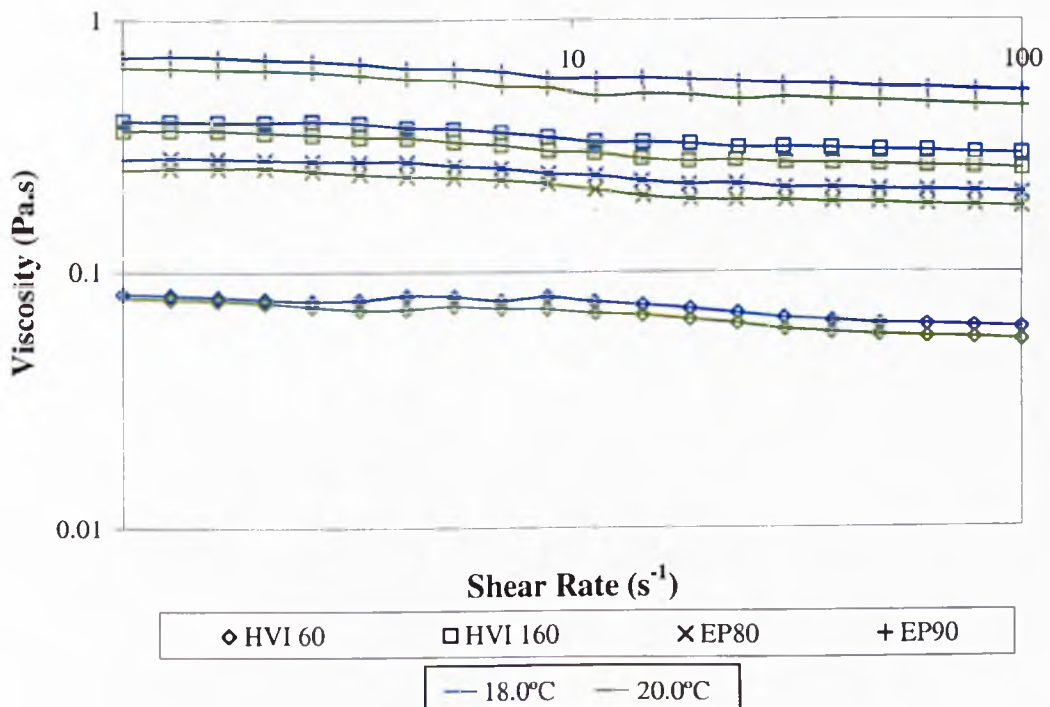
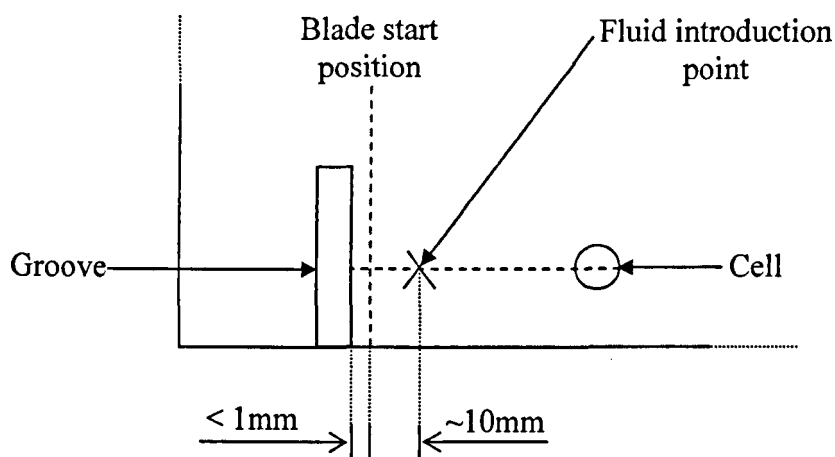


Figure 6.5: Graph of the measured viscosity of HVI 60, HVI 160, EP80 and EP90 oils in the shear rate range of  $1\text{-}100\text{s}^{-1}$  at  $18.0^\circ\text{C}$  and  $20.0^\circ\text{C}$ .

### Cell filling method

The rig was initially fitted with one of the 6 available test pieces (described in section 2.3.2) and a blade ( $10^\circ$ ,  $20^\circ$  or  $30^\circ$  – see section 2.3.3), to investigate the effect of cell geometry, blade angle and speed on filling behaviour.



*Figure 6.6: Diagram of the test piece upper surface illustrating initial positions of blade and fluid addition.*

The blade tip was positioned above the test piece just past the groove, as shown in Figure 6.6. 0.20ml of test fluid was introduced onto the test piece at a constant site; the fluid spread to the groove without overflow. The displacement gauge was zeroed to the test piece surface by lowering the blade tip until it came into contact with the surface. With the displacement gauge measuring the distance between tip and surface, the blade was then raised to the desired gap.

The blade speed was controlled via the rotational speed of the motor. The motor voltage, controlling the motor speed, was set using a digital multimeter prior to activating blade motion; the method used to convert the motor voltage into the linear blade speed is described in section 2.3.4. A separate switch controlling the direction of the motor shaft rotation initiated the blade motion. This action causes fluid to be moved along the test piece surface by the blade.

After the tip passes the cell, the blade no longer influences filling behaviour and so its motion was stopped. Raising the tip clear of the test piece and using the reverse rotational motion of the motor shaft enabled the blade to be reset back at its start position. All surfaces were wiped with a lint-free cloth, removing all but the thinnest layer of fluid. This was taken as the starting point for the next experiment; in screen printing, the cell would also be pre-wet once successful printing is achieved.

For each rig variable setup the experiment was repeated to obtain 5 filling results ensuring repeatability of the system. This process highlighted significant lack of repeatability for studying the filling behaviour with HVI 60 oil.

Test pieces and blades were cleaned off-rig as described in sections 2.3.2 and 2.3.3.

### **Capturing filling behaviour images**

Two views of the cell filling behaviour were observed concurrently using the optical system described in section 2.3.5; prior to use, the system was cleaned to ensure it was dust free. The camera system and lighting described in section 2.4.1 were positioned (Figure 6.7) to capture images in digital format.



*Figure 6.7: High speed camera aligned to capture cell filling events.*

The high speed camera was set to capture 750 frames per second. The image of the two views first needed to be focused, and it was found that a partially filled cell was best to generate images suitable for this. The location of the mirrors and beam splitter were adjusted to align both cell images without overlap. However, due to the nature of the beam splitter, an overlap of the overall test piece image occurs. Clarity of the image was improved by masking specific regions on the beam splitter (using matt black card), thus preventing light from outside the region of interest overlaying the second image.

Initially the rig was flooded with light using a 500W halogen light source. Although this enabled a greater frame rate on the camera to be set (1125 frames per second), the overall viewed images obtained little grey-scale contrast, lacking definition and made it difficult to identify filling behaviour. The final selected lighting system for image capture involved illuminating the cell using a twin fibre optic light source. One light output was directed at the test piece groove from the front face; the other light was aimed from underneath at the rear of the test piece towards to cell region.

After establishing the image capturing system, the cell filling procedure was initiated. The filling behaviour was recorded with the high speed camera system and associated video machine. The individual digital frames were downloaded as a series of image files (tif format) to allow analysis of the mechanisms involved in filling and air removal.

## 6.4 Experimental cell filling results and discussion

This section contains experimental results which have allowed these 4 different filling behaviours to be observed:

- Complete filling – all air is displaced by the liquid
- Partial filling – entrapped air (in a bubble form) is removed from the cell
- Incomplete filling – entrapped air remains in the cell
- No fill – no fluid enters the cell

The experimental variables were systematically studied, to generate a wide matrix of setups, from these variable ranges: 3 blade angles ( $10^{\circ}$ - $30^{\circ}$ ), gap distance set between 0.10-0.50mm, blade speed range of  $0.0003$ - $0.0116\text{ms}^{-1}$ , 6 cell geometries (1-3mm depth, 1-3mm diameter), and 4 fluids of a viscosity range 0.07-0.6 Pa.s. The work presented in this section summarises this extensive study.

Section 6.4.1 highlights features observed in the captured images to aid identifying the key aspects of the filling behaviour for the experimental images following this. Sections 6.4.2-6.4.6 contain image sequences of different filling behaviour. It is from these an understanding of the mechanisms involved was obtained. Section 6.4.8 uses two key filling events to generate a comparative method of the filling, and defines the average velocities measured within the cell (from captured images). This method is used in sections 6.4.9-6.4.11 to assist in identifying the experimental variables influence on the filling behaviour. Section 6.4.7 shows an example of how a surface defect on the test piece interferes with filling results.

### 6.4.1 Captured images

Figure 6.8 shows an example of a captured image from the high speed camera, containing 2 simultaneous views of the cell: one from beneath, and one from the side.

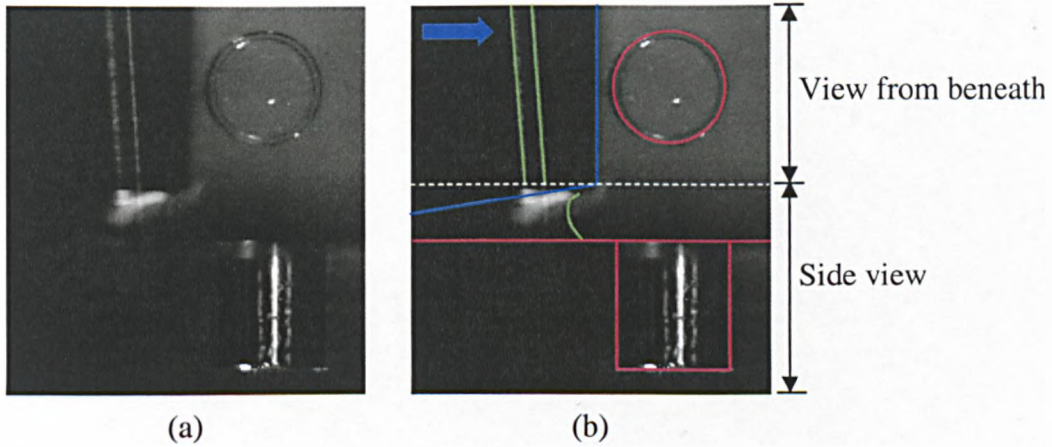


*Figure 6.8: (a) Photograph of two cell views captured simultaneously before the blade tip passes the cell. (Setup: HVI 160, 10° blade, 0.10mm gap, 15.00V motor setting, and cell geometry 3×Ø3)*

*(b) Key features of image (a) are highlighted: a white dashed line is positioned at the division of the two views, the green line indicates fluid menisci, the blue line locates blade edge, the blue arrow shows the blade direction, and the red line aligns with surface boundaries of the test piece or cell walls.*

Figure 6.8(b) highlights the location of image features corresponding with the equivalent photograph shown in Figure 6.8(a). The features include: cell walls, test piece surface, fluid menisci, and blade direction and location. As the blade passes over the cell, identification of these key features enables the filling behaviour to be observed.

The twin parallel green lines, shown in Figure 6.8(b), indicate the fluid meniscus as viewed from beneath the cell. The line further to the right highlights the location of fluid contact with the blade; the line on the left follows the leading edge of the meniscus contacting the test piece surface.



### 6.4.2 Complete filling

Figure 6.9 illustrates the simplified screen and gravure cells full of fluid. In both cases the subsequent evacuation of fluid to the substrate is not obstructed by air presence at the exit surface of the cell (this is highlighted with green arrows). Completely filled cells are desirable for both these printing techniques. The cells are assumed to have the same geometry when filling (i.e. open at the top) but in screen printing the fluid is printed onto the substrate when the base moves away.

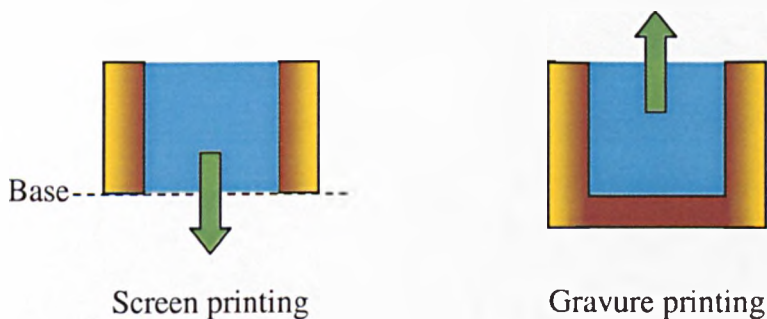


*Figure 6.9: Diagram of simplified completely filled screen and gravure printing cells.*

Complete filling was observed with all air removed before a layer of fluid coats the cell closing it. Cell closure, entrapping air in the form of a bubble, was also observed to result in complete filling. The bubble was removed ahead of the blade tip pass enabling further fluid to enter, replacing the bubble occupancy to fill the cell fully. However this event was observed only once, due to the unrepeatable nature of HVI 60 oil, and was not captured photographically either. Therefore a detailed description of the bubble removal has not been determined, but highlights the possibility of further filling types that may exist.

### Complete filling with no bubbles

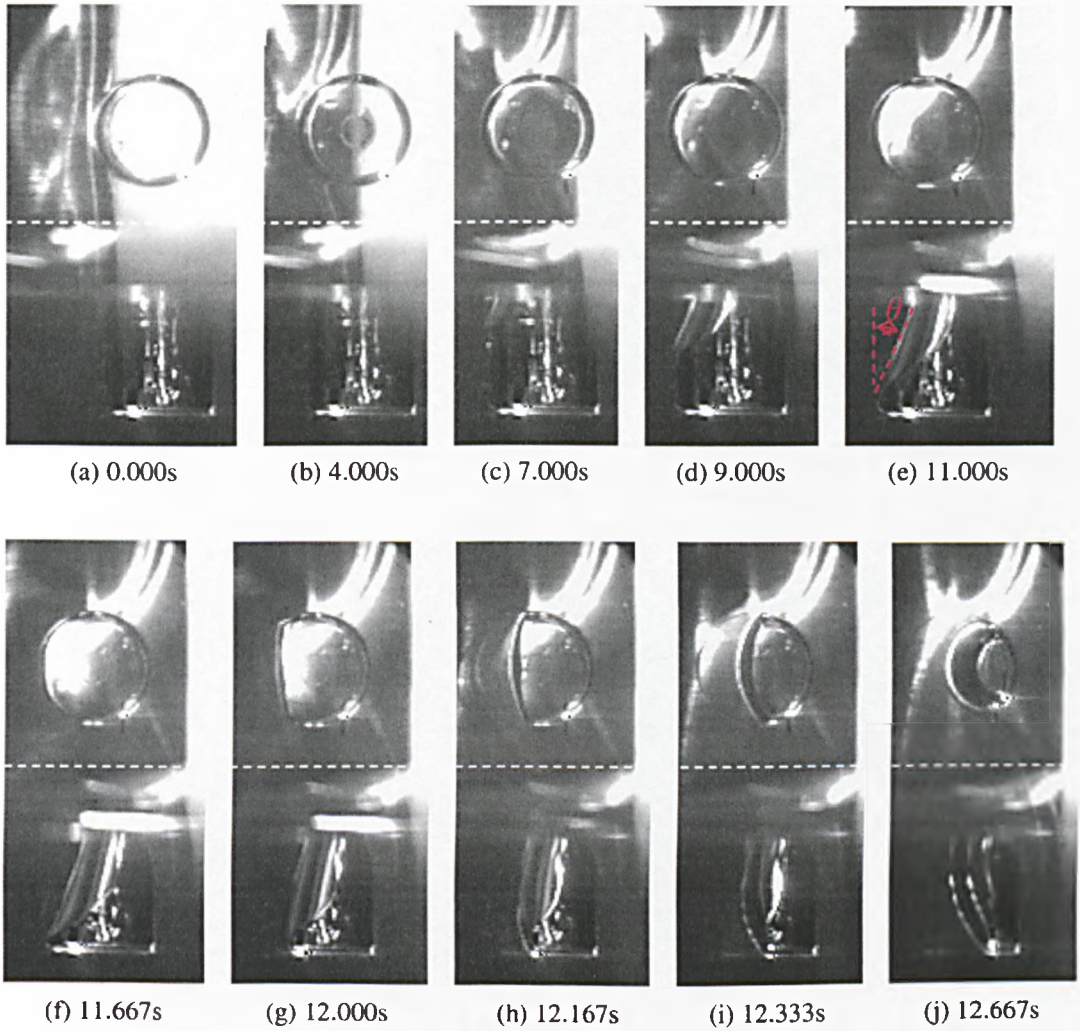


*Figure 6.10: Sequence of images (continued on the next page) showing the removal of air and consequent complete filling of the cell with oil. (Exp 25, ID# 10 setup: HVI 160, 10° blade, 0.10mm gap, 7.00V motor setting, and cell geometry 3×Ø3)*

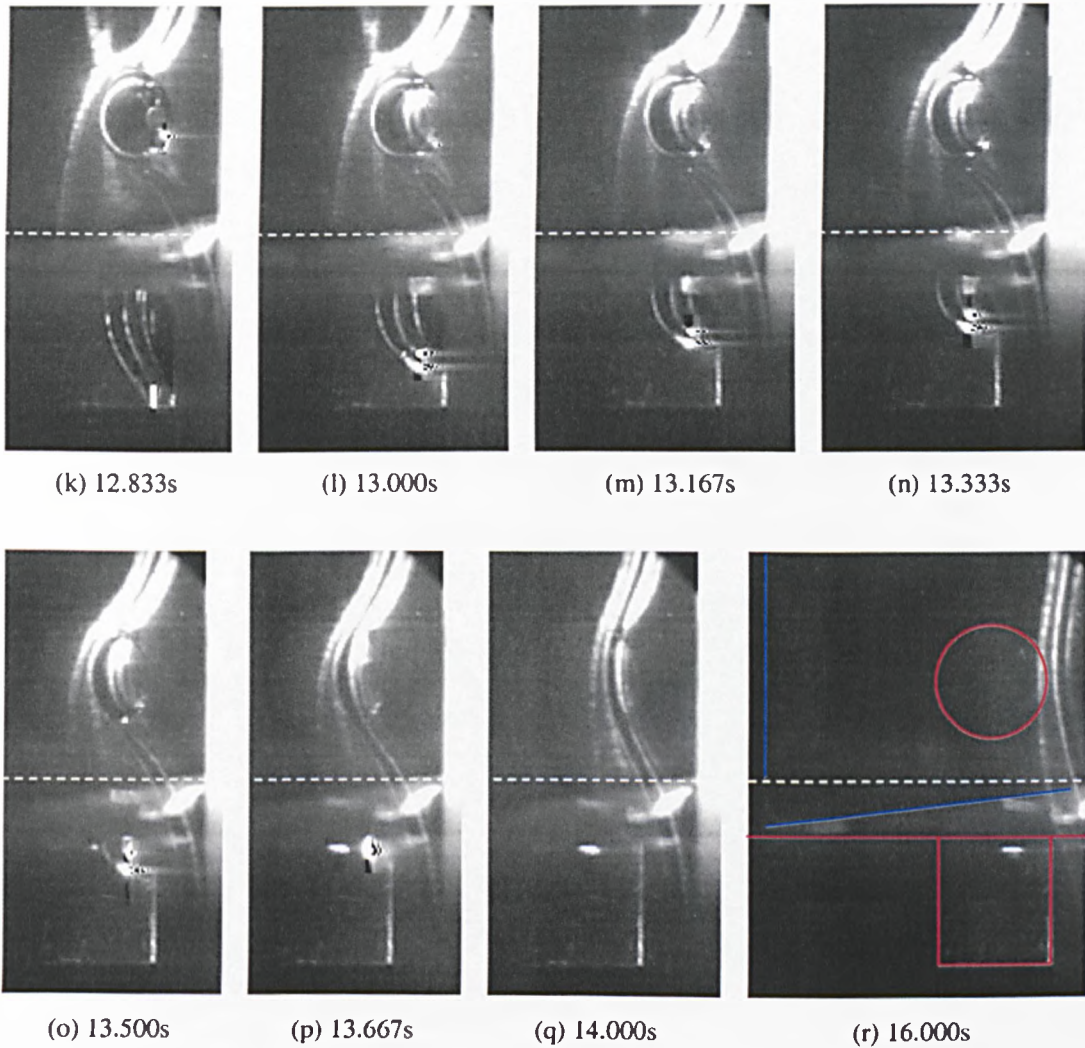


*Figure 6.10: Sequence continued from the previous page.*

Figure 6.10 consists of a series of captured photographic images showing complete filling behaviour of the cell. The initial image shows the fluid front reaching the edge of the cell (viewed from beneath). The subsequent images demonstrate that the fluid meniscus pins at the cell. The motion of the blade sweeps the interface forward, with this pinning delaying the fluid meniscus entry into the cavity (as shown in Figure 6.10(b)). The fluid front under the blade advances to approximately half the distance past the cell before the meniscus enters the cell.

The fluid front continues to move along the test piece with the blade motion. The meniscus entering the cell gradually moves down the wall towards the base as the pinning location spreads round the cell upper edge (Figure 6.10(b)-(e)). Figure 6.10(f) shows the meniscus reaching the cell base. The meniscus reverses contact angle at the base of the cell (Figure 6.10(f)-(g)). The cell geometry of the base aids meniscus motion to the opposite side. The meniscus at the base-wall corner structure advances so that it is actually ahead of the meniscus above it (Figure 6.10(g)-(k) shown in both views). This mechanism enables the base surface to be coated relatively quickly.

The initial pinning behaviour, at the top of the cell, is eventually overcome (shown in Figure 6.10(f) viewed from beneath) and the fluid front commences to be pulled across the top of the cell. As this front completes the pass over the cell, it results in cell closure.

After coating the base, this meniscus travels up the cell walls (Figure 6.10(l)-(p)) expelling remaining air from the cell. This action occurs faster than the cell closure action of the fluid front.

Figure 6.10(i)-(n) (viewed from beneath) show several important features relating to the fluid front as it is pulled across the cell. The change in shape indicates that weakened pinning at the cell edge causes the fluid to move faster than fluid at the centre of the top surface of the cell. The position of the central fluid front over the cell remains noticeably more constant than the other menisci. This is due to the blade motion and its ability to introduce fluid to the cell region; the fluid may either enter the cell or be pulled across it.

The blade moves relatively slowly in this observed situation, with the result that the amount of fluid entering the cell (during the fast base coat and upward wall action) is not exceeded by the amount of fluid the blade pushes into the cell region. This action causes delay to the advancement of the meniscus at the centre of the top of the cell. The observed time delay greatly assists air removal from the cell to achieve complete cell filling behaviour (Figure 6.10(q)).

Cell closure is eventually observed (Figure 6.10(r)) with the completed pass of the fluid front over the cell. This image highlights the location of the blade tip significantly upstream of the cell.

### **Conditions leading to complete cell filling**

A large blade angle and small gap increases the filling ability, and a slow blade speed enables the fluid meniscus to enter the cell, coat the base, and commence travel up the opposite cell wall before cell closure (governed predominantly by the blade speed) occurs.

The cell geometry aspect ratio (diameter:depth) should be high. This enables the time for the fluid to reach the cell base to be minimised, promoting the coating of this surface and completion of filling before closure. A fillet rounded cell edge at the top surface may potentially reduce the observed initial pinning and initiate fluid entering the cell with a reduced delay.

A reduction of fluid viscosity aids the promotion of total air evacuation from the cell, resulting in complete filling. However, the lower viscosity of HVI 60 oil had unwanted effects, due to the poor repeatability of the observed filling behaviour.

### 6.4.3 Partial filling

Figure 6.11 illustrates simplified screen and gravure cells partially full of fluid. With gravure printing, the presence of an air bubble could make evacuation out of the top of the cell problematic, whilst in screen printing it could affect the colour density.

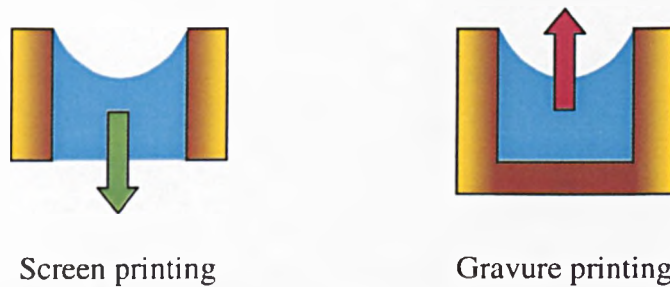
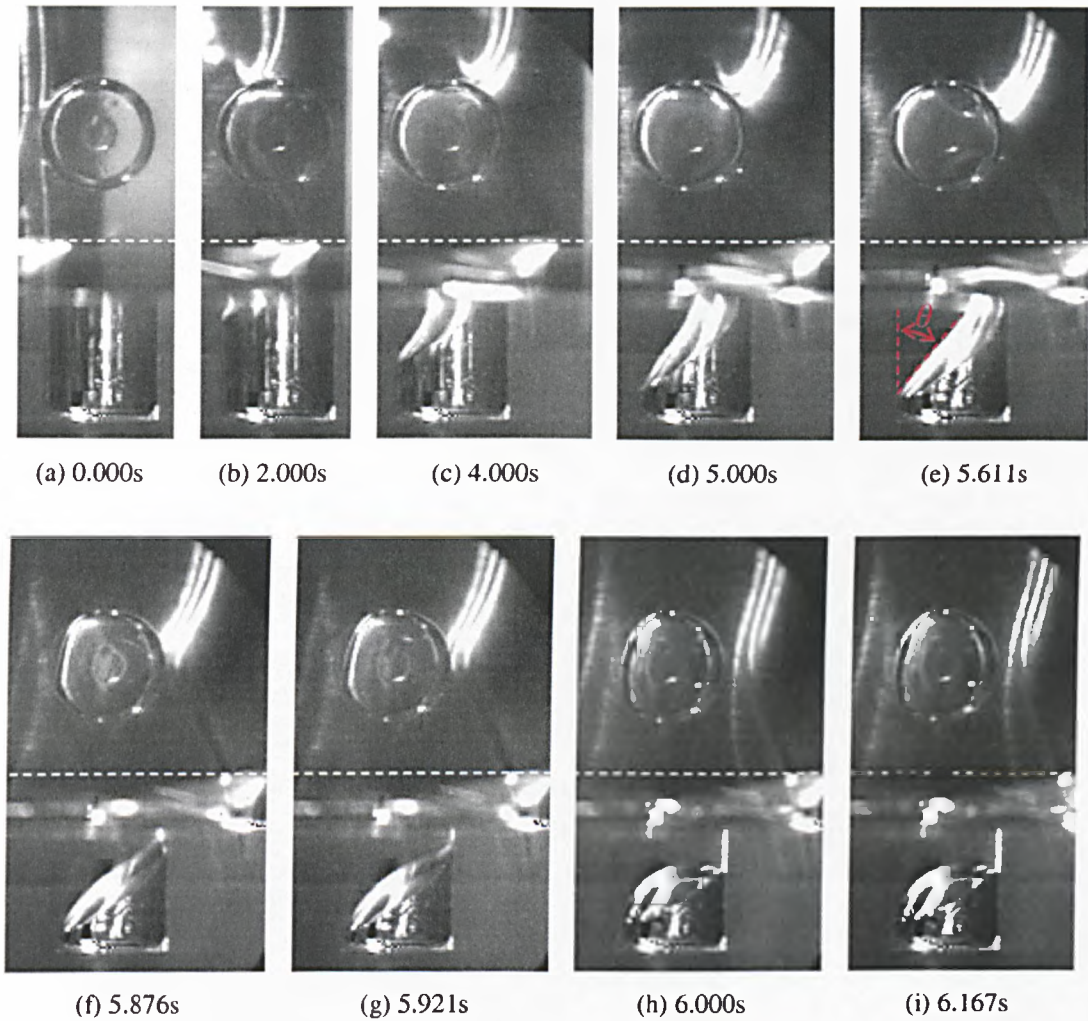


*Figure 6.11: Simplified diagram of partially filled cells. Ink transfer from the cells is potentially more successful with screen printing cells than gravure cells.*

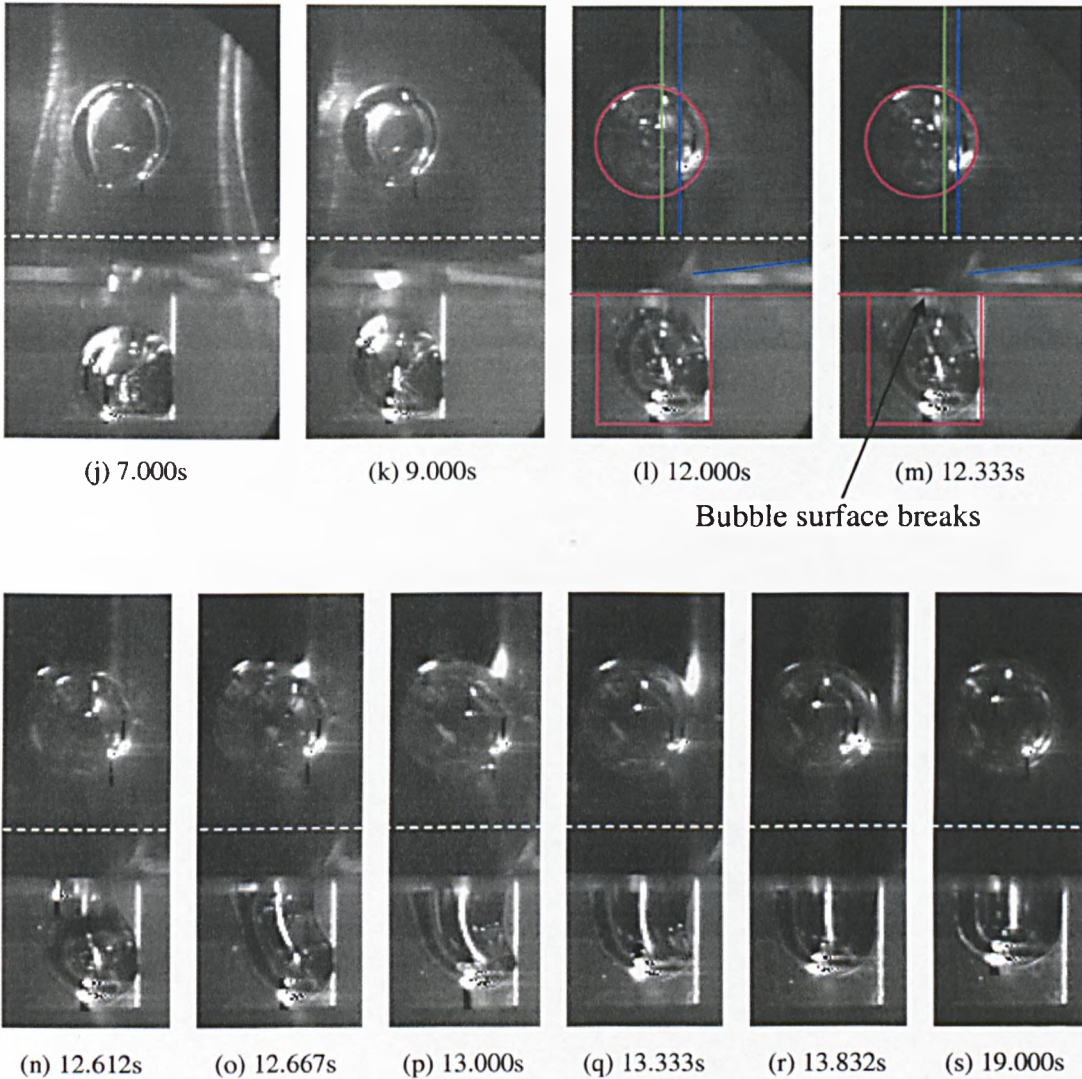
Partial filling occurs when a bubble of air is entrapped within the cell, as the blade passes. The bubble exit is essentially blocked by the presence of the blade, and so the bubble removal occurs not until the blade completes the pass over the cell.

Described below are four observed states of partial filling. The first two release the air from the cell as the blade passes; the last two expel air after the passing of the blade.

**Bubble released as blade tip passes (1)**



*Figure 6.12: Sequence of images (continued on the next page) showing bubble formation and subsequent removal as the blade tip passes. (Exp 24, ID# 9 setup: HVI 160, 10° blade, 0.10mm gap, 12.00V motor setting, and cell geometry 3×Ø3)*



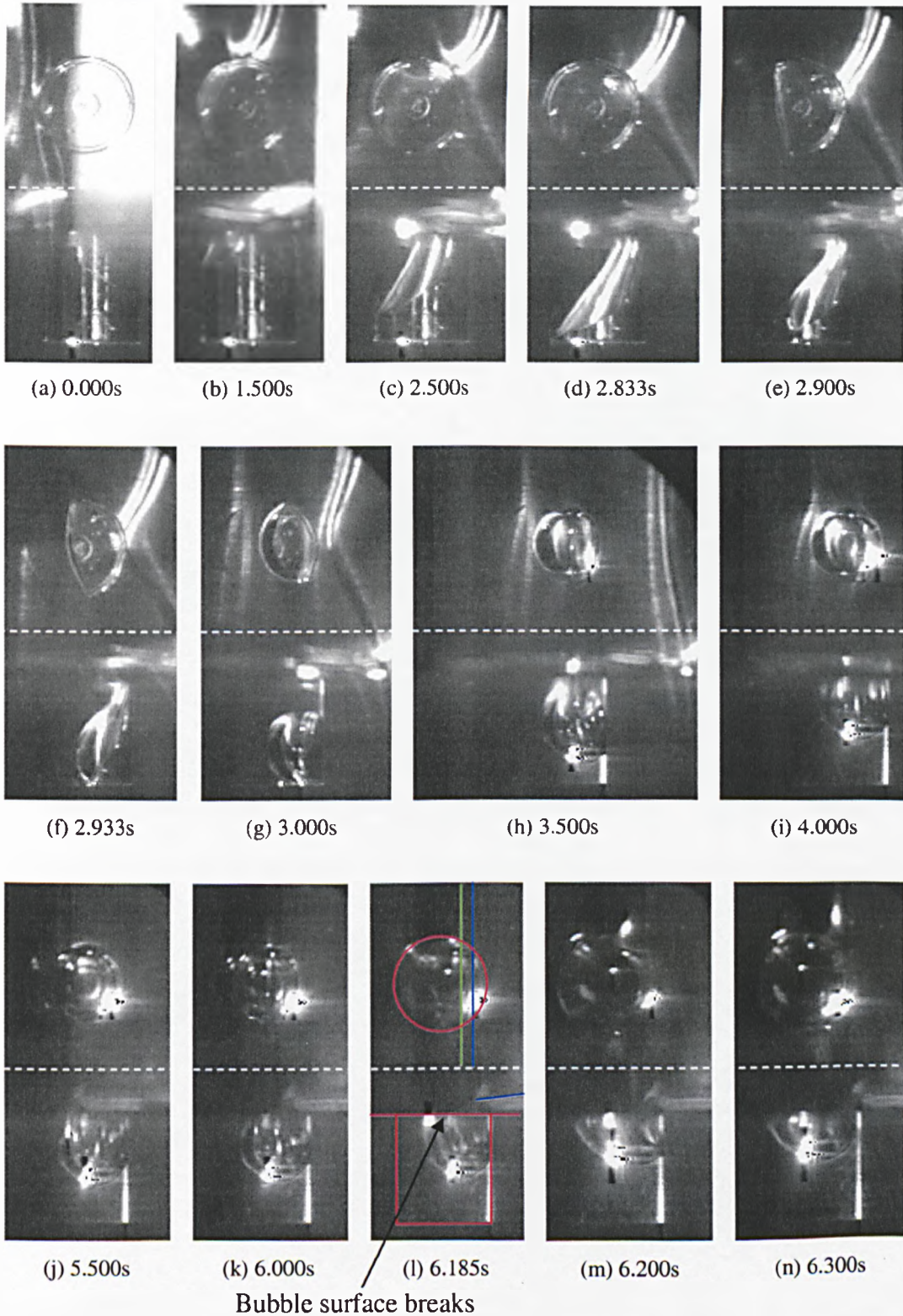
*Figure 6.12: Sequence continued from the previous page.*

Figure 6.12 shows a series of photographic images displaying the formation of partial filling from bubble entrapment and subsequent release as the blade tip passes the cell. Figure 6.12(a) shows the fluid front at the cell. The next image (Figure 6.12(b)) shows the pinning effect of the cell edge once again delaying the fluid entry to the cell, as observed previously for complete filling. Figure 6.12(c)-(e) show the fluid meniscus moving down the cell wall. The highlighted angle (Figure 6.12(e)) is greater than observed in complete filling Figure 6.10(e), and so here the action of the blade forcing fluid over the top of the cell occurs quicker than the motion of the fluid down the cell wall; cell closure is observed in Figure 6.12(f) resulting in entrapped air.



The next few images (Figure 6.12(g)-(k)) demonstrates what happens to the trapped bubble: the meniscus at the bottom of the cell coats the base, as observed in complete filling behaviour, whilst the meniscus near the top of the cell moves down the wall. Figure 6.12(k) shows the bubble lifting from the cell base as the base coating action continues.

The bubble remains in the cell as the blade tip passes over it (Figure 6.12(l)). Figure 6.12(m) shows that as the blade tip approaches the end of the cell, and therefore completes the pass over the top of the bubble, the bubble surface breaks resulting in the air escaping behind the blade. Figure 6.12(n)-(r) show the new meniscus spreading to the cell edges, with fluid flowing down the cell walls, to stabilise in the final state observed in Figure 6.12(s).

Bubble released as blade tip passes (2)

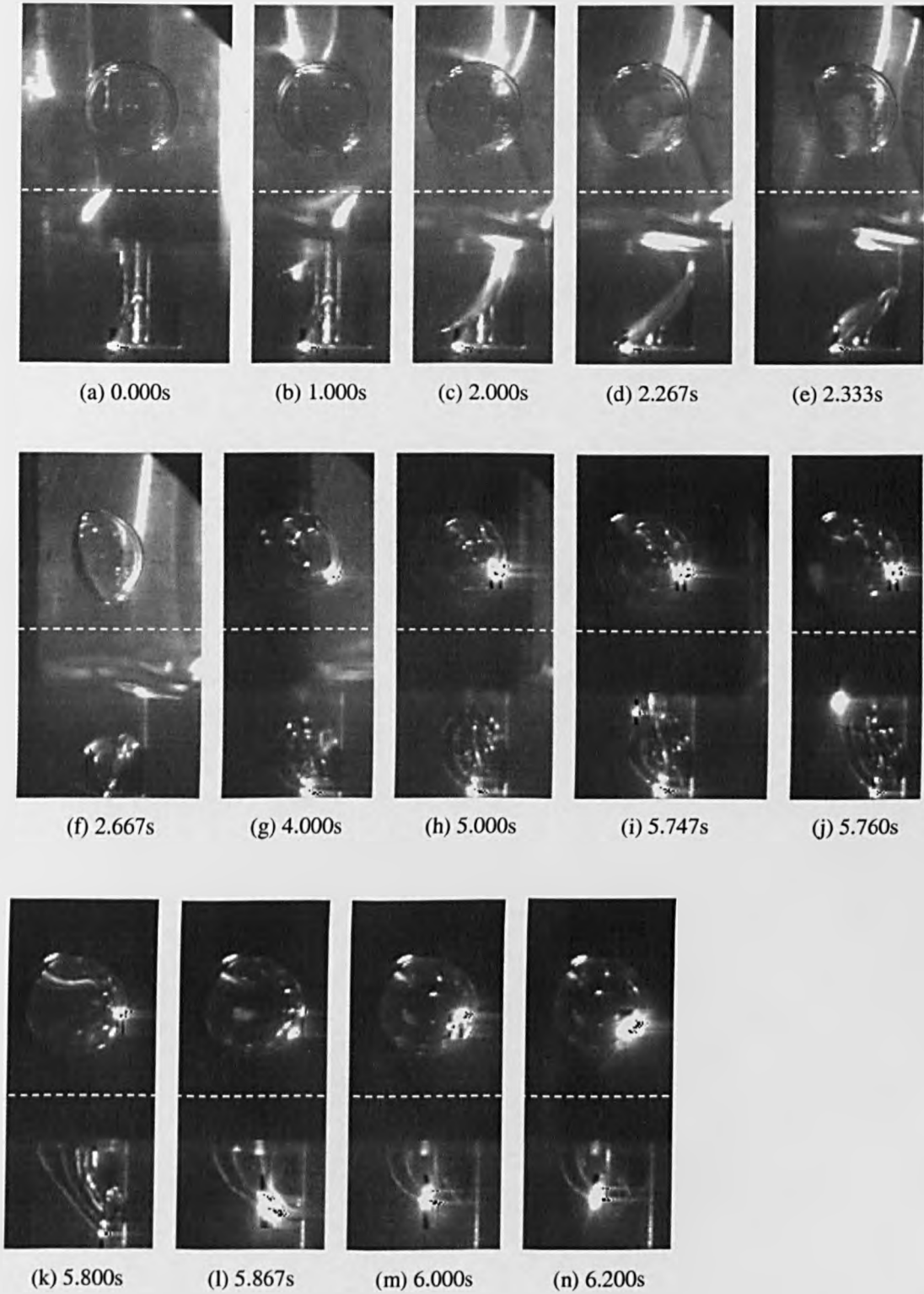
*Figure 6.13: Sequence of images showing bubble formation and subsequent removal as the blade tip passes. (Exp 46, ID# 32 setup: HVI 60, 10° blade, 0.10mm gap, 20.0V motor setting, and cell geometry 3×Ø3)*

The photographic images shown in Figure 6.13 demonstrate a bubble forming process, similar to that described in the previous example, however the conditions are such that the fluid starts to coat the base of the cell before the air is trapped by the advancing meniscus.

The initial images (Figure 6.13(a)-(d)) show filling to be essentially the same as for complete filling. The meniscus reaches the base and commences the base coat action before cell closure occurs (Figure 6.13(d)-(e)). The closure completes before base coating does resulting with entrapped air forming a bubble. The volume of fluid within the cell is greater than in the previous example and so the bubble is smaller.

The motion of the meniscus along the base continues, and the bubble lifts off the base rising to the top of the cell (Figure 6.13(g)-(i)). This occurs significantly faster than in the previous example since the meniscus has already started moving over the base. Despite the bubble reaching the top of the cell quicker, it remains at this location, unable to release from the cell, due to the blade maintaining fluid above the bubble, and essentially preventing an immediate exit (Figure 6.13(i)-(k)).

Figure 6.13(l)-(n) show bubble release occurring as the tip passes resulting in the new meniscus spreading to the cell edge, behaving the same as described previously in example 1 of partial filling.

Bubble removed after blade tip pass (3)

*Figure 6.14: Sequence of images showing formation of an air bubble that is removed after blade tip pass occurs. (Exp 41, ID# 27 setup: HVI 160, 20° blade, 0.10mm gap, 20.0V motor setting, and cell geometry 3×Ø3)*

The series of images in Figure 6.14 exhibit the behaviour observed in the previously described examples of cell filling. Figure 6.14(a)-(d) show fluid entering the cell and reaching the base as the fluid front passes across the cell closing it and trapping air. The bubble forms and lifts off the base in the same manner as example 2 of partial filling (Figure 6.14(e)-(h)). Figure 6.14(i) shows the bubble at the top of the cell, where it is released, apparently behaving the same as in example 2, but with no effect from the blade which is downstream from the cell. Therefore the resulting upward force (from the bubble's buoyancy) that enabled the bubble to rise exceeds the surface tension force when it bursts. Figure 6.14(j)-(m) show the same spreading of the new meniscus to the cell edge as observed previously in examples 1 and 2.

**Bubble removed after blade tip pass (4)**

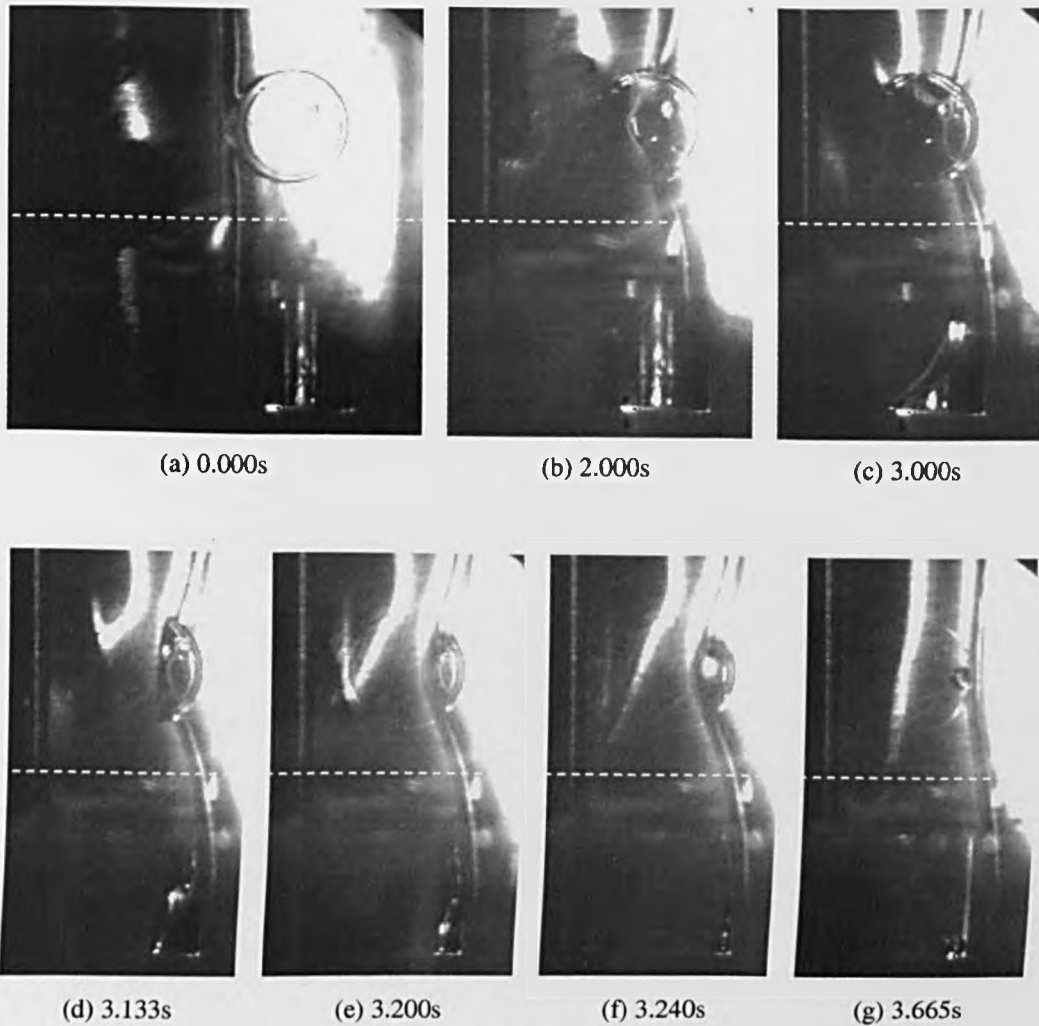


*Figure 6.15: Sequence of images showing formation of an air bubble that is removed after blade tip pass occurs. (Exp 31, ID# 16 setup: HVI 160, 30° blade, 0.10mm gap, 12.00V motor setting, and cell geometry 3×Ø3)*

The example shown in Figure 6.15 shows the formation of a small bubble. The filling behaviour is similar to the first example of complete filling. Figure 6.15(a)-(c) show fluid entering the cell. The position of the fluid front when the meniscus reaches the base (Figure 6.15(c)) is more advanced than observed with complete cell filling (Figure 6.10(f)). The central position of the fluid front progresses slower than that along the base, however cell closure is completed before the meniscus has moved fully along the base, resulting in air remaining within the cell (Figure 6.15(d)-(g)). Approximately

30s after the blade tip passes over the cell, the bubble was observed rising to the surface where eventually it burst; the blade having no effect on the bubble release.

### **Conditions for partial filling**

The main feature of partial filling behaviour is that the meniscus within a cell is located along the base as the cell closes. Due to the fast coating action of the base, this results in a significantly smaller variable range than the other filling types. To observe partial filling the variables need to be set between those of complete and incomplete filling (to be described in section 6.4.4).

The edge between the base and cell walls encourages the base coating action. Replacing this edge with a rounded feature may reduce this action and potentially enable partial filling to be more widely observed.

Once a bubble has formed, increasing the time of its rise to the cell surface so that the air is released behind the blade tip enables partial filling to be observed. Increasing the fluid viscosity encourages this.

#### 6.4.4 Incomplete filling

Figure 6.16 illustrates simplified screen and gravure cells incompletely full. The entrapped air at the base is the opposite situation to partially filled cells. The air presence hinders ink transfer from the screen cells (red arrow) but not from the gravure cells (green arrow).

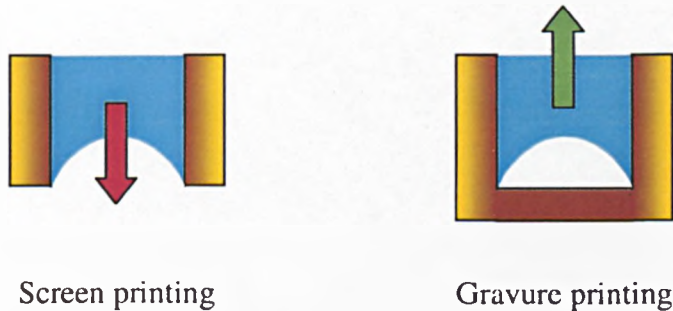


*Figure 6.16: Diagram of incomplete filling, highlighting that ink transfer is potentially more successful with gravure cells than screen printing cells.*

The mechanisms for achieving incomplete filling are initially similar to those associated with partial filling, entrapping air without forming a bubble. Described below are two examples of incomplete filling. The entrapped air in the first example does not deform, whereas in the second example deformation is observed at blade pass.



**Incomplete filling without deformation of entrapped air surface as blade passes**

**(1)**

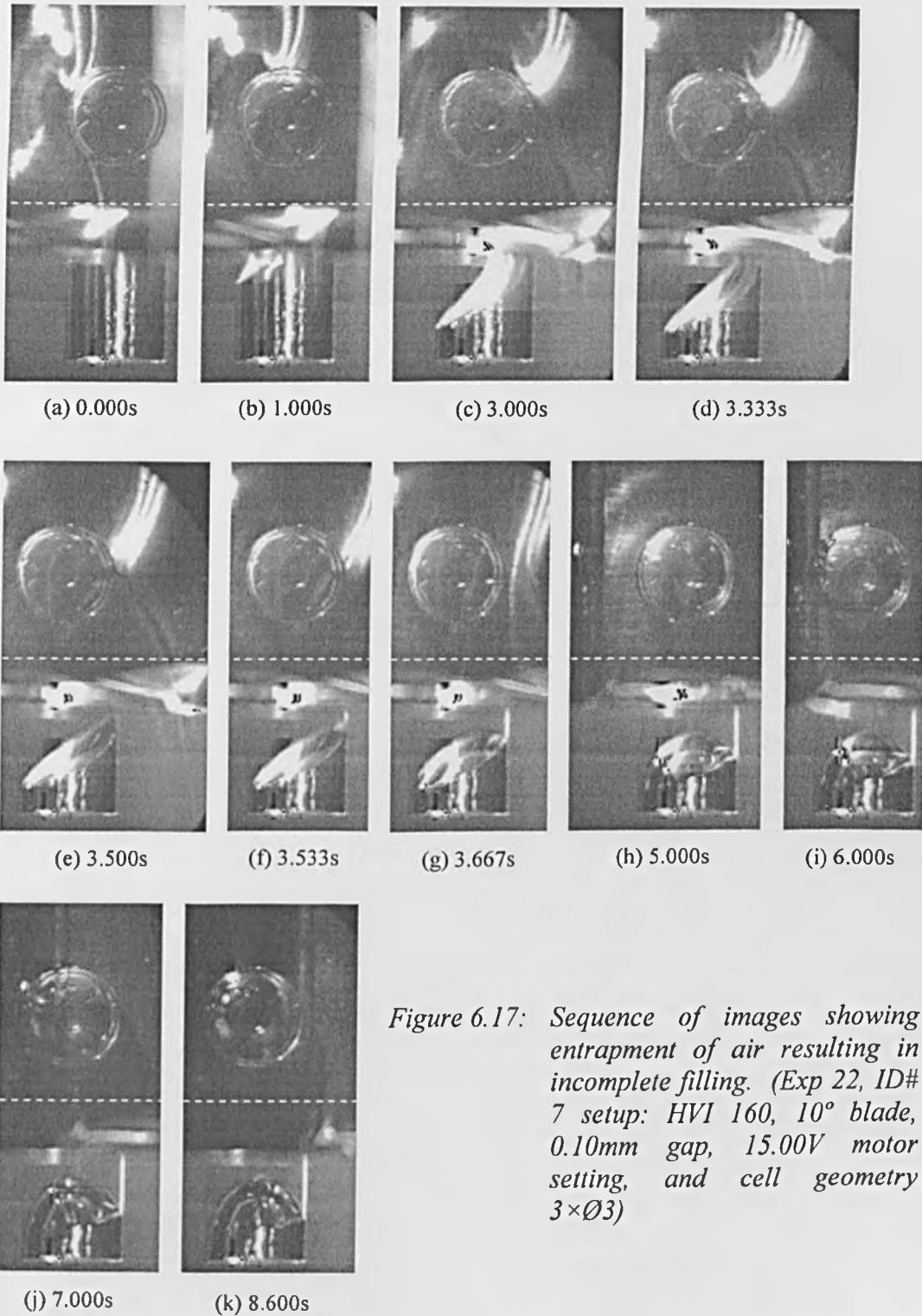


*Figure 6.17: Sequence of images showing entrapment of air resulting in incomplete filling. (Exp 22, ID# 7 setup: HVI 160, 10° blade, 0.10mm gap, 15.00V motor setting, and cell geometry 3×Ø3)*

Figure 6.17 shows a sequence of images producing an incompletely filled cell. Figure 6.17(a)-(d) show the initial filling behaviour is approximately the same as observed in partial filling. Figure 6.17(e) highlights that when the fluid front closes the cell the meniscus (within the cell) has not descended as far as the base. Without initiation of the fluid coating the base of the cell no bubble forms. The entrapped air surface initially reforms into a dome-like shape (Figure 6.17(f)-(i)). As the blade tip passes the cell, the shape of the air surface stays in an equilibrium state, apparently unaffected, with the air remaining trapped at the base of the cell (Figure 6.17(j)-(k)).

**Incomplete filling with deformation of the interface, between fluid and entrapped air, as blade passes (2)**

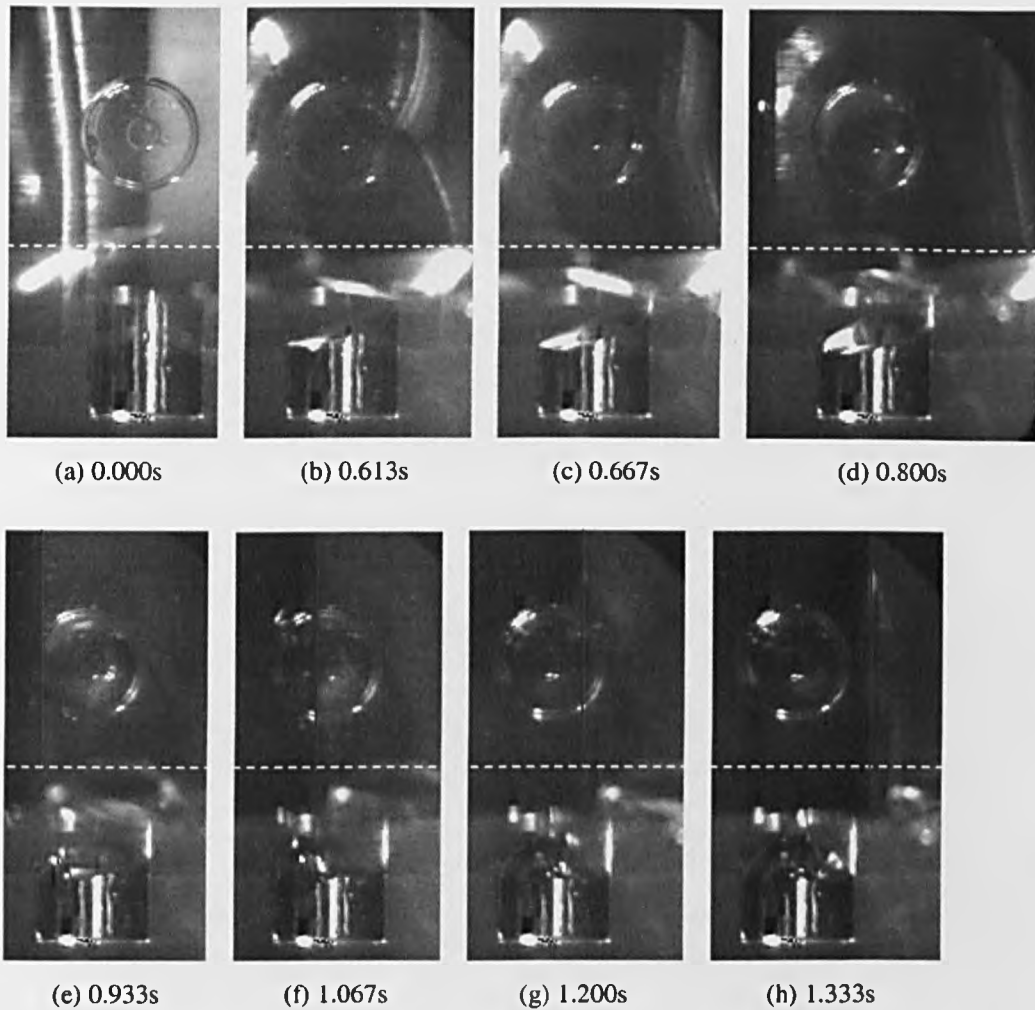


*Figure 6.18: Sequence of images showing the fluid meniscus entrapping air resulting in incomplete filling. The surface of entrapped air deforms as the blade passes. (Exp 21, ID# 6 setup: HVI 160, 10° blade, 0.10mm gap, 80.0V motor setting, and cell geometry 3×Ø3)*

The above example (Figure 6.18) is essentially the same as the previous example, but less fluid enters the cell before closure occurs (Figure 6.18(b)); the entrapped air is not a bubble, but the meniscus shape also develops into the dome-like structure (Figure 6.18(c)-(e)). The passing blade tip in this example influences the air surface shape in the cell. The tip passing over the cell causes fluid within the cell to move in its

direction and therefore the meniscus in contact with entrapped air distorts skewing in the opposite direction (Figure 6.18(f)). As the tip completes the pass, the air surface gradually resets to the stable dome-like structure (Figure 6.18(g)-(h)).

### **Conditions leading to incomplete filling**

Incomplete filling is observed with an extensive range of variable settings. The main difference for this filling behaviour, with the previous types, is that the menisci within the cells do not reach the base before cell closure occurs. Therefore increased cell depth (i.e. a small aspect ratio) encourages incomplete filling.

Setting the variables between partial filling and no filling should obtain incomplete filling behaviour. Increasing the blade speed and gap, and decreasing the blade angle introduce a reduced amount of fluid into the cell. Deformation of the entrapped air surface is more susceptible with thin layers of fluid at the cell top.

### 6.4.5 No fill

Figure 6.19 illustrates simplified screen and gravure cells remaining empty. This situation results in no ink transfer from such cells and is catastrophic to the print.

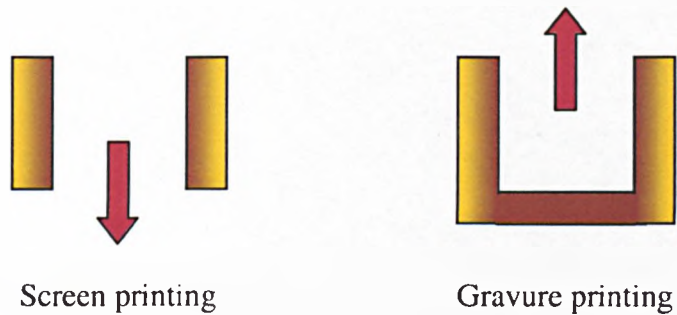


*Figure 6.19: Diagram of simplified screen and gravure printing cells containing no fluid.*

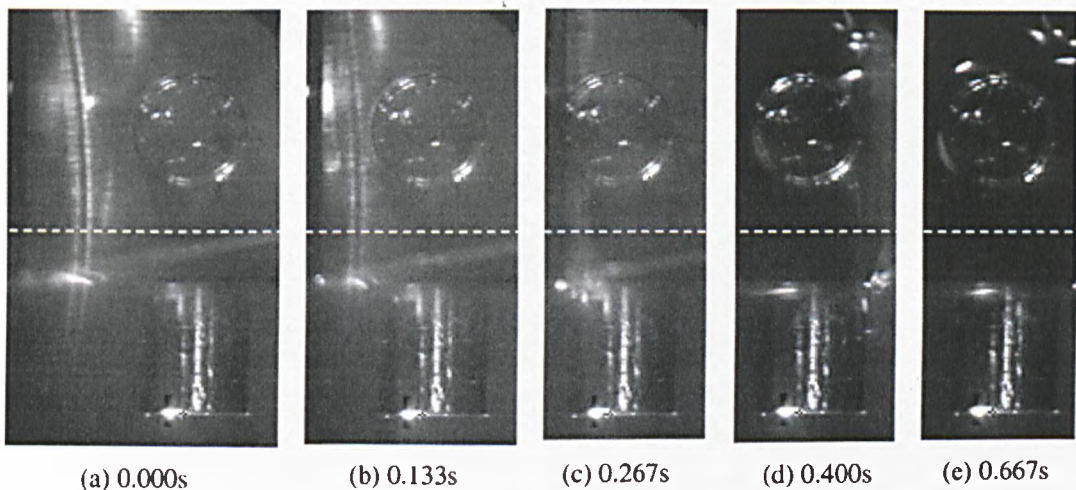


*Figure 6.20: Sequence of images showing the blade passing the cell with no fluid entering. (Exp 44, ID# 30 setup: HVI 160, 10° blade, 0.50mm gap, 100.0V motor setting, and cell geometry 3×Ø3)*

Figure 6.20 shows the blade tip pass over the cell without fluid entering. The fluid initially pins to the cell edge, continuing motion where cell is not present (as observed

in the previously described filling types). The fluid front reaches the far side of the cell without any fluid entering, resulting with the cell remaining unfilled.

### **Conditions for no filling**

The opposite variable settings to achieve complete filling result in no filling. Therefore to obtain no filling behaviour the blade angle should be small, the gap large and blade speed fast. These settings prevent the filling motion of menisci entering the cell.

A smaller aperture diameter of the cell increases the propensity for no filling. For true “no filling” the depth of the cell is irrelevant, and therefore eliminates a direct relation between aspect ratio and the filling type. The cell design and subsequent manufacture of the sharp edge encourages pinning; this phenomena promotes no filling behaviour.

#### 6.4.6 Incomplete filling changing to partial filling

This was observed to occur when an incompletely filled cell was not in an equilibrium state. It was observed for two instance types described below.

The first type occurred after the blade tip passed (shown in Figure 6.21). The time taken for incomplete filling to become unstable could occur within a second after the tip passed or be greater than several minutes, in which case the blade could not be responsible for the filling type change.

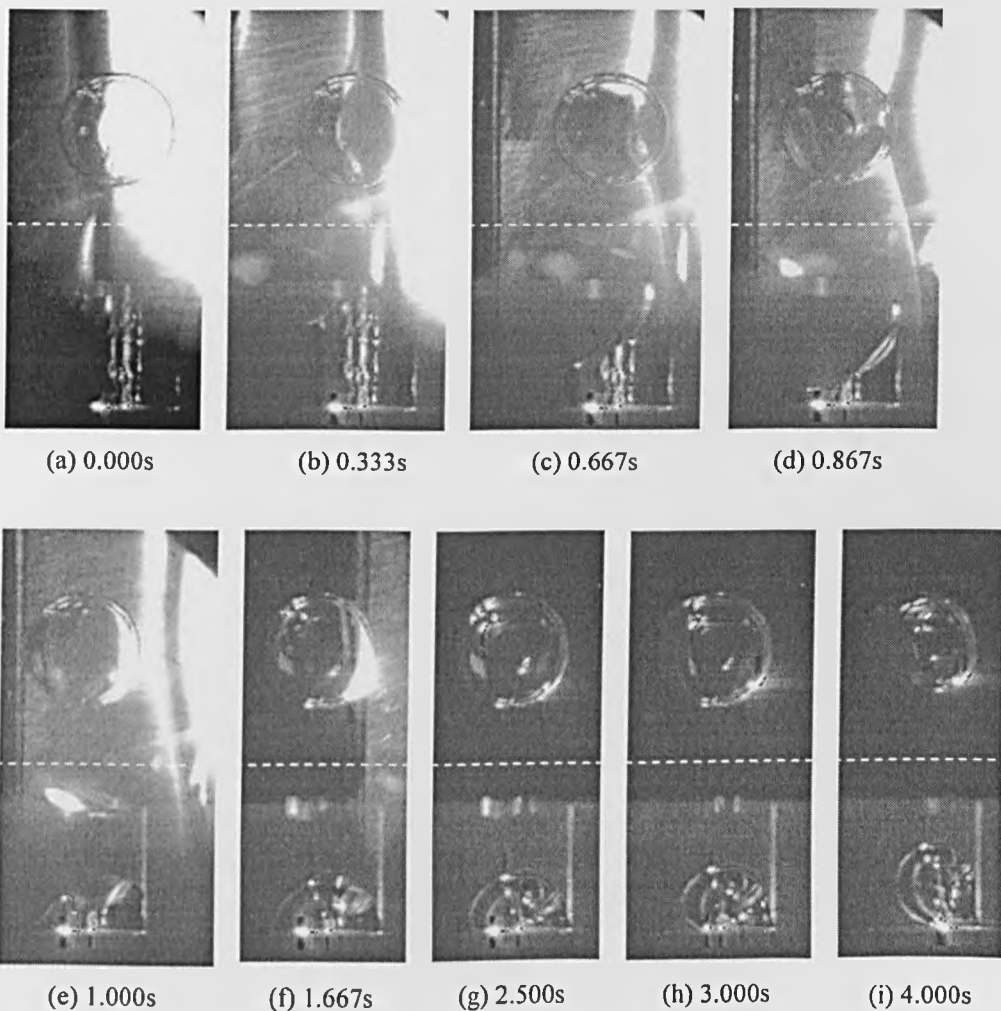


*Figure 6.21: Sequence of images (continued on the next page) showing the meniscus passing along the base of the cell forming an enclosed bubble which is subsequently removed. (Exp 35, ID# 21 setup: HVI 160, 30° blade, 0.10mm gap, 40.0V motor setting, and cell geometry 3×Ø3)*

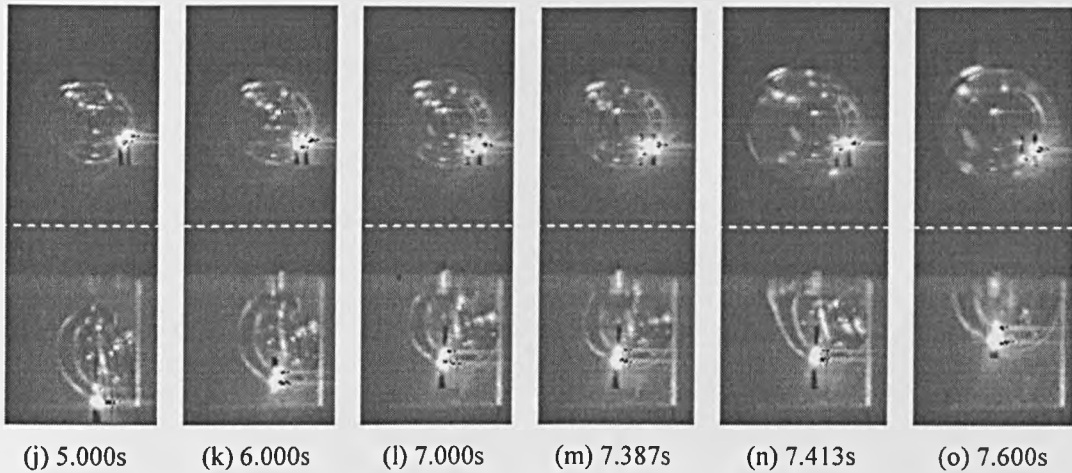


*Figure 6.21: Sequence continued from the previous page.*

The meniscus within the cell is initially pinned for the filling type to be termed incomplete filling (development shown in Figure 6.21(a)-(f)). Incomplete filling with the optimum fluid added to the cell without bubble formation involves pinning of the meniscus at the junction between cell wall and base; however the position of the meniscus does not necessarily remain stable, as observed in Figure 6.21(g). Breakdown in the pinning enables fluid to flow along the base and initiate formation of a bubble (Figure 6.21 (g)-(h)); air in the form of an enclosed bubble rises to the top of the cell and consequently is expelled, resulting in a delayed partially filled cell (Figure 6.21(i)-(o)).



The second type of incomplete filling showing a transition to partial filling is the case when the pinning in the cell occurs in close proximity to the top of the cell and so a very thin layer of fluid resides suspended across the cell top. Figure 6.22(a)-(d) show this is achieved with mechanisms of incomplete filling behaviour.

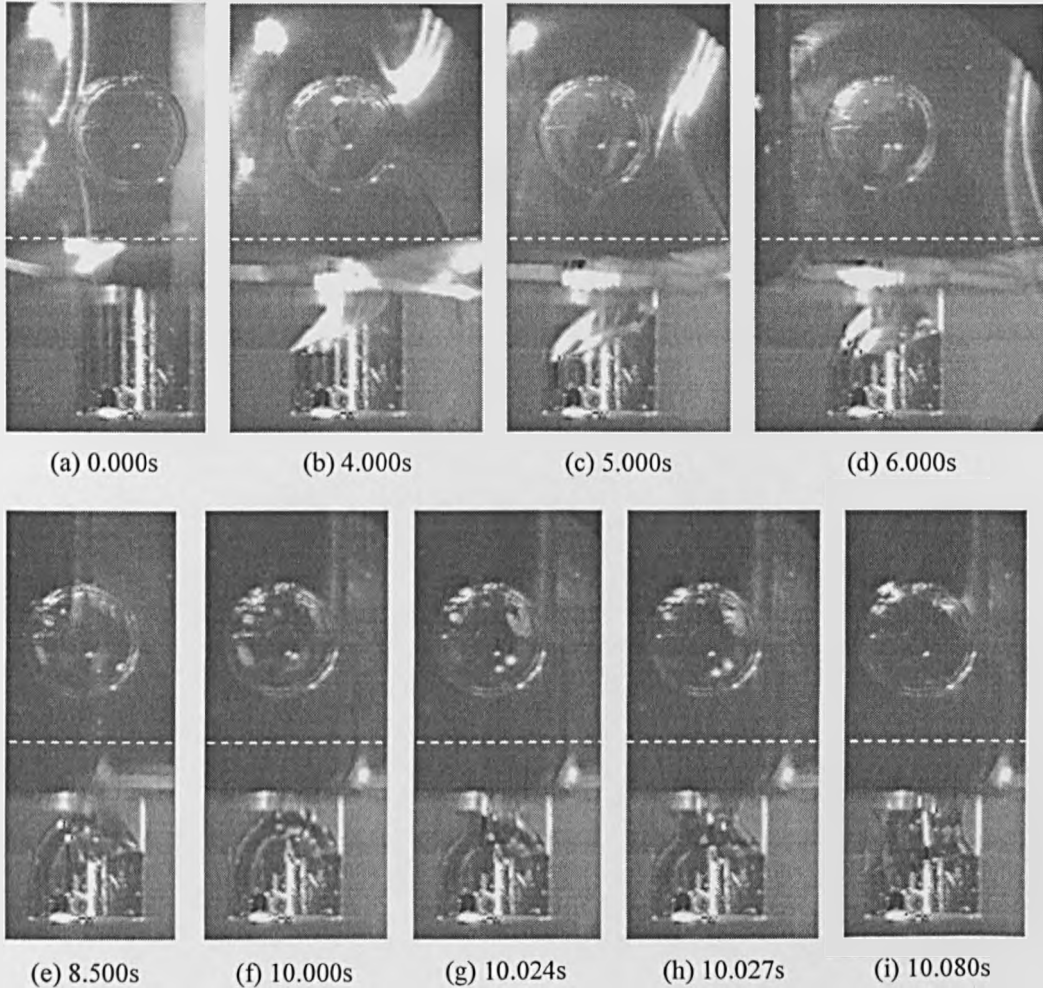


*Figure 6.22: Sequence of images (continued on the next page) showing a thin layer of fluid added to the cell which breaks converting incomplete filling to partial filling. (Exp 23, ID# 8 setup: HVI 160, 10° blade, 0.10mm gap, 13.50V motor setting, and cell geometry 3×Ø3)*

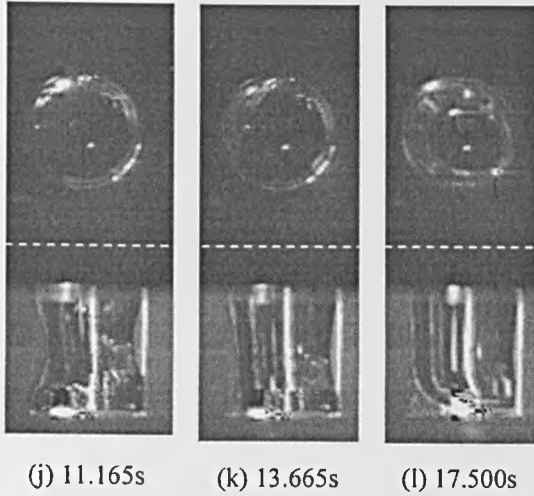


*Figure 6.22: Sequence continued from previous page.*

The passing of the blade tip fails to release the entrapped air (Figure 6.22(e)-(f)) and so the filling type is termed incomplete filling. After the blade passed the behavioural change in filling type occurs. The fluid layer at the cell surface is insufficiently thin to remain stable resulting with a break in the fluid (Figure 6.22(g)) and subsequent migration to cell walls flowing down to the base due to gravity (Figure 6.22(h)-(k)). The fluid eventually maintains a stable partially filled cell state (Figure 6.22(l)).

### 6.4.7 Effect of a manufactured flaw on the surface ahead of the cell

A surface defect occurred in the manufacture of a test piece containing a  $3 \times \text{Ø}3$  cell. The flaw was located approximately 1mm ahead of the cell, as shown in Figure 6.23(a).

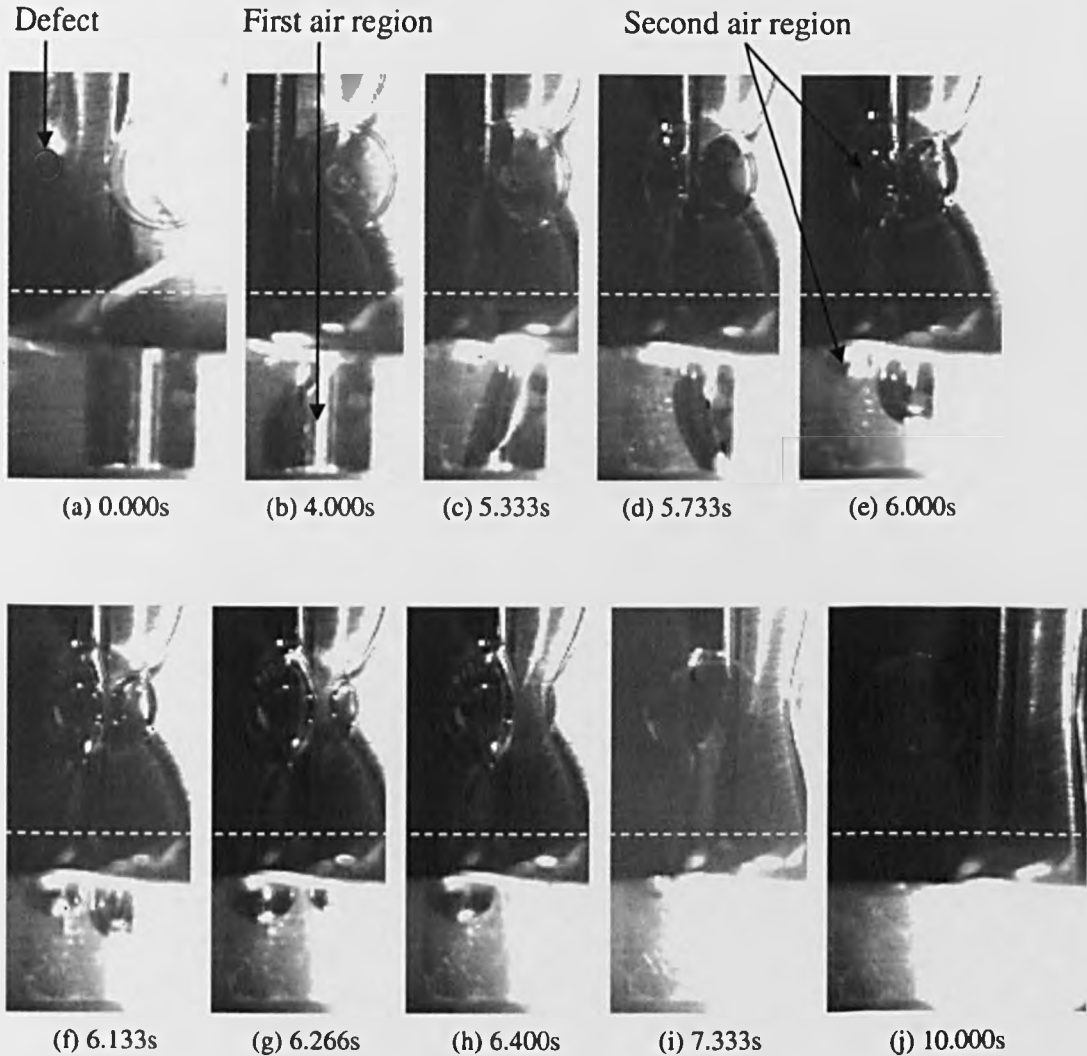


*Figure 6.23: Sequence of images showing the effect a manufactured surface flaw has on the filling behaviour. (Setup: EP80, 30° blade, 0.10mm gap, 10.00V motor setting, and cell geometry  $3 \times \text{Ø}3$ )*

The initial stages (Figure 6.23(a)-(c)) conform to that observed applying the same conditions to the test piece with no surface defect. The presence of the surface defect causes a second region of air, not observed with the other test pieces, to be introduced into the cell. This occurs behind the blade tip, where the surface defect causes

entrapment of air which is ultimately pulled into the cell by the fluid trail attached to the tip.

The air region behind the tip progressively increases, as shown in Figure 6.23(d)-(g); as this occurs the evacuation of air ahead of the tip continues, apparently unaffected by the second air region. Figure 6.23(h) shows the completion of the air removal from the first region. This impacts on the second air region, enabling further fluid to enter the cell (due to blade pressure) since the blade tip has not completed the pass over the cell (Figure 6.23(i)).

The final state of the cell is almost that of complete filling, but the presence of the second air region is not totally removed (Figure 6.23(j)); therefore the resulting filling is only partial. For the equivalent test piece, with no surface defect but the same setup of variables, the resulting behaviour was complete filling. Consequently the surface defect interfered with filling behaviour adversely, transferring less liquid into the cell. This highlights that the dynamics of multiple cells are more complex than those for single cells; nevertheless this work does highlight some important mechanisms at work for the filling process.

### 6.4.8 A comparison of fluid velocities within the cell

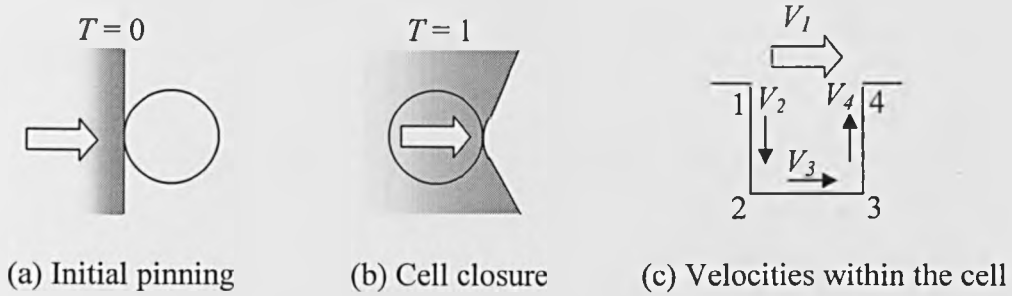


Figure 6.24: Simplified diagram of the view underneath the cell showing two key events used to define a non-dimensional time expression for filling behaviour comparison: (a) meniscus front reaches the cell edge and initially pins ( $T=0$ ); (b) cell closure occurs as the fluid coats the opposite cell edge ( $T=1$ ); (c) average velocities of the meniscus within the cell.

Figure 6.24(a)-(b) depict a method for comparing filling behaviour as a proportion of the overall time difference incurred between the initial pinning and cell closure (as calculated using equation (6.1)). Some filling behaviour continues after cell closure (i.e. bubble release in partial filling, and meniscus stabilisation in incomplete filling that occur at  $T>1$ ) but the type of filling behaviour encountered will be determined at or before  $T=1$ , and so for the majority of the following comparisons (sections 6.4.9-6.4.11) only the range  $0 \leq T \leq 1$  is applied.

$$T = \frac{t - t_{\text{initialpinning}}}{t_{\text{cellclosure}} - t_{\text{initialpinning}}}, \quad (6.1)$$

where  $T$  = non-dimensional time,

$t$  = actual filling time investigated,

$t_{\text{initialpinning}}$  = actual time initial pinning occurs,

$t_{\text{cellclosure}}$  = actual time cell closes.

Figure 6.24(c) highlights 4 key locations within a cell:

- 1 – corresponds with the top edge of the cell, where pinning initially occurs and where oil commences entry into the cell
- 2 – the location of where the oil meniscus within the cell reaches the base
- 3 – the location of where the oil has covered the base of the cell
- 4 – the location of where oil pulled across the cell reaches the far side establishing cell closure; it is also possible that the oil meniscus within the cell may also reach point 4

The average velocities of the oil meniscus within the cell ( $V_2$ ,  $V_3$ ,  $V_4$ ) are calculated between these 4 locations. The velocities are established by the cell dimensions and the time taken to reach each point (determined from the captured images of a specific filling type). At point 1 the oil initially pins, and hence entails a delayed entry into the cell.  $V_2$  is calculated as the average velocity of the fluid descending the side wall of the cell, and so does not include the delay time,  $t_{delay}$ .  $V_1$  is defined as the average velocity of the oil pulled across the top of the cell between point 1 and 4. Oil reaching all 4 points is dependent upon the filling type.

### Terminology

**Filling time** – time taken between these two events, for the advancing meniscus: initial reaching of the cell (point 1), to subsequently move across to the other side (point 4), closing the cell. Hence the filling time is defined as  $t_{cellclosure} - t_{initialpinning}$ .

**Non-dimensional time,  $T$**  – defined in equation (6.1).

**Delay,  $t_{delay}$**  – the time fluid is pinned at the edge of the cell top. I.e. the time taken for the fluid to initiate entry into the cell from initially reaching the cell (at point 1).

**Proportional time delay,  $T_{delay}$**  – delay term expressed non-dimensionally.  $T_{delay}$  is calculated using equation (6.1), where  $t_{delay}$  replaces the “ $t$ ” term.

### 6.4.9 Effect of varying fluid

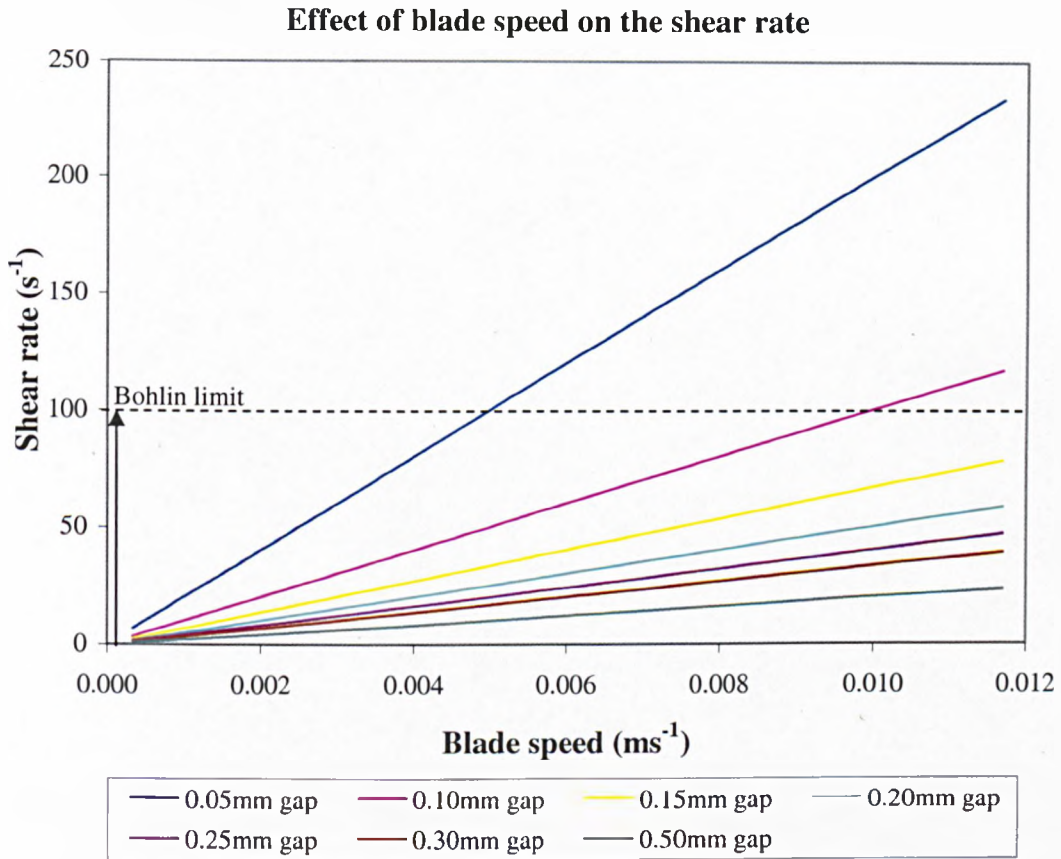


Figure 6.25: Graph of expected shear rates for the cell filling rig.

Figure 6.25 shows the calculated shear rates (using equation (6.2)) the blade exerts on the fluids used in the cell filling operation.

$$\text{Shear rate} = \frac{U}{H_o}, \quad (6.2)$$

where  $U$  is blade speed, and  $H_o$  is the gap between blade tip and test piece surface.

These values are significantly less than shear rates encountered in the process of screen printing. Since the gap setting (between blade tip and test piece surface) were rarely set less than 0.10mm, the expected shear rate range lies within that of the typical measurable Bohlin apparatus: 1-100s<sup>-1</sup> (depicted also in Figure 6.25). This validates

the direct use of the measured viscosities without applying power law adjustments (used previously in chapter 4 to extend the shear rate range).

The measured viscosities of the oils were shown previously in Figure 6.5 and indicated little variation in this range. Temperature affects oil viscosity; and so variation was minimised (monitored fluctuating  $\pm 0.5^{\circ}\text{C}$ ) enabling the test oil viscosities to remain constant.

After initial studies, HVI 60 proved to be an unsuitable fluid for the purpose of investigating the cell filling behaviour with the current rig arrangement. The initial region of spread of this fluid (i.e. prior to blade contact and sweep) varied greatly and is likely to be responsible for the subsequent inconsistent observed filling behaviour. The single groove of the test piece did not provide a constant initial state. Conversely for the other test oils (HVI 160, EP80 and EP90), this groove facilitated repeatable filling results by maintaining reproduction of the initial fluid state, and hence providing a basic means of control.

The introduction of further grooves along the boundary of the blade path may have improved the repeatability of the initial HVI 60 spread coverage, but this would inadvertently deteriorate captured image clarity of cell filling or even interfere with the spread along the test piece enforced by blade action.

Table 6.1 summarises a comparison of the filling behaviour between HVI 160, EP80 and EP90 oils. All other experimental setup variables were maintained: cell geometry  $3 \times \text{Ø}3$ ,  $10^{\circ}$  blade,  $0.0007\text{ms}^{-1}$  blade speed, and 0.10mm gap. The measured parameters are defined in section 6.4.8.



Oil	Av. viscosity (Pa.s)	Filling type	Filling time (s)	Delay, $t_{delay}$ (s)	$T_{delay}$	$V_1$ ( $ms^{-1}$ )	$V_2$ ( $ms^{-1}$ )	$V_3$ ( $ms^{-1}$ )	$V_4$ ( $ms^{-1}$ )
HVI 160	0.3	Complete	7.1	1.7	0.25	0.0004	0.0007	0.0047	0.0300
EP80	0.2	Complete	8.5	2.8	0.33	0.0004	0.0007	0.0027	0.0113
EP90	0.6	Incomplete	7.7	2.0	0.26	0.0004	0.0004	–	–

N.B. ■ indicates the control setup

*Table 6.1: Comparative results between fluids.*

Table 6.1 indicates that, in general, less viscous fluids are more likely to fill the cell successfully. The investigated fluids behaved approximately the same regarding the proportional time delay. EP90 (most viscous) was observed to have the slowest  $V_2$  speed, resulting with the meniscus within the cell not reaching the cell base and filling only incompletely. HVI 160 and EP80 behave comparably, both achieving base coating and complete filling. However, the lower viscosity oil (EP80) coated the base at a slower speed and overall cell closure required greater time to complete. This suggests the base coating and final evacuation of the air from the cell may not be directly related to the fluid viscosity, and instead the surface tension forces (particularly at the base corner edge) become the dominating force promoting surface wetting and filling of the cell.

### 6.4.10 Effect of blade variables

As shown previously in Figure 6.25 of section 6.4.9, the blade variables affect the shear rate of the fluid: higher shear rates were obtained with faster blade speeds and smaller gaps between blade tip and test piece surface. Although smaller gaps increased the filling ability, increasing the blade speed opposed this action. Therefore there is not a direct relation between generated shear rates and the filling behaviour.

The method described in section 6.4.8 is applied to compare a selection of blade parameter setups, taken from the much wider study. The experimental variables that were held constant were the choice of fluid (HVI 160 oil) and the cell geometry ( $3 \times \emptyset 3$ ); selecting a cell geometry with aspect ratio 1.0 justifies comparing velocities at various stages within the cell. The results are summarised in Table 6.2.

Blade angle	Blade speed ( $\text{ms}^{-1}$ )	Gap (mm)	Filling type	Filling time (s)	Delay, $t_{\text{delay}}$ (s)	$T_{\text{delay}}$	$V_1$ ( $\text{ms}^{-1}$ )	$V_2$ ( $\text{ms}^{-1}$ )	$V_3$ ( $\text{ms}^{-1}$ )	$V_4$ ( $\text{ms}^{-1}$ )
10°	0.0007	0.10	Complete	7.1	1.7	0.25	0.0004	0.0007	0.0047	0.0300
20°	0.0007	0.10	Complete	6.4	1.5	0.24	0.0005	0.0008	0.0058	0.0173
30°	0.0007	0.10	Complete	6.5	1.6	0.24	0.0005	0.0009	0.0042	0.0080
10°	0.0010	0.10	Partial	4.9	1.0	0.20	0.0006	0.0008	0.0010	0.0006
10°	0.0019	0.10	Incomplete	2.5	0.5	0.18	0.0012	0.0011	–	–
10°	0.0031	0.10	Incomplete	1.7	0.3	0.19	0.0017	0.0017	–	–
10°	0.0056	0.10	Incomplete	0.9	0.2	0.18	0.0033	0.0022	–	–
10°	0.0094	0.10	Incomplete	0.5	0.05	0.11	0.0059	0.0032	–	–
10°	0.0116	0.10	Incomplete	0.4	0.05	0.12	0.0075	0.0042	–	–
10°	0.0007	0.15	Partial	8.0	1.5	0.18	0.0004	0.0005	0.0009	0.0045
10°	0.0007	0.20	Incomplete	8.2	1.7	0.21	0.0004	0.0004	–	–
10°	0.0007	0.25	Incomplete	7.8	2.3	0.29	0.0004	0.0004	–	–
10°	0.0007	0.30	Incomplete	8.4	2.4	0.29	0.0004	0.0004	–	–
10°	0.0007	0.50	Incomplete	7.3	2.1	0.30	0.0004	0.0004	–	–

N.B. ■ indicates the control setup

Table 6.2: Comparative results of the blade variables: angle, speed and gap.

## Blade speed

The dominant parameter affecting  $V_1$  is the blade speed: increasing the blade speed increases  $V_1$ . This impacts on the overall filling time of the cell and also upon the delay, with the effect of reducing both of these times (shown in Table 6.2). In general, increasing the blade speed also reduces the proportional time delay. However, the position of the advancing meniscus, on the test piece surface, progresses further along the cell edge (before fluid enters the cell) for faster blade speeds (highlighted in Figure 6.26). This implies that the speed of the advancing meniscus slows significantly (more so for faster blade speeds) between the delay and cell closure events. Therefore once fluid initiates flow into the cell, the effect on the flow over the cell decreases. However this effect is not strong enough to greatly influence the filling behaviour, and so faster blade speeds have the effect of decreasing the filling ability observed.

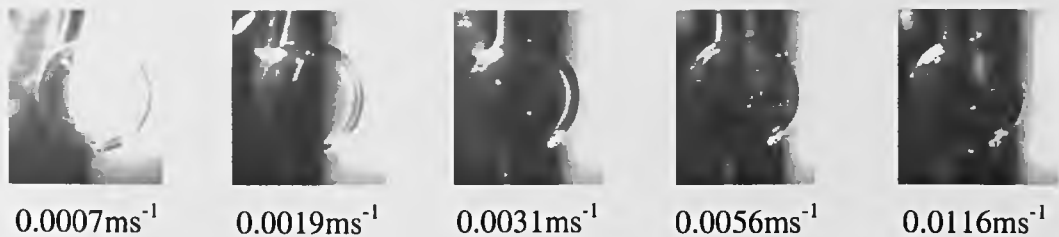


*Figure 6.26: Photographs captured from the underside view of the cell, showing the fluid meniscus position as fluid commences entry to the cell (i.e. end of delay period) for a range blade speeds.*

$V_2$  increases with blade speed, but not as significantly as  $V_1$ . Therefore the likelihood of the meniscus reaching the base is gradually reduced as blade speed increases. This effect also adds to the decreasing probability of filling ability as the speed of the blade is increased. The blade speed has no obvious effect on  $V_3$  or  $V_4$ .

## Blade Angle

The blade angle has negligible effect on the proportional time delay value, with no obvious effect on  $V_1$  or  $V_3$  (shown in Table 6.2). However, the blade angle does significantly affect initial filling of the cell, in particular between the delay stage and

the fluid reaching the base of the cell (i.e.  $V_2$ ). Increased blade angle causes an increase in  $V_2$ .

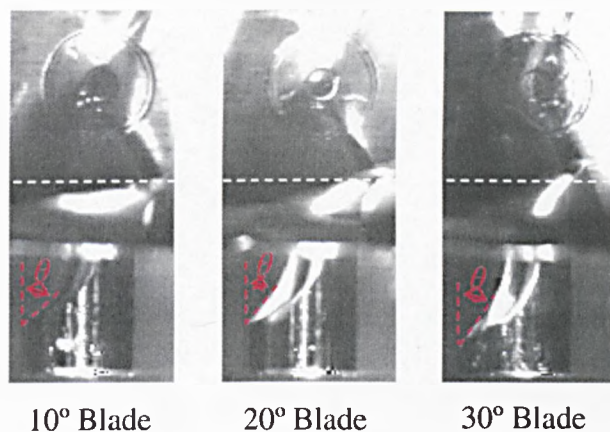


*Figure 6.27: Effect of blade angle on filling.*

The photographs in Figure 6.27 are selected at the same non-dimensional time,  $T=0.65$ . The captured images show that a larger blade angle induces a smaller contact angle of the meniscus during descent – the distance the fluid is pulled across the cell top remains approximately constant but the flow down the cell wall is affected by the blade angle. The variation in the highlighted angles of Figure 6.27 indicates a greater velocity ( $V_2$ ) is experienced with the operation of greater angled blades. This is confirmed in Table 6.2. It is this behaviour that promotes cell filling ability, demonstrating that the larger blade angles improve the filling ability.

In the cases compared in Table 6.2, it is noted that  $V_4$  decreases as the blade angle decreases. However, the fluid movement coating up the cell wall is more likely to be limited by the position and surface tension of the fluid meniscus, rather than direct blade interaction.

The relation between the average velocities is:

$$V_1 < V_2 < V_3 < V_4$$

## Gap

The selected setups shown in Table 6.2 observed a range of filling types from complete filling (0.10mm gap) to incomplete filling (greater than 0.20mm gap). For all incomplete filling types there is no value of  $V_3$  or  $V_4$ . Varying the gap had no effect on  $V_1$ ,  $V_3$ , or  $V_4$ .  $V_2$  appears to decrease as the gap distance is increased, therefore reducing filling ability; this is observed most significantly when looking at the different filling types i.e. increases in the gap eventually generate incomplete filling behaviour, at which point  $V_2$  appears to be constant, but is slower than the values recorded for smaller gaps producing complete and partial filling types. Generally the indication is that proportional time delay increases as gap increases. This combined with the effects the gap has on  $V_2$  confirms that increased gap distance impedes filling ability.

### 6.4.11 Effect of cell geometry

Table 6.3 summarises the effect of cell geometry (depth, diameter) on the filling behaviour observed, with the other variable conditions are maintained constant: HVI 160 oil, 10° blade, 0.0007ms<sup>-1</sup> blade speed, and 0.10mm gap. The speed of the advancing meniscus,  $V_1$ , is unaffected by the cell geometry. An increased filling ability is observed with larger diameter and shallower cells.

Cell depth (mm)	Cell $\varnothing$ (mm)	Volume (mm <sup>3</sup> )	Aspect ratio	Filling type	Filling time (s)	Delay, $t_{delay}$ (s)	$T_{delay}$	$V_1$ (ms <sup>-1</sup> )	$V_2$ (ms <sup>-1</sup> )	$V_3$ (ms <sup>-1</sup> )	$V_4$ (ms <sup>-1</sup> )
1	2	$\pi$	2.0	Bubble at surface	4.2	3.5	0.82	0.0005	0.0038	0.0042	Not clear
2	1	$0.5\pi$	0.5	Incomplete	2.9	2.3	0.77	0.0003	0.0014	–	–
2	2	$2\pi$	1.0	Bubble at surface	4.3	3.5	0.80	0.0005	0.0017	Not clear	Not clear
2	3	$4.5\pi$	1.5	Complete	7.4	2.6	0.35	0.0004	0.0005	0.0031	0.0375
3	2	$3\pi$	0.7	Incomplete	4.8	3.5	0.74	0.0004	0.0013	–	–
3	3	$6.75\pi$	1.0	Complete	7.1	1.7	0.25	0.0004	0.0007	0.0047	0.0300

N.B.   indicates the control setup   indicates secondary control setup

Table 6.3: Comparative results of the cell geometry.

#### Cell depth

The evidence in Table 6.3, suggests that the cell depth has no influence upon the delay time,  $V_1$ ,  $V_3$ , or  $V_4$ . The speed of the meniscus to reach the cell base,  $V_2$ , is not constant – an increased cell depth reduces the average  $V_2$  speed. This, together with the physical increase of the length of cell wall to coat increases the time taken for the meniscus to reach the cell base. The implication of this is a reduction in the filling ability. Increasing the cell depth reduces the likelihood of the meniscus coating the base. Indeed for an infinite cell depth there is no mechanism for either complete or partial filling types, resulting in only incomplete filling being achievable. Therefore this suggests that in screen printing, if the mesh threads do not have sufficient contact with the surface ink is to transfer onto (i.e. the substrate) effective coating of the

“base” will not be achieved. An increased mesh thickness may therefore deteriorate quality of ink transfer.

### **Cell diameter**

The cell diameter affects the filling time – the greater the diameter, the longer it takes for the advancing meniscus over the top of the cell to reach the far side and close it, therefore increases the filling time. This in turn, increases the filling ability of such a cell. The influence of the cell diameter on the fluid movement within the cell seems to have little effect.

In general (from Table 6.3), the smaller the diameter, the greater the proportional time delay: diameters of 1mm and 2mm had significantly greater values of  $T_{delay}$ , than the cells with a diameter of 3mm. The impact of increasing the  $T_{delay}$ , will reduce filling ability. The shape of the corner at the top of the cell is likely to greatly influence the delay times experienced. All the cells investigated had sharp corners which promote a pinned effect of the advancing meniscus, preventing direct entry into the cell. A smoother corner edge should reduce pinning, and therefore reduce the time required for the fluid to reach the cell base – improving likelihood of filling. Investigating such top edge corner shapes is beneficial to understanding the filling behaviour of screen meshes, since the individual threads have smooth shape changes (mimicking a compressed circular cross-sectional profile). Therefore it is expected that the delays experienced here from the sharp 90° corner would be significantly less, or perhaps not even exist for threads in a screen mesh – promoting cell filling. However, the complex geometry of interwoven threads creates regions that do have less smooth geometric changes than considering an individual thread.

### Aspect ratio

As noted previously, the filling ability of a cell increases for larger diameter and shallower cells. Since the aspect ratio is defined as diameter ÷ depth, this implies the higher the aspect ratio improves the success of filling. The aspect ratio however cannot be used as an isolated parameter for indication of expected filling behaviour. The results summarised in Table 6.3, show different filling types are observed for two cells of the same aspect ratio (2×Ø2 and 3×Ø3 both have aspect ratios of 1.0). The smaller of the two cells, is less likely to fully evacuate all air. This is due to the pressure differences across the air-oil interface, which is greater for smaller bubbles (defined by Laplace's Law – equations (6.3-6.4) – previously described in Figure 4.14 of section 4.3.1) inherent to form within the smaller sized cells. The smaller cells effectively support air bubbles at the surface, resulting in air residing within the cell. The pressure exerted from the blade pass is less likely to have an impact upon the smaller bubbles or smaller regions of entrapped air, which also adds to the filling restriction.

#### Laplace's law:

$$\text{For a single interface surface, } \Delta P = \frac{2\sigma}{r}, \quad (6.3)$$

$$\text{and for a bubble interface, } \Delta P = \frac{4\sigma}{r}, \quad (6.4)$$

where  $P$  is pressure,  $\sigma$  is surface tension, and  $r$  is the radius of a capillary.

### Edge effect

The initial edge at the top of the cell has been noted to delay the filling procedure. This type of edge may effectively be termed a convex edge. The concave edge at the cell base promotes filling. This geometry causes the fluid to excel in proximity to such a feature – observed in all images captured from underneath the cell where fluid commences coating of the base. This is similar to the observations of Dong, M. and Chatzis, I. (1995), where the fluid wetting within the edge region of square capillaries corners progressed ahead of the flow.



## 6.5 Summary

The conclusions from the work of this chapter are:

- Observed cell filling behaviour can be categorised by four types: complete filling, partial filling, incomplete filling and no fill.
- Complete filling occurs when all air within the cell is removed prior to cell closure action.
- Partial filling occurs due to entrapment of air within the cell as it closes. The fluid meniscus in the cell is at the base, enabling the air (in the form of a bubble) to rise to the cell surface and be removed.
- Incomplete filling is similar to partial filling, except the fluid meniscus does not reach the cell base prior to cell closure. Entrapped air remains within the cell.
- No filling occurs when the blade passes without causing any fluid to enter the cell.
- More complete filling was encountered through adjusting the variable settings to: slow blade speed, large blade angle, small gap between blade tip and test piece surface, low viscosity fluids, and large diameter shallow cells.
- Fluid viscosity is most dominant on the filling behaviour as the fluid enters the cell until it reaches the base – lower viscosity fluids are more likely to reach the base quicker, promoting cell filling. However, viscosity does not seem to be directly related to the base coat behaviour.
- The blade speed dominates the speed of the advancing meniscus over the top of the cell,  $V_1$ , and so greatly influences the cell closure time. The blade angle dominates the meniscus speed entering the cell and descending towards the cell base,  $V_2$ , and therefore greatly influences the observed filling behaviour.
- Increased cell depth delays the meniscus reaching the base, without which complete filling becomes unattainable. Increased cell diameter increases the time the cell is effectively open, which assists with the total replacement of air by the filling fluid.

## Chapter 7

### Conclusions and future work

---

#### 7.1 Conclusions

In chapter 3, the experimental work into screen printing investigated the effect of a wide range of press settings on the average wet film thickness transferred to the print (prior to any subsequent treatment such as curing). The peel-off rate and substrate roughness were shown to have had no significant influence; however, the type of ink and mesh geometry greatly affected the printed film thickness.

The work of chapter 3 was extended in chapter 4 to establish the percentage of fluid transferred in the process by considering both the initial and final states of the mesh and substrate. This investigation, during the metering squeegee stroke, revealed that a given mesh fills to approximately the same initial volume regardless of the ink type.

Photographic images taken from above the screen mesh, revealed that the metering stroke only partially filled the mesh – this was confirmed using white light interferometry. In general, ink fills to a level approximately half way up the mesh. This finding led to amendments to the basic model (model 1 – chapter 4) used by industry for estimating printed film thickness (which assumes the initial state of a mesh to be full), and to the subsequent development of models (models 2-5 – chapter

4) to more accurately predict the initial state of the ink and mesh geometry. Although these models of the (simplified) threads within a mesh show that fine geometric detail has little influence on the volume unoccupied by the threads, the mesh thickness is a dominating factor for determining the potential volume available in a mesh to hold ink.

Models 4 and 5 incorporate the concept of ink filling to a predefined height within the mesh. Both calculate accurately (at a cost of considerably complicating the mathematics of the problem from the original model 1) the amount of ink within a mesh compared with the experimental initial filled mesh state, and so these models may be used with confidence as a predictive tool for other mesh geometries not necessarily considered in this thesis. This amount of initial ink, expressed as a thickness, is suggested here to be a more realistic estimate of the current theoretical maximum ink thickness (calculated from model 1), which severely over-predicts the thickness. Even with these models, if the assumption of 100% ink transfer is applied, as commonly done, the printed film thickness would still be significantly larger than observed in practice.

As observed in chapters 3 and 4, the transfer from the meshes did vary depending on the fluid and mesh geometry, resulting in printing a range of film thicknesses. The work of chapter 4 discounted the fluid viscosity or density as factors responsible for any significant variation in printed film thickness.

Photographic images of the mesh state after ink transfer to the substrate, revealed two types of menisci shape for the residual ink: square-like and circular. Circular menisci are consistent with a greater amount of ink remaining in the mesh, after the print process is completed. The surface tension forces of these circular menisci (held within the mesh cells) are more prone to draw ink from the knuckle regions and effectively “close” the cell. This behaviour was captured photographically. The location of the “closed” cells varied and so was independent of local cell features.

The Ink Transfer Model (ITM) – developed by Abbott, S., Gaskell, P. and Kapur, N. (2001, private communication) – was used to predict the fractional transfer from an

idealised mathematical mesh and the expected printed thickness. The ITM calculations are heavily dependent upon the geometry of an isolated thread rather than the overall woven structure of the thread when combined into a mesh. When compared to the experimental results of chapters 3 and 4, the calculated results under-predict the percentage transfer whilst the film thickness results are consistently over-predicted – this is as a consequence of the assumption that the mesh initially fully fills with ink.

In chapter 5, computational fluid dynamic (CFD) simulations were used to model the problem of the mesh separating from the substrate (as studied experimentally in chapters 3 and 4) using FLOW3D software. The problem studied is that of a stationary obstacle (representing a mesh thread) positioned almost in contact with a lowering plane (mimicking the action of peel-off of a lowering substrate), surrounded by fluid as a simplification of the screen printing process. As observed in chapters 3 and 4, both the thread diameter and spacing influences the final film thickness. Increasing the spacing between successive threads introduces more ink into the system. Consequently this increases the amount of ink transferred to the substrate under the action of peel-off.

Using FLOW3D, a parametric study over a wide range of fluid properties (viscosity, surface tension, contact angle, density) showed that none of them had an effect on either the average print thickness or the percentage of ink transferred to the substrate. In addition, there was no variation with the peel-off rate. This is in accordance with the experimental studies into these parameters.

The predictions of the shape of the interface from FLOW3D revealed an elongated ink bridge between the base of the thread and the ink on the substrate surface, which ultimately broke to give a print.

In chapter 6, experiments were conducted to further the understanding of the ink filling behaviour of screen meshes, through the use of an idealised cell geometry that was filled with oil by the action of a moving blade. The images of the filling process, captured at high speed, identified four types of filling behaviour: complete filling –

removal of all air; partial filling – entrapped air that forms a bubble before being released from the cell; incomplete filling – entrapped air which is not removed; and no fill.

Increased filling ability is observed using a large blade angle operating at a slow swipe speed, with the tip positioned close to the test piece surface. The fluid beneath the blade advances towards the cell (under the blade swipe action) and is initially held due to a pinning effect at the edge of the cell. In general, the pinning on a smaller diameter cell results by the higher proportional time delay (proportion of delay of the overall filling time). Once the fluid overcomes the pinning at the cell edge, low viscosity fluids exhibit a better filling ability. The geometry of the cell is found to greatly affect the filling, and fluid is more likely to fill a cell of large diameter and small depth.

## **7.2 Suggested future work**

### **7.2.1 Mesh filling process**

Based on the mesh ink filling investigations of chapter 4, these areas warrant further studies:

Firstly an experimental study of how ink is introduced into and subsequently moves through the mesh could provide significant insight into the mechanisms involved. Experimentally, this could be investigated by starting with the mesh in contact with a clear (viewing) window and use of a high speed camera.

Secondly, it is fundamental to the understanding of screen printing as to why the mesh fills to the level it does, which is significantly below the height of the mesh thickness. There are a number of possibilities as to why this occurs, including:

- Deformation of the mesh as the blade passes may account for the under-filling.
- Deformation of the substrate.
- Fluid interaction with the blade, mesh and substrate.

- Deformation of the blade to follow the local contours of the mesh, effectively “digging” into the cells and removing ink in a scraping action from below the peak height.

Some preliminary insight into the filling of an isolated idealised cell was investigated in the work of chapter 6. To extend this work, and make it more relevant to the screen printing process, there are a number of proposals. Firstly the geometry of the cell could be altered to more accurately represent that of a screen mesh cell:

- The filling of cells other than of circular cross sections, such as square, could be studied to represent the filling behaviour of mesh features such as an individual cell opening.
- Altering the profile of the cell edges, so that these are rounded would have a profound effect on the pinning experienced prior to fluid entering the cell, and would also model a real thread surface more faithfully.
- The presence of the surface defect ahead of the test cell had significant impact on the filling characteristics, and so this suggests a sequence of cells would display a more complex behaviour than that of a single cell. Experiments of multiple cell sequences could reveal the mechanisms involved.

The effect of contact angle on the filling behaviour of idealised cells can be investigated by changing the material of the test piece and hence the cell walls.

### **7.2.2 Mesh emptying process**

From chapters 3, 4 and 5, more work needs to be done to assess the parameters that determine the ink transfer from the mesh. The experimental results reveal the type of ink used affects this transfer, and yet the numerical results indicate that the transfer behaviour does not depend on viscosity, surface tension, density or even surface energy of the mesh. The transfer variations could be due to factors such as particle interaction or viscoelastic behaviour of the ink. A detailed assessment of these factors needs to be carried out.

It is also suggested that viewing the mesh from above, to observe and capture images of the behaviour of the fluid as it is transferred onto the substrate are carried out.

From the FLOW3D simulations of chapter 5, which predicted a peaked feature on the substrate beneath the thread, it is suggested that the development of such a feature is experimentally studied by:

- Design and manufacture a purpose built rig to investigate the specific problem of how a single idealised cell empties (similar to the cell filling rig).
- Adapting of the cell filling rig to also mimic cell emptying – fluid fills the cell via blade action (into the cell from the top) and empties via a controlled lowering action (representing peel-off) of the cell base (or substrate) from the cell – then the transfer for each type of cell filling (e.g. incomplete filling) can also be explored.

The FLOW3D results calculate a region of ink suspended on the underside of the threads' surface throughout the printing process. It is proposed that experimentally the underside state of the mesh (after the printing stage) is examined to investigate the presence of this feature. The presence of ink below the mesh may affect the transfer of ink to the substrate of following prints – and so is another suggested area of study to further the understanding of thread interaction in the screen printing process.

### **7.2.3 Simulations and geometric thread models**

From the development of geometric thread models in chapter 4 and the simulations performed in chapter 5, suggestions for further work include:

- More complex geometry, to represent screen mesh threads, can be imported into FLOW3D after being created in a CAD package, such as IDEAS. Through this the woven structure of the threads can be considered.

- The initial ink height within the FLOW3D representation of the mesh unit should be lowered from the 100% initial filled level, so as to be more comparable with this observation that was experimentally revealed.
- FLOW3D encountered problems of interface smearing. Other CFD methods will not have this issue, although will typically be less efficient, but it is suggested that these may also be investigated.
- The geometry of the threads in model 5 (chapter 4) assume a constant circular cross-section which results in the model's value of mesh thickness being significantly greater than experimental meshes. It is suggested that the geometry of model 5 be adapted from a constant circular cross-section to that of an ellipse, based upon the measurements taken from a typical mesh – to ensure the mesh thickness is the same.

#### **7.2.4 Related work**

Further information about the true mesh geometry can be investigated by:

- Gaining more information about the knuckle geometry.
- Generating a replica of the mesh geometry (through the use of a mould) will greatly assist as a measuring aid.



## Appendix 1

### Experimental measurement theory of viscosity

A rheometer is used to measure fluid viscosity. It consists of 2 stainless steel plates, one of which remaining stationary whilst the other rotates at a known angular velocity. The shear rate that the fluid has exerted on it is calculated (using equation (A1.1)). The rheometer measures the produced torque which is converted into shear stress, and combined with shear rate to establish the viscosity (using equations (A1.2) and (A1.3)).

$$\text{Shear rate} = C_1 \times \text{torque} \quad (\text{A1.1})$$

$$\text{where } C_1 = \frac{3}{2\pi r^3}$$

$$\text{Shear stress} = C_2 \times \omega \quad (\text{A1.2})$$

$$\text{where } C_2 = \frac{1}{\theta} \text{ (for cone and plate set-up)}$$

$$\text{and } C_2 = \frac{3r}{4} \text{ (for parallel plate set-up)}$$

$$\text{Viscosity} = \text{shear stress} \div \text{shear rate} \quad (\text{A1.3})$$

There are several combinations of geometries that can be used in a rheometer. Two common types are: cone and plate, and parallel plates. The advantage of using the cone geometry is that the shear rate remains constant across the radius of the cone. This is not the case for the flat plates though, and so should not be used if a specific value of shear rate is required. The advantage of using the parallel plates is that the viscosity at higher shear rates can be investigated. With parallel plates the gap between them is not pre-determined and so can be varied; decreasing the gap results in higher shear rates.

The tip of the cone is removed and essentially blunted, when manufactured, to avoid surface damage to the plate surface whilst in operation. The gap between the cone and plate is established by theoretically extending the cone geometry to form a tip which does contact the plate, as shown in Figure A1.1.

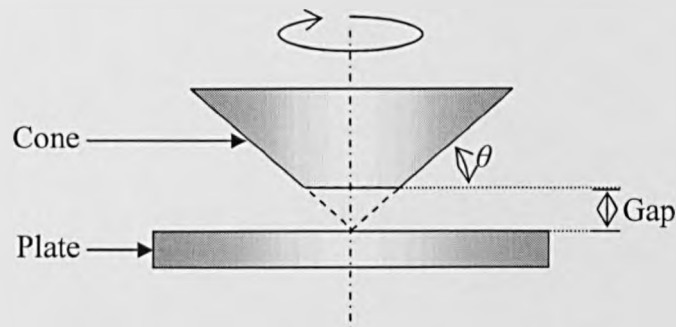


*Figure A1.1: Diagram determining the required gap used between cone and plate surfaces.*

The required gaps for the cone and plate geometry are shown in Table A1.1; the volume of test fluid to introduce, ensuring correct filling, is also shown.

Cone geometry	$\theta$	Gap ( $\mu\text{m}$ )	Volume of test fluid (ml)
4° 40mm diameter	4°	150	1.4
1° 60mm diameter	1°	30	1.0

*Table A1.1: Gap setting and test fluid volume for available cone and plate geometry.*

## **Appendix 2**

### **Printed film thickness**

---

The following graphs are the printed film thickness results for the 90-40 and 120-34 meshes. The same 10 printing fluids were tested at the 10 peel-off rates as described in section 3.2. The ITM model results are also plotted.

## 90-40 mesh results

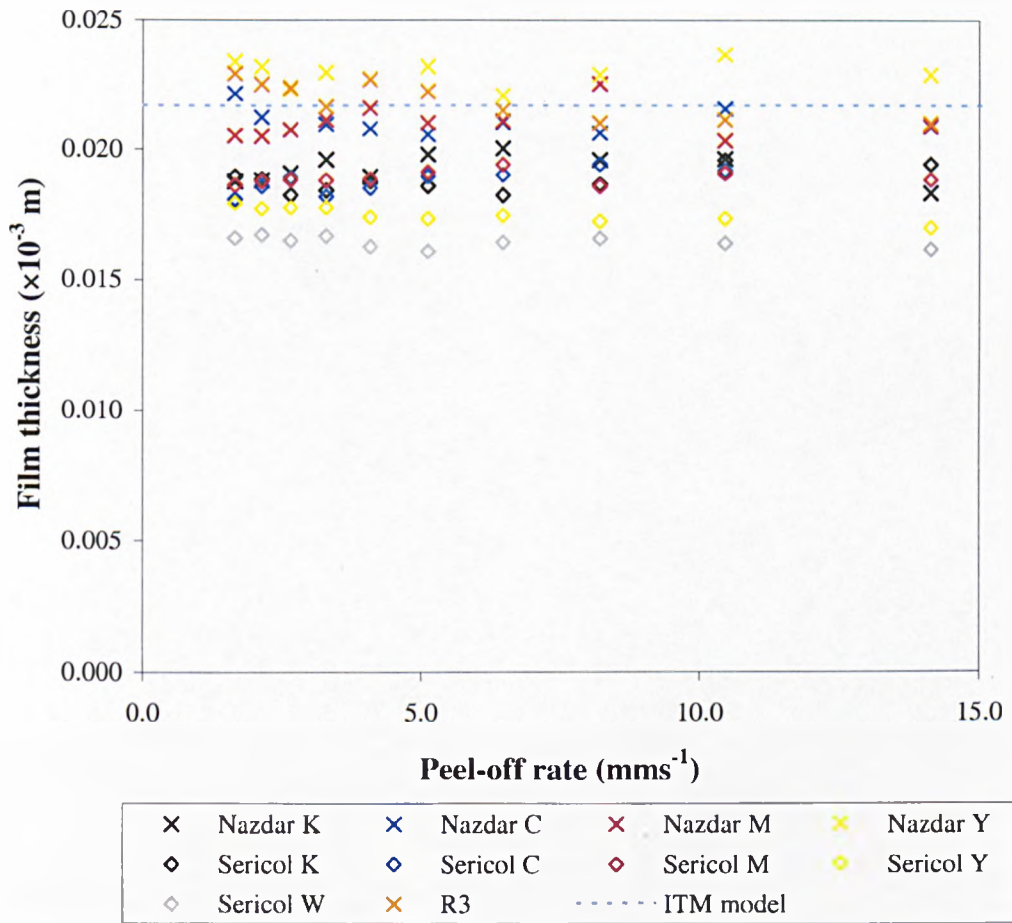


Figure A2.1: Average film thickness using 90-40 mesh for a range of mesh-substrate separation rates.

## 120-34 mesh results

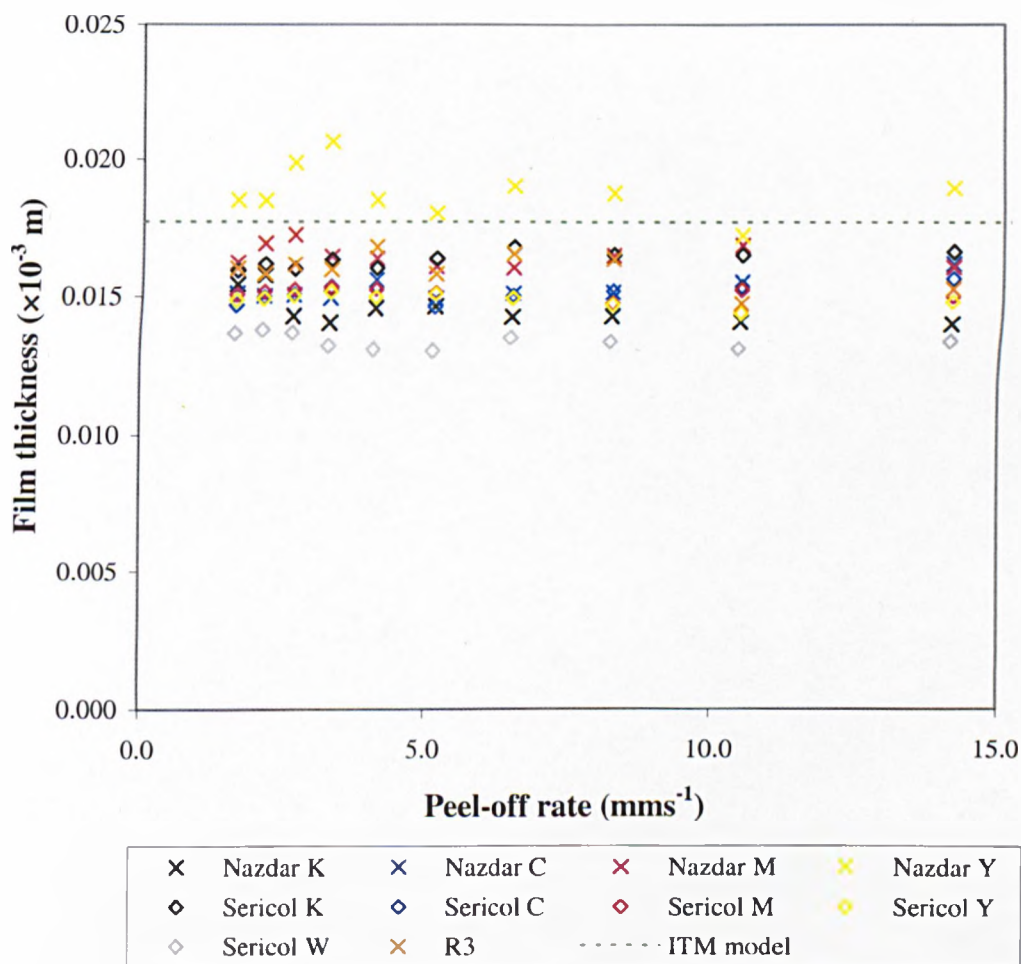


Figure A2.2: Average film thickness printed on 120-34 mesh for a range of mesh-substrate separation rates.

### Discussion of these results

The results for printing with these meshes agree with those in section 3.4.1. For each mesh the printing fluid used causes a spread of printed film thicknesses. Each individual test fluid generates significantly less film thickness variation. The peel-off rate has negligible effect on the film thickness. ITM thickness predictions tend to be greater than the experimental printed thicknesses.

## **Appendix 3**

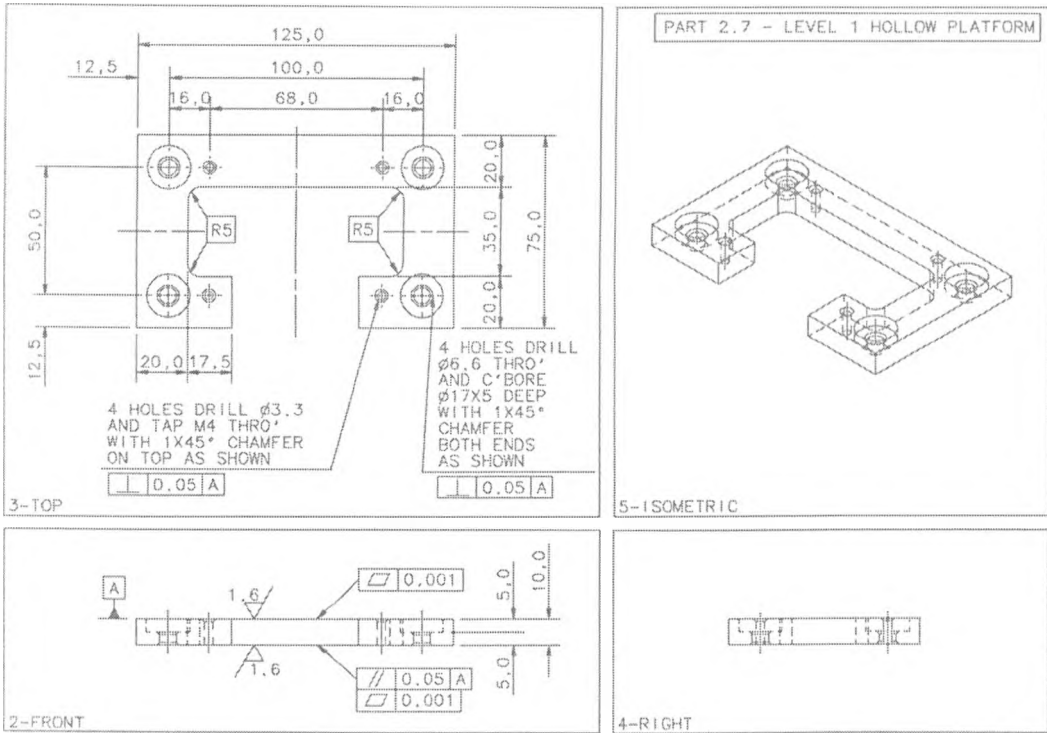
### **Cell filling rig design drawings**

---

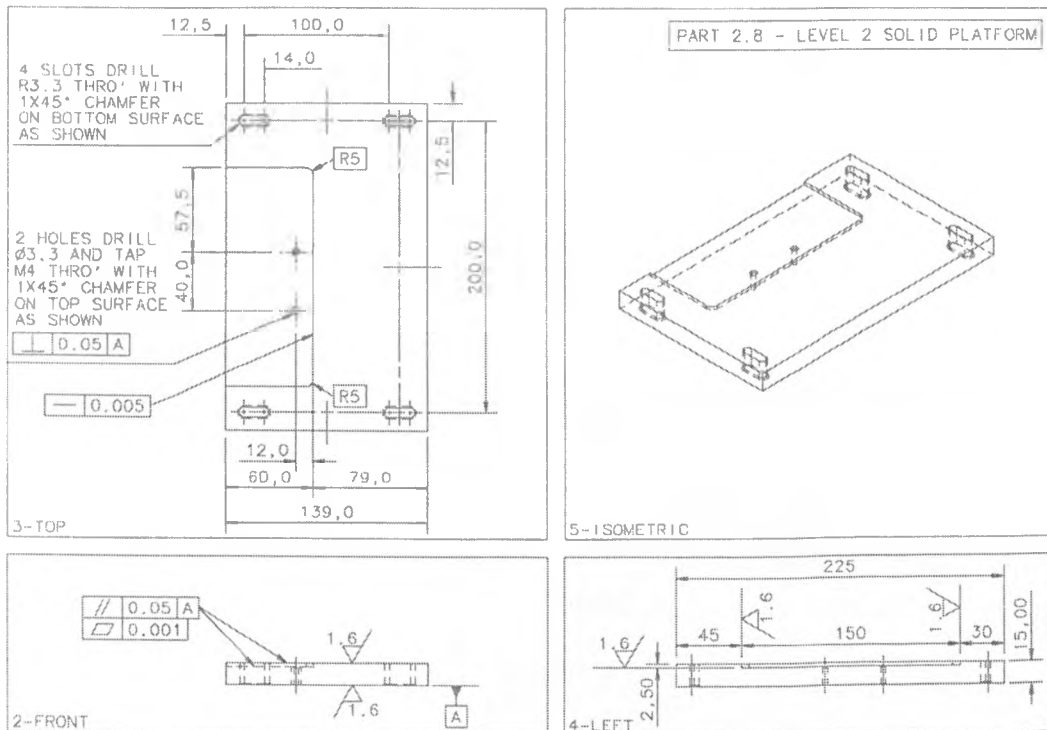
The draft design drawings of rig components in sections A3.1-A3.4 were produced using IDEAS software. These drawings were generated from initial construction of 3D models for each component. Assembly drawings to combine rig components were also produced. Section A3.5 highlights the mounting positions of the support stands on the breadboard. Section A3.6 contains images of the components forming the rig at various stages showing where each is aligned and positioned.

### A3.1 Platform designs

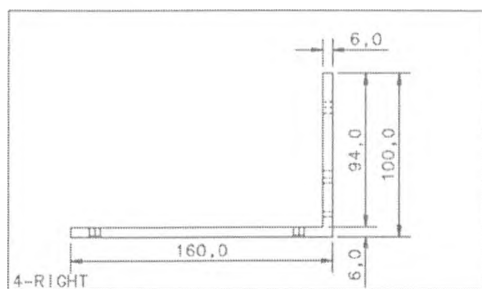
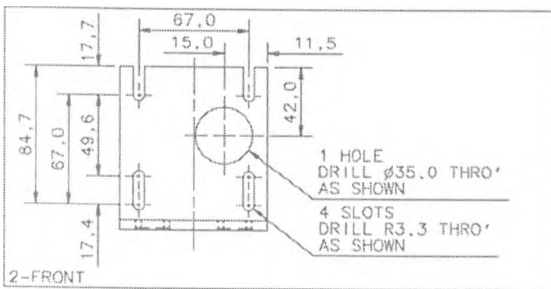
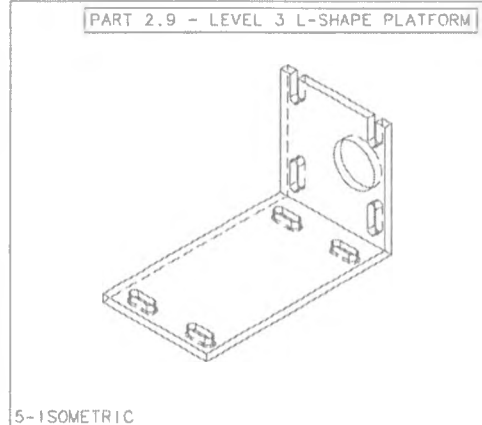
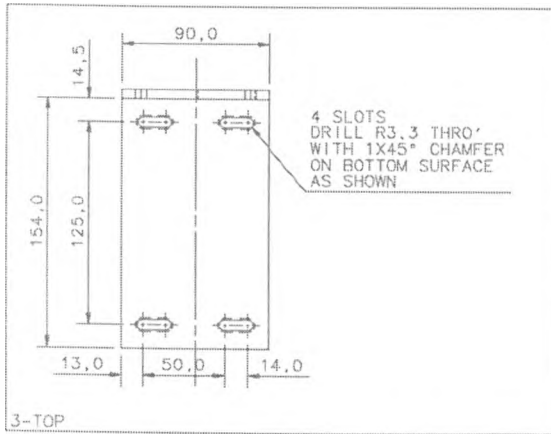
#### Platform 1



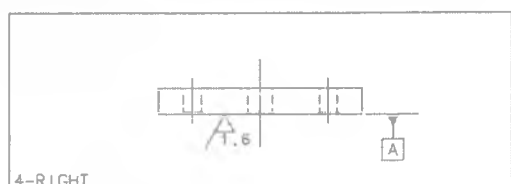
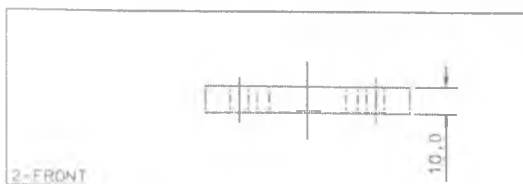
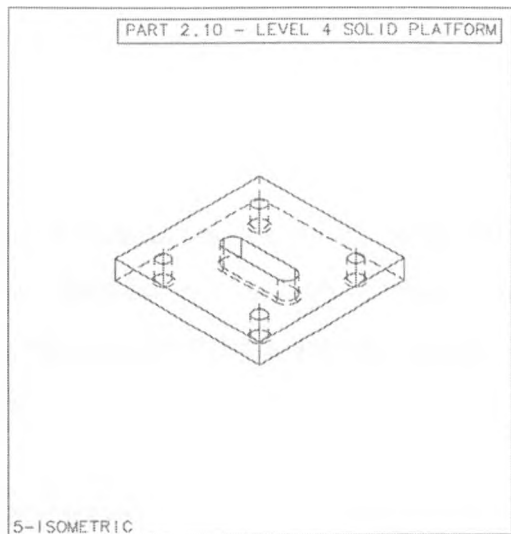
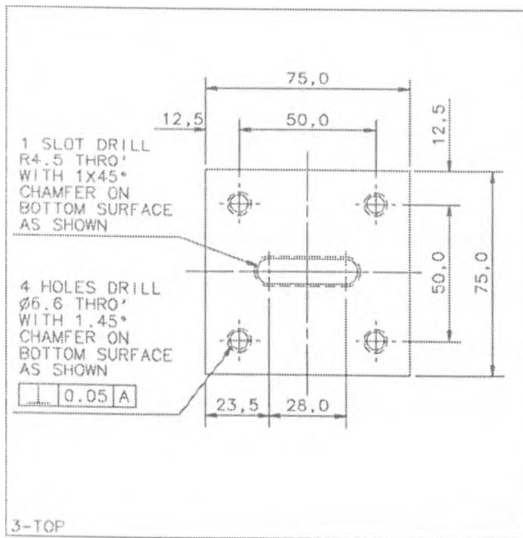
#### Platform 2



**Platform 3**



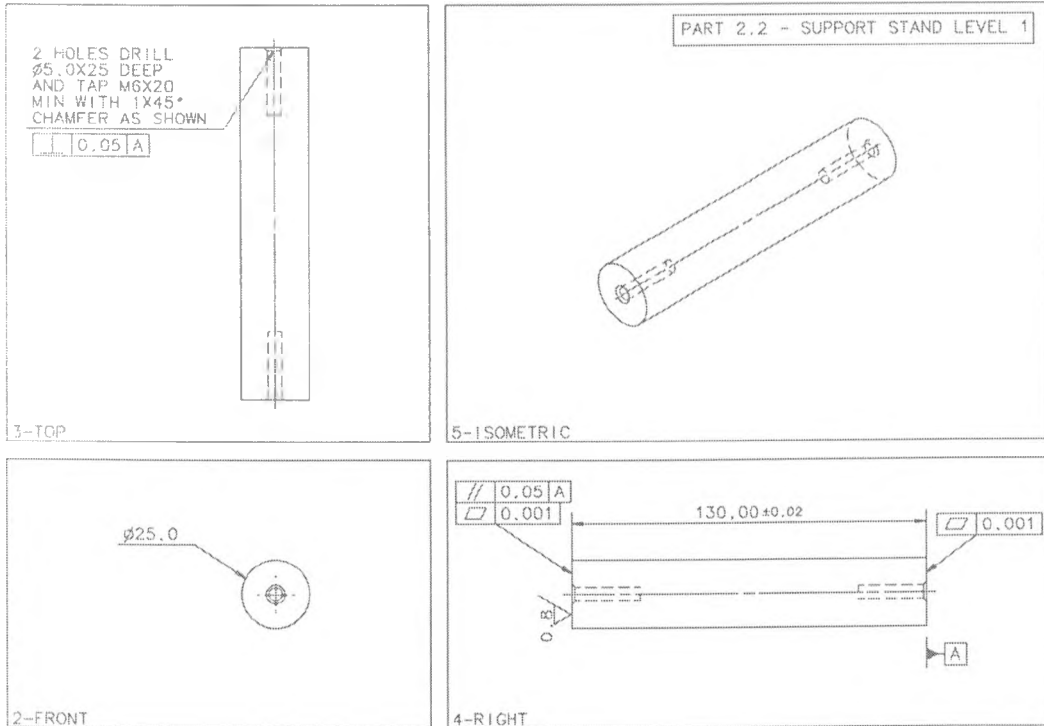
**Platform 4**





## A3.2 Support stand designs

### Support stand for platform 1

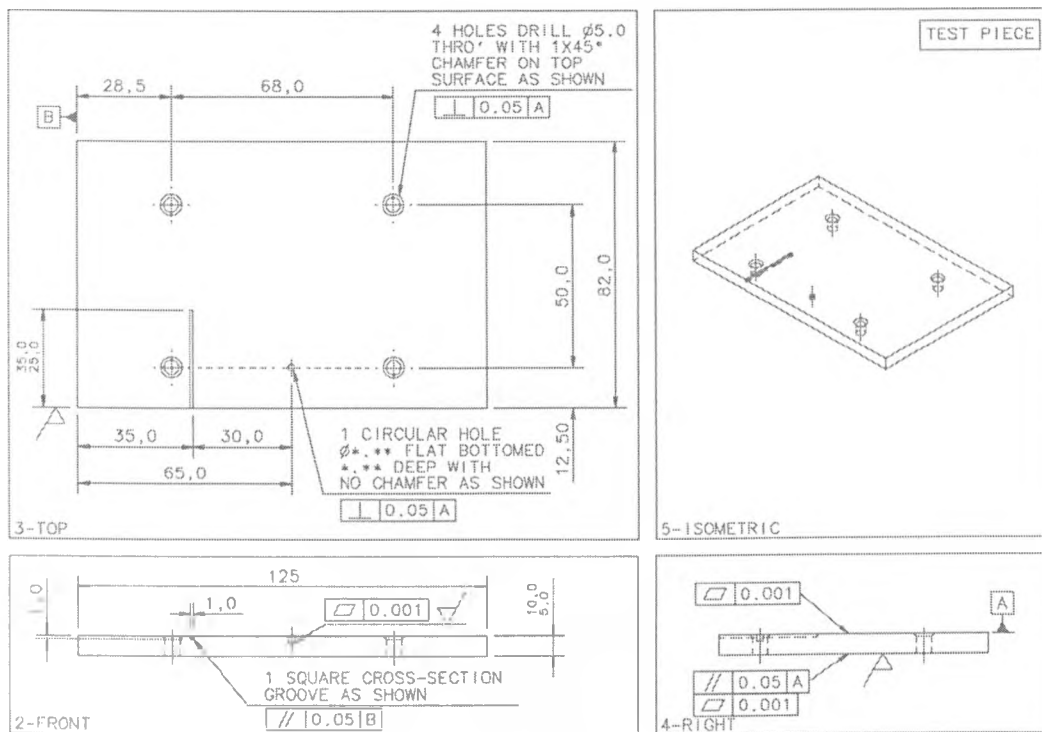


### Support stand for platform 2-4

The draft drawings of these components are not included in this section, since they are essentially the same as the support stand for platform 1. The only difference is the length of the stand, which is  $130.00 \pm 0.02$  mm for platform 1 support stands. The equivalent length for platform 2-4 stands are:

- support stand for platform 2:  $175.00 \pm 0.02$  mm
- support stand for platform 3:  $147.00 \pm 0.02$  mm
- support stand for platform 4:  $158.00 \pm 0.02$  mm

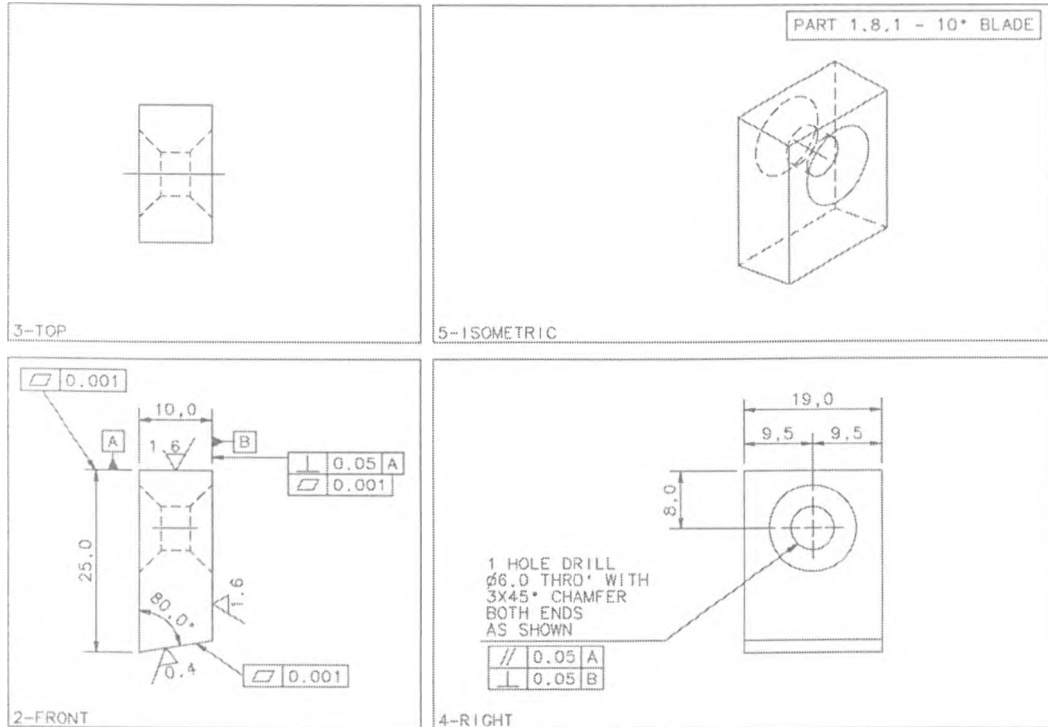
### A3.3 Test piece and cell design



The test cell is labelled “1 circular hole”. The draft drawing does not specify the hole diameter or depth, but the required dimensional range of the test cell is shown in Table 2.2 of section 2.3.2.

### A3.4 Blade drive “inbuilt” components

#### 10° blade

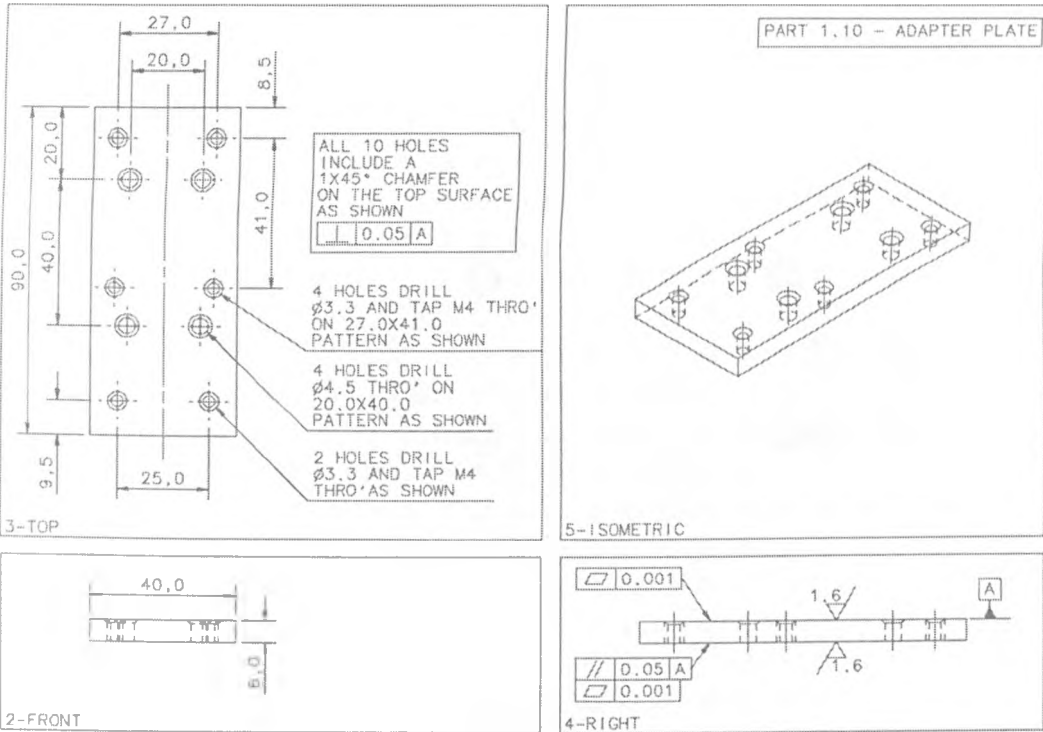


#### 20° and 30° blades

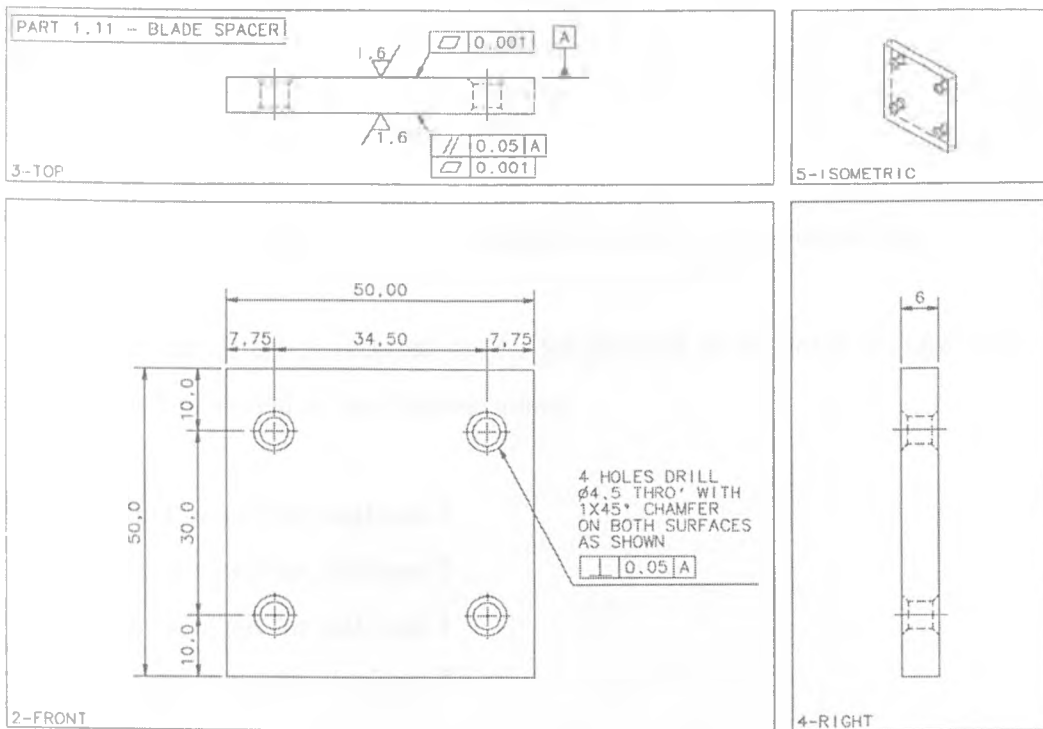
The draft drawings of these blades are not shown in this section, due to the similarity with the 10° blade. The only difference is the tip angle, shown as 80.0° on the above draft drawing for the 10° blade. The appropriate tip angle for the 20° blade is 70.0°, and 60.0° for the 30° blade. The machining directions on the 10° blade draft drawing are the same as those specified for the 20° and 30° blade manufacture.



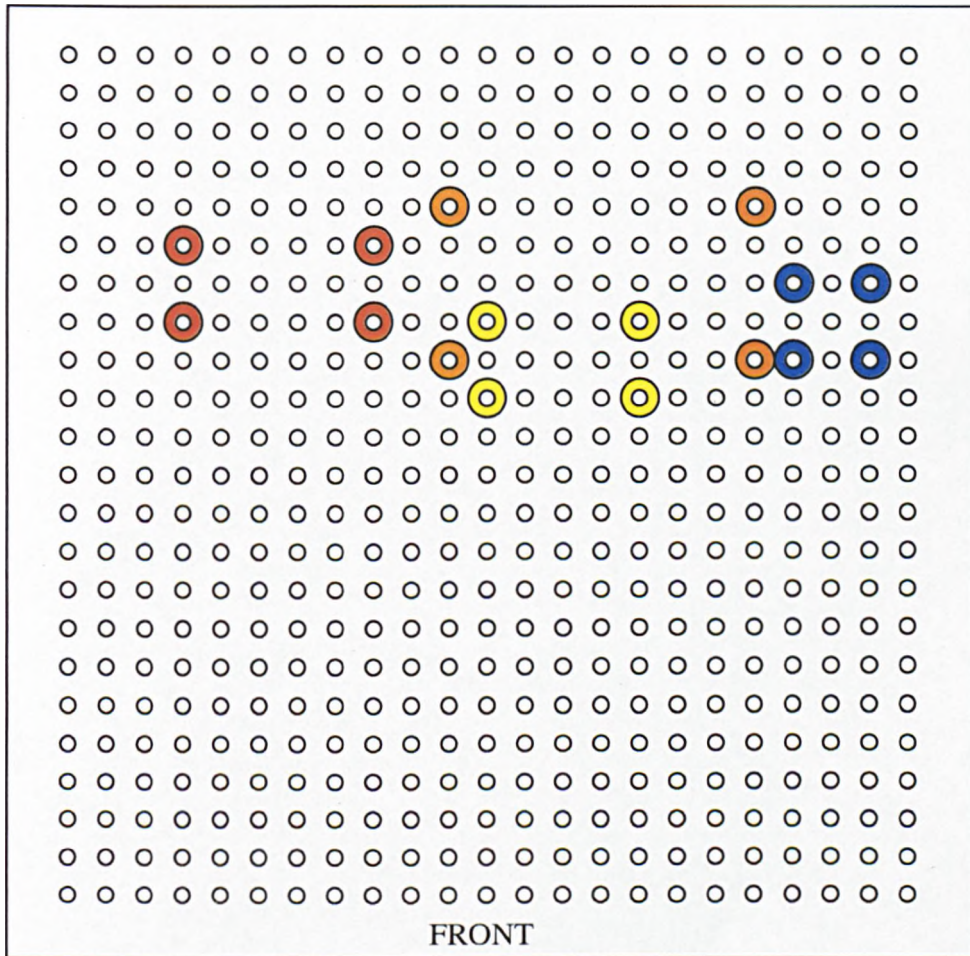
**Adaptor plate**



**Blade spacer**







### A3.5 Location of the support posts on the breadboard



*Figure A3.1 Location sites of the support stands on the breadboard.*

The support stands are positioned on the breadboard as shown in Figure A3.1. The stands are colour-coded in the diagram using:

-  Support stand for platform 1
-  Support stand for platform 2
-  Support stand for platform 3
-  Support stand for platform 4

### A3.6 Combination of the components constructing the rig

Figure A3.2-A3.4 show 3D images generated using IDEAS software. The images show how the components align with each other to form the rig.

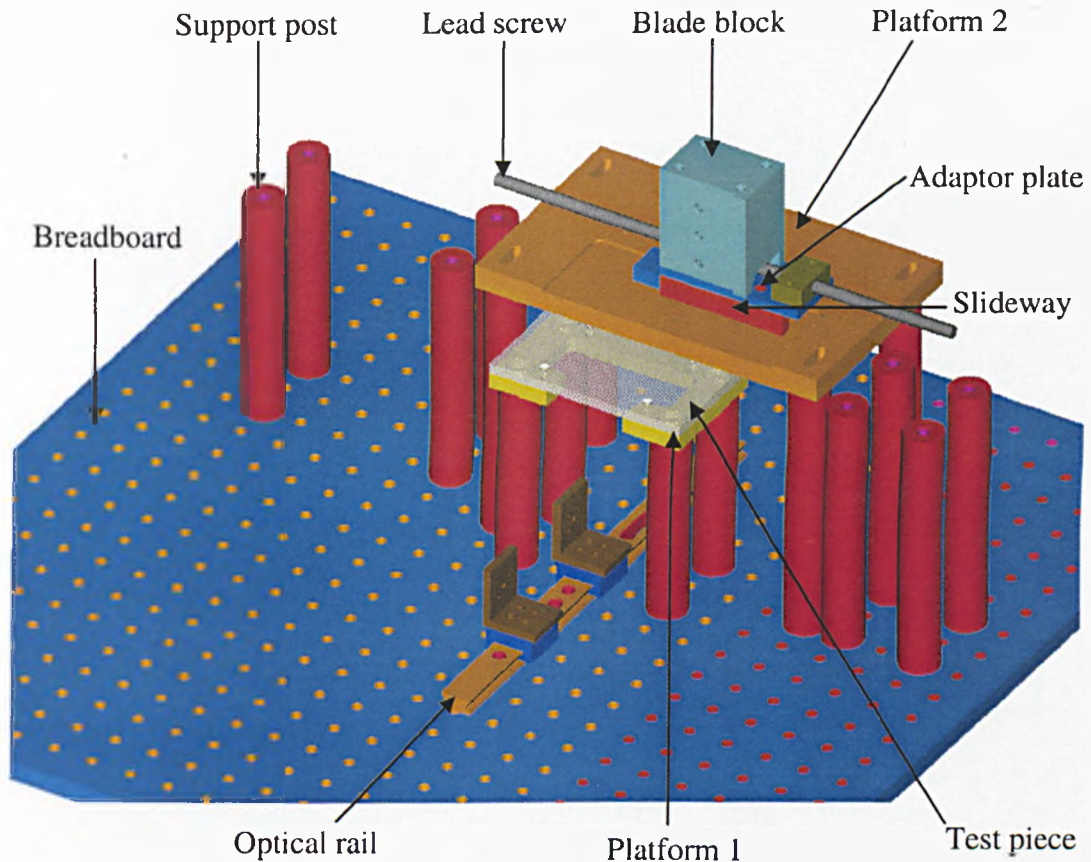


*Figure A3.2: Image of some of the rig components mounted on the breadboard.*

Figure A3.2 shows some of the rig components. All support stands are located on the breadboard as shown in Figure A3.1. The optical rail is also directly mounted to the breadboard. On the rail, there are two wide optical rail carriers each connected to a short angle bracket which hold the beam splitter and right-angled mirror.

Platforms 1 and 2 are also shown in Figure A3.2. The test piece is located on platform 1. Platform 2 has a slideway fixed to it; secured to the slideway is the adaptor plate, which the blade block and lead screw are attached to.

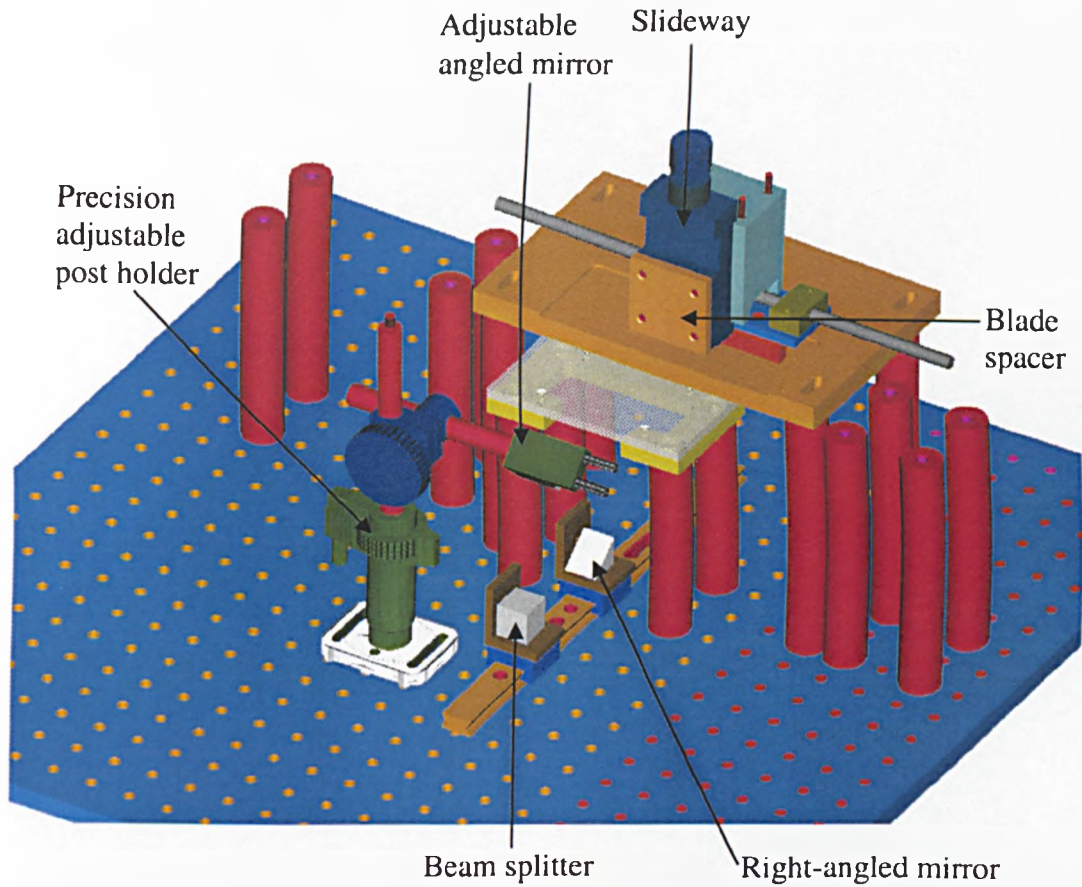


*Figure A3.3: Image of the rig partially completed incorporating all optical components and some components of the blade drive section.*

Figure A3.3 introduces a few more components than shown in Figure A3.2. The beam splitter and right-angled mirror are in place, and the remaining optical components are shown in alignment with these and the test piece cell. The blade spacer is fitted to the slideway that was not shown in Figure A3.2, and this component is mounted to the blade block.



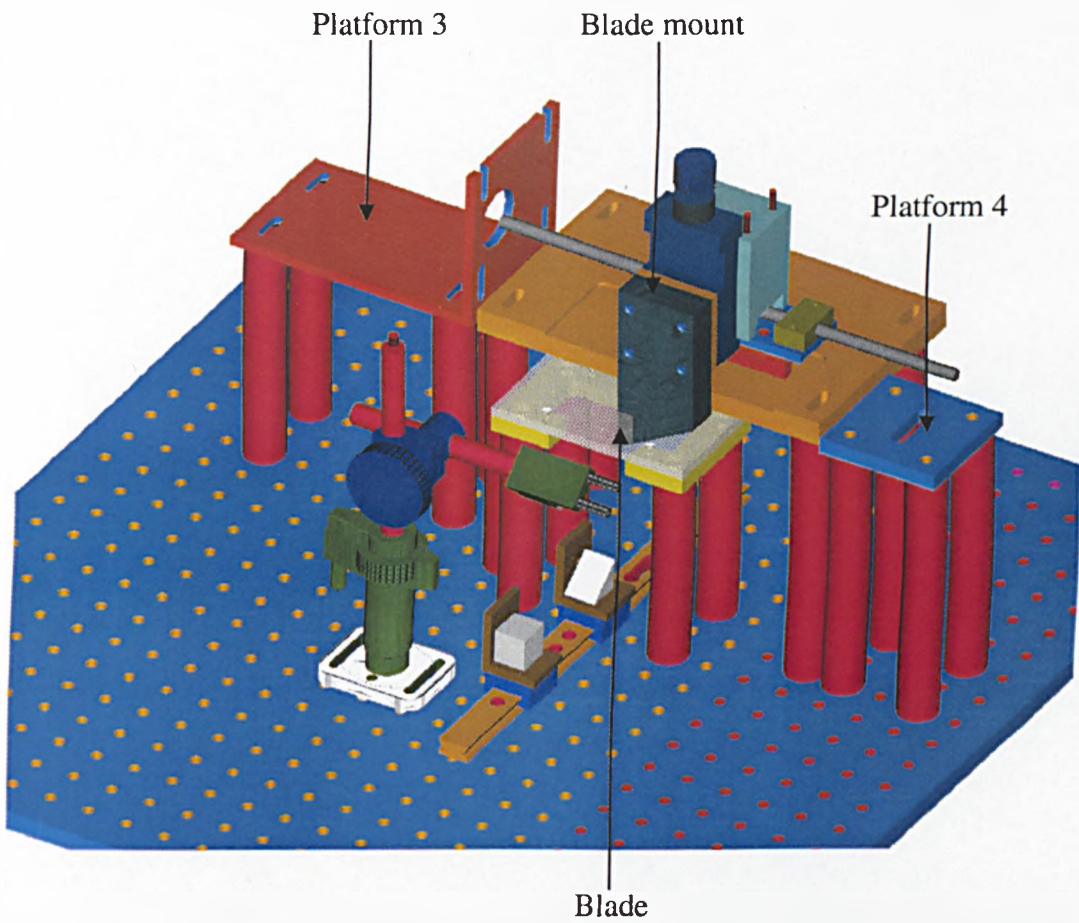


*Figure A3.4: Image of the rig without: the motor, flexible coupling and end bearing.*

A few more components are incorporated to form the image in Figure A3.4. These include the remaining two platforms, the blade mount and the blade. For the image of the complete rig see Figure 6.1.

## References

- Abbott, S., Gaskell, P. and Kapur, N. (2001, private communication) Ink transfer model (ITM): A mathematical model for predicting liquid transfer.
- Aernouts, T., Vanlaeke, P., Poortmans, J. and Heremans, P. (2004) Polymer solar cells: Screen-printing as a novel deposition technique. *Proceedings of SPIE - The International Society for Optical Engineering*. **5464**, p252-260.
- Anderson, J. (2003a) Mesh movement and its impact on screen tension part 1. *Screen Printing -Cincinnati-*. **93**(3), p44-48.
- Anderson, J. (2003b) Mesh movement and its impact on screen tension part 2. *Screen Printing -Cincinnati-*. **93**(4), p52-59.
- Arshak, K., Korostynska, O. and Clifford, S. (2004) Screen printed thick films of NiO and LaFeO<sub>3</sub> as gamma radiation sensors. *Sensors and Actuators, A: Physical*. **110**(1-3), p354-360.
- Avery Dennison – Troubleshooting Printing and Processing of Avery Reflective Sheeting* (2001) [Online]. [Accessed on 3<sup>rd</sup> February 2002]. Available from World Wide Web: <http://www.reflectives.averydennison.com/rfdtech/IB834.pdf>
- Barker, M. J. (c1999) Screen inks. In: R. H. Leach and R. J. Pierce, (eds). *The Printing Ink Manual*. Netherlands: Kluwer Academic Publishers. p599-635.
- Birkenshaw, J. W. (c1999) Screen inks. In: R. H. Leach and R. J. Pierce, (eds). *The Printing Ink Manual*. Netherlands: Kluwer Academic Publishers. p42-52.
- Claypole, T. C., Gethin, D. T., Jewell, E. H. and Appleton, W. (1996) Distortion of the image by the screen printing process. *TAGA*. p69-85.

Claypole, T. C., Gethin, D. T. and Danias, J. (1997) Dot gain and ink transfer behaviour in the screen printing process. *Surface Coatings International*. **5**, p222-229.

Claypole, T. C. (2002) Can you see through your inks? *International Paper Board Industry*. p98-100.

Cummings, E. A., Linquette-Mailley, S., Mailley, P., Cosnier, S., Eggins, B. R. and McAdams, E. T. (2001) A comparison of amperometric screen-printed, carbon electrodes and their application to the analysis of phenolic compounds present in beer. *Talanta*. **55**(5), p1015-1027.

Dong, M. and Chatzis, I. (1995) The imbibition and flow of a wetting liquid along the corners of a square capillary tube. *Journal of colloid and interface science*. **172**, p278-288.

Ertl, P., Wagner, M., Corton, E. and Mikkelsen, S. R. (2003) Rapid identification of viable *Escherichia coli* subspecies with an electrochemical screen-printed biosensor array. *Biosensors and Bioelectronics*. **18**(7), p907-916.

Fawehinmi, O. B., Gaskell, P. H., Jimack, P. K., Kapur, N. and Thompson, H. M. (2005) A combined experimental and computational fluid dynamics analysis of the dynamics of drop formation. *Proceedings of the Institution of mechanical engineers Part C: Journal of Mechanical Engineering Science*. **219**, (accepted for publication on 31<sup>st</sup> May 2005).

*Flow Science, excellence in CFD flow modelling software* (2005) [Online]. [Accessed on 30<sup>th</sup> March 2005]. Available from World Wide Web: <http://www.flow3d.com>

Fox, I., Bohan, M., Claypole, T. and Gethin, D. (2003) Film thickness prediction in halftone screen-printing. *Proceedings of the Institution of mechanical engineers Part E: Journal of Process Mechanical Engineering*. **217**, p345-359.

Ghiurcan, G. A., Lui, C.-C., Webber, A. and Feddrix, F. H. (2003) Development and characterization of a thick-film printed zinc-alkaline battery. *Journal of the Electrochemical Society*. **150**(7), A992-A927.

Hamblyn, S. M., Jewell, E. H., Claypole, T. C. and Gethin, D. T. (2002) An investigation into screen printing using UV process colour inks. *Surface Coatings International Part B: Coatings Transactions*. **85**(2), p95-104.

Hirt, C. W. and Nichols, B. D. (1981) Volume of Fluid (VOF) Method of dynamics of free boundaries. *Journal of Computational Physics*. **39**, p201-225.

Hohl, D. and Hunt, D. (1992) Physical changes in polyester mesh during tensioning. *Screen Printing Technical Foundation*. p1-19.

Hohl, D. (1995) Estimating ink deposit in screen printing: improving your accuracy. *SPTF Practical Application Bulletin*. **April**, p1-14.

Hohl, D. (1997a) Controlling off-contact. *SGIA Journal*. **4<sup>th</sup> Quarter**, p5-11.

Hohl, D. (1997b) Research for the real world. *Screen Graphics*. **March/April**, p20-24, p90.

Hohl, D. (1998) Estimating ink... the SPTF way. *SGIA Journal*. **April**, p21-27.

Huner, B. (1989) A simplified analysis of blade coating with applications to the theory of screen printing. *The International Society of Hybrid Microelectronics*. **12**(2), p88-94.

Hunt, D. and Hohl, D. (1990) SPTF model for determining wet ink deposit thickness from tensioned polyester fabrics. *Screen Printing Technical Foundation*.

Hunt, D. and Hohl, D. (1996a) A guideline to wet and dry ink deposit measurement methods: part 1. *Screen Printing Technical Foundation*. p1-11.

Hunt, D. and Hohl, D. (1996b) A guideline to wet and dry ink deposit measurement methods: part 2. *Screen Printing Technical Foundation*.

Hunt, D. and Hohl, D. (1996c) A guideline to wet and dry ink deposit measurement methods: part 3. *Screen Printing Technical Foundation*. 1-13.

Hunt, D. (1999) Understanding the mechanism: the essence of process control. *SGIA Journal*. 3<sup>rd</sup> Quarter, p51-55.

Jabbour, G., Radspinner, R. and Peyghambarian, N. (2001) Screen printing for the fabrication of organic light-emitting devices. *IEEE Journal on selected topics in quantum electronics*. 7(5), p769-773.

Koenen Screen Printing Fabric (2003) [Online]. [Accessed 25<sup>th</sup> February 2005] Available from World Wide Web: <http://www.koenen.de>

Kühberger, M., Gritzner, G., Fuger, R., Eisterer, M., Tonies, S. and Weber, H. W. (2005) Superconducting MgB<sub>2</sub> films on MgO substrates. *Applied Physics A: Materials Science and Processing*. 80(1), p127-129.

Lee, C.-H., Lee, C.-S and Ha, Y.-H. (1999) Color consistency between different printing materials using got gain and intensity compensation. *IEEE Transactions on Consumer Electronics*. 45(4), p1016-1024.

Liang, T.-X., Sun, W. Z., Wang, L.-D., Wang, Y. H. and Li, H.-D. (1996) Effect of surface energies on screen printing resolution. *IEEE Transactions on Components, Packaging, and Manufacturing Technology – Part B*. 19(2), p423-425.

Llobet, E., Ivanov, P., Vilanova, X., Brezmes, J., Hubalek, J., Malysz, K., Gracia, I., Cane, C. and Correig, X. (2003) Screen-printed nanoparticle tin oxide films for high-yield sensor microsystems. *Sensors and Actuators, B: Chemical*. 96(1-2), p94-104.

Lomas, M. and Short, I. (1999) Screen printing variables and their effect on print paste consumption. *Journal of the society of dyers and colourists*. **115**(9), p262-269.

Mannan, S. H., Ekere, N. N., Lo, E. K. and Ismail, I. (1993) Predicting scooping and skipping in solder paste printing for reflow soldering of SMT devices. *Soldering and Surface Mount Technology*. (15), p14-17.

Mannan, S. H., Ekere, N. N., Ismail, I. and Lo, E. K. (1994) Squeegee deformation study in stencil printing of solder pastes. *IEEE Transactions on components, packaging, and manufacturing technology*. Part A, **17**(3), p470-476.

Martin, R. E., Stirling, A. J. and L'Archevêque, J. V. R. (1974) – The fabrication of reproducible thick film resistors. In: *Machine Design: Electron Components Conference, 24th, Proceedings*. 13<sup>th</sup>-15<sup>th</sup> May 1974, Washington, DC, USA. p192-198.

McCue, G. (2003) Understanding your options in screen cleaning and reclaiming. *Screen Printing -Cincinnati-*. **93**(1), p52-56.

Messerschmitt, E. (1982) Rheological considerations for screen printing inks. *Screen Printing -Cincinnati-*. p62-65.

Owczarek, J. A. and Howland, F. L. (1990) A study of the off-contact screen printing process - I: Model of the printing process and some results derived from experiments. *IEEE Transactions on Components, Hybrids and Manufacturing Technology*. **13**(2), p358-367.

Pardo, D. A., Jabbour, G. E. Peyghambarian, N. (2000) Application of screen printing in the fabrication of organic light-emitting devices. *Advanced Materials*. **12**(17), p1249-1252.

- Parikh, M., Quilty, W. and Gardiner, K. (1991) SPC and setup analysis for screen printed thick films. *IEEE Transactions on Components, Hybrids and Manufacturing Technology*. 14(3), p493-498.
- Riemer, D. E. (1973) Screen printing as a volumetric deposition process. *American Ceramic Society Bulletin*. 52(9), p713.
- Riemer, D. E. (1974) Deposition weight, a powerful tool for the thick-film process. *Proc., International Society for Hybrid Microelectronics Symposium*. p347.
- Riemer, D. E. (1987) The shear and flow experience of ink during screen printing. *Proceedings of the 1987 International Symposium on Microelectronics. International Society for Hybrid Microelectronics*. p335-340.
- Riemer, D. E. (1988) Analytical engineering model of the screen printing process: Part 1. *Solid State Technology*. p107-111.
- Ruff, M. (2001) Screen print densitometry. *SGIA Journal*. 3<sup>rd</sup> Quarter, p3-8.
- Ruschak, K. J. (1982) Boundary conditions at a liquid/air interface in lubrication flows. *Journal of fluid mechanics*. 119, p107-120.
- Saati (2002a) [Online]. Available from World Wide Web: <http://www.saati.com>
- Saati (2002b) *Saatilene table of fabric technical specifications*. Saati Print.
- Sefar (1999a) *Table of fabric technical specifications*. Sefar Group.
- Sefar (1999b) *Handbook for Screen Printers*. Sefar Printing Division. p1.7-1.15, p9.4-9.11.
- Sergent, J. (1985) Thick and thin film microelectronics professional advancement course notes.

Sericol (2002) *The sericol guide to UV screen printing*. Sericol Limited. p7-9.

*Stencils Unlimited: Frameless stencils* (2004) [Online]. [Accessed on 20<sup>th</sup> May 2005].

Available on World Wide Web:

[http://www.stencilsunlimited.com/frameless\\_stencils.php](http://www.stencilsunlimited.com/frameless_stencils.php)

Stephens, J. (1996) *Screen Process Printing*. London: Blueprint

Swiatek, Z., Beltowska, E., Maziarz, W and Krok, F. (2003) Characterization and properties of a modified Si solar cell emitter by a porous Si layer. *Materials Science and Engineering B: Solid-State Materials for Advanced Technology*. **101**(1-3), p291-296.

Thompson, B. (2004) *Printing materials: Science and technology*. Leatherhead: Pira International. p410-415.

*TKB-4U Technical paper about Printing of SMT Solderpaste* (2001) [Online]. [Accessed 20<sup>th</sup> May 2005]. Available from World Wide Web:

<http://www.tkb-4u.com/articles/printing/printstmsol/printsmtsol.php#factors>

Traversa, E., Carotta, M. C. and Martinelli, G. (2000) Nano-sized semiconducting oxide powders for thick film gas sensors: from powder processing to environmental monitoring devices. *Nanophase and Nanocomposite Materials III. Symposium (Materials Research Society Proceedings)*. **581**, p121-132.

Turkusic, E., Kalcher, J., Kahrovic, E., Beyene, N. W., Moderegger, H., Sofic, E., Begic, S. and Kalcher, K. (2005) Amperometric determination of bonded glucose with an MnO<sub>2</sub> and glucose oxidase bulk-modified screen-printed electrode using flow-injection analysis. *Talanta*. **65**(2), p559-564.